The response of stable water isotopes in precipitation and the surface ocean to tropical climate variability

Josephine Brown

Submitted in total fulfilment of the requirements
of the degree of Doctor of Philosophy

School of Earth Sciences
University of Melbourne

February, 2004

Abstract

Stable water isotope records may be used to reconstruct tropical climate variability on seasonal to glacial time scales. Isotopic ratios in precipitation are archived in tropical ice cores, and may be interpreted as records of precipitation, temperature and atmospheric circulation variability in the tropics. Isotopic ratios in the carbonate skeletons of coral and foraminifera record local and mean ocean isotopic ratios as well as sea surface temperature.

Reconstruction of past climate from isotopic records requires assumptions about the isotope–climate relationship on the relevant time scale. In order to test these assumptions, an isotopic tracer scheme in the Melbourne University General Circulation Model is used to simulate the isotope–climate relationship for present day and Last Glacial Maximum climate. A scheme to calculate surface ocean and river runoff isotopic ratios is developed and used to test the sensitivity of the surface ocean isotopic distribution to changes in climate forcing.

Present day climate from 1950–1999 is simulated using observed sea surface temperatures and sea ice coverage, and the interannual variability of the modelled isotopic ratios in precipitation and the surface ocean are compared with observational records. On interannual time scales, the modelled isotopic ratios in tropical precipitation are predominantly controlled by precipitation amount. The isotopic signal also reflects strong modes of tropical climate variability, including El Niño–Southern Oscillation and monsoon variability.

The modelled surface ocean isotopic ratios respond to interannual precipitation and evaporation variability, with a strong El Niño–Southern Oscillation signal in the tropical Pacific. The isotopic variability archived in coral and foraminiferal carbonates reflects both sea surface temperature and local precipitation and evaporation changes, and a modelled "coral" isotopic ratio is able to reproduce this dependence in the simulated present day climate.

Simulations of Last Glacial Maximum climate are carried out with standard

CLIMAP boundary conditions and with cooled tropical sea surface temperatures to examine the isotopic sensitivity to tropical climate forcing under glacial conditions. The isotopic ratios in precipitation over the Andes and Tibetan Plateau respond to changes in precipitation, temperature and atmospheric circulation. The simulated change in isotopic ratios in tropical precipitation at the LGM is not controlled by a single climate parameter, but instead results from a combination of climate forcings.

Surface ocean isotopic ratios respond to changes in the large scale distribution of precipitation and evaporation under glacial conditions. As a result, interpretation of glacial coral and foraminiferal records under the assumption of unchanged local surface ocean isotopic ratios is found to lead to substantial errors in reconstructed sea surface temperatures.

The incorporation of isotopic tracers into General Circulation Models allows the simulation of the complex response of isotopic ratios in precipitation and the surface ocean to large scale changes in climate. As the isotopic response to tropical climate variability on glacial time scales differs from that on interannual time scales, present day isotope–climate relationships cannot be uniformly applied to the interpretation of glacial isotopic records. Instead a combined approach of modelling and palaeoclimate reconstruction from both marine and continental isotopic records is recommended to produce a consistent reconstruction of past climate.

Declaration

This is to certify that:
(i) the thesis comprises only my original work towards the PhD except where indicated in the Preface;
(ii) due acknowledgement has been made in the text to all other material used;
(iii) the thesis is less than 100,000 words in length, exclusive of tables, maps, bibliographies and appendices.

Acknowledgements

I would like to thank my supervisor Ian Simmonds for his encouragement and support, and numerous helpful discussions during the development of this project. I would also like to acknowledge David Noone for assistance with the model and advice in the development of the surface ocean scheme, as well as for stimulating discussions on all questions isotopic and assistance with numerical analysis. Thanks also to Ian Smith for useful advice on climate modelling and the analysis and presentation of my results.

I would also like to acknowledge Richard Wardle for assistance with the trajectory analysis and improving the performance of the model, and Kevin Keay for assistance with statistical and programming questions. Tony Hirst from CSIRO Atmospheric Research kindly provided ocean model output for use in the surface ocean isotopic scheme. I would also like to thank Georg Hoffmann at the LSCE in France for his hospitality during my visit in 2002, and for useful discussions about isotopic modelling.

Many thanks to my fellow meteorology PhD students, in particular thanks to Pandora Hope for interesting discussions about LGM climate, help with NCAR graphics, and for moral support. Also thanks to Lyn, Eun Pa and the rest of the met gang for their support and friendship and to my housemate and workmate Ursula for her encouragement and understanding. Finally, I would like to thank my family and friends for their support over the last three and a half years. In particular thanks to Mum, who has contributed meals, proof reading and constant encouragement.

Contents

List of Figures

List of Tables

Chapter 1

Introduction

1.1 Preliminary comments

An understanding of natural climate variability in the tropics on a range of time scales is important for the prediction of the response of tropical climate to anthropogenic climate change. As instrumental records of tropical climate are limited to the last few centuries in most cases, the use of proxy records to reconstruct climate variability on longer time scales is an important component of such investigations. Stable water isotope ratios archived in ice cores, coral and foraminiferal carbonate and other proxy records can be used to reconstruct past tropical precipitation, temperature and atmospheric circulation.

The interpretation of isotopic records of tropical climate requires assumptions about the relationship of isotopic ratios in precipitation and the surface ocean to the relevant climate parameters. These assumptions are commonly derived from examination of present day isotope–climate relationships. However the application of present day seasonal or interannual isotope–climate relationships to the interpretation of climate variability on glacial time scales requires that these relationships are valid under climate conditions which may be greatly different to the present day.

While isotopic ratios in tropical precipitation may be primarily influenced by precipitation amount on seasonal and interannual time scales, changes in temperature, moisture source regions and atmospheric transport may be important on glacial time scales. Similarly, while marine isotopic records from the upper ocean may respond mainly to local sea surface temperature (SST) changes on interannual time scales at a given location, under glacial conditions the local precipitation and evaporation balance may be the main control on the surface ocean isotopic ratio at the same location.

1.2 Aims

The primary aim of this study is to determine the extent to which present day relationships between tropical climate and isotopic ratios in precipitation and the surface ocean may be applied to interpretations of isotopic records of past climate. Using a modelling approach, the limitations of tropical palaeoclimate reconstruction using present day relationships will be quantified.

The first component of this study aims to identify the present day isotope–climate relationships for tropical precipitation and the surface ocean on seasonal and interannual time scales. Employing a climate model with isotopic tracers, which includes an isotopic surface ocean scheme developed for this study, the controls on the modelled isotopic signal will identified. The modelled isotopic distribution will also be compared with observational records to validate the modelled isotopic response to tropical climate variability.

The model will then be used to simulate the climate of the Last Glacial Maximum (LGM), and the mean shift in both climate and isotopic distributions will be compared. The relationship between changes in tropical temperature, precipitation and circulation and the isotopic anomalies in precipitation and the surface ocean constitute the isotope–climate relationship on glacial time scales. The glacial relationship and the relationships on present day seasonal and interannual time scales will be compared and the implications for palaeoclimate reconstruction discussed.

1.3 Outline of thesis

In **Chapter 2** the fundamental processes governing stable water isotopic variability are outlined. The observed spatial and temporal variability of isotopes in precipitation and the surface ocean is described, and the specific characteristics of the isotope–climate relationship in the tropics is outlined. Archives of isotopic ratios in precipitation in tropical ice cores, and surface ocean isotopic ratios in coral and foraminifera are described. Finally, previous atmospheric and ocean modelling studies of water isotopes in the tropical climate are briefly surveyed.

Chapter 3 describes the Melbourne University General Circulation Model (MUGCM) and the stable water isotope tracer scheme implemented in the model. The climatological distributions of surface temperature, pressure, precipitation and atmospheric circulation simulated by the model are compared with observations. The parameterisation of isotopic fractionation processes is described and the modelled isotopic distribution is validated in comparison with observed isotopic ratios in precipitation. The results of sensitivity tests of the modelled isotopic distribution to changes in land distribution and SST gradients are also presented.

In **Chapter 4** modifications to the isotopic tracer scheme are described. The inclusion of a scheme to calculate surface ocean isotopic ratios from atmospheric moisture fluxes is outlined, and the modelled surface ocean isotopic distribution compared with observations. The implementation of an isotopic river runoff scheme and the contribution of the simulated runoff to the surface ocean isotopic distribution is described, and the modelled runoff isotopic ratios verified against observations. Upper ocean horizontal transport is modelled with the inclusion of modelled ocean currents in the surface ocean isotopic scheme. The prognostic snow scheme in the model is also modified to incorporate isotopic tracers and the contribution of snow melt to continental runoff examined.

In **Chapter 5** the results of a simulation of present day climate from 1950–1999 are presented. Forcing the model with observed monthly SSTs and sea ice coverage, the resulting seasonal and interannual tropical climate variability is described. The main features of interannual climate variability in the tropics, El Niño–Southern Oscillation (ENSO) and monsoon variability, are compared with the observed modes and with other modelling studies in order to determine how well the model simulates the tropical climate.

The isotopic response to the simulated climate is then described both in terms of precipitation and surface ocean isotopic ratios. The response of isotopes in precipitation to changes in precipitation amount, surface temperature and atmospheric circulation on interannual time scales is examined. The surface ocean isotopic response to changes in precipitation and evaporation is also examined. The modelled isotopic distribution is compared with observational records and with the signal in ice core and coral records in order to validate the simulation of the present day isotope–climate relationship.

In **Chapter 6** model simulations of the climate of the LGM are presented. The LGM climate is simulated with two different sets of SST boundary conditions in order to test the sensitivity of the tropical climate and isotopic distribution to specific SST forcings. The modelled LGM climate is described and the response of isotopes in precipitation and the surface ocean to glacial climate conditions is outlined. The isotopic distribution in precipitation and the surface ocean is compared with continental and marine isotopic records from the LGM, and the agreement of the two simulations with isotopic records is discussed.

The differences between present day and LGM isotopic ratios in precipitation and the surface ocean are compared with changes in temperature, precipitation, evaporation and atmospheric circulation to identify the main factors in the glacial to present day shift in tropical isotopic values. The tropical LGM to present day isotope–climate relationships identified are compared with the relationships on present day seasonal and interannual time scales.

In **Chapter 7** the results of the study are summarised and the implications for the reconstruction of tropical climate from isotopic records are outlined. The role of modelling isotopes in precipitation and the surface ocean in improving and validating palaeoclimate reconstructions is discussed.

Chapter 2

Stable water isotopes and tropical climate

A range of empirical and theoretical studies have laid the foundations for the use of stable water isotope ratios in investigating the hydrologic cycle and interpreting isotopic palaeoclimate records. Early empirical studies investigated the main physical processes governing isotopic fractionation of water molecules under laboratory conditions. Simple models based on these empirical studies were applied to the interpretation of observational records from the global network of sampling stations, and from a range of local and regional observations. More recently, the development of sophisticated numerical models incorporating water isotope tracers has led to further advances in the understanding of the isotopic response to climate variability on a range of temporal and spatial scales.

The physical processes governing equilibrium and non-equilibrium isotopic fractionation, reevaporation and exchange are described below. The observed spatial distribution of isotopes in precipitation is then outlined with reference to the main spatial isotope–climate relationships. The observed response of isotopes in the hydrologic cycle to tropical climate variability on daily to inter-annual time scales is outlined. Isotopic records of palaeoclimate in tropical ice cores and marine carbonates are described. Finally, previous modelling studies of isotopes using atmospheric and ocean models incorporating isotopic tracers are surveyed.

2.1 Isotopic fractionation

2.1.1 Equilibrium fractionation

Hydrogen exists naturally in two stable isotopic forms (^{1}H, protium and ^{2}H or D, deuterium) while oxygen has three stable isotopic forms (^{16}O, ^{17}O and ^{18}O). Water molecules can therefore occur with any combination of these isotopes, although the only three forms existing in readily measurable quantities are $H_2^{18}O$, HDO and the "normal" water molecule $H_2^{16}O$.

The ratio of isotopically heavy to normal water is commonly expressed in parts per thousand (‰) relative to the ratio in Standard Mean Ocean Water (SMOW):

$$\delta = (\frac{R_{sample}}{R_{SMOW}} - 1) \times 1000 \tag{2.1}$$

where the standard ratios are given by R = 0.15595×10^{-3} for HDO [*De Wit et al.*, 1980] and R = 2.00520×10^{-3} for $H_2^{18}O$ [*Baertschi*, 1976].

The ratio of isotopically heavy water to normal water is altered at phase transitions due to the different saturation vapour pressures of the isotopic species. Thus the ratio of the saturation vapour pressures of the normal and isotopically heavy water (e and e_i respectively) gives the (equilibrium) fractionation factor $\alpha = e/e_i$ [*Craig*, 1961; *Dansgaard*, 1964]. The fractionation factor is greater than unity as the condensate is isotopically enriched relative to the vapour. The reverse relationship holds for evaporation, with the fractionation factor inverted.

The temperature dependence of vapour pressure implies that the fractionation factor is also dependent on temperature:

$$\alpha \propto exp\frac{L_i m_i - Lm}{RT} \tag{2.2}$$

where L and L_i are the latent heats of fusion, m and m_i are the molecular weights for normal and isotopically heavy water respectively, R is the ideal gas constant and T is the temperature.

The fractionation factors are found empirically as a function of temperature, $T(K)$, expressed as series expansions, for the liquid to vapour change [*Majoube*, 1971a]:

$$\begin{aligned} ln\alpha_{HDO} &= \frac{24.844}{T^2} \times 10^3 - \frac{76.248}{T} + 52.612 \times 10^{-3} \\ ln\alpha_{H_2^{18}O} &= \frac{1.137}{T^2} \times 10^3 - \frac{0.4156}{T} - 2.0667 \times 10^{-3} \end{aligned} \tag{2.3}$$

In the case of solid to vapour fractionation, the formulations of *Merlivat and Nief* [1967] for HDO and *Majoube* [1971b] for H_2^{18}O are used:

$$\begin{aligned} ln\alpha_{HDO} &= \frac{16288}{T^2} - 9.34 \times 10^{-2} \\ ln\alpha_{H_2^{18}O} &= \frac{11.839}{T^2} - 28.224 \times 10^{-3} \end{aligned} \tag{2.4}$$

Total equilibrium model

The "closed system" model of equilibrium fractionation assumes that the two phases are in contact in a closed system and reach total equilibrium, as may occur within a well-mixed cloud during stratiform or convective precipitation formation. The fractionation due to condensation assuming total equilibrium is:

$$\frac{q_{ic}}{q_c} = \alpha(T)\left(\frac{q_{iv}}{q_v}\right) \tag{2.5}$$

where q_c and q_{ic} are the normal water mixing ratio and the isotopic water mixing ratio for the condensate, q_v and q_{iv} are the same for the vapour and $\alpha(T)$ is the fractionation factor at temperature T.

Rayleigh distillation model

The other commonly used model of fractionation is the Rayleigh distillation ("open system") model which assumes that the condensate is instantly removed after formation, such as may occur when solid condensate is formed during convection. The Rayleigh model also assumes that a constant fractionation factor may be used to describe the process. In this case, isotopic equilibrium exists only between the vapour and the newly formed condensate:

$$\frac{dq_{iv}}{dq_v} = \alpha(T)\left(\frac{q_{iv}}{q_v}\right) \tag{2.6}$$

Integrating from the initial mixing ratio (q_i, q) to the final state (q_i', q') and assuming that the fractionation coefficient is constant for the process, the following relation is obtained:

$$q_{ic}' = q_{ic} \left(\frac{q_v'}{q_v} \right)^{\alpha} \tag{2.7}$$

The ratio of final to initial water mixing ratios (q_v'/q_v) is described as the "rainout" from the initial moisture, and according to the Rayleigh model, for a given initial isotopic ratio the resulting isotopic depletion depends only on the rainout. As condensation proceeds, the depletion of the vapour increases, producing greater instantaneous and total isotopic depletion of the precipitation compared with the total equilibrium case. Real physical processes will therefore lie between the two extreme cases of total equilibrium and Rayleigh distillation.

2.1.2 Non-equilibrium processes

When phase changes occur too rapidly for isotopic equilibrium to be established, fractionation must be described in terms of non-equilibrium effects. Under non-equilibrium conditions the extent of fractionation depends on the different rate of molecular diffusivity of the isotopic species compared with the normal water molecule, hence the term kinetic fractionation or "kinetic effects". Kinetic fractionation therefore differs from equilibrium fractionation which depends on the molecular weights of the different isotopic species and their resulting saturation vapour pressures.

Kinetic effects occur during evaporation into an atmosphere with relative humidity of less than 100%, or where there are strong surface winds removing the vapour as it forms [*Merlivat and Jouzel*, 1979]. Kinetic fractionation is also significant during the formation of solid condensate at very low temperatures (below −20°C) where the atmosphere around the condensate will become super-saturated [*Jouzel and Merlivat*, 1984]. During the reevaporation of falling drops below the condensation level, kinetic fractionation occurs in the boundary atmospheric layer between the liquid surface and the free atmosphere [*Stewart*, 1975].

Deuterium excess

As the ratio of molecular diffusivities is approximately the same for HDO and $H_2^{18}O$, the kinetic effects are also similar, whereas equilibrium fractionation is approximately eight times greater for HDO than for $H_2^{18}O$. The observed ratio of HDO to $H_2^{18}O$ in global precipitation is described by the Meteoric Water Line (MWL) [*Craig*, 1961]:

$$\delta\mathrm{D} = 8\delta^{18}\mathrm{O} + 10‰ \tag{2.8}$$

The slope of 8 is approximately the value which results from Rayleigh condensation of precipitation at 100% humidity, or the ratio of equilibrium fractionation factors at around 25–30°C [*Kendall and McDonell*, 1998]. The intercept of +10‰ is due to the average kinetic enrichment of vapour evaporating from the ocean with near surface relative humidity of 85% at around 20°C. Without kinetic effects, the intercept would be $\delta = 0‰$, the SMOW value (assuming this is the mean ocean value). A measure of the extent of kinetic effects is the "deuterium excess", d:

$$d = \delta\mathrm{D} - 8\delta^{18}\mathrm{O} \tag{2.9}$$

Evaporation into an atmosphere with less than 100% relative humidity increases d from zero at the surface ocean, and d also increases with increasing SST, implying a decrease towards high latitudes: *Johnsen et al.* [1989] find that d increases with SST by +0.35‰/°C and with decreasing relative humidity by −0.43‰/%. Increased precipitation d values are found due to kinetic effects during the formation of solid condensate at very low temperatures under supersaturation. During (rapid) reevaporation into a dry and warm atmosphere below the condensation level, the deuterium excess of precipitation decreases [*Dansgaard*, 1964].

The deuterium excess of precipitation can be used to diagnose information about climatic conditions at the ocean source region, assuming that kinetic effects related to condensation and post-condensation processes are not significant. If this is the case, the deuterium excess is determined by the rate of evaporation at the source, being a function of atmospheric relative humidity, wind speed and SST.

As HDO and $H_2^{18}O$ vary in parallel except for kinetic effects, $H_2^{18}O$ will be discussed with applicability to both isotopic species unless otherwise stated.

The deuterium excess will be used to illustrate the extent of kinetic fractionation causing deviation from the MWL.

2.1.3 Reevaporation and exchange

As the condensate falls through vapour below the condensation level, it undergoes both molecular exchange with the surrounding vapour and evaporation of some of the condensate [*Craig et al.*, 1963; *Stewart*, 1975]. Diffusive molecular exchange occurs with isotopically heavier vapour near the ground, leading to an enrichment relative to the initial precipitation. The extent of exchange will diminish as the isotopic ratio of the lower level vapour decreases and approaches that of the condensate. Thus during more extensive precipitation events the enrichment due to exchange is reduced.

Additional isotopic fractionation occurs as some of the condensate evaporates while passing through non-saturated layers below the formation level, leading to an isotopic enrichment of the condensate. Reevaporation is believed to occur with non-equilibrium kinetic effects when the surrounding atmosphere has a very low relative humidity and hence the reevaporation is too rapid for equilibrium to be reached [*Stewart*, 1975]. No fractionation will occur for reevaporation of solid condensate due to the extremely slow rate of molecular diffusion in the solid phase (10^{-14} m^2s^{-1} at 0°C) [*Jouzel and Merlivat*, 1984; *Jouzel et al.*, 1987b].

2.2 Spatial distribution of isotopes

2.2.1 Isotopes in precipitation

The systematic monitoring of stable water isotope ratios in precipitation began with the establishment of the International Atomic Energy Agency/World Meteorological Organisation Global Network of Isotopes in Precipitation (GNIP) in 1961 [*IAEA/WMO*, 2001]. Since then, stable water isotope ratios as well as temperature, pressure and precipitation amount have been measured on a monthly basis at more than 550 stations around the globe (Figure 2.1). Many of the isotopic records are discontinuous and cover different periods of time. The spatial coverage of the network is also limited, with a large number of stations in the Northern Hemisphere mid-latitudes and sparse coverage of the Southern Hemisphere and tropical oceans.

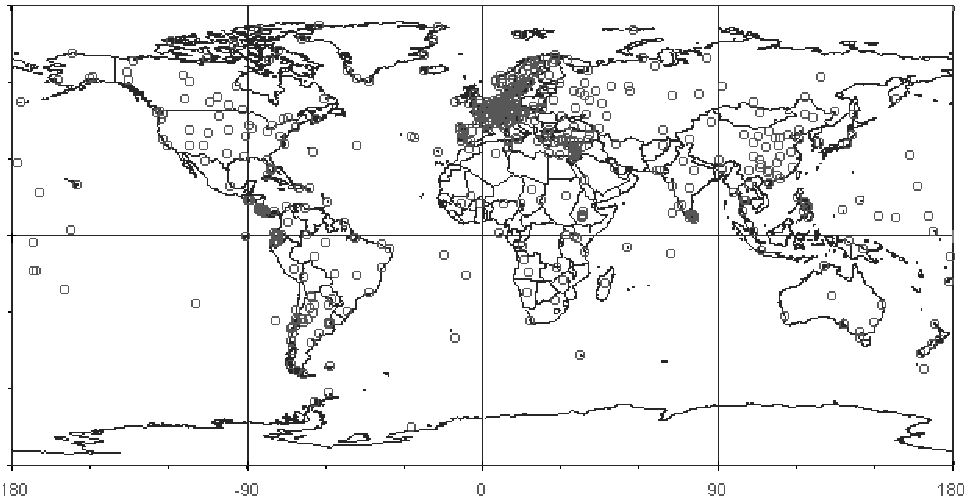

Figure 2.1: Stations of the Global Network of Isotopes in Precipitation. From *IAEA/WMO* [2001].

Stable water isotope δD and δ^{18}O values are archived in the GNIP database, and the spatial and temporal distributions of the observed isotopic ratios have been discussed in many studies of isotope–climate relationships [eg. *Dansgaard*, 1964; *Rozanski et al.*, 1993; *Araguás-Araguás et al.*, 2000]. The spatial distribution of isotopes in precipitation has been found to vary with local surface temperature and precipitation amount, distance inland from ocean moisture source ("continentality") and altitude. These relationships are described below.

Temperature effect

The correlation between surface temperature and precipitation δ^{18}O was first identified by *Dansgaard* [1964], and confirmed by later studies [eg. *Rozanski et al.*, 1993; *Araguás-Araguás et al.*, 2000]. This so-called "temperature effect" leads to an increasing isotopic depletion with latitude in the spatial distribution of δ^{18}O, as seen in Figure 2.2. The relationship produces a strong linear correlation between annual mean surface temperature and precipitation δ^{18}O at mid- and high latitudes. This spatial temperature–isotope correlation has been utilised in the reconstruction of past temperature variability from isotopic records in polar ice cores [eg. *Jouzel et al.*, 1987a], as discussed in Section 2.4.

The spatial isotope–temperature relationship is the result of increased iso-

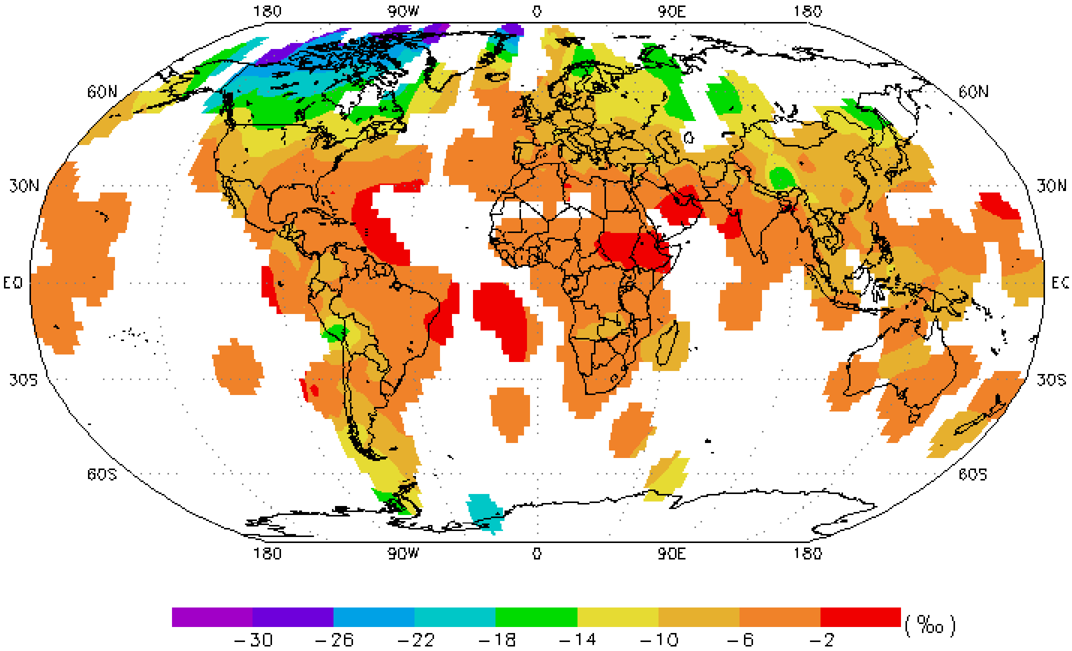

Figure 2.2: Observed (GNIP) annual average precipitation δ^{18}O. From *IAEA/WMO* [2001].

topic depletion of precipitation as moisture is transported towards higher latitudes. The progressive cooling of atmospheric moisture leads to preferential rainout of the heavy isotope. Assuming a Rayleigh distillation model, the atmospheric vapour becomes progressively isotopically lighter, leading to isotopically lighter precipitation. While the real system also includes entrainment and mixing of air masses with different condensation histories, the strong observed temperature–δ^{18}O correlation at mid- and high latitudes suggests that Rayleigh distillation provides an adequate first-order description of the isotopic processes.

It should be noted that it is largely the variation of the extent of rainout with temperature rather than the temperature dependence of the fractionation factor itself that is the leading mechanism for the temperature–δ^{18}O relationship [eg. *Hoffmann and Heimann*, 1997]. While fractionation does increase at cooler temperatures (Equations 2.3 and 2.4), this effect is a small component of the total isotopic depletion compared with the rainout of the heavy isotope due to cooling of atmospheric vapour.

Amount effect

At locations with an annual average surface temperature above approximately 15°C it is found that the linear temperature–δ^{18}O relationship breaks down [*Dansgaard*, 1964]. In the tropics the seasonal and interannual temperature range is small and the moisture source for precipitation is generally local. In these conditions, the main source of isotopic depletion is rainout within local convective systems, where a high proportion of the initial atmospheric vapour may be precipitated out, leading to strong isotopic depletion. The extent of isotopic depletion will therefore be correlated with the local precipitation amount, the isotopic "amount effect".

The amount effect is seen in the GNIP observations (Figure 2.2) with tropical δ^{18}O values being lower in regions of high precipitation, including the Inter-Tropical Convergence Zone (ITCZ) and the western Pacific Warm Pool [eg. *Rozanski et al.*, 1993; *Araguás-Araguás and Froehlich*, 1998]. A significant correlation between precipitation amount and δ^{18}O is most clearly identified for tropical island locations, where the conditions reflect the surrounding ocean with local and isotopically fairly uniform precipitation moisture sources. For tropical continental areas, isotopic depletion may also depend on changes in moisture source and transport such as those associated with the monsoon [*Hoffmann and Heimann*, 1997]. As a result, linear precipitation amount–δ^{18}O relationships are generally identified on a regional or local scale only.

Physically, the vertical circulation of vapour within convective cells results in cooling of the moisture and progressive isotopic depletion with rainout. Therefore the amount effect can be seen as equivalent to the temperature effect except that the cooling occurs vertically rather than horizontally. As the strength of local convective rainout will depend on factors such as the position of the ITCZ or orographic forcing, it will not necessarily be correlated with surface temperature, hence the break-down of the temperature effect in the tropics [*Hoffmann and Heimann*, 1997].

In addition to the rainout of heavy isotopes during condensation, the extent of reevaporation and exchange under the condensation level is believed to contribute the amount effect. The higher relative humidity during intense convective events reduces both reevaporation and exchange, and hence reduces the isotopic enrichment of the resulting precipitation. These post-condensation effects are argued by *Dansgaard* [1964] to be the primary cause of the amount effect. However *Yapp* [1982] compares observational samples for which post-condensation processes are minimal and finds that a significant component of the amount effect is due to the intensity of precipitation events and the total amount of precipitation.

Continental and altitude effects

As moisture is transported inland from oceanic source regions, depletion in the heavy isotope occurs during precipitation events. Thus the further inland the precipitation site, the higher the depletion, resulting in a "continental effect" [eg. *Rozanski et al.*, 1982]. This effect is seen in the GNIP observations with greater isotopic depletion inland over all major continental areas, although the depletion may also be associated with increased surface elevation. This effect also contributes to the seasonal variation in precipitation isotopic ratios for those regions influenced by the Asian and Indian monsoon. The wet season brings moist, isotopically less depleted air from oceanic sources whereas during the dry season the circulation reverses bringing isotopically depleted continental air masses [*Hoffmann and Heimann*, 1997].

Some continental precipitation will originate from lakes, rivers and soil moisture reservoirs due to evaporation over land surfaces. Evapotranspiration is known to preserve the isotopic ratio of the ground moisture source [*Zimmerman et al.*, 1967] as the amount of water in the leaves is small compared to the amount of water passing through them [*White and Gedzelman*, 1984]. Therefore moisture added to the atmospheric vapour from continental evaporation will have the same isotopic ratio as the local precipitation and soil moisture.

As local precipitation will generally be more isotopically depleted than oceanic moisture, continental recycling reduces the isotopic ratio of the vapour compared to oceanic evaporation [*Koster et al.*, 1993]. However as recycling reduces the net rainout of moisture during inland transport, it increases the isotopic ratio of the vapour compared to a situation of no recycling, reducing the continental precipitation δ^{18}O gradient. This is particularly important for precipitation over the Amazon basin, where a large proportion of moisture is recycled [*Gat and Matsui*, 1991].

The cooling of atmospheric moisture during orographic lifting over mountain ranges will also lead to isotopic rainout with altitude. The vertical temperature gradient produces an isotopic depletion with elevation of between -0.15‰ and -0.5‰/100 m for $H_2^{18}O$ and -1‰ to -4‰/100 m for HDO [*Siegenthaler and

Oeschger, 1980]. The altitude effect is significant for tropical and subtropical ice core records from the Andes and Tibetan Plateau where substantial cooling occurs as moisture is transported from sea level to the condensation level above mountain ice caps [*Grootes et al.*, 1989; *Thompson et al.*, 2000a].

The separation of continental and altitude effects from other (temperature, amount) effects is somewhat arbitrary as these are simply empirical relationships inferred from the observed isotopic distribution. The rainout of moisture with continentality and altitude is generally associated with cooling, as well as with the local precipitation amount and the total precipitation during transport. In all cases the underlying factor in the isotopic content of precipitation is the extent of rainout from the original vapour, which may occur through local convection, orographic lifting, or gradual rainout during transport from ocean source to inland continental sites.

2.2.2 Vertical atmospheric isotope distribution

The vertical distribution of isotopes in tropospheric water vapour can be estimated from a Rayleigh model assuming a mean moist adiabatic lapse rate, and constant mean relative humidity at all atmospheric levels [*Araguás-Araguás et al.*, 2000]. The specific humidity is therefore a function of elevation above ground level, and the water vapour content decreases exponentially with height. The isotopic content of water vapour in the Rayleigh model depends only on the ratio of specific humidity at a given height to the initial surface specific humidity, and so the isotopic ratio is predicted to also decrease exponentially.

Measurement of the vertical profile of deuterium ratios in the troposphere up to altitudes of 5 km have been carried out over Germany [*Taylor*, 1972] and the USA [*Ehhalt*, 1974], with a number of vertical profiles obtained over a year in each case. The observed profile decreases strongly with height in the lower atmosphere despite vertical mixing. *Rozanski et al.* [1982] suggest that isotopic exchange within the cloud may be partly responsible for the steepness of this profile. It is also suggested that the observed increase of δD above the tropopause may be due to the oxidation of isotopically enriched methane producing water vapour in the stratosphere.

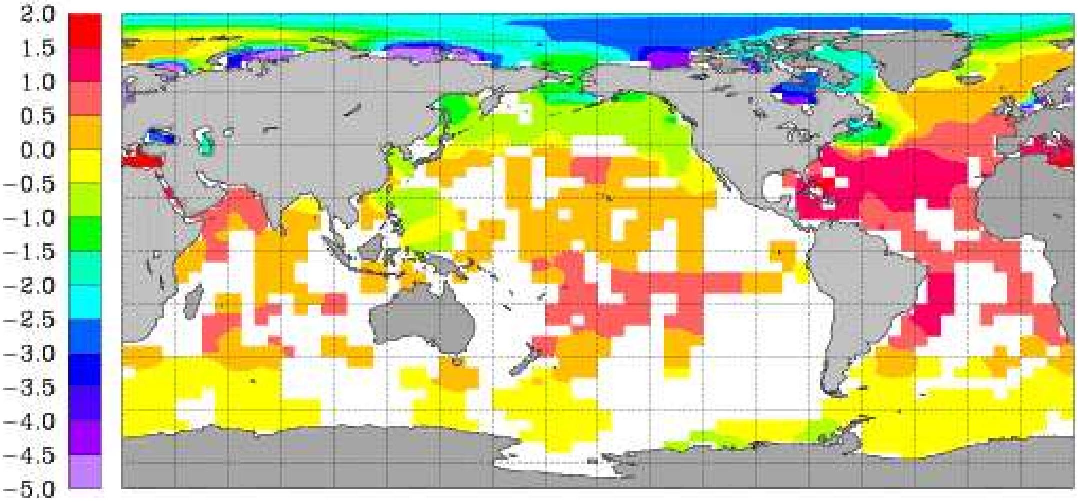

Figure 2.3: Observed (GSO) ocean δ^{18}O from upper 50 m of ocean. From *Bigg and Rohling* [2000].

2.2.3 Oceanic isotope distribution

Surface ocean δ^{18}O is not spatially or temporally constant, but varies in response to local precipitation and evaporation, as well as vertical and horizontal ocean transport, river runoff and sea ice melting and formation. As precipitation will generally have lighter δ^{18}O value than the surface ocean, influx of precipitation will cause the surface ocean δ^{18}O to decrease, while evaporation preferentially removes the lighter isotopic species, enriching the surface ocean δ^{18}O. Inflow of isotopically depleted continental runoff, particularly Northern Hemisphere snow melt, produces lighter surface ocean δ^{18}O.

The NASA-GISS Global Seawater Oxygen-18 (GSO) database includes data from over 17,000 seawater isotopic measurements made since 1950 [*Schmidt*, 1999a; *Bigg and Rohling*, 2000]. The data from all measurements in the top 50 m of the ocean is interpolated onto a $4° \times 5°$grid to provide a global map of surface ocean δ^{18}O as shown in Figure 2.3. The observed surface δ^{18}O values are in the range of +2.5‰ to −6‰, with most tropical and mid-latitude values falling within the range of ±2‰. The lowest observed values are located in high latitudes in the Northern Hemisphere due to runoff of isotopically light continental precipitation. The isotopic ratios are most strongly enriched in the vicinity of the subtropical anticyclones, in particular in the Atlantic Ocean, where evaporation exceeds precipitation.

The deep ocean vertical isotopic profile has also been measured in a number of ocean surveys, and the results collated in the NASA-GISS GSO database [*Bigg and Rohling*, 2000]. The ocean isotopic content is essentially a tracer of ocean water masses, being chemically and dynamically passive. The isotopic content of the upper ocean varies more widely than that of the deep ocean, where mixing produces mean isotopic ratios characteristic of each water mass. For example, Antarctic Bottom Water has a mean isotopic content of δ^{18}O = -0.2‰ while North Atlantic Deep Water has a mean δ^{18}O = +0.25‰ [*Paul et al.*, 1999].

2.3 Isotopes and tropical climate variability

In tropical regions the correlation between precipitation amount and δ^{18}O replaces the temperature–isotope relationship of high latitudes as the dominant climate–isotope relationship, as discussed above. However the specific local relationship between precipitation δ^{18}O and climate parameters such as precipitation amount, temperature and atmospheric circulation varies depending on the time scale being considered. A similar variation of the controls on precipitation δ^{18}O with time scale applies to high latitudes, as discussed by *Noone* [2001] and *Noone and Simmonds* [2002].

The different tropical precipitation δ^{18}O–climate relationships on synoptic, seasonal and interannual time scales will be outlined in relation to basic theoretical considerations and observational studies. These relationships are examined further in Chapters 3 for the modelled isotope climatology, in Chapter 5 for the simulated climate from 1950–1999 and in Chapter 6 in relation to the climate of the LGM. The behaviour of the surface ocean isotopic ratio will not be discussed in detail as the surface ocean δ^{18}O–climate relationship is similar on all time scales for which the mean ocean isotopic ratio does not change.

2.3.1 Synoptic scale variability and tropical cyclones

The amount effect on monthly and seasonal time scales can be considered to be the cumulative effect of isotopic rainout within synoptic scale precipitation events on a time scale of days. *Yapp* [1982] investigated the physical relationship between precipitation intensity and the amount effect using rainfall samples from tropical island locations. This study found that both the intensity of precipitation and isotopic depletion within precipitation events depended on the initial and final temperature of condensation. A strong intensity–δ^{18}O relationship was therefore found where the initial temperature of condensation, the initial δ^{18}O of the source moisture and the extent of rainout were approximately constant.

The most intense precipitation events in the tropics are associated with tropical cyclones. *Lawrence and Gedzelman* [1996] found that tropical cyclones typically have isotopic ratios below the normal tropical precipitation range, forming a distinct population separate from the other tropical or summer precipitation. They found that a series of 166 rain samples from storms that struck near Houston, Texas from 1985 to 1992 had a mean isotopic value of $-2.9‰$, while a set of 47 rain samples from five tropical cyclones that made landfall in the western Gulf of Mexico from 1988 to 1993 had a mean isotopic value of $-9.4‰$.

Lawrence and Gedzelman [1998] also found that the isotopic ratios of precipitation from tropical cyclones decrease rapidly inward, with the lowest values found near the eye wall of the cyclone. They explained this as a result of exchange and evaporation undergone by the moisture as it passed through successive rain bands inside the tropical cyclone. The low isotopic ratios from tropical cyclone precipitation are a result of the longevity, size and high precipitation efficiency (rainout) of the systems. Over time the mean isotopic ratio of the precipitation approaches that of the source vapour.

Noone and Simmonds [2002] and *Treble et al.* [submitted] found a similar bimodal structure in the frequency distribution of isotopic ratios from daily precipitation samples recorded at Margate in Tasmania, Australia. The bimodal distribution of precipitation δ^{18}O was attributed to different types of precipitation events, with the greater isotopic depletion being associated with strong frontal systems and meridionally transported low pressure systems, indicating that the amount effect is also important on the time scale of individual events at mid-latitudes.

2.3.2 Seasonal variability

Precipitation in the tropics is highly seasonal, with the monsoon or summer wet season bringing the majority of precipitation to many regions. The seasonal distribution of precipitation δ^{18}O is strongly inversely related to the seasonal cycle of precipitation amount, while local surface temperature may be positively correlated, uncorrelated or negatively correlated with δ^{18}O depending on the influence of precipitation, circulation and moisture source variability. Examples of the different seasonal δ^{18}O–temperature and δ^{18}O–precipitation relationships are shown in Figure 2.4 using GNIP monthly observations from a tropical island station, a continental station influenced by the Indian monsoon and a station in central Brazil dominated by the seasonal migration of the ITCZ.

The seasonal isotopic signal at tropical ocean and island locations is dominated by the precipitation amount effect. As the vapour source is isotopically uniform, and the seasonal temperature range is small, the isotopic signal is inversely related to the amount of precipitation, with an observed correlation of $r = -0.9$ for monthly anomalies at GNIP tropical island stations [*Hoffmann and Heimann*, 1997]. At Truk, central Pacific Ocean (7.97°N, 151.86°E), the annual temperature range is only 0.3°C, and the lowest δ^{18}O values are observed in the Northern Hemisphere summer when the ITCZ is located at this latitude, leading to enhanced convection and higher precipitation.

The isotopic ratio of precipitation from continental regions strongly influenced by monsoonal activity is more affected by changes in circulation and moisture source than tropical ocean regions. In the Indian and Asian monsoon region there are two isotopically different moisture sources — depleted continental vapour and less depleted vapour from the Indian and Pacific Oceans, producing isotopic variability independent of local precipitation amount or temperature [*Araguás-Araguás and Froehlich*, 1998]. Observations from this region display a lower correlation between δ^{18}O and precipitation amount ($r = -0.8$) than is seen for tropical ocean stations [*Hoffmann and Heimann*, 1997].

The seasonal isotopic signal at New Delhi, India (28.58°N, 77.2°E) as shown in Figure 2.4 illustrates the influence of the Indian monsoon, with moisture reaching this inland location after travelling from the source region in the Bay of Bengal. The seasonal cycle of δ^{18}O is not directly related to either local temperature or precipitation, although the amount relationship appears stronger despite the large annual temperature range. The largest precipitation totals are seen in July and August, while the strongest isotopic depletion occurs a month later in September as the seasonal reversal of circulation to the northwest occurs [*Araguás-Araguás and Froehlich*, 1998].

A different seasonal isotope–climate relationship is seen at inland continental sites such as Manaus in central Brazil (3.12°S, 60.02°W), where the isotopic signal is positively correlated with temperature but controlled by the seasonal

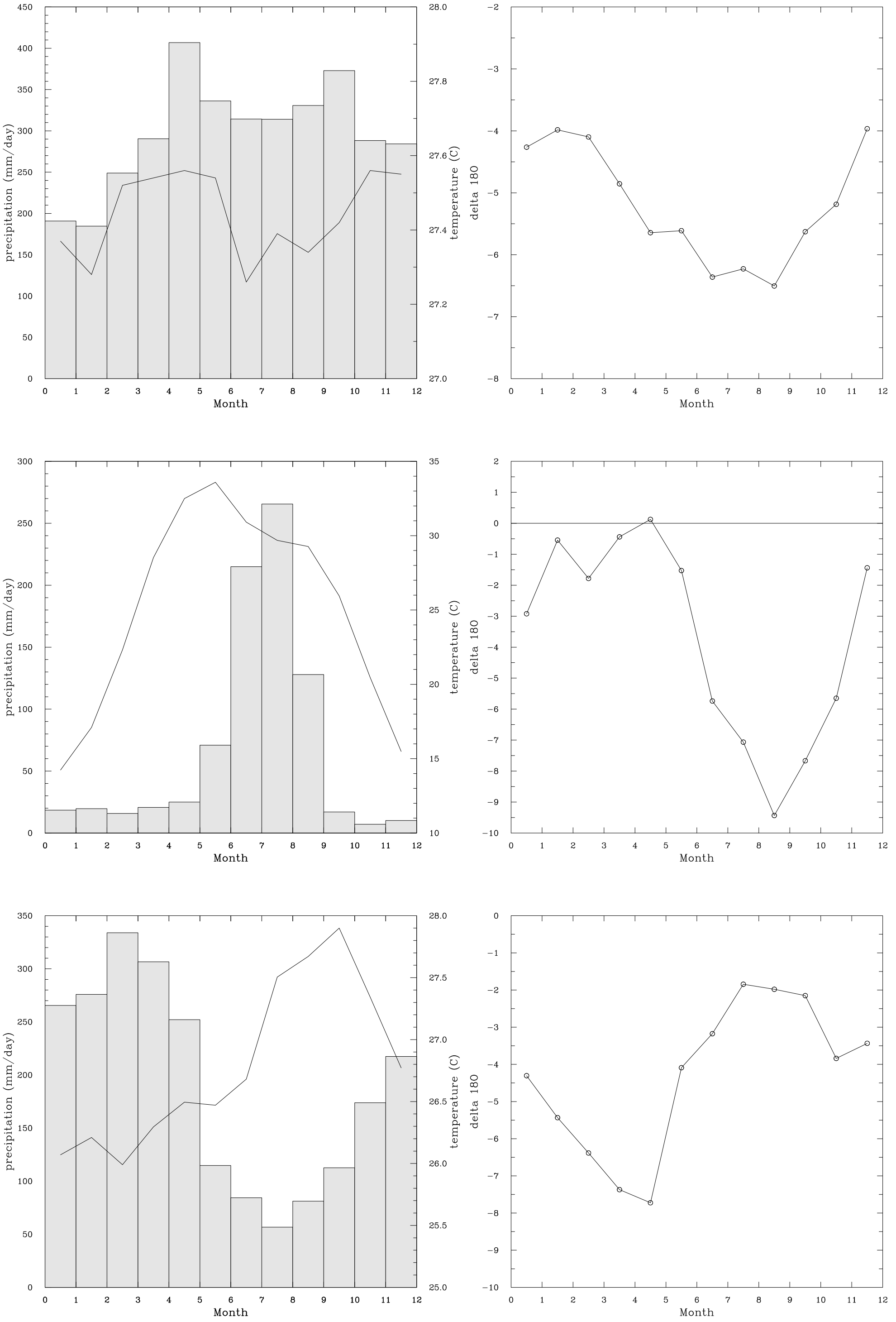

Figure 2.4: Seasonal cycle of precipitation (histogram) and surface temperature (line), left, and precipitation δ^{18}O, right, at Truk, Pacific Ocean (top); New Delhi, India (middle) and Manaus, Brazil (bottom). Data from GNIP monthly observations averaged over 1968–1977 for Truk, 1960–2000 for New Delhi and 1965–1990 for Manaus.

variation of convection and rainout over the Amazon basin. The largest precipitation totals occur in the Southern Hemisphere summer wet season, with correspondingly greater isotopic depletion. *Grootes et al.* [1989] describe the large annual cycle in rainout over the Amazon as the dominant control over the seasonal cycle of isotopic ratios in precipitation reaching the Quelccaya ice cap in Peru.

2.3.3 Interannual variability

On interannual time scales, the isotopic signal in tropical precipitation may be expected to respond to precipitation and temperature changes in a similar manner to the seasonal relationship. The variable strength of the summer monsoon rainfall will produce a magnification of the seasonal isotopic response to precipitation and continental rainout variability. Interannual variability in the position of the ITCZ and strength of the Walker circulation associated with ENSO will also lead to changes in precipitation amount and isotopic depletion.

In regions where seasonal isotopic variability is dominated by precipitation amount, large changes in temperature or circulation on interannual time scales may produce a mean change in the isotopic δ^{18}O value which is larger than the interannual isotopic response to precipitation variability. The temperature–isotope correlation is generally positive over continental areas on interannual time scales, as greater isotopic depletion will occur in response to cooler temperatures over land and the association of cooler conditions with increased precipitation.

The nature of interannual isotopic variability is of relevance to the interpretation of annually resolved ice core and marine coral and foraminiferal records (see next Section). Such records may either integrate the annual signal as a precipitation-weighted total or record the component of the isotopic signal associated with a particular season (eg. wet season snow fall, summer foraminiferal carbonate growth). The interannual isotope–climate relationship may also offer insights into the relationship on longer (glacial) time scales.

El Niño-Southern Oscillation

The strongest mode of tropical climate variability on interannual time scales is ENSO. Much of the interannual isotopic signal in the tropics is associated with ENSO-related climate anomalies, leading to the use of tropical ice core and coral isotope records to reconstruct ENSO variability (see next Section). For the purpose of this study, we define ENSO as the large-scale atmosphere-ocean interaction involving anomalous equatorial Pacific SSTs and sea level pressure, linked with changes in the zonal Walker circulation and a shift in the location and intensity of tropical convergence zones and convective activity [eg. *Kiladis and Diaz*, 1989; *Ropelewski and Halpert*, 1996].

During El Niño events, the central and eastern tropical Pacific Ocean becomes anomalously warm due to a reduction of upwelling along the Peruvian coast. The easterly trade winds which form the low level component of the Walker circulation are weakened and the vertical Walker circulation alters, bringing increased precipitation to the eastern and central Pacific associated with ascending air and drought to the western Pacific as dry air descends with the downward branch of the cell. The opposite phase of the oscillation, La Niña, is associated with cool SST anomalies in the eastern Pacific and strengthening of the trade winds bringing increased precipitation to the western Pacific and decreased precipitation to the eastern Pacific.

As ENSO alters moisture transport and the distribution of precipitation in the tropics it will produce isotopic anomalies in precipitation and the surface ocean. El Niño (La Niña) produces positive (negative) precipitation anomalies in the central Pacific and negative (positive) precipitation anomalies over the western Pacific and Indonesian region with correspondingly depleted and enriched isotopic ratios in precipitation. The amount of evaporation also varies in response to SST changes, particularly over the eastern equatorial Pacific, altering the isotopic ratio of the surface ocean.

Continental sites may experience isotopic variability due to shifts in moisture transport and centres of convergence associated with ENSO, as seen over northern Australia, Indonesia and tropical South America. For example, tropical South American precipitation amounts are highly sensitive to ENSO, which causes the displacement of the region of maximum precipitation associated with the ITCZ. During El Niño (La Niña) the northward (southward) displacement of the ITCZ leads to dry (wet) conditions over northeast Brazil [*Sperber and Palmer*, 1996] while over the Amazon increased precipitation leads to greater rainout with a resulting change in the isotopic depletion locally and over the Andes [*Vuille et al.*, 2003b].

Monsoon and decadal variability

The Indian and Asian monsoon systems are also known to vary on interannual time scales, partially driven by selective interaction with ENSO [*Webster and Yang*, 1992]. Indian monsoon rainfall has been found to be associated with Pacific Ocean SSTs, with increased monsoon rainfall corresponding to periods of cooler SSTs in the central and eastern Pacific [eg. *Ropelewski and Halpert*, 1996]. Interannual monsoon variability may also occur in response to changes in land surface temperature and soil moisture, or changes in snow cover and land albedo [eg. *Hahn and Shukla*, 1976; *Meehl*, 1994].

The isotopic response to interannual variability in monsoon strength is not well documented, although decadal periods associated with variability of the Indian monsoon have been identified in Indian Ocean coral isotopic records [eg. *Charles et al.*, 1997]. As the seasonal monsoon isotopic signal results from changes in rainout of moisture during inland transport, a weaker monsoon would be expected to result in reduced depletion due to rainout. In addition, *Hoffmann and Heimann* [1997] argue that a weaker monsoon may lead to reduced transport of depleted moisture inland leading to a further relative enrichment of local isotopic δ^{18}O values at continental sites.

Lower frequency modes of tropical climate variability may also influence isotopic ratios in precipitation and the surface ocean. For example, the decadal variability in the Pacific known as the Pacific Decadal Oscillation (PDO) is known to alter the distribution of precipitation in a similar manner to ENSO [*Zhang et al.*, 1997], and may therefore produce ENSO-like signals in the tropical isotopic distribution. Marine and continental isotopic records may also respond to long term trends in temperature and precipitation such as those associated with anthropogenic climate change [eg. *Gagan et al.*, 2000; *Thompson*, 2000].

2.4 Tropical ice core records

A number of ice cores have been recovered in recent decades from the tropical Andes and subtropical Tibetan Plateau. Ice cores archive the precipitation isotopic ratio, although factors such as sublimation and post-depositional smoothing of the record may alter the isotopic signal. Ice cores also incorporate tracers such as dust, soluble aerosols and chemical tracers which may be used to date the ice and reconstruct information about wind strength and aridity in

Core site	Location	Height	Length
Quelccaya, Peru	13.56°S, 70.50°W	5670 m	1,500 yr
Huascaran, Peru	9.07°S, 77.37°W	6048 m	20,000 yr
Sajama, Bolivia	18.06°S, 68.53°W	6542 m	25,000 yr
Illimani, Bolivia	16.37°S, 67.46°W	6350 m	18,000 yr
Guliya, Tibetan Pl.	35.17°N, 81.29°E	6200 m	500,000 yr
Dunde, Tibetan Pl.	38.06°N, 96.25°E	5325 m	40,000 yr
Dasuopu, Tibetan Pl.	28.23°N, 85.43°E	7200 m	1,000 yr

Table 2.1: Tropical and subtropical ice cores from the Andes and Tibetan Plateau: location, height above sea level and length of isotopic record.

the moisture source region [*Bradley*, 1999].

The locations of ice core sites in the Andes and Tibetan Plateau and the length of the isotopic records contained in the cores are listed in Table 2.1. The interpretation of the seasonal and interannual controls on precipitation and ice core isotopic ratios for these records is discussed below. Some of the main interpretations of glacial scale variability in tropical ice core isotopic records are also outlined.

2.4.1 Description of ice core records

Andean ice cores

There are four main ice core sites located in the tropical South American Andes: Huascaran and Quelccaya in Peru and Sajama and Illimani in Bolivia, as shown in Figure 2.5. Huascaran [*Thompson et al.*, 1995], Illimani [*Ramirez et al.*, 2003] and Sajama [*Thompson et al.*, 1998] contain records extending to the Last Glacial State (LGS). Quelccaya [*Thompson et al.*, 1985, 1986] contains a shorter 1500 year record with annual resolution, while the other cores contain annually resolved isotopic records in the upper layers.

On seasonal time scales, the majority of Andean precipitation falls during the summer wet season when easterly winds bring moisture from the Atlantic via the Amazon basin and solar heating of the Altiplano Plateau drives enhanced convection. During the dry winter season, precipitation over both the Amazon and Andes is greatly reduced. The seasonal isotopic signal in precipitation over the Andes is therefore largely driven by the change in the rainout of

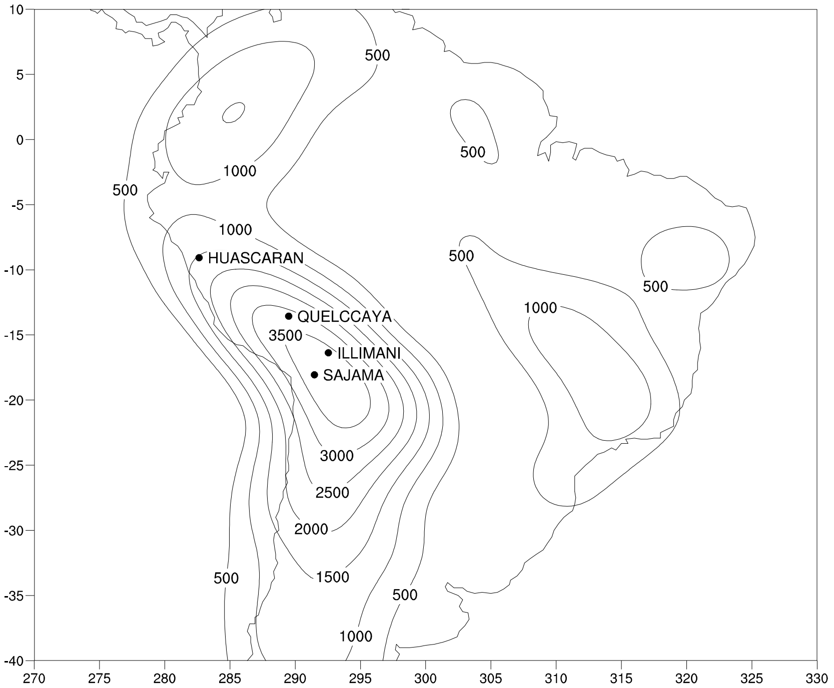

Figure 2.5: Location of Huascaran, Quelccaya, Sajama and Illimani ice core sites in tropical Andes and model topography (metres above sea level).

moisture over the Amazon [*Grootes et al.*, 1989]. The greater extent of rainout and vertical cooling associated with convection over the Andes in summer also contributes a local amount effect to the isotopic signal [*Thompson et al.*, 1984]. The combined processes of rainout over the Amazon and during orographic lifting are shown in Figure 2.6.

Thompson et al. [2000a] provide an alternative description of the processes producing the large seasonal isotopic signal in terms of the change in the mean condensation level (MCL) over the entire tropical South American region. Using the observed seasonal cycle of isotopic depletion and assumed vertical atmospheric profile, they calculate the condensation level required to produce the observed isotopic rainout. The calculated 2 km seasonal variation of the MCL is due to the seasonal meridional migration of the ITCZ over tropical South America. *Thompson et al.* [2000a] suggest that the "vertical temperature effect" model may be physically equivalent to the seasonal change in convection and rainout over the Amazon discussed by *Grootes et al.* [1989].

The coherence between the ice core records from the four different Andean sites is discussed by *Hoffmann et al.* [2003] who find that the isotopic records show nearly identical interannual variability. This is explained as a result of the

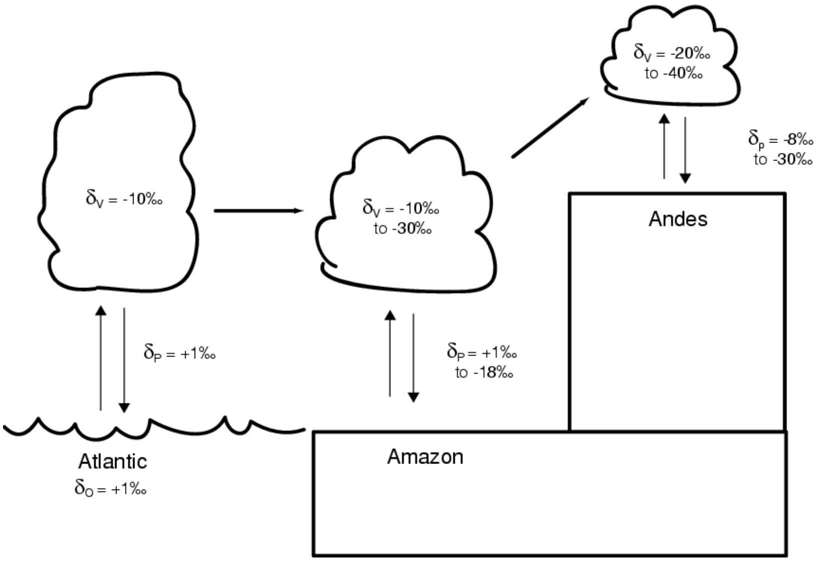

Figure 2.6: Isotopic fractionation of Andean precipitation. Approximate δ^{18}O values of Atlantic ocean ($\delta^{18}O_o$), vapour ($\delta^{18}O_v$) and precipitation ($\delta^{18}O_p$) are given for both summer and winter, with more depleted summer values due to greater rainout over Amazon. Adapted from *Grootes et al.* [1989].

common moisture source, with the isotopic ratio of precipitation responding to variability in the extent of rainout over the Amazon basin. On longer (millenial) time scales, *Ramirez et al.* [2003] find that the Huascaran and Illimani records show similar variability while the Sajama record reflects the different conditions on the west of the Bolivian Altiplano with a greater influence of moisture from the Pacific and from local lakes.

Warming trends over the Twentieth Century are also recorded in tropical ice core isotopic records, for example the Quelccaya isotopic record shows enrichment of up to 2‰ from 1979–1991, as well as a shift in the 0°C isotherm which threatens the existence of the glacial ice cap [*Thompson et al.*, 2000a]. The upper section of the isotopic record in Huascaran, Peru also exhibit an enrichment of 1.5‰ over the 1970s–1990s [*Thompson et al.*, 1995].

Tibetan ice cores

Several ice core sites are located on the Tibetan Plateau (Figure 2.7) where the isotopic signal is influenced by the Asian monsoon as well as local conditions on the Plateau. Guliya [*Thompson et al.*, 1997] is the longest record, extending to

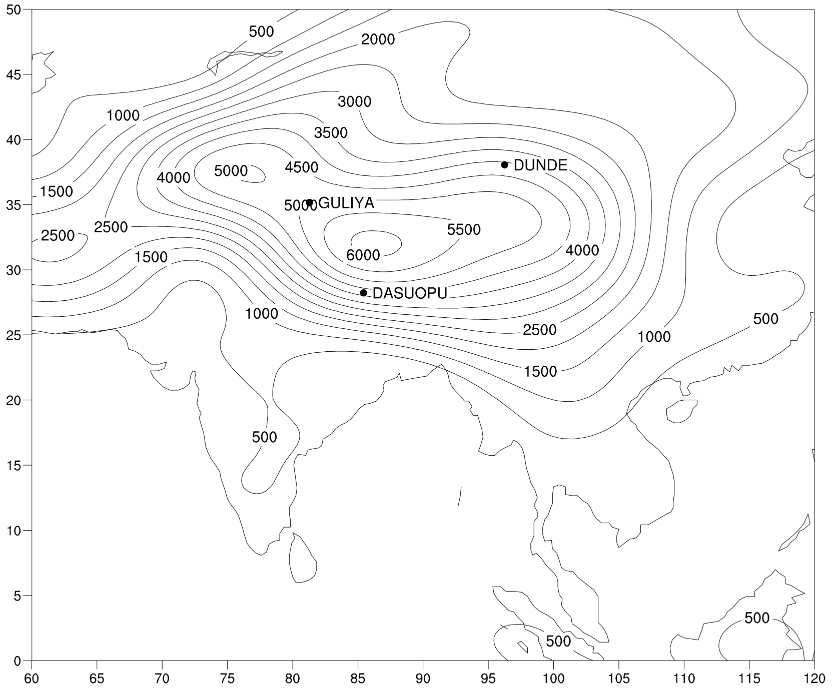

Figure 2.7: Location of Dunde, Guliya and Dasuopu ice core sites on the Tibetan Plateau and model topography (metres above sea level).

500,000 years before present (BP). Dunde [*Thompson et al.*, 1989] is a 40,000 year record from the northern Tibetan Plateau, and Dasuopu [*Thompson et al.*, 2000b] is an annually resolved 1000 year record from the southern region of the Plateau. The altitude effect is evident in the ice core isotopic ratios as the lowest elevation site (Dunde) has the smallest average isotopic depletion while the highest (Dasuopu) has the most depletion, while sharing the same moisture sources [*Thompson*, 2000].

The seasonal isotopic signal over the Tibetan Plateau involves the combined influence of precipitation amount and temperature. *Araguás-Araguás and Froehlich* [1998] find an approximate boundary between the amount and temperature effect regimes at the northernmost extent of the ITCZ during Northern Hemisphere summer. The Guliya and Dunde sites lie to the north of this latitude in north-western China, under the dominant influence of the mid-latitude westerlies [*Simmonds et al.*, 1999]. The Dasuopu site lies to the south in the region directly influenced by the Asian and Indian monsoons. All sites receive the majority of precipitation in the wet summer months [*Yao et al.*, 1999]. At Dunde and Guliya, the seasonal temperature cycle dominates, producing a positive temperature–δ^{18}O correlation [*Yao et al.*, 1997], while at Dasuopu the amount effect produces greater depletion during the warm summer monsoon months [*Thompson et al.*, 2000b]

On interannual time scales the isotopic signal in the Dasuopu cores is interpreted by *Thompson et al.* [2000b] as responding to changes in intensity of the Asian monsoon. Weaker monsoons result in a decrease in precipitation during inland moisture transport, leading to enriched δ^{18}O at Dasuopu. They also find that snowfall δ^{18}O is significantly correlated with temperature on the northern half of the Tibetan Plateau and both Dunde and Dasuopu isotopic signals show statistically significant correlations with Northern Hemisphere temperature anomalies on decadal time scales.

2.4.2 Tropical ice core records of ENSO

As the Andean ice cores are located in a region strongly influenced by ENSO, causing precipitation over the Amazon basin source region to vary, the isotopic ratio in Andean ice cores is expected to be influenced by ENSO. Correlations between indices of ENSO and observed (GNIP) isotopic records from tropical South America show that δ^{18}O is more enriched (depleted) during El Niño (La Niña) phases due to a decrease (increase) in precipitation [*Vuille et al.*, 2003b].

Accumulation at Quelccaya is observed to be reduced in El Niño years [*Thompson*, 2000] while the Huascaran record is seen to display a lagged δ^{18}O–ENSO relationship with Pacific SST anomalies due to reduced precipitation over the Amazon during El Niño events [*Henderson et al.*, 1999]. *Vuille et al.* [2003b] find that the dominant interannual mode of δ^{18}O variability from Huascaran, Quelccaya and Sajama is highly correlated with Nino3.4 SST indices ($r = 0.92$ for 1973–1984).

New results from the Sajama ice core suggest a strong relationship with ENSO [*Bradley et al.*, 2003]. The interannual δ^{18}O signal at Sajama is found to be positively correlated with tropical Pacific SSTs, with a spatial correlation pattern resembling the dominant ENSO mode of SST variability. The mechanism proposed to explain this relationship is reduced accumulation during El Niño events and an associated increase in the freezing height over the Andes, leading to an enrichment in Sajama ice core δ^{18}O.

Isotopic records from the Tibetan Plateau ice cores also contain ENSO signals due to the interaction between ENSO and the Asian monsoon. The Dasuopu ice core record suggests that ENSO years may have an enriched δ^{18}O

Core site	**Location**	**PD δ^{18}O**	**LGM δ^{18}O**	**$\Delta\delta^{18}$O**
Sajama, Bolivia	18.06°S, 68.53°W	-16.8	-22.1	-5.4
Huascaran, Peru	9.07°S, 77.37°W	-18.5	-22.9	-4.4
Guliya, Tibetan Pl.	35.17°N, 81.29°E	-14.4	-18.5	-4.1
Dunde, Tibetan Pl.	38.06°N, 96.25°E	~ -10	~ -12	~ -2
GISP2, Greenland	72.06°S, 38.05°W	-35.0	-39.7	-4.7
Byrd, Antarctica	79.59°S, 119.31°W	-32.8	-40.5	-7.6
Vostok, Antarctica	78.28°S, 124.10°W	-56.4	-61.1	-4.8

Table 2.2: Polar and tropical ice cores: present day (PD) δ^{18}O, LGM δ^{18}O and Δ δ^{18}O (LGM – PD). Adapted from *Thompson et al.* [1998].

signal, due to reduced snowfall during El Niño leading to less deposition of the more depleted monsoon precipitation [*Thompson*, 2000]. The interannual Dasuopu record is also correlated with Pacific Ocean SSTs [*Bradley et al.*, 2003], displaying a similar relationship to the Sajama record, confirming the basin-wide connection between Andean and Tibetan ice core δ^{18}O records identified by *Thompson* [1992].

2.4.3 Tropical ice core records of LGM

A number of high latitude isotopic records extending to the LGM have been obtained from ice cores from sites in Greenland and Antarctica. Ice core records of the LGM have also been recovered from Huascaran, Peru and Sajama and Illimani, Bolivia in the Andes, and Dunde and Guliya on the Tibetan Plateau as outlined in Table 2.2. As shown in Figure 2.8, isotopic depletion at the LGM can be identified in both tropical and polar ice core records, suggesting that the isotopic record reflects a synchronous global change in climate.

The LGM δ^{18}O values in ice core records from Vostok in East Antarctica are 4.8‰ lower than modern values in the upper ice core [*Jouzel et al.*, 1987a], while at Byrd in West Antarctica LGM δ^{18}O values are 7.6‰ lower than the present day [*Johnsen et al.*, 1972]. In Greenland, δ^{18}O values in the GISP2 core are 4.7‰ lower at the LGM [*Grootes et al.*, 1993]. The isotopic ratio in polar ice cores is generally interpreted as a record of temperature which is reconstructed using the modern spatial temperature–isotope relationship [eg. *Jouzel et al.*, 1987a], although the limitations of this reconstruction technique

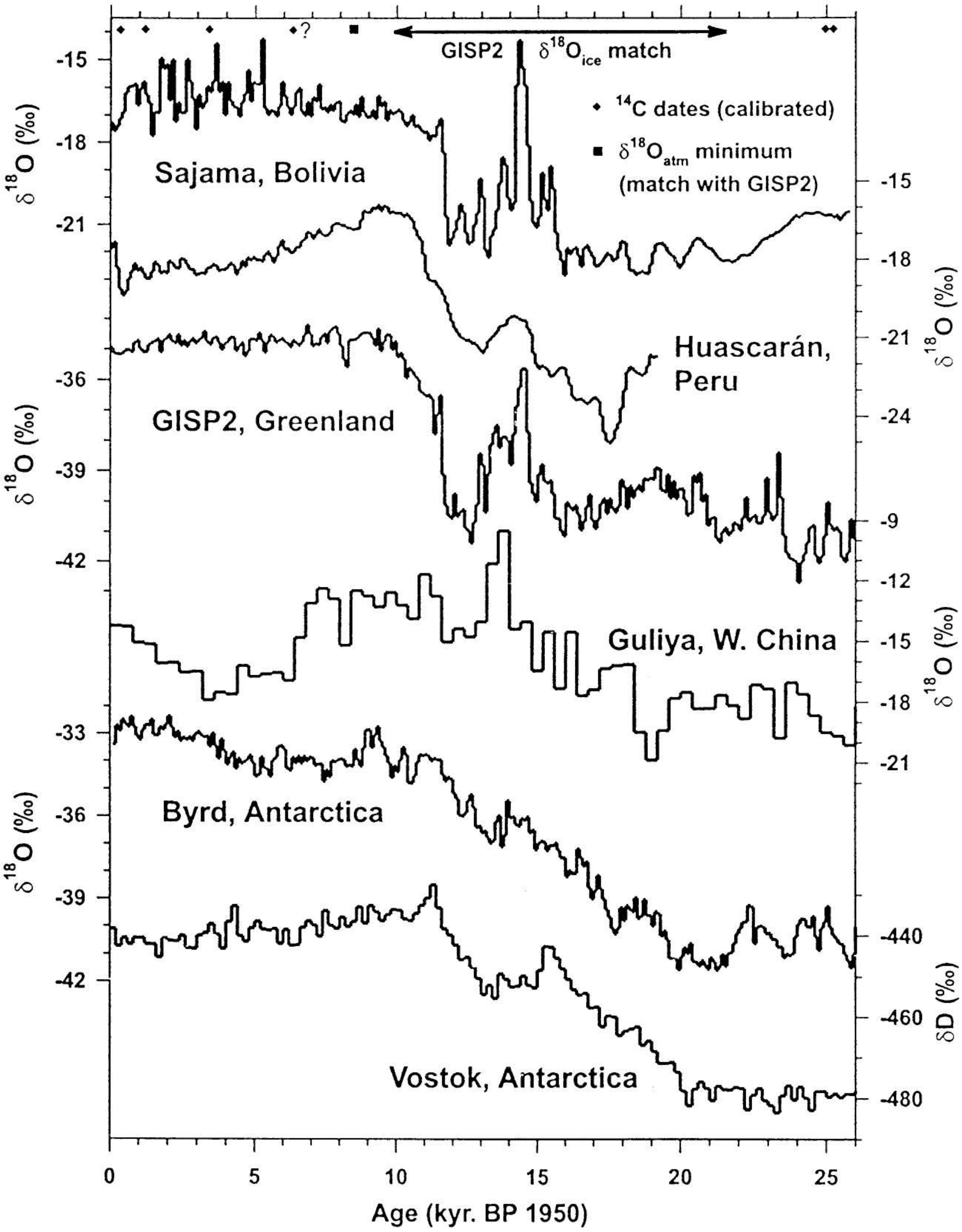

Figure 2.8: Tropical and polar ice core records from 25,000 years BP to present showing common isotopic depletion at the LGM. From *Thompson et al.* [1998].

have been examined in many studies [eg. *Jouzel et al.*, 1997; *Noone*, 2001].

The measured LGM δ^{18}O anomaly at Sajama is −5.4‰ [*Thompson et al.*, 1998], while the mean δ^{18}O of LGM ice at Huascaran is −4.4‰ less than the modern value [*Thompson et al.*, 2000a]. The common LGM isotopic depletion observed in tropical and high latitude ice cores has led *Thompson et al.* [2000a] to interpret the Andean signal as a record of cooling of up to 8–12°C at the LGM. Cooling of SSTs over the Atlantic and land surface temperatures over the Amazon would lead to a enhanced vertical cooling and rainout of moisture over the Andes as the lapse rate steepens under cooler conditions [*Pierrehumbert*, 1999]. Changes in the atmospheric humidity at sea level and in the mid-troposphere may also increase rainout [*Broecker*, 1997].

A newly recovered Andean ice core record from Illimani, Bolivia, extends back to approximately 18,000 years BP where isotopic depletion of ~ -4‰ relative to the present day corresponds to LGS conditions [*Ramirez et al.*, 2003]. The isotopic record at Illimani appears to be similar to that at Huascaran, while the Sajama record displays common depletion at the LGM followed by strong isotopic enrichment reaching a maximum at around 14,000 years BP. *Ramirez et al.* [2003] suggest that the common LGM isotopic depletion of approximately −5‰ over the Andes may be interpreted as reflecting an increase in precipitation over the Amazon and Altiplano of 300 mm/year, assuming the present day interannual isotope–precipitation relationship may be applied to the glacial record.

The LGM isotopic depletion in the Dunde ice core from the Tibetan Plateau is −2‰ [*Thompson et al.*, 1989] while the signal in the Guliya core is −4.1‰, which is interpreted by *Thompson et al.* [1997] as implying cooling over the Tibetan Plateau. Increased dust and decreased soluble aerosol concentrations in the Tibetan ice cores suggest that the region was colder, wetter and dustier at the LGM than at the present day [*Thompson*, 2000]. The seasonal and interannual dependence of Tibetan ice core δ^{18}O on precipitation amount and rainout of monsoon moisture suggests that wetter conditions at the LGM may explain a component of the observed isotopic depletion.

2.5 Marine isotopic records

Marine palaeoclimate proxies such as fossil corals and ocean sediments containing foraminiferal remains are of great importance for the reconstruction of tropical palaeoclimates. Both coral and foraminifera incorporate oxygen from ocean water into their calcium carbonate skeletons, recording information about ocean water isotopic ratios and SSTs via biological temperature-dependent fractionation. Analysis of marine isotopic records is often combined with a range of other methods including faunal assemblage techniques, alkenone palaeothermometry and trace element analysis to determine SST, precipitation and evaporation variability.

2.5.1 Description of marine records

Coral isotopic records

Massive reef-building corals grow within the range of latitudes with SSTs above around 20°C (approximately 30°S–30°N) in the upper 20 m of the ocean. The seasonal cycle of coral growth leads to annual layering being present in the coral skeleton allowing precise annual chronologies to be constructed [*Knutson et al.*, 1972; *Barnes and Lough*, 1993]. In the case of fossil corals accurate dating can be carried out using Uranium/Thorium dating methods [*Gagan et al.*, 2000].

Coral calcium carbonate ($CaCO_3$) skeletons incorporate oxygen from ocean water with the preferential uptake of the heavy ^{18}O. The concentration of the heavy isotope in the coral carbonate decreases with increasing ocean temperature due to biological fractionation processes, leading to a temperature dependence of the coral isotopic $\delta^{18}O$ value with an approximately linear relationship of 0.22‰/°C [*Gagan et al.*, 2000]. Calibration of the coral $\delta^{18}O$/SST slope has indicated that while the relationship varies with factors such as coral growth rate, annual average SSTs can be reconstructed with an accuracy of ±0.25°C [*Barnes et al.*, 1995].

In addition, the coral isotopic ratio will depend on the ocean isotopic ratio from which the oxygen is incorporated. On interannual time scales the coral isotopic ratio is therefore influenced by SST and the local precipitation minus evaporation balance which determines the local surface ocean isotopic ratio. In regions where SST does not vary significantly, the coral $\delta^{18}O$ value is interpreted as a precipitation minus evaporation record, and therefore also as a record of local salinity.

In regions where precipitation amount is not highly variable, coral $\delta^{18}O$ is interpreted as a proxy for SST. Where both SST and local ocean $\delta^{18}O$ vary substantially, a combined signal is produced. Both warmer SSTs and increased precipitation produce depleted coral δ^{18}O values resulting in an amplified isotopic signal when these two components vary in phase, such as during ENSO events.

Foraminiferal isotopic records

The carbonate shells of foraminifera incorporate ocean water oxygen with a temperature dependent fractionation as for corals. In the case of planktonic (near-surface-dwelling) foraminifera the conditions in the surface ocean are recorded, whereas the isotopic ratio in benthic (bottom-dwelling) foraminiferal shells is a function of the mean (long term or well-mixed) ocean isotopic ratio and temperature. Foraminifera are preserved in ocean sediments which can be retrieved from sediment cores, providing an extended record of ocean temperature and isotopic ratio.

Foraminiferal δ^{18}O values are also used to calculate palaeosalinity using the inferred ocean δ^{18}O values and present day δ^{18}O/salinity regressions [*Duplessy et al.*, 1993; *Rostek et al.*, 1993]. However the validity of applying present day δ^{18}O/salinity relationship to past climate conditions which may have substantially different advection and freshwater budgets has been questioned by *Rohling and Bigg* [1998] and *Schmidt* [1999b].

In addition to considerations of the component of the isotopic signal due to temperature and local ocean δ^{18}O changes, interpretation of planktonic foraminiferal isotopic ratios requires assumptions about the rate of dissolution (secondary calcification in the deep ocean) and bioturbation, as well as changes in the abundance and ecology of the foraminiferal species under different climate conditions [*Schmidt*, 1999b].

Other marine palaeotemperature proxies

The range of marine fauna found at a particular location is observed to vary with ocean temperature, forming the basis for the technique of faunal assemblage analysis [*Imbrie and Kipp*, 1971]. The technique uses the abundance of various species in modern day (core-top) records corresponding to a known surface temperature to develop a temperature–abundance transfer function for reconstruction of palaeotemperature from marine sediment cores. The faunal assemblage technique was applied by the CLIMAP project (see Chapter 6) in the global reconstruction of SSTs at the LGM [*CLIMAP Project Members*, 1976].

Limitations to this technique include the possible contamination of core-top records by older material via bioturbation [eg. *Bradley*, 1999].

The technique of alkenone palaeothermometry relies on the response of molecules in the membranes of certain marine phytoplankton to SST changes allowing the proportion of unsaturated alkenones to be used to reconstruct past temperature. This technique is often applied in concert with coral or foraminiferal isotope measurements, allowing the SST component of the isotope record to be identified and the residual component to be interpreted as a salinity (precipitation minus evaporation) record [*Rostek et al.*, 1993]

The substitution of trace elements Sr and Mg for Ca in the carbonate skeletons of corals and foraminifera has also been found to depend on ocean temperature. The ratio of Sr/Ca and Mg/Ca is applied as a palaeothermometer alone or in combination with δ^{18}O records from the same samples [eg. *McCulloch et al.*, 1994; *Beck*, 1992]. The calibration of Sr/Ca and Mg/Ca ratios with temperature has been questioned by *De Villiers et al.* [1995] and *Barnes et al.* [1995] who argue that the effects of growth rate and interspecies variation might alter the temperature relationship.

As each method of reconstructing SST and local ocean δ^{18}O has limitations, multiple reconstructions at the same location using independent methods are often used to provide greater confidence in the result [eg. *Koutavas et al.*, 2002]. However such techniques may not be completely independent as they may all be less accurate under climate conditions greatly different to the present day or where bioturbation or other disturbances have occurred. The importance of using multiple samples in order to reduce uncertainty in factors such as coral growth parameters for single records has also been highlighted by *Taylor et al.* [1995].

2.5.2 Marine records of interannual variability

ENSO signals are recorded in coral isotopic ratios due to the impact of ENSO on local SST or ocean δ^{18}O, or frequently a combination of SST and δ^{18}O signals associated with precipitation or evaporation anomalies. In the central Pacific, warmer SSTs and wetter conditions combine during El Niño events to generate lower coral δ^{18}O values, as seen in coral records from Christmas Island [*Evans et al.*, 1998] and Tarawa Atoll [*Cole and Fairbanks*, 1990; *Cole et al.*, 1993a]. Corals from Papua New Guinea, Indonesia and Fiji also display interannual variability which is strongly correlated with ENSO [*Tudhope*, 1995; *Fairbanks*, 1997; *Le Bec et al.*, 2000]. Variability in continental runoff associated with ENSO is also recorded in corals in the Great Barrier Reef off the coast of north-eastern Australia [*Lough*, 1991; *McCulloch et al.*, 1994].

Longer time scale variability in the tropical climate is also recorded in coral isotopic records. Records extending for several centuries at Panama and the Galapagos Islands reveal decadal variability which is inversely correlated, and may reflect the meridional migration of the ITCZ [*Linsley et al.*, 1994; *Dunbar et al.*, 1996]. Decadal variability is also seen in coral records at Vanuatu in the western Pacific [*Quinn et al.*, 1993], the Seychelles [*Charles et al.*, 1997] and the Great Barrier Reef [*Druffel and Griffen*, 1993].

Such multi-century records are able to extend the tropical climate record prior to instrumental records and to provide information about variability at a number of locations across the tropical oceans, revealing climate teleconnections and interaction between modes of variability such as ENSO and the monsoon. For example, at Malindi in the western Indian Ocean, a 194-year coral δ^{18}O record includes decadal variability which appears to be coherent with tropical Pacific SSTs [*Cole et al.*, 2000]. A central Pacific coral record has been found to reflect decadal variability in the Atlantic, Pacific and Indian Oceans [*Cobb et al.*, 2001]. At the Seychelles in the Indian Ocean, decadal variability in coral isotopic ratios suggests a relationship between Indian Ocean SSTs and monsoon strength [*Charles et al.*, 1997].

2.5.3 Marine records of LGM

Both fossil corals and planktonic foraminifera in marine sediments are used to construct isotopic records of the LGM. Planktonic foraminiferal records from the tropical Pacific and Atlantic display similar isotopic anomalies at the LGM to benthic foraminifera which respond to deep ocean conditions. As there is only a small change in deep ocean temperatures over glacial time scales this suggests only small (less than 2°C) changes in tropical ocean SSTs at the LGM [*Broecker*, 1986]. These results are in conflict with coral δ^{18}O and Sr/Ca ratios from Barbados in the tropical Atlantic [*Guilderson et al.*, 1994] and Vanuatu in the western tropical Pacific [*Beck et al.*, 1997] which suggest SST cooling of the order of 5°C.

A number of isotopic records have been retrieved from the western Pacific

Warm Pool, and have been used to examine the variation of salinity and SST in this region under glacial conditions. *Martinez et al.* [1997] obtained 57 isotopic records from planktonic foraminiferal sediment cores in the western Pacific Warm Pool region. The modern (core-top) isotopic values were subtracted from the LGM values to give anomalies ranging from +1.0‰ to +2.5‰ with a mean value of +1.76‰. When the isotopic offsets due to SST and ice volume changes were subtracted, the remaining local surface ocean δ^{18}O anomalies were in the range +0.2‰ to +0.5‰.

De Deckker et al. [2003] calculated an enrichment of the surface ocean north of Australia of up to +1.0‰ from LGM planktonic foraminiferal sediment cores, indicating drier conditions (lower precipitation and/or higher evaporation) and thus increased salinity in the Indo-Pacific Warm Pool at the LGM. *Visser et al.* [2003] concluded that there was no change in Warm Pool δ^{18}O values at the LGM as they measured planktonic foraminiferal isotopic anomalies which were compatible with observed Mg/Ca SST changes of −3.6°C. However this SST anomaly is substantially larger than −2°C change calculated by *De Deckker et al.* [2003] for the LGM Warm Pool, while *Stott et al.* [2002] found a change in LGM summer surface δ^{18}O of +1.0‰ in the same region.

Koutavas et al. [2002] inferred unchanged local δ^{18}O in the eastern equatorial Pacific at the LGM from Mg/Ca records, foraminiferal δ^{18}O records and alkenone palaeothermometry from the Galapagos Islands. These records implied an SST cooling of −1.2°C while records from sites north of the equator suggested greater cooling of up to −3°C. The reduction in the meridional SST gradient was suggested to lead to a mean southward shift of the ITCZ in a similar manner to modern El Niño events. Greater cooling in the western Pacific than the eastern Pacific at the LGM may have produced a mean El Niño-like state with weakened Walker and Hadley circulations.

Guilderson et al. [2001] identified an isotopic depletion of −2.3‰ in fossil LGM corals from Barbados in the tropical North Atlantic. Correcting for a global ice volume change of −1.2‰ yielded a residual of −1.1‰ which corresponds to cooling of 5°C. As a large component of the present day variability in the ocean δ^{18}O at this location is due to Amazon discharge, *Guilderson et al.* [2001] estimated that a halving of Amazon discharge would lead to an increase of 0.2‰ in surface ocean δ^{18}O, reducing the SST cooling estimate to 4°C.

2.6 Previous isotopic modelling studies

We have seen that the processes which govern isotopic ratios in precipitation and the ocean are highly complex. As we have indicated, simple regression relationships between isotopic ratios and components of climate may be misleading. For these reasons, there has been a trend over recent years to extend the understanding of isotopic processes by developing models incorporating the fundamental physics and chemistry of isotopes in the hydrologic cycle. This approach has been undertaken with a range of physically-based atmosphere and ocean models, and the present work is a contribution to that development. We summarise below some of the key studies which have represented advances in this new approach, with an emphasis on studies of isotopes in the tropical climate and interannual and glacial variability of the isotopic record.

2.6.1 Rayleigh models

Simple Rayleigh distillation models have been used to simulate isotopes in precipitation following the original formulations of *Dansgaard* [1964] and *Craig and Gordon* [1965]. *Merlivat and Jouzel* [1979] used a Rayleigh model with the addition of kinetic effects during evaporation from the surface ocean to explain the global δ^{18}O–δD relationship. *Jouzel and Merlivat* [1984] included kinetic fractionation during snow formation to improve the representation of the global isotope/temperature slope and the δ^{18}O–δD relationship. The "mixed cloud model" of *Ciais and Jouzel* [1994] incorporated mixed cloud processes with the inclusion of supercooled water and the appropriate fractionation and kinetic effects for cloud liquid and solid formation.

As discussed by *Jouzel et al.* [1987b], Rayleigh models are limited in their ability to capture the complexity of the observed isotopic signal as they do not reflect the complexity of dynamical and microphysical processes such as entrainment and reevaporation. The Rayleigh modelling approach also does not allow for changes in surface ocean conditions, topography, precipitation formation mechanisms or atmospheric circulation without making simplifying assumptions about the impact of such changes on initial vapour isotopic ratio and rainout during moisture transport.

2.6.2 Atmospheric GCMs

An alternative approach which captures the complex dynamic and thermodynamic influences on the isotopic signal is the incorporation of isotopic tracers into atmospheric General Circulation Models (GCMs). This approach requires the specification of the relevant isotopic equilibrium and kinetic fractionation during phase transitions, as well as the parameterisation of the effects of reevaporation, exchange and convective mixing and specification of the surface ocean isotopic ratio.

The first implementation of an isotopic tracer scheme in an atmospheric GCM was carried out by *Joussaume et al.* [1984] using the Laboratoire de Météorologie Dynamique (LMD) model. This was followed by the development of isotopic tracers in the Goddard Institute for Space Studies (GISS) model [*Jouzel et al.*, 1987b]. *Hoffmann and Heimann* [1998] incorporated isotopic tracers into the University of Hamburg ECHAM model. *Noone* [2001] developed an isotopic tracer scheme in the University of Melbourne model (MUGCM) and most recently, *Mathieu et al.* [2002] describe the implementation of isotopic tracers in the National Center for Atmospheric Research (NCAR) GENESIS model.

Present day climate

Simulations of present day climate have been carried out with each of the isotopic GCMs, and the main features of the observed GNIP spatial isotopic distribution are generally well reproduced by the models. *Joussaume et al.* [1984] carried out a perpetual January simulation with the LMD model and found that the model was able to simulate the main features of the observed isotopic distribution including the temperature, amount, continentality and altitude effects. *Jouzel et al.* [1987b] found that the GISS model reproduced the temperature–isotope relationship at high latitudes and the amount–isotope relationship in the tropics in a three-year simulation.

Cole et al. [1993b] used the GISS GCM to simulate January and July climate for strong warm (1982–1983) and cold (1955–1956) ENSO events in order to identify the relationship between interannual isotopic variability and climate parameters such as temperature and precipitation. The tropical isotopic response was dependent on precipitation amount. On interannual time scales, temperature–isotope correlations were weak in the tropics and extratropics due to interannual temperature variability being associated with precipitation and circulation changes. In contrast, latitudinal, seasonal and glacial temperature variability produced a stronger correlation between isotopic ratios and temperature.

The study of *Cole et al.* [1999] discussed the influence of changes in temperature, precipitation amount and moisture source region on the isotopic composition of precipitation for a 13-year simulation with the GISS model using observed SSTs from 1979–1991. Using a moisture source region tracer scheme, the variability in the proportion of moisture from 19 source regions was compared with isotopic variability. Changes in precipitation amount and the proportion of moisture from local versus non-local sources were found to be the dominant controls on isotopic ratios in precipitation on interannual time scales.

Hoffmann and Heimann [1998] simulated present day climate with T21 and T42 resolution versions of the ECHAM model as well as carrying out a simulation from 1979–1989 with the T21 version. The variability in the modelled isotopic ratios on time scales from days to years was examined. A strong isotopic response to ENSO variability was identified in the central Pacific, associated with changes in precipitation amount. The isotopic content of river runoff was also simulated using a river runoff scheme in the ECHAM model, and the modelled runoff δ^{18}O compared with observed river isotopic ratios.

A five-year simulation of present day climate and four-year simulation of LGM climate with the T42 version of the ECHAM model was carried out by *Hoffmann and Heimann* [1997], with a focus on the Asian monsoon. The study found that atmospheric circulation strongly affects the seasonal cycle of water isotopes in the Asian monsoon area. The model successfully simulated the influence of temperature, precipitation and circulation on the isotopic content of precipitation in the monsoon region for the present day climate.

Werner and Heimann [2002] used the ECHAM model forced with SSTs from 1950–1994 to examine the interannual variability of isotopes in Greenland and Antarctic precipitation. They attempted to associate variability in isotopic ratios and deuterium excess with climate parameters locally and regionally using multivariate regression techniques. Correlations with indices of ENSO and North Atlantic Oscillation were also identified in the modelled isotopic record.

A new high resolution T106 ($\sim$1°$\times$ 1°) version of the ECHAM model has been used to simulate the isotopic signal over the steep localised topography of the Andes [*Vuille et al.*, 2003b]. The results were compared with those from the

T42 version of the ECHAM model and the GISS model at 4°× 5° resolution with raised topography (using 90% of the observed elevation rather than 50% in the standard topography) over the Andes. All three models are able to simulate the main features of the interannual variability of temperature and precipitation over the region, and the resulting correlation between isotopic ratios in Andean precipitation and ENSO variability.

LGM climate

A number of modelling studies of LGM climate have been carried out with atmospheric GCMs containing isotopic tracer schemes, including early studies with LMD model [*Joussaume and Jouzel*, 1993] and the GISS model [*Jouzel et al.*, 1994]. These studies were primarily concerned with the interpretation of polar isotopic records and the validity of the isotope–temperature reconstruction technique. The modelled tropical isotopic response to LGM climate included an enrichment due to the imposed increased surface ocean isotopic δ^{18}O value, and precipitation δ^{18}O anomalies associated with changes in precipitation amount.

The LGM simulation of *Hoffmann and Heimann* [1997] focused on the response of the Asian monsoon to glacial conditions. The changes in SSTs, snow and sea ice coverage lead to a cooler Asian continent, reducing the land-ocean gradient in summer and increasing it in winter. This produced a weakening of the south-westerly summer monsoon and a strengthening of the north-easterly winter monsoon. The modelled Hadley circulation was also weaker with resulting tropical aridity and increased subtropical precipitation in the western Indian Ocean and Pacific Ocean.

This study found that isotopic ratios in the tropics had an average enrichment compared with the present day of +2‰ to +3‰ in the region 45°S to 45°N. The meridional δ^{18}O gradient was also increased, with a relative isotopic depletion of around −8‰ at high latitudes. Increased precipitation in the northern Pacific and Indian Oceans resulted in more depleted isotopic ratios. In the Asian monsoon region positive isotopic anomalies resulted from the weaker summer monsoon causing decreased rainout of Pacific moisture and a decrease in the proportion of continental moisture originating from more distant oceanic sources.

A study with the GISS atmospheric model was carried out by *Charles et al.* [2001] with the imposition of three different LGM SST boundary conditions with contrasting tropical SST distributions. The first simulation used standard

CLIMAP SSTs, while the second used CLIMAP SSTs with an imposed tropical SST cooling of up to 5°C and a third simulation used SSTs derived from an ocean model experiment with modern ocean heat transports. The different SST boundary conditions were found to produce changes in continental temperature and precipitation distributions. At high latitudes the isotopic ratios followed temperature changes, while in the tropics the CLIMAP simulation produced little change in δ^{18}O. The simulations with cooled tropical SSTs produced lower tropical continental δ^{18}O values associated with cooler land surface temperatures and increased precipitation and recycling of continental moisture over land.

A simulation of LGM climate was also carried out with MUGCM [*Noone*, 2001; *Noone and Simmonds*, 2001]. The tropical climate simulated by the model included a strengthened Hadley circulation and increased easterly trade winds. As a result, precipitation was increased over the tropical convergence zones of the Pacific, Atlantic and Indian Oceans as seen in Figure 7.9 of *Noone* [2001]. The summer monsoon was weakened and hence precipitation over northern Australia and southeast Asia was reduced.

The isotopic response to the modelled LGM climate, shown in Figure 7.10 of *Noone* [2001], included a small enrichment of tropical δ^{18}O due to the surface ocean enrichment. There were large positive isotopic anomalies in the western Pacific associated with a reduction in precipitation, and the weakened monsoon led to positive δ^{18}O anomalies over northern Australia. Increased isotopic depletion occurred in those areas such as the subtropical anticyclone regions where warmer SSTs produced increases in precipitation.

2.6.3 Ocean box models

Simple box models of the surface ocean have been used to calculate the isotopic ratio based on the balance between precipitation and evaporation and the equivalent isotopic fluxes [eg. *Craig and Gordon*, 1965]. Such models can be applied to observed or modelled fluxes in the form of offline calculations, or coupled to an atmospheric model to provide a representation of the interaction between surface ocean and atmospheric isotopic ratios.

Juillet-Leclerc et al. [1997] constructed an offline surface ocean box model using atmospheric water and isotopic fluxes from the GISS model to calculate the surface ocean δ^{18}O value at each grid point. The model included damping to an observed deep ocean δ^{18}O with an empirical diffusion coefficient. This model was able to reproduce the tropical and mid-latitude meridional gradient of surface ocean δ^{18}O but did not include the influence of coastal runoff or sea ice.

Delaygue et al. [2000] calculated box model δ^{18}O also using GISS atmospheric water and isotopic fluxes as well as runoff and iceberg discharge from the GISS model runoff scheme. Sea ice melt and formation was not included as the fractionation is minimal, 2‰ for new sea ice and 0.05‰ for mature ice [*Strain and Tan*, 1993]. The same deep ocean and diffusion values were used as for *Juillet-Leclerc et al.* [1997] and a "salinity" tracer was calculated for comparison with observed salinity. The box model was able to capture the zonal distribution and the Atlantic enrichment of the salinity and δ^{18}O distribution but failed to reproduce the observed smoothing due to upwelling and surface currents. *Delaygue et al.* [2001] also used a box model and ocean GCM to investigate the δ^{18}O/salinity relationship in the Indian Ocean under present day and LGM conditions.

2.6.4 Ocean GCMs

Stable water isotopes have also been included as tracers in several ocean GCMs. No fractionation occurs within the ocean, so once the surface incoming (precipitation) and outgoing (evaporation) isotopic fluxes are specified the surface isotopic concentration is transported as a passive tracer associated with a given body of water.

Paul et al. [1999] incorporated isotopic tracers into an ocean GCM based on the MOM2 model, with surface oxygen isotope ratios calculated from observed salinity via basin-specific δ^{18}O/salinity slopes. The isotopic surface fluxes were applied so that the upper ocean values were damped towards the input δ^{18}O values with the appropriate depth and mixing time scales. This simulation was able to produce a deep ocean distribution resembling observed vertical δ^{18}O profiles, but the use of present day δ^{18}O/salinity slopes limits the application of this approach for palaeoclimate simulations.

Schmidt [1998] used the GISS ocean model with climatological precipitation, prognostic evaporation and runoff from the GISS atmospheric GCM river runoff scheme. The ocean model was initialised with observed isotopic depth–latitude fields. Isotopic ratios in precipitation were calculated via an empirical regression with temperature while precipitation amount and isotopic evaporation was calculated prognostically. The resulting distribution of upper ocean δ^{18}O was found to be largely in agreement with observations. The regional δ^{18}O/salinity slopes were calculated from the model output and the present day spatial slopes were found to differ from the seasonal and longer-term spatial relationships.

This approach was extended by *Schmidt* [1999b] who used the GISS ocean model with isotopic ratios in precipitation taken from GISS isotopic atmospheric GCM output, and evaporation and isotopic evaporative fluxes again calculated prognostically. This was an improvement on the empirical regression used in *Schmidt* [1998] which was taken from mainly continental station data and did not capture the tropical amount effect well. *Schmidt* [1999b] also calculated the isotopic content of planktonic foraminifera from known empirical relations with ocean isotopic content and SST.

Delaygue et al. [2000] incorporated both normal water and isotopic fluxes from the GISS atmospheric model into the OPA ocean GCM. Runoff was taken from the GISS model with isotopic ratios determined by the isotopic ratios of precipitation. In addition, a passive "salinity" term was calculated from the atmospheric hydrological fluxes in order to simulate the isotope/salinity slope. The model was run for 2000 years to spin-up the deep ocean and then for a further 200 years. The distribution produced was found to match observations of the surface ocean more accurately than a simple box model, indicating the role of horizontal transport in determining the surface ocean δ^{18}O distribution.

A simulation of present day and LGM ocean δ^{18}O was carried out by *Wadley et al.* [2002] using the Southampton–East Anglia (SEA) ocean GCM. The isotopic fluxes were calculated in the same manner as *Schmidt* [1998], with an offset of +1.2‰ at the LGM to account for the change in the mean ocean ratio. The modelled present day and LGM δ^{18}O/salinity slopes were found to be substantially different, leading to errors in palaeosalinity reconstructions employing the present day slope.

The next phase of isotopic modelling is represented by the use of coupled atmosphere–ocean isotopic models such as that being developed by *Schmidt et al.* [2001]. However such coupled models are computationally expensive to run and require long integrations to equilibrate the ocean (and ocean isotopic distribution). It is therefore likely that a role will remain for atmospheric GCMs with isotopic tracers in order to carry out multiple integrations of a range of climate scenarios. The implementation of simplified box or slab oceans containing isotopic tracers coupled to atmospheric models also offers a promising approach for simulating the interaction between the upper ocean and atmospheric isotopic distributions.

Chapter 3

Modelling isotopes in precipitation

3.1 Introduction

The incorporation of stable water isotope tracers into atmospheric GCMs represents an advance in the investigation of isotope–climate relationships from the use of simple Rayleigh distillation models, as described in Chapter 2. GCMs allow isotopic ratios in vapour and precipitation to be traced through the hydrologic cycle with the effect of changes in source regions, atmospheric mixing and transport fully represented. Isotopic tracer schemes in GCMs therefore provide a powerful tool for the examination of the spatial and temporal variability of isotopes in precipitation under a range of climate conditions.

As outlined in the previous chapter, stable water isotope tracer schemes have been implemented in the LMD [*Joussaume et al.*, 1984], GISS [*Jouzel et al.*, 1987b], ECHAM [*Hoffmann and Heimann*, 1998] and GENESIS models [*Mathieu et al.*, 2002]. The study of *Noone* [2001] included the incorporation of isotopic tracers into the MUGCM, the model which is used in this study.

We first describe the MUGCM and the formulation of the isotopic tracer scheme in the model. The model climatology and resulting distribution of isotopic ratios in precipitation are then compared with observations. The variability of the modelled isotopic distribution is also discussed, and the results of idealised experiments testing the sensitivity of isotopes in precipitation to changes in continental locations and SST gradients are presented.

3.2 Description of the MUGCM

The MUGCM is a spectral atmospheric model based on that described by *Bourke et al.* [1977]. The horizontal resolution of the model is determined by the rhomboidal truncation of the spectral series at wavenumber 21 (R21 resolution, 3.25° latitude × 5.625° longitude) or wavenumber 31 (R31 resolution, 2.25° × 3.75°). The model can has nine vertical levels in sigma ($\sigma = P/P_S$) pressure coordinates including two levels in the stratosphere. The lowest level ($\sigma = 0.991$) is approximately 75 m above the surface.

3.2.1 Boundary conditions

The incoming solar radiation is determined from the orbital equations of *Berger* [1978]. The given model run year is used to determine incoming radiation based on the Earth's angle of inclination, orbital obliquity and date of perihelion. The radiation scheme is that of *Fels and Schwarzkopf* [1975] and *Schwarzkopf and Fels* [1991]. The model also includes soil-moisture-dependent heat capacity and land surface albedo [*Laval and Picon*, 1986].

Ozone and carbon dioxide concentrations are prescribed from observational data. The ozone profiles are zonally averaged values from the TOMS satellite [*McPeters et al.*, 1996]. The carbon dioxide concentrations are calculated for a given mean atmospheric concentration, which in the case of control simulations is set at the 1995 value of 345 ppmv. Atmospheric water vapour, a prognostic model variable, is also used in the radiative calculations.

For control simulations, SSTs are prescribed from the *Reynolds* [1988] average monthly SST values from 1982–1987. These are interpolated within the model to provide daily values. A prognostic sea ice scheme is available for the model [*Wu et al.*, 1997], but prescribed sea ice concentrations are used for this study. The sea ice concentrations are prescribed from observations from the DSMP SSM/I satellite data set [*Watkins and Simmonds*, 1995]. The sea ice fraction is given for each ocean grid point, and the model then calculates fractional heat and moisture fluxes from the ice and open water (lead) fraction according to the parameterisation of *Simmonds and Budd* [1990]. This parameterisation represents a more realistic representation of the air–sea interactions in polar regions than the assumption of complete sea ice coverage [*Simmonds and Budd*, 1991].

A prognostic snow scheme has also been developed for the MUGCM [*Wal-*

land and Simmonds, 1996] and a modified version of this scheme which incorporate isotopic tracers is tested in Chapter 4. Elsewhere, prescribed snow coverage is used. The mean seasonal cycle of snow coverage is prescribed from observational data from the NIMBUS 7 satellite for April 1979 to March 1985 [*Weaver and Iroisi*, 1988]. Alternative SST, sea ice and snow boundary conditions are used to simulate different climates such as the LGM.

Cloud cover in the model is calculated by an interactive cloud scheme developed by *Argete and Simmonds* [1996] which calculates fractional cloudiness from relative humidity at three (lower, middle and upper) levels in the atmosphere.

The model topography is based on the $1^\circ \times 1^\circ$ data set of *Gates and Nelson* [1975]. The topography is spectrally transformed to the model resolution, then the truncated spectral representation is transformed back to grid point form in order to estimate the sub-gridscale orography from the difference between the truncated output and the initial data. The spatial variance of this difference at each model grid point is used to provide an “envelope topography” which is added to the raw spectral topography to simulate the role of mountain peaks and other sub-gridscale features in atmospheric dynamical forcing.

3.2.2 Water vapour transport

In one version of the MUGCM, moisture is represented as a spectral field. However this produces a number of problems for the accurate simulation of water isotopes, particularly at high latitudes [*Noone and Simmonds*, 2002]. Spectral representation is not well suited to rapidly varying fields such as moisture, and the finite truncation of the spectral series inevitably produces errors in the representation of such fields. In addition, the exponential dependence of water vapour amount on temperature leads to large anomalies at low temperatures, magnifying errors due to the finite spectral truncation relative to the size of the signal. The spectral representation of moisture can also lead to some negative mixing ratios, which cannot be accommodated by an isotopic tracer scheme.

In order to overcome these problems, a semi-Lagrangian moisture transport scheme based on that of *Williamson and Rasch* [1989, 1994] was added to the MUGCM as described by *Noone and Simmonds* [2002]. This scheme allows calculation of moisture mixing ratios entirely on a grid using a two-step calculation, with vertical and horizontal interpolation to find the upstream mixing ratios. One of the shortcomings of this scheme is that mass conservation cannot be guaranteed, leading *Williamson and Rasch* [1994] to advocate the use of a mass fixer. However, as discussed by *Noone and Simmonds* [2002], such a mass fixer results in a decoupling of the isotopic species, introducing non-physical isotopic anomalies. Sensitivity testing showed that the mass loss due to non-conservation of moisture during transport is small compared with the physical sources, particularly in the tropics. As the use of semi-Lagrangian moisture transport represents a substantial improvement compared with spectral Eulerian transport, the limitations imposed by non-conservation of moisture within the scheme are considered to be acceptable.

3.2.3 Hydrologic cycle

The representation of evaporation and precipitation is of crucial importance to the simulation of isotopic ratios in precipitation. The formulation of evaporation and precipitation in the model as well as the soil moisture scheme which provides the source of evaporated moisture over non-ocean surfaces are described below. Modifications to the model's hydrologic cycle for the representation of isotopic tracers are presented in the following Section.

Evaporation

Surface fluxes of momentum, sensible heat and latent heat (evaporation) are calculated via Monin-Obukhov similarity theory following the approach of *Louis* [1979] and *Tiedtke et al.* [1979] as outlined in *Simmonds* [1985]. The rate of evaporation is proportional to the mixing ratio gradient in the surface layer, as estimated from the difference between the mixing ratio at the surface (assumed to be the saturation mixing ratio) and the ratio at the lowest atmospheric model level.

The evaporation, E, is calculated as:

$$E = C_D \rho C_w |v| (q_{sat}(T_S) - q_{atm}) \tag{3.1}$$

where C_D is the exchange (drag) coefficient which depends on wind speed, stability and surface roughness length, v is the horizontal wind, ρ is the air density, C_w is the surface wetness (set to unity over ocean and dependent on upper level soil moisture over other surfaces), and q_{sat} and q_{atm} are the saturated mixing ratio at temperature T_S and the mixing ratio at the first atmospheric level respectively. The roughness length is calculated from the friction velocity over ocean, and is set to a constant value over land as described in *Simmonds* [1985].

When the humidity at the surface is lower than that in the atmosphere above (for example, due to nocturnal cooling), the mixing ratio gradient will be negative and the moisture flux will be towards the surface, representing the formation of dew or frost depending on whether the surface temperature is above freezing. Dew and frost is calculated as a surface moisture flux (rather than precipitation) in the model, and results in a decrease in the mixing ratio at the first atmospheric level and a negative contribution to the evaporation at that grid point.

Precipitation

Condensation is calculated by the Moist Convective Adjustment scheme of *Manabe et al.* [1965]. In this scheme the environmental lapse rate and saturation are calculated for the given atmospheric layer. If the atmosphere is unsaturated and unstable, temperatures are adjusted to stability representing dry convection. If the atmosphere is stable but saturated, large scale condensation occurs to reduce the moisture content to saturation level, representing large scale (stratiform) precipitation without convection. Finally if the atmosphere is both unstable and saturated moist convection occurs with adjustments to both the temperature and moisture content of the layer.

When condensation occurs, reevaporation is allowed as the condensate falls through lower unsaturated layers. The condensate is assumed to evaporate completely, and the temperature of the layer adjusted accordingly. If the layer is now supersaturated the mixing ratio is adjusted back to saturation and the excess moisture continues to fall as condensate. This procedure is repeated at each level in the column, and it is assumed that condensate will always undergo reevaporation if the underlying atmospheric layers are unsaturated.

Once all condensation and reevaporation adjustments have been calculated, the resultant change in the precipitable water of the column represents the total precipitation for the time step. This scheme does not take into account the role of small scale convection in the tropics due to moisture flux convergence, and so is expected to underestimate the precipitation due to such processes. The initiation of condensation whenever saturation is reached in a layer may lead to excessive precipitation when moisture is transported over raised topography in the model.

Land surface hydrology

The land surface hydrology is represented with the two-layer soil moisture scheme of *Deardorff* [1977] with modifications by *Hunt* [1985] as implemented in the MUGCM by *Yang* [1989]. The upper (surface) layer penetrates to a depth of 12 cm (d_1) representing the depth of diurnal variation, and variations in upper layer moisture content are able to capture short term (hours to days) changes in soil moisture. The lower layer is 50 cm deep (d_2) and interacts with the surface by diffusive exchange with the upper layer, with the variability of the lower layer being associated with longer term (monthly and seasonal) changes in soil moisture. The coefficients of exchange and damping time scales of the model are tuned to represent a maximum time scale of a few weeks for soil moisture response.

The equations for the surface layer moisture fraction w_g and the bulk moisture fraction w_b are given:

$$\frac{\partial w_g}{\partial t} = -C_1 \frac{(E-P)}{\rho d_1} - C_2 \frac{w_g - w_b}{\tau} \tag{3.2}$$

$$\frac{\partial w_b}{\partial t} = -\frac{(E-P)}{\rho d_2} \tag{3.3}$$

where C_1 and C_2 are dimensionless constants, E is evaporation, P is precipitation, ρ is the density of water and τ is the mixing time scale for the upper layer, taken to be one day.

The upper layer is saturated if the moisture content exceeds a saturation depth, set to three-quarters of the maximum content of the layer or field capacity. The lower layer is saturated if the moisture fraction exceeds 0.32 (a depth of 16 cm). The field capacity for each soil layer does not vary geographically. Any excess in either layer, after the total fluxes between both layers and between the upper layer and the atmosphere have been calculated, is treated as runoff. In the standard version of the MUGCM runoff is discarded and no longer interacts with the atmospheric hydrologic cycle. An alternative version of the model, described in Chapter 4, includes a river runoff scheme which transports runoff to the ocean.

While many GCMs now employ more complex land surface schemes, including the parameterisation of geographically variable soil and vegetation types, simple bucket models such as the scheme of *Deardorff* [1977] are still widely used [eg. *IPCC*, 2001]. This scheme is able to capture the diurnal variability of surface soil moisture and hydrologic fluxes, which *Simmonds and Hope* [1998] demonstrate produces important feedbacks with local precipitation. The development of a more sophisticated land surface scheme is beyond the scope of this study, and the existing formulation is believed to be adequate for the purpose of simulating the isotopic response to large scale climate forcing.

3.3 Isotopic tracer scheme

An isotopic tracer scheme has been implemented in the MUGCM, as described fully by *Noone* [2001]. Following the approach adopted in the other isotopic tracer schemes discussed in Chapter 2, the MUGCM scheme incorporates the isotopic species of water in parallel to normal water but with fractionation at phase transitions included. The parameterisation of equilibrium and non-equilibrium isotopic fractionation during evaporation, condensation and reevaporation is described below.

3.3.1 Surface fluxes

Over land, evaporation in the model occurs without fractionation, with the isotopic ratio of the evaporated moisture equal to that in the upper soil layer, representing evapotranspiration without fractionation as discussed in Chapter 2. As the model has no separate land surface designation for bare soil and vegetation, all evaporation from land is treated in the same manner, with the isotopic ratio determined by the ratio in the upper soil layer. No fractionation during evaporation is also assumed for ice, snow and frozen soil as the low diffusivity of the isotopic species in the solid phase prevents isotopic exchange.

Over ocean, the fluxes of the isotopic species are calculated with a bulk parameterisation similar to that for normal water:

$$E_i = C_{Di} \rho C_w |v| (q_{isat}(T_S) - q_{iatm}) \tag{3.4}$$

where the isotopic saturation value is calculated assuming isotopic equilibrium with the ocean surface so that:

$$q_{isat} = q_{sat} R_{ocean} / \alpha(T_s) \tag{3.5}$$

for ocean surface isotopic ratio R_{ocean} with fractionation factor $\alpha(T_s)$ at surface temperature T_s. It is via the calculation of the surface atmospheric isotopic ratio above the ocean that the ocean isotopic ratio influences the atmospheric ratio, as discussed further in Chapter 4.

The drag coefficient C_{Di} is modified to account for kinetic fractionation by the formula: $C_{Di} = (1 - k)C_D$ where k is a factor which depends on the near-surface (10 m) wind speed and on the isotopic diffusivity. The value of k depends on the flow regime, divided into smooth (laminar) and rough (turbulent) flow according to the surface layer model of *Brutsaert* [1975].

Following the approach of *Jouzel et al.* [1987b], a linear fit is used to estimate k from the surface wind speed, so that for $H_2^{18}O$, $k = 0.006$ for the smooth regime ($v < 7$ m/s) and for the rough regime, $k = 0.0002856v + 0.00082$ for $v \geq 7$ m/s. The ratio of the kinetic fractionation factors for HDO and $H_2^{18}O$ is constant and close to unity ($k(D)/k(^{18}O) = 0.88$) [*Merlivat*, 1978] as kinetic fractionation depends only on the molecular diffusivities of the isotopic species.

When dew forms over land or ocean the negative evaporation (dew) condenses at the ratio of the first atmospheric level, undergoing fractionation. If the surface is frozen, the dew forms as frost and kinetic effects occur. In the case of frost formation, kinetic fractionation is parameterised as for the formation of solid condensation under conditions of supersaturation (see next Subsection).

3.3.2 Atmospheric processes

For large scale or stratiform precipitation, total equilibrium fractionation occurs as the drop size is assumed to be small and full isotopic exchange between vapour and condensate is able to occur before the condensate is removed. The temperature of the layer is adjusted to take account of the formation of condensate, and the mean of the fractionation factors at the temperature before and after the adjustment is used. As the model does not allow for separate budgets of solid and liquid cloud water, fractionation is with respect to ice if the initial and final temperatures of the layer are below $-10°$C.

Kinetic effects are included for temperatures below $-20°$C for both large scale and convective precipitation, as the rate of molecular diffusivity of the isotopic species in the supersaturated vapour around solid condensate dominates equilibrium fractionation at these temperatures. The effective fractionation factor (α_{eff}) is calculated following the parameterisation of *Jouzel et al.* [1987b]:

$$\alpha_{eff} = \frac{S\alpha}{\alpha(D/D')(S-1)+1} \tag{3.6}$$

where S is the supersaturation factor representing the ratio of the saturation vapour pressure over water to that over ice. This factor is parameterised as a function of temperature T(°C) using the regression $S = 1 - 0.003T$ following *Jouzel and Merlivat* [1984]. D and D' are the molecular diffusivities of normal water and the isotopic species.

In the case of convective precipitation Rayleigh distillation is assumed for solid condensate (temperatures less than −10°C) which will rapidly fall from the layer, and fractionation is with respect to ice. Total equilibrium is assumed for the formation of liquid condensate. In both cases the mean of the mass-weighted temperature within the unstable block and the final temperature of each level within the block is used for the calculation of the fractionation factor.

The *Manabe et al.* [1965] convection scheme does not include a representation of small scale convective updrafts which overshoot the unstable layer and undergo vertical cooling at high altitudes in tropical convective towers. The model may therefore be expected to underestimate the extent of fractionation in the tropics associated with such localised convection. The convection scheme calculates a net fractionation appropriate to the conditions at the cloud base, equivalent to moisture rising and condensing at the lifting condensation level.

To parameterise the effect of vertical mixing due to entrainment and detrainment within convective plumes, an alteration is made to the scheme following *Joussaume et al.* [1984]. When two or more adjacent layers within a column are found to be convectively unstable, the mass-weighted isotopic ratio of the entire block is calculated and the isotopic content of the layers within the block adjusted to represent convective diffusion. This adjustment will result in a decrease in the isotopic ratios in the upper levels of the column and an increase in the isotopic ratios in the lower levels, although subsequent reevaporation of upper level condensate at lower levels will act to reduce the effect of the adjustment.

Reevaporation is incorporated without fractionation in the case of reevaporation from ice, and with fractionation and kinetic effects for liquid precipitation. Kinetic effects are parameterised via an “undersaturation” parameter based on effective humidity following *Stewart* [1975] and *Joussaume and Jouzel* [1993]. The fractionation factor is replaced with an effective factor as in Equation 3.6, with the ratio of diffusivities modified: $(D'/D)^{0.58}$ and the supersaturation factor S replaced with an effective humidity $h = (h_o + 3)/4$ [*Jouzel et al.*, 1987b] where h_o is the initial local humidity.

An efficiency factor is applied based on precipitation type (convection or large scale) to represent the distribution of drop sizes, which is not explicitly modelled. The rate of isotopic equilibration between the drop and its surroundings depends on drop size, with small drops undergoing fractionation more readily than large drops. Following *Hoffmann and Heimann* [1998], 45% of the condensate is fractionated in the case of convective precipitation which consists predominantly of large drops, while for large scale precipitation consisting of a majority of small drops, 95% is fractionated.

The extent to which this convective parameterisation is adequate for isotopic modelling is discussed by *Noone* [2001]. In the case of large scale (low resolution) studies, the *Manabe et al.* [1965] convection scheme is adequate. Similarly for studies of polar precipitation, the representation of convective precipitation is not crucial. However, in studies of tropical precipitation where the intensity of convective activity strongly influences the resulting isotopic ratios, the representation of convective processes in the model becomes more important. The ability of the MUGCM to simulate the seasonal and interannual tropical precipitation and isotopic distribution is therefore validated below for the mean model climatology and in Chapter 5 for a transient simulation of climate from 1950–1999.

3.4 Validation of atmospheric model

The model climatology for the MUGCM (Version IX) is described by *Noone* [2001]. The version of the model used in this study includes some updates, and so the climatology of the latest version of the model is presented here and compared with observations. Modelled seasonal averages of mean sea level pressure (MSLP), two-metre temperature and precipitation are taken from a 20-year control run with *Reynolds* [1988] monthly SSTs after a five year spin up period.

3.4.1 Mean sea level pressure

The modelled MSLP is compared with the National Centers for Environmental Prediction (NCEP) Reanalysis [*Kalnay et al.*, 1996] data which was obtained from the NOAA-CIRES Climate Diagnostics Center. The seasonal December-January-February (DJF) and June-July-August (JJA) averages of the NCEP data from 1979–2002 are compared with the seasonal averages from the model. As the modelled MSLP is extrapolated from the surface pressure adjusted via the hydrostatic approximation to sea level, the values are of limited meaning over high topography.

The modelled and NCEP MSLP for DJF and JJA are shown in Figures 3.1 and 3.2. In DJF the simulation correctly reproduces the position of the subtropical anticyclones although slightly overestimating their central pressure by about 2 hPa. The Aleutian Low is also situated over the Bering Sea, rather than over Alaska as simulated in the previous version of the model. The simulation of the Icelandic Low is also improved.

In JJA, the model simulates the Northern Hemisphere subtropical anticyclones but overestimates their central pressure. The model continues to simulate an overly strong meridional pressure gradient in the Southern Hemisphere midlatitudes. The high pressures over Antarctica in the NCEP JJA average is known be unphysical.

3.4.2 Two-metre temperature

The screen height temperature two metres above the surface (T_{2m}) is calculated in the model following the *Louis* [1979] boundary layer formulation:

$$T_{2m} = T_s - \left(\frac{H}{1.35 k u_* \rho c_p}\right) log_e \left(\frac{z_{2m}}{z_0}\right) \tag{3.7}$$

where k is the Von Karman constant, z_o is the roughness length, ρ is the air density, c_p is the heat capacity at constant pressure and u_* is the friction velocity calculated from the drag coefficient via $C_D = |u_*/u|^2$. The modelled temperatures are compared with two-metre temperatures from the NCEP Reanalysis, described above. The modelled and NCEP DJF and JJA two-metre temperatures are shown in Figures 3.3 and 3.4.

Over ocean the modelled and NCEP temperatures closely follow the SSTs, with only small differences due to the lower resolution of the spectral topogra-

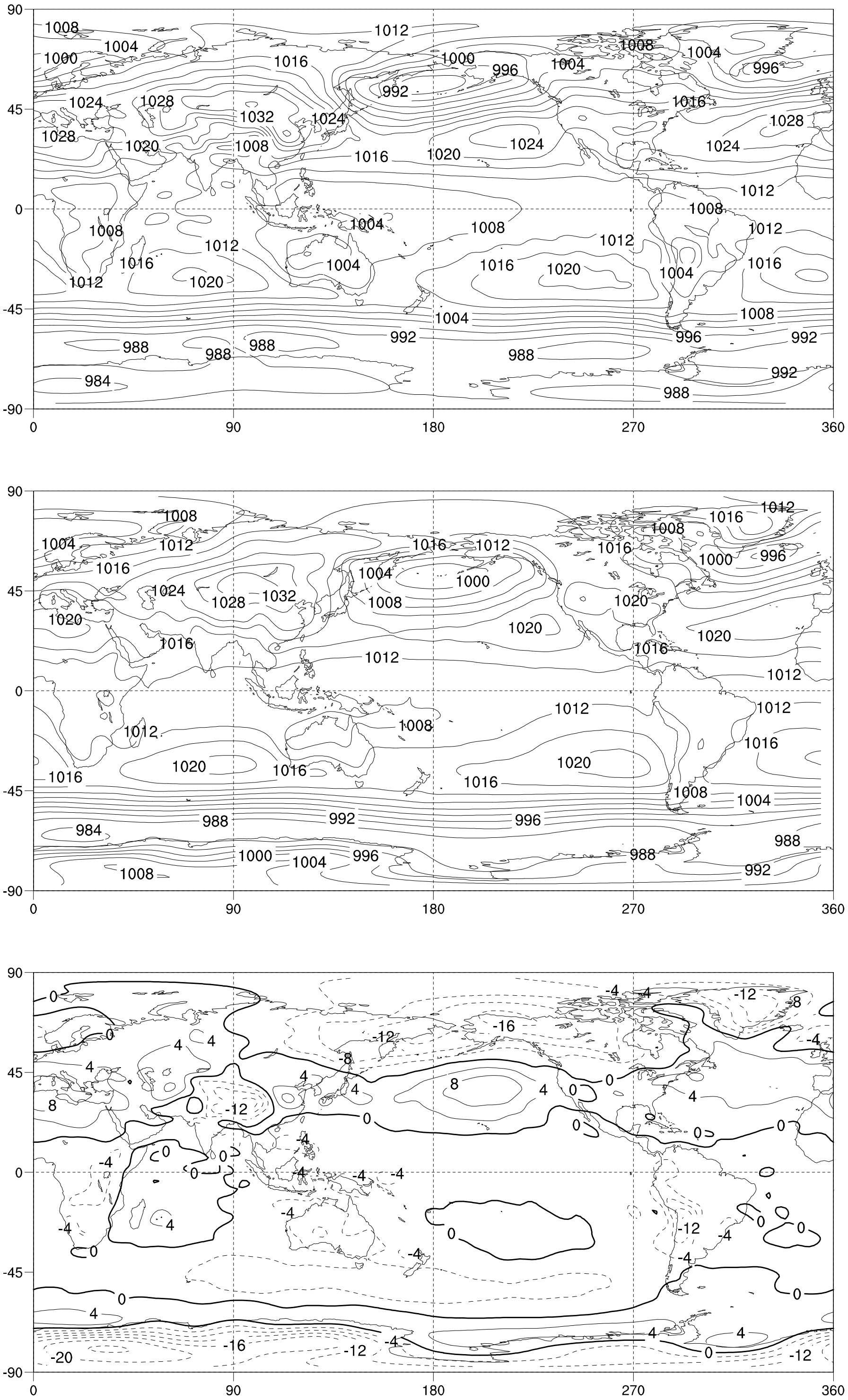

Figure 3.1: DJF mean sea level pressure: MUGCM (top), NCEP (middle) and difference (bottom). Contour interval is 4 hPa.

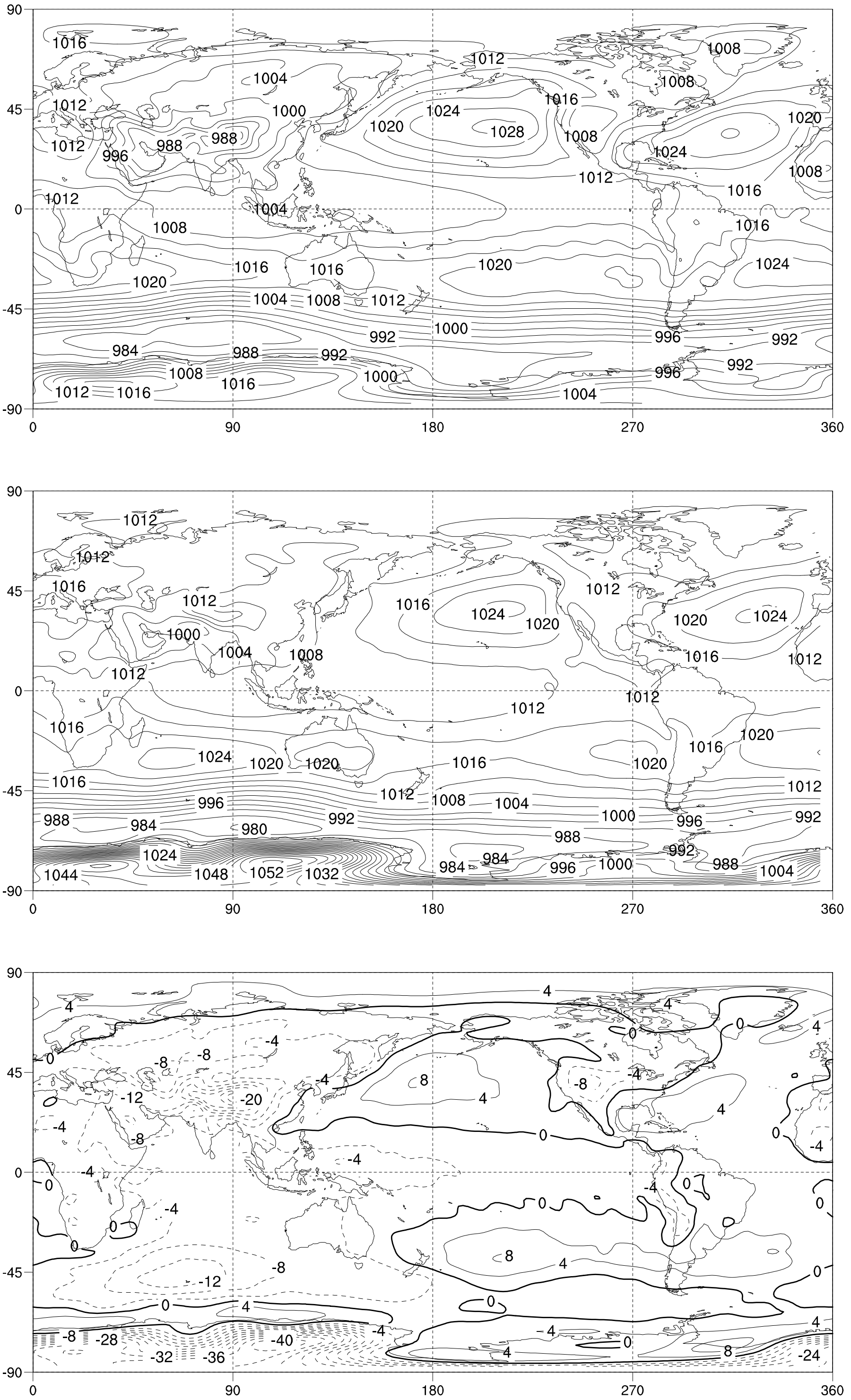

Figure 3.2: JJA mean sea level pressure: MUGCM (top), NCEP (middle) and difference (bottom). Contour interval is 4 hPa.

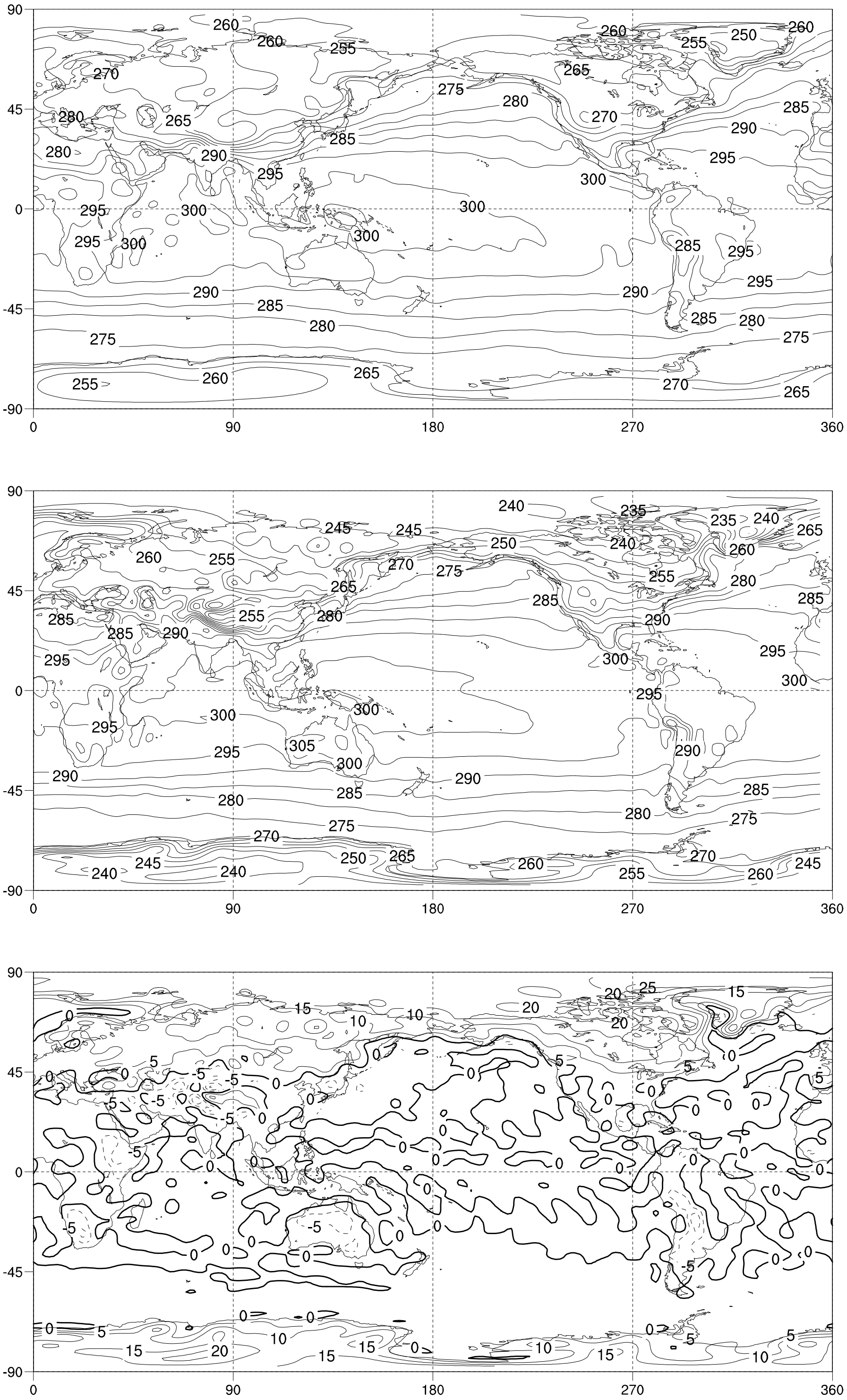

Figure 3.3: DJF two-metre temperature: MUGCM (top), NCEP (middle) and difference (bottom). Contour interval is 5°K.

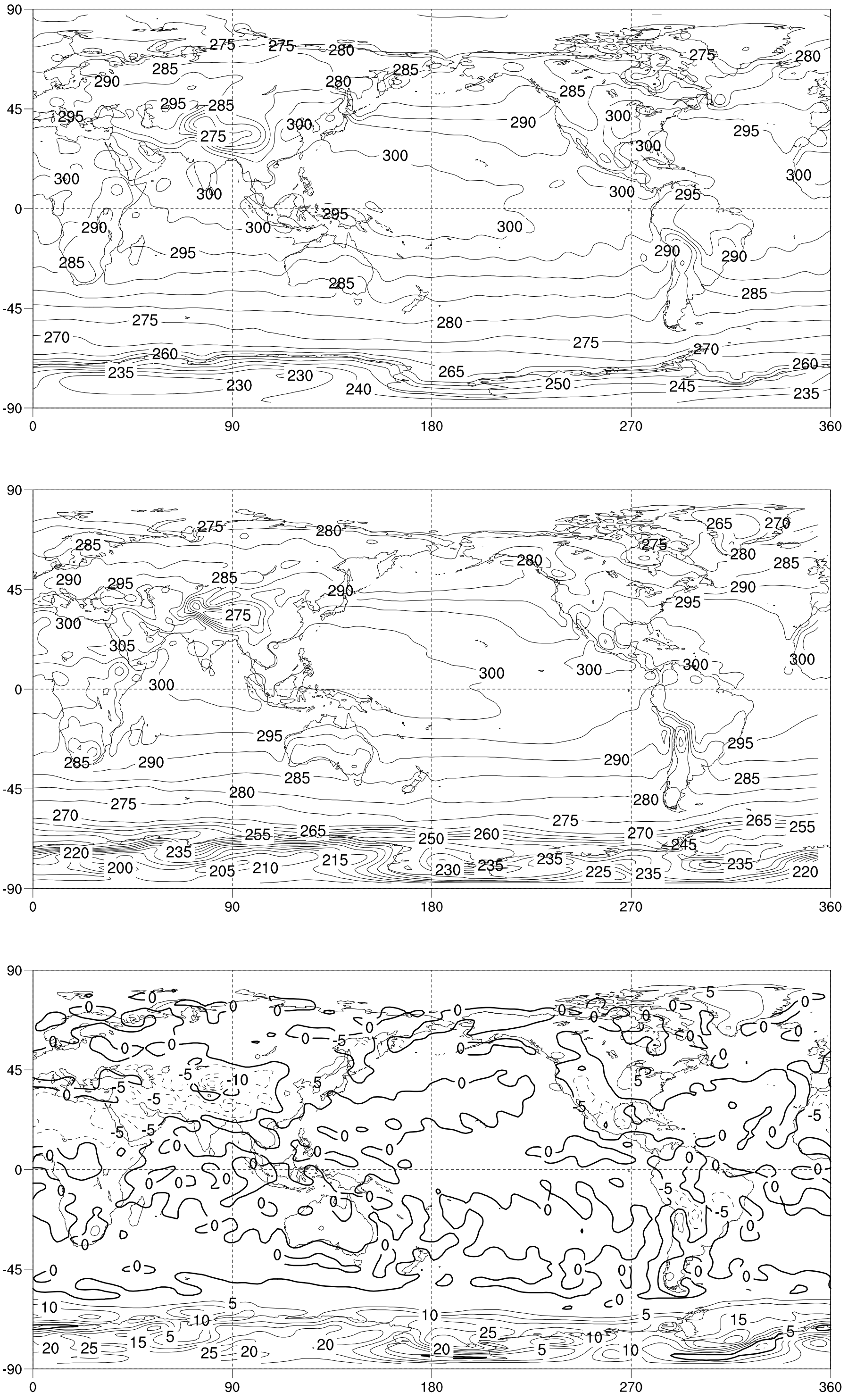

Figure 3.4: JJA two-metre temperature: MUGCM (top) and NCEP (middle) and difference (bottom). Contour interval is 5°K.

phy in the MUGCM producing spectral “ripples” in the modelled field. Large differences in two-metre temperature are seen over regions of high topography where the lower resolution model topography underestimates the elevation and hence the surface cooling.

It can be seen that the MUGCM simulates overly warm polar temperatures in both hemispheres in winter, and underestimates the temperature gradient over Northern Hemisphere continents. Antarctica is around 10°K too warm due to the lower topography in the model although the seasonal range in Antarctica and Greenland is well reproduced. Tropical and mid-latitude continents appear too cool, particularly in the summer, which *Noone* [2001] ascribes to the limitations of the treatment of soil moisture and land surface albedo in the model.

3.4.3 Precipitation

The modelled precipitation is compared with precipitation data averaged over 1979–2001 from *Xie and Arkin* [1996]. The Xie and Arkin data set includes gauge measurements, satellite observations and model prognoses from ECMWF analyses. The modelled and observed DJF and JJA precipitation is shown in Figures 3.5 and 3.6. The modelled and observed seasonal precipitation signal associated with the monsoon is discussed further in Chapter 5.

The model simulates too much precipitation over elevated topography, including over Papua New Guinea and Sumatra in the western Pacific, the Himalayas, the South American Andes and the North American Rocky Mountains. This is a result of the limitations of the *Manabe et al.* [1965] convection scheme over steep localised topography. When moist air is advected over raised topography following sigma pressure surfaces, the rapid cooling leads to large-scale condensation which exceeds that observed [*Noone*, 2001].

The model simulates too little precipitation over tropical and mid-latitude oceans, particularly in the region of the ITCZ. This may be a result of the excess precipitation over topography removing moisture from regions downwind. The South Pacific Convergence Zone (SPCZ) and South Atlantic Convergence Zone (SACZ) are reproduced, although the precipitation amounts are somewhat underestimated for JJA. The excessive precipitation in the SACZ region in the version of the model described by *Noone* [2001] is no longer simulated. The precipitation in arid areas including Australia and the Sahara as well as the

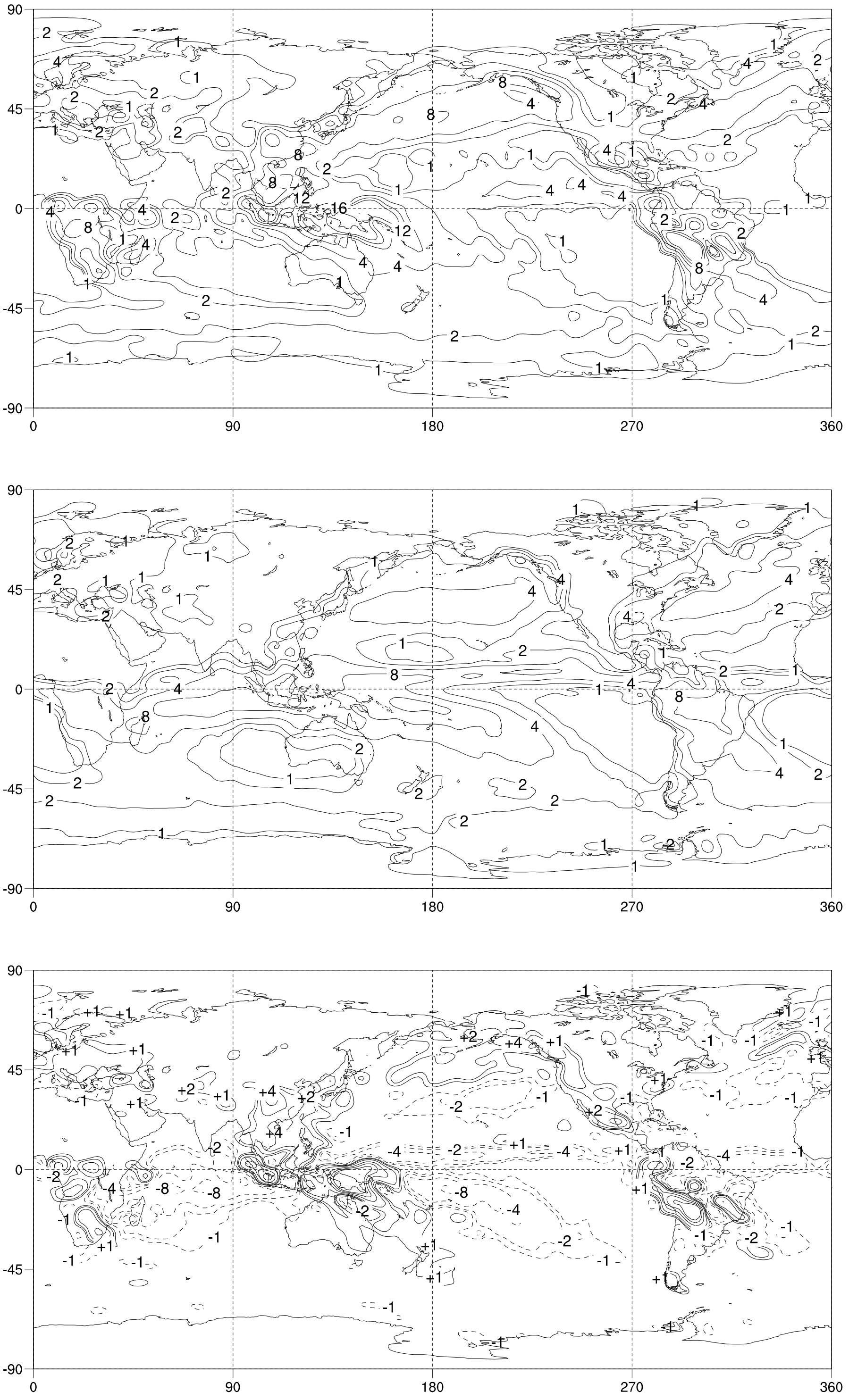

Figure 3.5: DJF precipitation: MUGCM (top), Xie and Arkin (middle) and difference (bottom). Contours are 1, 2, 4, 8, 12, 16 mm/day.

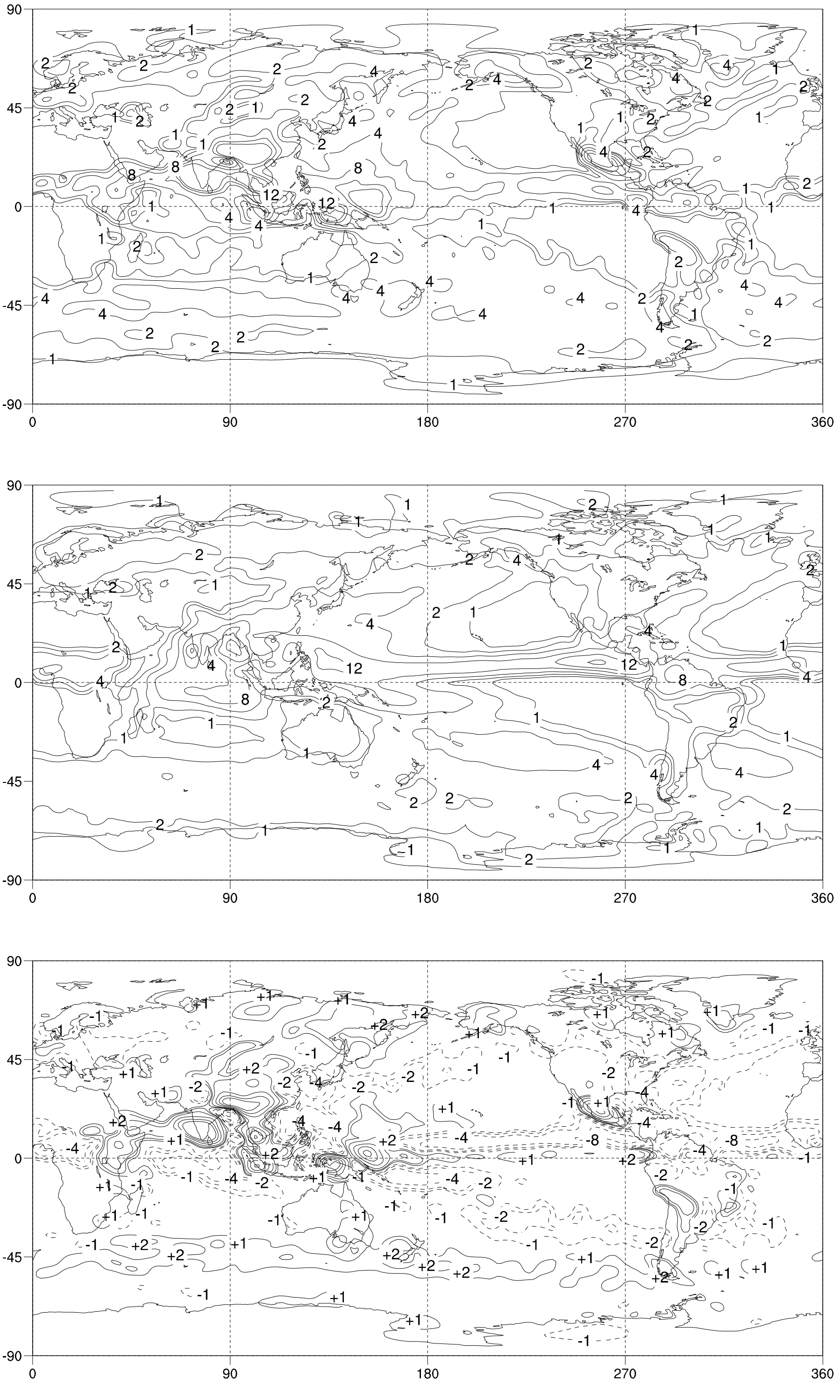

Figure 3.6: JJA precipitation: MUGCM (top), Xie and Arkin (middle) and difference (bottom). Contours are 1, 2, 4, 8, 12, 16 mm/day.

polar regions is well simulated.

In general, climate models have some difficulty in correctly simulating the distribution of precipitation, as discussed by *Gates et al.* [1999] in relation to the results of the Atmospheric Model Intercomparison Project (AMIP). The simulation of precipitation in the MUGCM is comparable to that in other atmospheric GCMs of similar resolution, and is improved over the eastern tropical Pacific and tropical Atlantic sectors compared with the previous version of the model.

3.5 Validation of isotopic tracer scheme

3.5.1 Global distribution of isotopes

The seasonal average (DJF, JJA and DJF – JJA) distributions of δ^{18}O for the model control run are shown in Figure 3.7. The precipitation-weighted mean δ^{18}O values from GNIP stations for the same months are shown in Figure 3.8. The GNIP data is taken from stations with a minimum of three years data for the relevant months. The values are averaged over areas with a high density of stations (more than one station within 500 km).

The highest modelled δ^{18}O values are seen in the subtropical Pacific and Atlantic anticyclone regions where low precipitation amounts results in little depletion of the heavy isotope from the atmospheric vapour. Over most of the tropical ocean, the source for convective precipitation is local moisture resulting in little isotopic rainout between source and precipitation sites. The modelled mean DJF and JJA δ^{18}O values match the observations well in this region. Greater isotopic depletion is associated with the ITCZ and the western Pacific Warm Pool regions of high precipitation.

The seasonal cycle of δ^{18}O is small over tropical oceans, with typically 0–5‰ difference between DJF and JJA values both for the model and observations. The seasonal cycle is of the opposite sign in the tropics compared with mid- and high latitudes, as the tropical isotopic signal is dominated by the difference between the summer wet season and winter dry season. In some mid-latitudes regions, greater temperature variability as well as the opposite seasonality of precipitation (wetter winters) produces a reversed seasonal isotopic signal. This is most clearly seen over central Asia where the limit of the extent of the Asian monsoon marks the boundary between positive and negative modelled DJF –

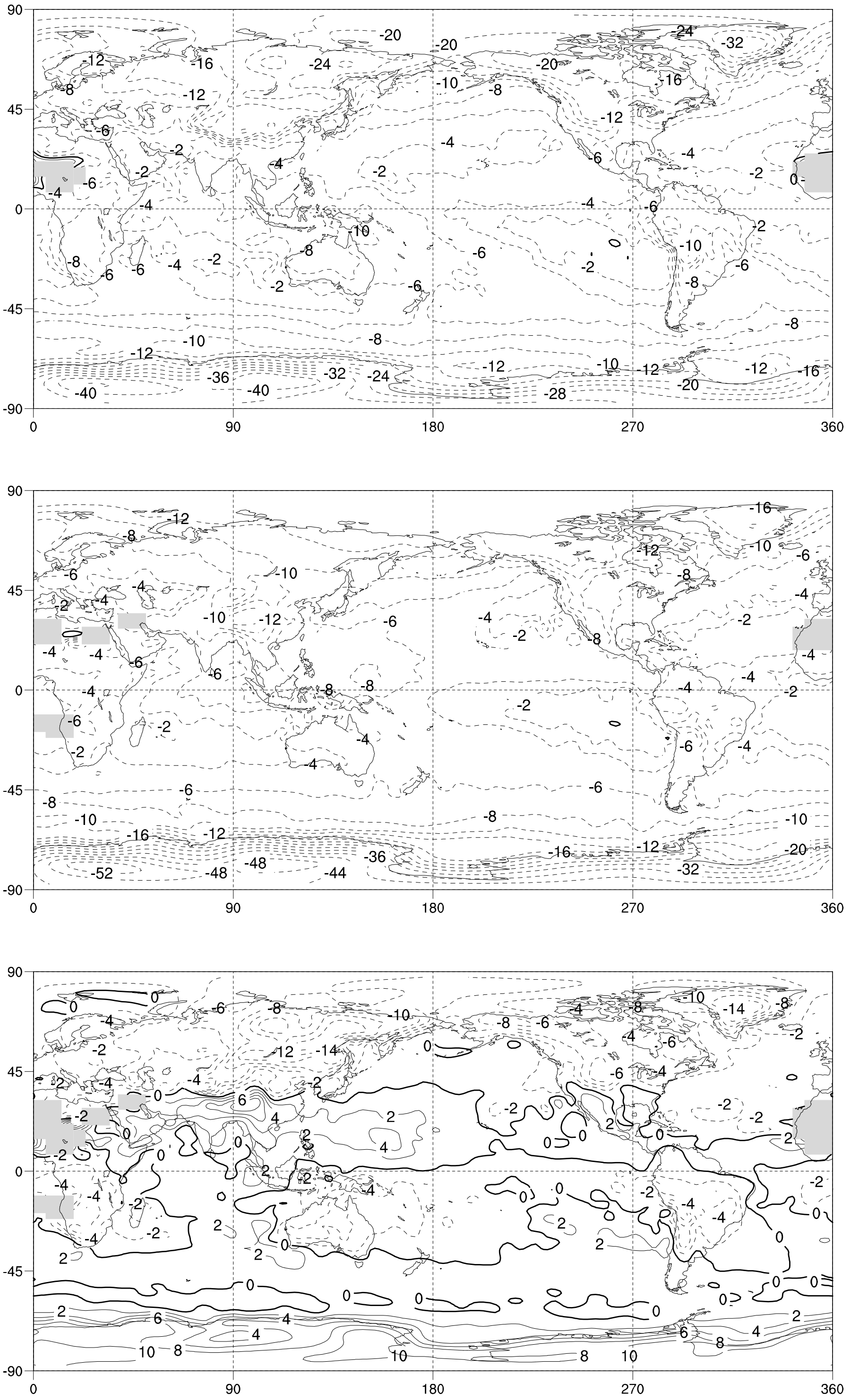

Figure 3.7: Modelled average precipitation δ^{18}O: DJF (top), JJA (middle) and DJF – JJA (bottom). Contour interval is 2‰.

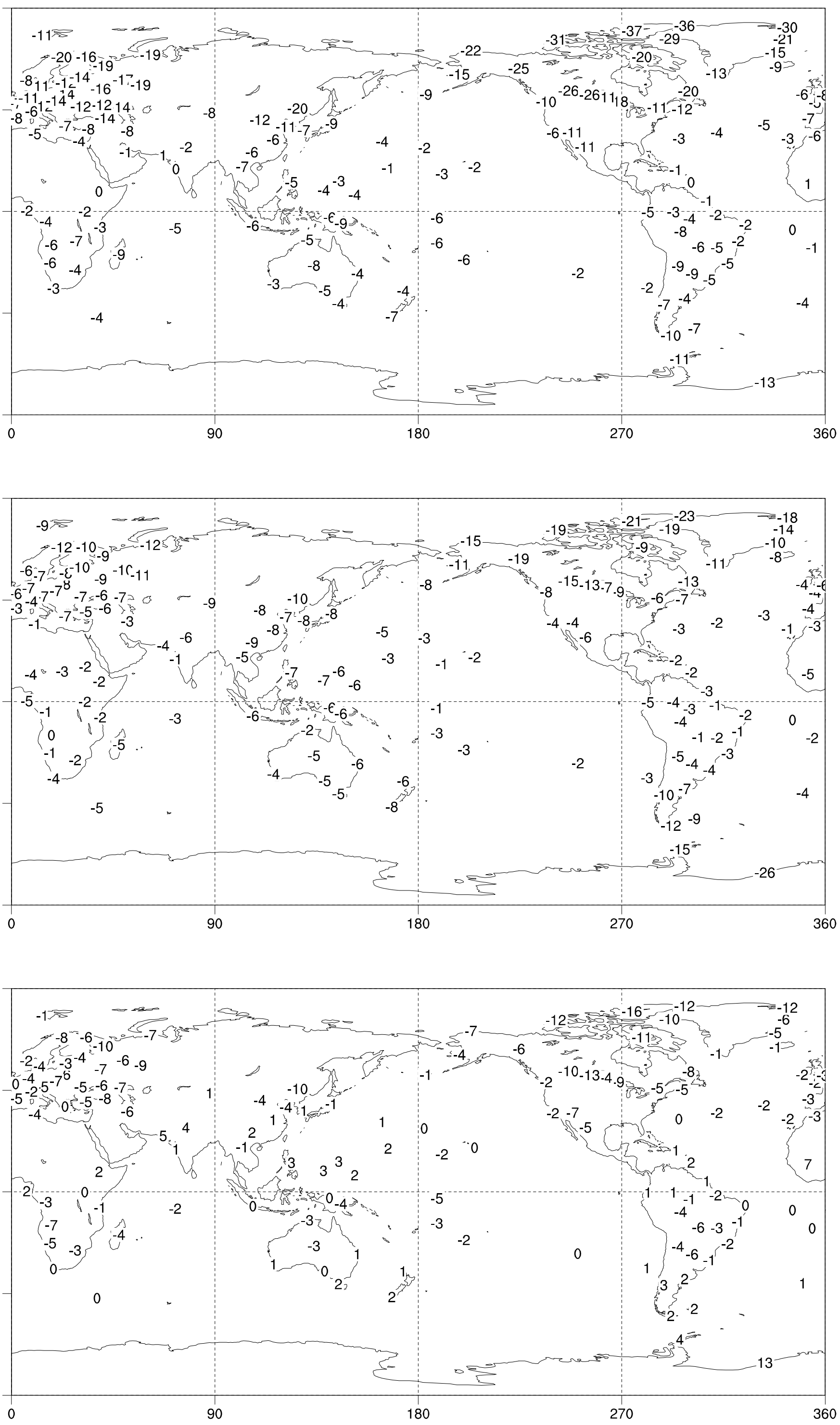

Figure 3.8: Observed average precipitation δ^{18}O: DJF (top), JJA (middle) and DJF – JJA (bottom). Values are rounded to the nearest integer.

JJA isotopic values.

The main discrepancies between modelled and observed seasonal δ^{18}O values are explained by limitations of the modelled precipitation and temperature distributions. The excess precipitation simulated over topography, particularly in tropical areas such as southeast Asia, leads to overly large isotopic depletion in these areas. Over regions such the Andes, the Himalayas and the Antarctic continent the lower elevation of the model topography leads to underestimation of cooling associated with orographic lifting of moisture and underestimation of isotopic depletion, a limitation identified in other isotopic GCMs including the GENESIS model [*Mathieu et al.*, 2002].

In general however there is a close correspondence between the modelled and observed δ^{18}O values, with modelled values being generally within 2‰ of observations. The model reproduces the main features of increased isotopic depletion at high latitudes (temperature effect), inland over continents (continentality effect), at high elevations (altitude effect) and in regions of high precipitation (amount effect) seen in the observed distribution.

3.5.2 HDO–$H_2^{18}O$ relationship

The relationship between HDO and $H_2^{18}O$ is a function of the relative importance of equilibrium and kinetic fractionation measured by the deviation from the Meteoric Water Line as outlined in Chapter 2. The slope of the modelled line (Figure 3.9) is 8.07 compared with 8.17 for GNIP observations when all the data are included. However the data is somewhat nonlinear, and the slope and intercept depend on which data are included for the regression [*Noone*, 2001].

Noone [2001] comments that the modelled HDO–$H_2^{18}O$ relationship depends on the parameterisation of kinetic effects via the supersaturation factor as given in Equation 3.6. While this factor could have been adjusted to produce an $H_2^{18}O$/HDO slope closer to the observed slope, the same function as that used in other GCM isotopic tracer schemes was adopted for consistency.

The deuterium excess ($d = \delta D - 8\delta^{18}O$) is a second-order parameter which is less well reproduced by isotopic GCMs than the δ^{18}O or δD values. The modelled and observed GNIP annual average deuterium excess distributions are shown in Figure 3.10. The mean global deuterium excess (intercept of the slope in Figure 3.9) for the model is 6.5‰ while the observed value is 11.02‰. The ECHAM and GENESIS models also systematically underestimate the observed

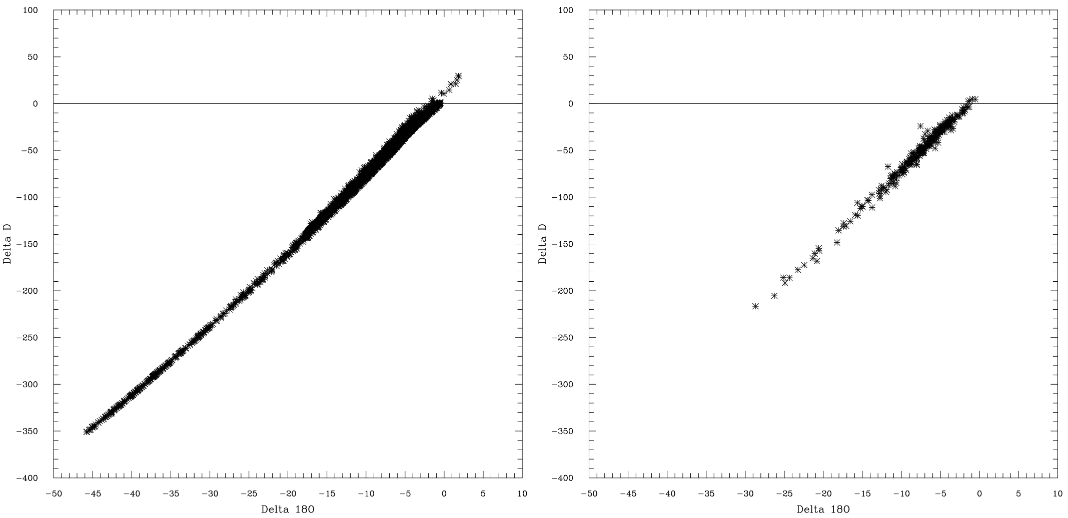

Figure 3.9: Modelled (left) and observed (right) annual average δ^{18}O versus δD.

deuterium excess by 2–4‰[*Hoffmann and Heimann*, 1998; *Mathieu et al.*, 2002].

This underestimation of deuterium excess may be due to the representation of boundary layer processes over the ocean, as discussed by *Mathieu et al.* [2002]. They carry out sensitivity tests of the modelled parameterisation of kinetic fractionation during evaporation and find that taking account of non-neutral stratification in the constant-flux layer above the ocean is important. While the standard parameterisations assume neutral stratification [*Merlivat and Jouzel*, 1979], when the parameterisation is modified to allow for non-neutral stratification the mean modelled deuterium excess is within 0.5‰ of the observed value.

The MUGCM reproduces the observed maximum deuterium excess values over the Middle East due to evaporation of source moisture over the Caspian and Mediterranean Seas under conditions of low relative humidity and warm SSTs. This feature is also well reproduced by the ECHAM model but not by the GENESIS model. High values are also seen over the Himalayan region associated with the formation of snow and ice with kinetic effects. The model also reproduces this effect, as does the GISS model [*Jouzel et al.*, 1987b] and the ECHAM model [*Hoffmann and Heimann*, 1998].

High deuterium excess values due to kinetic effects during snow formation are observed over inland Greenland and Antarctica. The model is able to reproduce

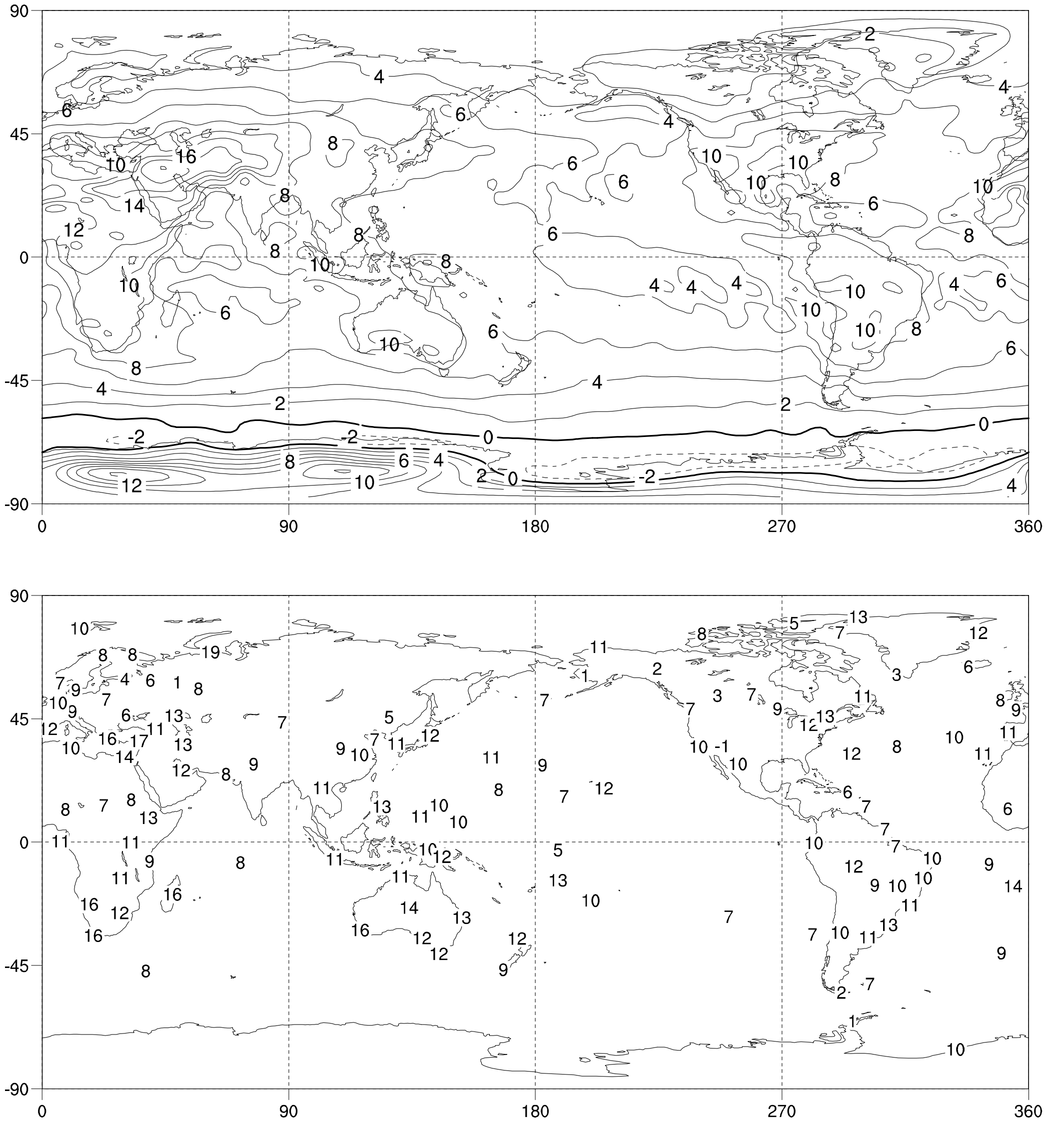

Figure 3.10: Modelled (top) and observed (bottom) annual average deuterium excess. Contour interval is 2‰.

this effect well over Antarctica with values of up to +15‰ in East Antarctica, although values over Greenland only reach around +5‰, possibly due to the limited surface cooling with elevation due to model resolution.

Deuterium excess decreases with latitude over the oceans as evaporation occurs from cooler SSTs and under conditions of higher relative humidity. This is seen in the model with the lowest values found on the Antarctic coast. While low values are also observed in this region, for example at Argentine Island ($d = +1$‰), the negative modelled d values suggest that reevaporation may be overestimated in this area. No other model produces negative deuterium excess values near Antarctica except for the LMD model [*Joussaume and Jouzel*, 1993] which simulates negative deuterium excess over many continental areas due to an overestimation of reevaporation.

The model does not reproduce the observed low deuterium excess values over arid inland continental areas such as parts of Africa or North America (values as low as −18‰ to −20‰ are recorded at Mali in Africa and California in the United States in GNIP observations, [*IAEA/WMO*, 2001]). Low deuterium excess over arid areas is seen in the GENESIS model and overestimated by the LMD model but not reproduced by the GISS model, which *Jouzel et al.* [1987b] suggests may be due to the lack of kinetic effects for reevaporation outside convective clouds and above the cloud base in the GISS isotopic scheme.

3.5.3 Spatial temperature–isotope relationships

The spatial temperature–δ^{18}O relationship was first described by *Dansgaard* [1964] from early GNIP observations. This linear relationship is observed to hold for locations with annual average temperatures below 15°C above which the precipitation amount effect is dominant, as outlined in Chapter 2.

Using GNIP observations from 1950–2000, a slope of 0.55‰/°C is obtained for stations with temperatures below 15°C, which is higher than the observed slope of 0.69‰/°C given by *Dansgaard* [1964]. The slope obtained from annual average data at each model grid point (Figure 3.11) is 0.79‰/°C for the same temperature range [*Noone*, 2001]. However the slope differs depending on whether the modelled data at cold high latitude grid points, which are beyond the range of the GNIP observational network, are used. If only those points falling within the latitude range of GNIP stations are used, the modelled slope is 0.62‰/°C, which compares well with a slope of 0.64‰/°C for the extended

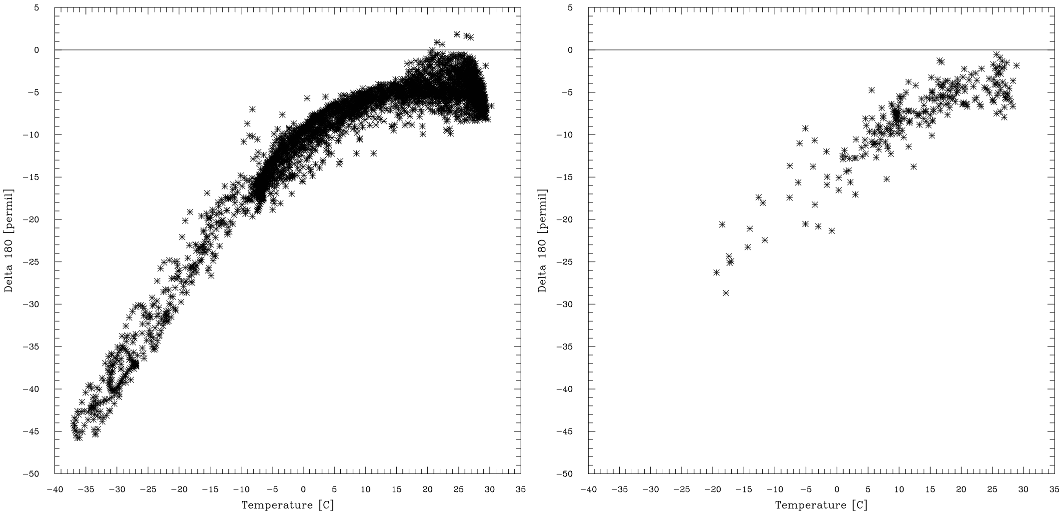

Figure 3.11: Modelled (left) and observed (right) annual average δ^{18}O versus surface temperature.

observational data set of *Joussaume and Jouzel* [1993].

The temperature at which the linearity of the modelled slope breaks down is closer to 0°C than the observed value of 15°C. *Hoffmann and Heimann* [1998] note that the LMD model shows a breakdown of the temperature–δ^{18}O relationship close to 0°C also, whereas the GISS and ECHAM models simulate a linear relationship at temperatures up to 15°C. This may be related to the different representations of convective processes and vertical diffusion in the models.

3.5.4 Temporal climate–isotope relationships

The modelled interannual temperature and precipitation–δ^{18}O correlations are compared with the observed correlations to determine whether the model reproduces the observed interannual isotope–climate relationships in the tropics. The model was forced with observed SSTs and sea ice coverage from 1950–1999 (see Chapter 5) in order to produce interannual variability. The monthly anomalies of surface temperature, precipitation amount and amount-weighted anomalies of δ^{18}O were calculated for the 50-year model run and the correlations between δ^{18}O and temperature and precipitation calculated at each grid point, as shown in Figure 3.12. The statistical significance of the correlations was calculated using Student's t-test.

The correlation between δ^{18}O and temperature is positive polewards of ap-

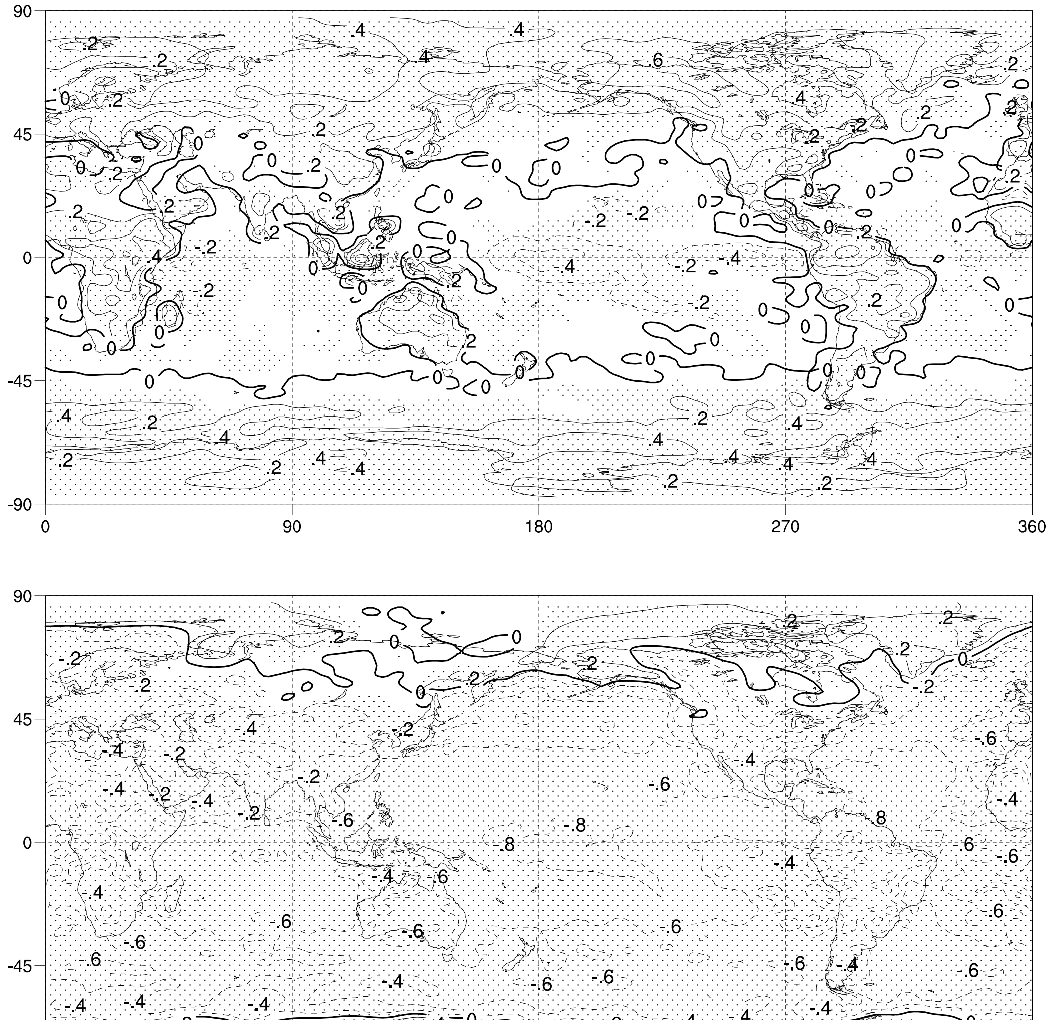

Figure 3.12: Correlations between modelled monthly anomalies of surface temperature and δ^{18}O (top) and precipitation and δ^{18}O (bottom). Contour interval is 0.2. Stippled correlations are significant at 95% confidence level.

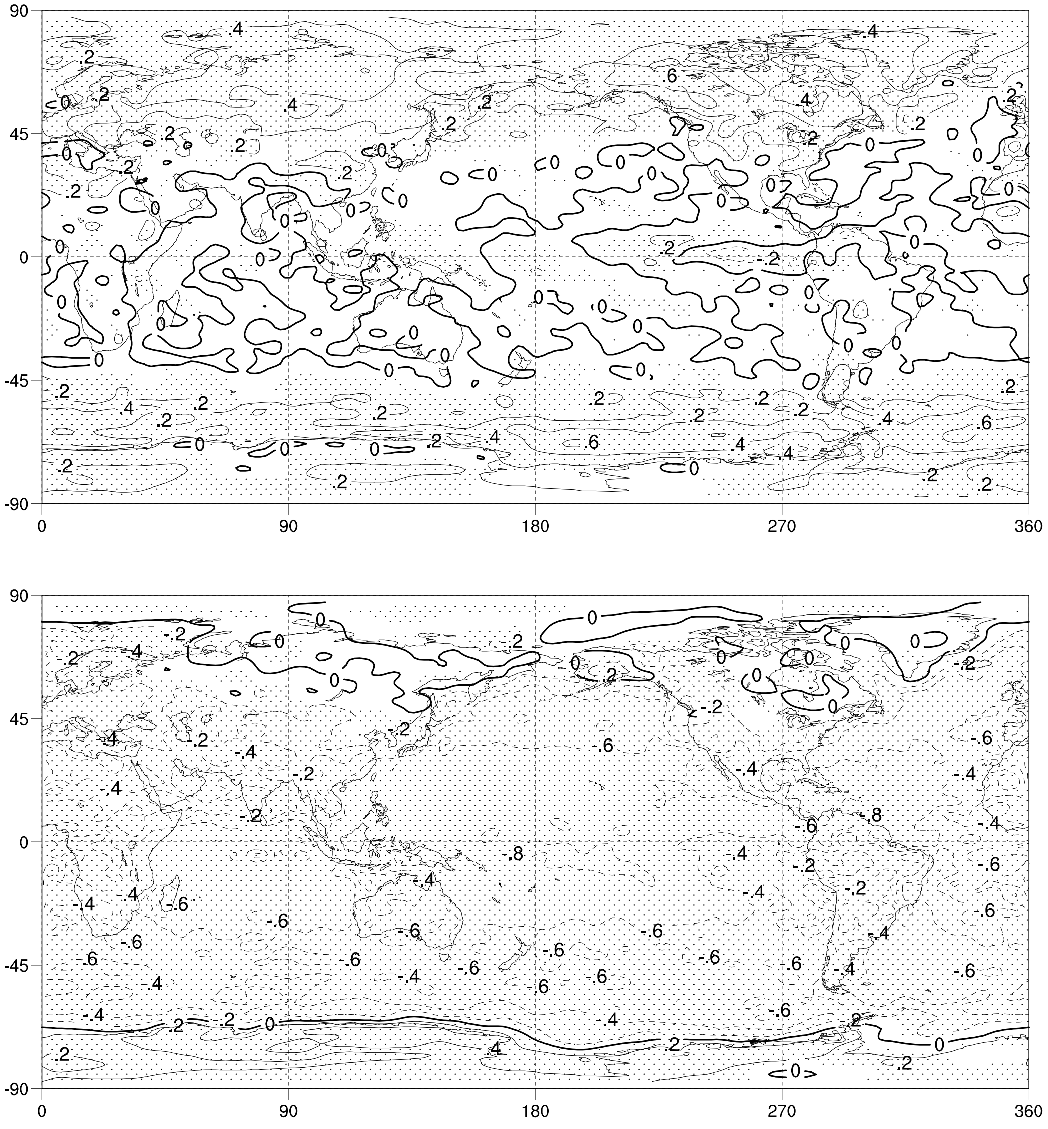

Figure 3.13: Partial correlations between modelled monthly anomalies of surface temperature and $\delta^{18}O$ (top) and precipitation and $\delta^{18}O$ (bottom) with the effect of precipitation and temperature respectively removed. Contour interval is 0.2. Stippled correlations are significant at 95% confidence level.

proximately 45° as expected from the temperature effect, as cooling with poleward transport of moisture is associated with rainout of the heavy isotope at mid- and high latitudes. A positive correlation is seen over continental areas including tropical continents where cooler surface temperatures are associated with increased precipitation and hence isotopic depletion. A negative temperature–isotope relationship is seen in the tropical ocean basins where temperature influences isotopic depletion via the precipitation amount effect. In these regions, warmer temperatures are associated with increased local evaporation, convective activity and precipitation and hence more negative δ^{18}O values on seasonal and interannual time scales.

The correlation between precipitation amount and δ^{18}O is found to be negative for all regions except over polar continents and sea ice. In general, higher precipitation amounts lead to greater isotopic depletion at a given location, however at high latitudes large precipitation amounts occur with stronger advection of less isotopically depleted mid-latitude moisture as well as warmer than usual local temperatures [*Noone et al.*, 1999; *Noone*, 2001].

The interaction between the temperature and amount controls on δ^{18}O was also investigated by calculating the partial correlation between each of the variables and δ^{18}O with the influence of the blind variable removed (Figure 3.13). It can be seen that the temperature–isotope correlations in the tropics and mid-latitudes are substantially reduced when the effect of precipitation amount is reduced, as expected. The major significant tropical temperature–isotope correlation which remains is in the eastern equatorial Pacific where SST variability due to ENSO influences the isotopic signal (see Chapter 5).

The modelled precipitation–isotope correlation is not generally reduced when the influence of temperature is removed, except for in some polar regions where the positive correlation between precipitation amount and δ^{18}O is reduced in the partial correlation.

For comparison, observed temperature, precipitation and amount-weighted δ^{18}O monthly anomalies were calculated for all GNIP stations with more than three years of data. As shown in Figure 3.14 the observed correlations are generally of the same sign and within 0.1 of the modelled correlations. The temperature–δ^{18}O correlations are predominantly negative over tropical oceans and positive over tropical continents as well as at most high latitude stations.

The observed partial correlations (Figure 3.15) are similar to the modelled partial correlations, although the tropical temperature–δ^{18}O correlations are

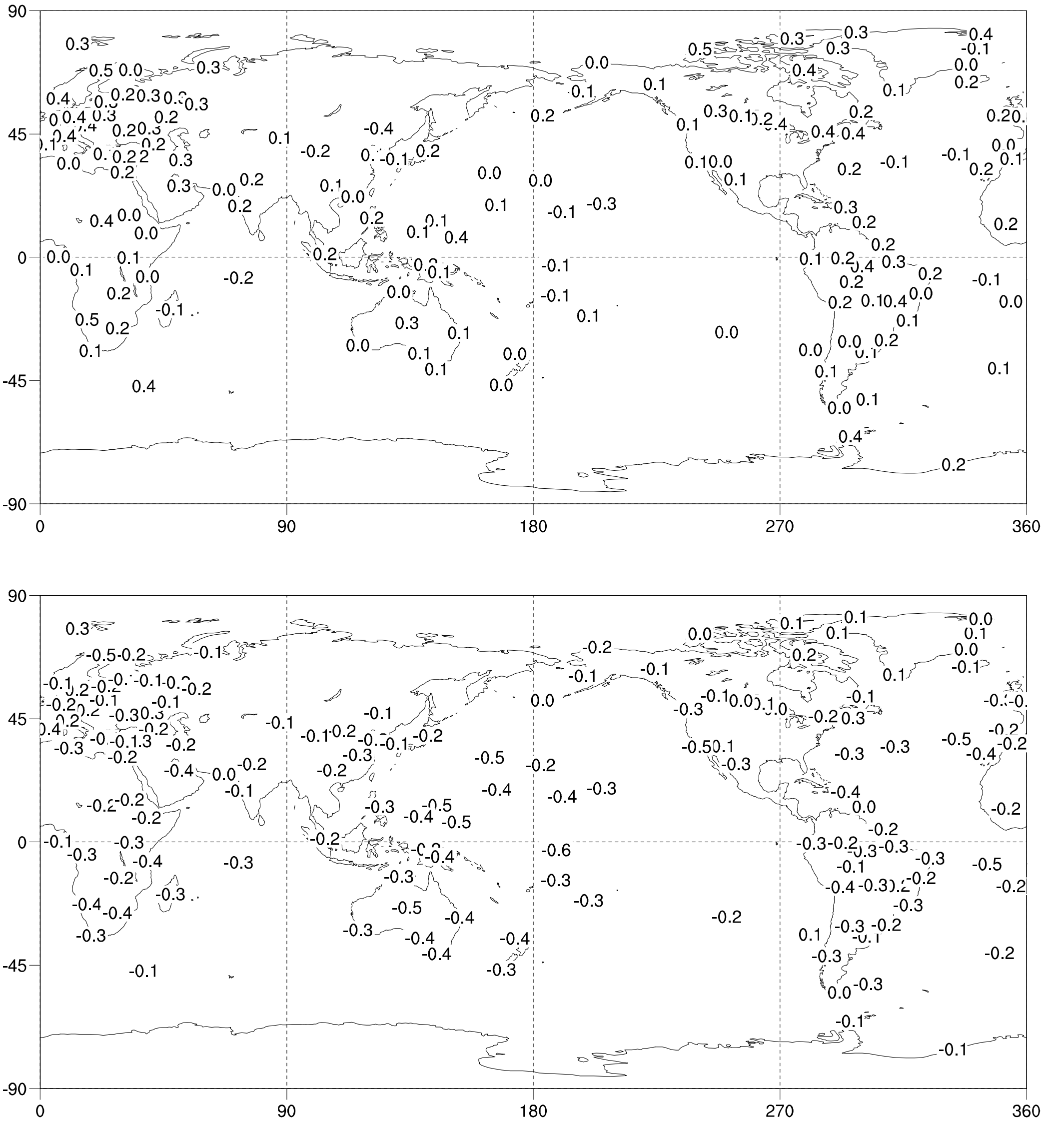

Figure 3.14: Correlations between observed monthly anomalies of surface temperature and $\delta^{18}O$ (top) and precipitation and $\delta^{18}O$ (bottom).

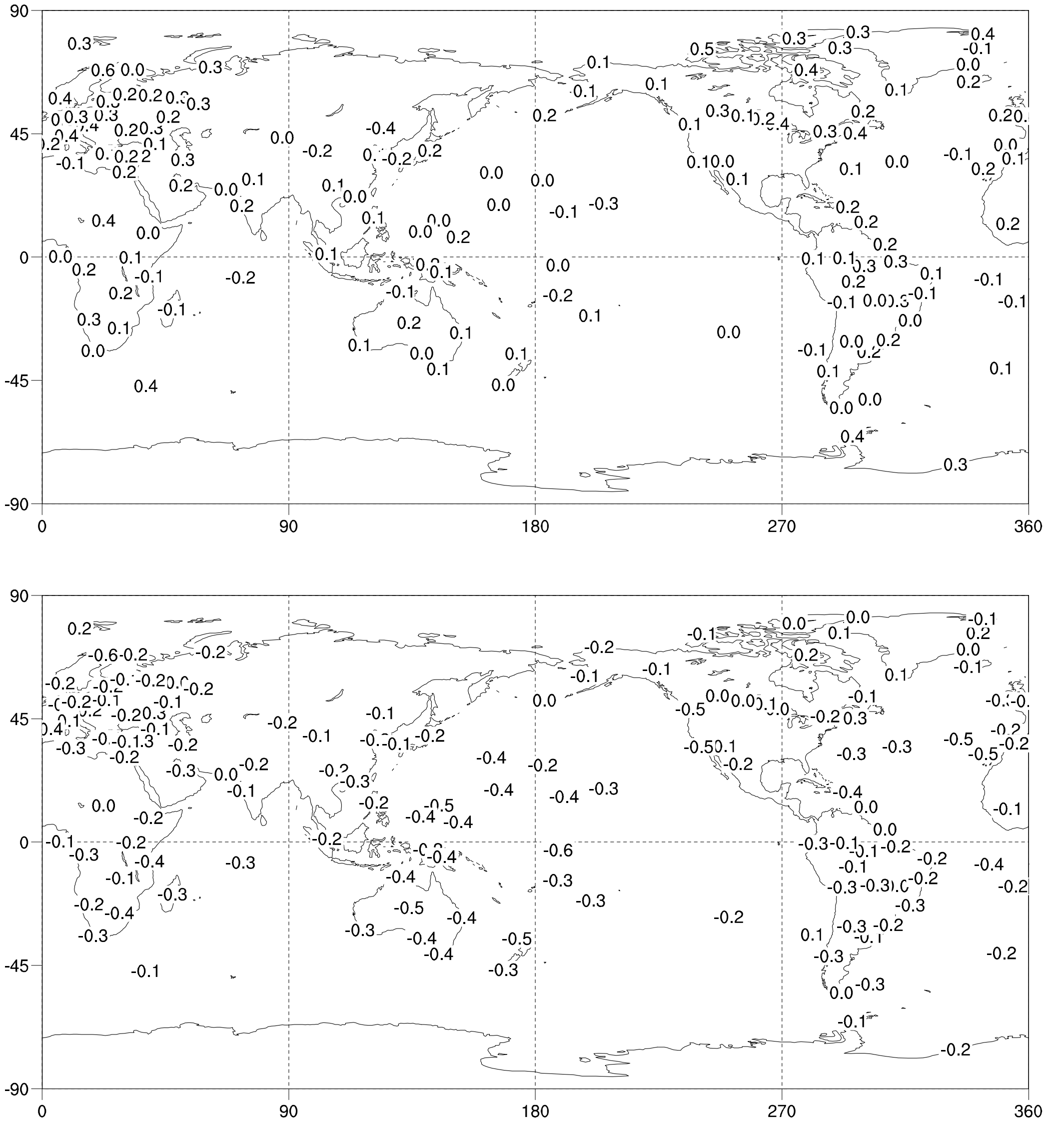

Figure 3.15: Partial correlations between observed monthly anomalies of surface temperature and $\delta^{18}O$ (top) and precipitation and $\delta^{18}O$ (bottom) with the effect of precipitation and temperature respectively removed.

not so strongly reduced with the influence of temperature removed. In a few cases partial correlations are larger than raw correlations indicating that the blind variable acts to mask the correlation. It is also noted that both the modelled and observed correlations between temperature and precipitation and δ^{18}O are generally smaller than 0.5, indicating that local variability of circulation and other factors determine a substantial component of the isotopic signal on monthly and interannual time scales.

3.6 Sensitivity tests

We have examined the formulation of the isotopic tracer scheme and the climatological distribution of isotopic ratios in precipitation produced by the model for simulations of present day climate. As we will later apply the model to very different palaeoclimate conditions, obtaining an assessment of the response of the modelled isotopic distribution to dramatic, idealised changes is instructive.

Two sets of idealised sensitivity experiments were carried in order to investigate the response of isotopes in precipitation to changes in the distribution of precipitation, evaporation and temperature for simplified scenarios. The insights gained through these experiments contribute to the interpretation of the more complex changes in climate forcing associated with interannual and glacial climate variability.

3.6.1 Sensitivity to location of continents

The continentality effect implies that the distance inland from the ocean will be related to the extent of isotopic depletion in precipitation. However the depletion observed over mid-latitude and polar continental areas also frequently corresponds to the transport of moisture from warmer oceanic source regions polewards, thus combining a temperature and continentality signal. In order to investigate the interaction between temperature, precipitation amount and continentality isotope responses where transport inland is associated with the opposite temperature gradient, a series of idealised experiments with zonally average SSTs and modified continents were carried out.

The first experiment consisted of an aqua-planet ("AQUA") simulation with all continents (and topography) and sea ice removed, and zonally averaged SSTs imposed. The SSTs used were the annual average Southern Hemisphere SSTs zonally averaged from the control run boundary conditions with all values below freezing set to 273.2°K and the same zonal average SST distribution repeated symmetrically in the Northern Hemisphere. The model was run with constant SSTs over the annual cycle. As the atmosphere experiences the seasonal cycle of radiative forcing, this resulted in approximately meridionally symmetrical solar input over the annual cycle.

Four further experiments were carried out with a single land area extending from 10°S–10°N (referred to as "L10"), from 25°S–25°N (L25), from 45°S–45°N (L45) and from 60°S–60°N (L60) and all other regions set to ocean with the same SSTs as prescribed in the AQUA simulation. The modelled zonal averages of surface temperature, precipitation and δ^{18}O from the second decade of twenty-year simulations are shown in Figure 3.16. It can be seen that the surface temperatures for the continental areas in L10 and L25 are warmer than the AQUA SSTs while the surface temperatures for L45 and L60 are cooler over land than the AQUA SSTs.

The precipitation response to the imposed SST and land surface forcing is complex. For the AQUA, L10 and L25 experiments a tropical "ITCZ" and mid-latitude precipitation maxima are still present. However in the L45 and L60 experiments the restriction of net global evaporation due to land coverage in the tropics and mid-latitudes leads to low precipitation amounts in the tropics and mid-latitudes with maxima over the polar ocean. The highest precipitation totals ($\sim$ 12 mm/day) are seen at the equator in the L10 experiment where the presence of the narrow band of land appears to enhance convergence, while the L25 experiment has far less precipitation ($\sim$ 1 mm/day) at the equator with a reduction in evaporation due to the tropics being covered by land.

The complex nature of the temperature and precipitation responses to the five different scenarios is reflected in the different zonal average δ^{18}O signals produced. The AQUA simulation produces isotopic depletion at the equator and around 45° where the precipitation maxima are located. The highest isotopic values are seen in the subtropical arid zones, and also at the poles, despite cooler temperatures, where precipitation is at a minimum.

A very similar isotopic distribution to AQUA is seen for the L10 experiment, with a slight equatorward shift in the maximum δ^{18}O values and a slightly higher minimum at the equator due to warmer local surface temperatures. The L25 simulation again follows a similar zonal isotopic distribution with the exception that the equator is a local maximum due to the far lower precipitation here

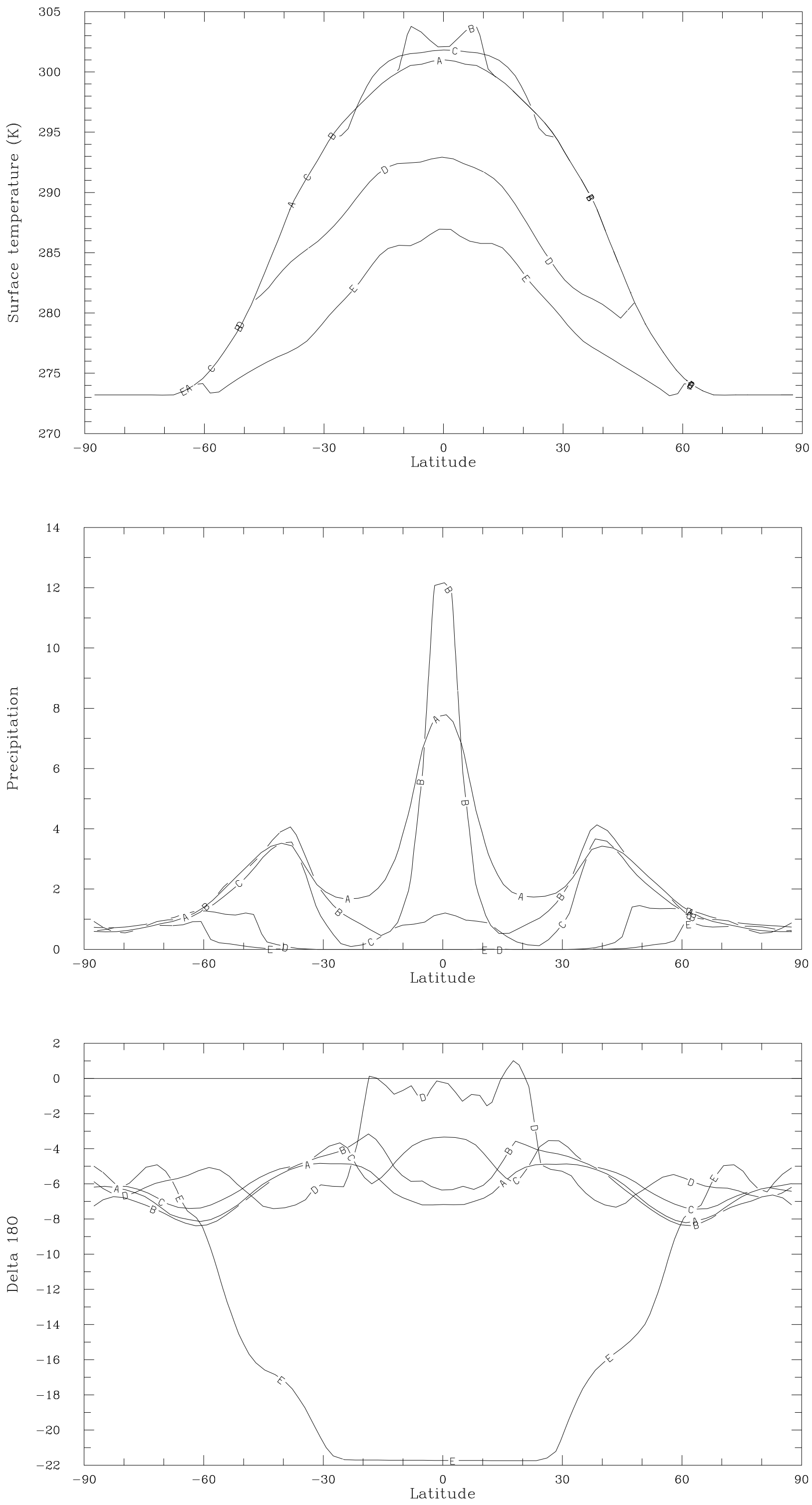

Figure 3.16: Zonal average surface temperature (top), precipitation (middle) and δ^{18}O (bottom) for AQUA (A), L10 (B), L25 (C), L45 (D) and L60 (E) experiments. Units are °K, mm/day and ‰.

compared with AQUA and L10.

The isotopic signal in the L45 simulation between 30°S–30°N consists of noise due to the very low precipitation amounts in this domain. Precipitation is negligible in the L60 simulation between 30°S–30°N, so the plotted δ^{18}O value is spurious. The signal from 30° polewards in the L45 experiment reflects the higher precipitation over the ocean close to 45°, with a decline towards the poles possibly due to isotopic rainout of mid-latitude moisture. The L60 experiment produces a δ^{18}O maximum in the region of relatively higher precipitation at the edge of the ocean at around 60° with increasing depletion towards the equator as rainout of the heavy isotope proceeds with precipitation.

The dependence of the observed linear δ^{18}O–temperature relationship on the specific present day distribution of continents is highlighted by comparing the control modelled δ^{18}O/temperature slope with that from each of the experiments (Figure 3.17). The linear relationship seen in the control simulation (and observations, see Figure 3.11) extends from temperatures of −40°C to around +15°C although departing somewhat from a linear relationship above 0°C. The AQUA slope approaches this distributions between 2°C to 15°C, while at lower temperatures (over polar oceans) and at high temperatures (over the tropics) the temperature–δ^{18}O relationship breaks down. A similar temperature–δ^{18}O relationship is seen for L10 and L25 with the same scatter above $\sim$ 15°C suggesting the role of the amount effect at warmer latitudes.

There is a reversal of the δ^{18}O/temperature slope (more isotopic depletion at warmer temperatures) at temperatures above +15°C for the AQUA and L10 experiments which may be a result of increased precipitation with warmer temperatures. In L25, the same effect is over-ridden by the relatively low precipitation amounts inland towards the equator, while in L45 the temperature effect breaks down entirely, and instead a large isotopic scatter is seen over land with positive δ^{18}O values reflecting very low precipitation amounts and increased reevaporation. The L60 experiment shows a complete reversal of the observed δ^{18}O/temperature slope, with δ^{18}O values decreasing towards the equator due to the progressive rainout of moisture evaporated from the polar oceans.

The results of this sensitivity experiment illustrate the way in which the isotopic signal in precipitation is not a simple function of local surface temperature or precipitation amount but also has an in-built dependence on continental distribution. While the surface temperature decreased from equator to poles in all simulations, the isotopic distribution did not follow this distribution in any

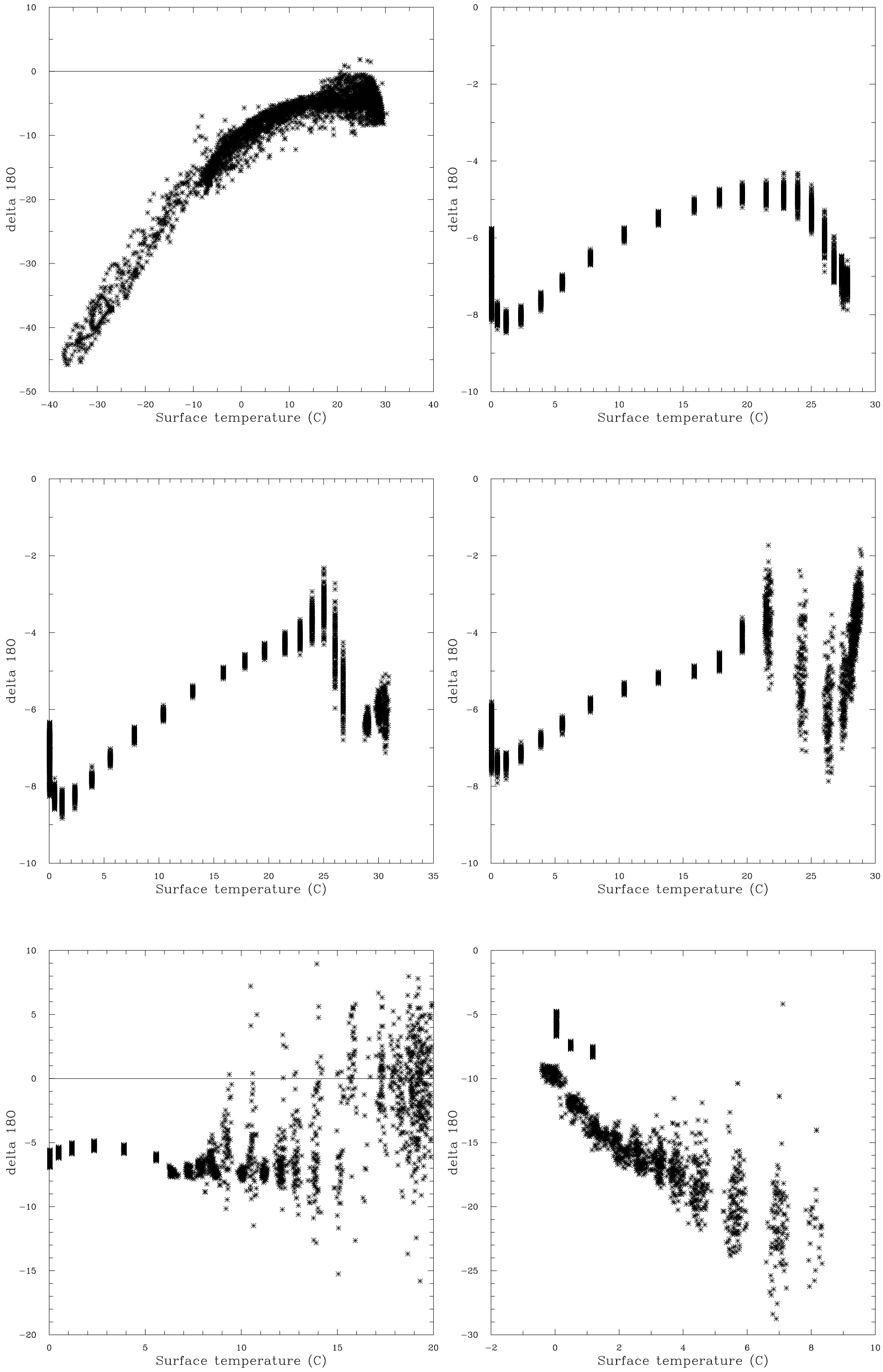

Figure 3.17: δ^{18}O versus surface temperature: control (top left), AQUA (top right), L10 (middle left), L25 (middle right), L45 (bottom left) and L60 (bottom right) experiments. Note the variable scales.

case, even for the simplified AQUA scenario.

In these experiments the extent of isotopic depletion is influenced by local temperature and precipitation as well as meridional SST gradients and the extent of rainout during transport from ocean moisture source regions. The reversal of the expected temperature–isotope relationship in the L60 experiment with polar oceans underlines the fundamental dependence of isotopic depletion on the extent of moisture rainout. The observed δ^{18}O–temperature relationship is therefore shown to reflect the association of this process with poleward transport towards cooler latitudes in the present day global climate.

3.6.2 Sensitivity to SST gradients

In order to explore the relationship between SST gradients and isotopic ratios in precipitation a further set of idealised experiments was carried out. As examined by *Rind* [2000], the climate responds to changes in SST gradients differently to changes in the mean SST value. While the global mean precipitation amount is determined by the mean value of tropical SSTs, the meridional distribution of precipitation is determined by the SST gradient rather than the mean SST value at any given latitude. The isotopic response to SST gradient and mean SST changes should therefore differ, allowing the different isotopic signals in continental and marine records in response to such SST changes to be predicted.

Three idealised experiments were carried out: a mean decrease in all SSTs by 5°C ("MEAN"), an increased meridional SST gradient with 5°C cooling at the equator and 10°C cooling at the poles ("INCR") and a decreased meridional SST gradient with 5°C cooling at the equator and unchanged polar SSTs ("DECR"). As the change in SST at the equator is the same in all three experiments, it is possible to compare changes in tropical precipitation, evaporation and δ^{18}O to identify the influence of SST gradient changes.

The zonal mean SST, precipitation and δ^{18}O anomalies (compared with a present day control simulation) for each of the three experiments is shown in Figure 3.18. The total precipitation is reduced in all three experiments due to the mean tropical SST cooling. In all three experiments, the precipitation decreases are greatest around the latitudes of 10°–20° and around 60° in both hemispheres. Small increases in precipitation are seen at the equator in MEAN and INCR and in the subtropics in DECR.

The isotopic ratio in precipitation is seen to decrease on average due to the

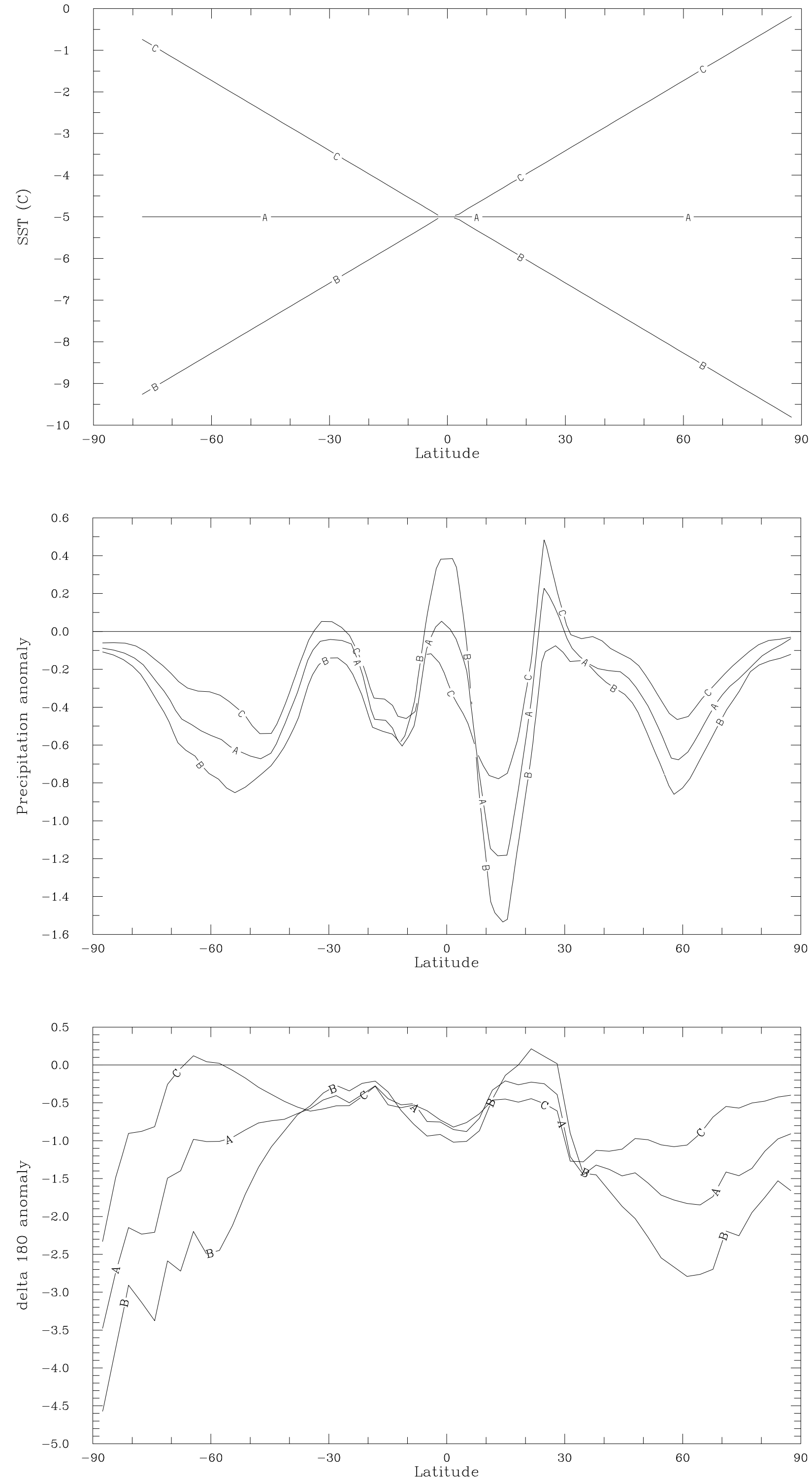

Figure 3.18: Zonal average SST (top), precipitation (middle) and precipitation δ^{18}O (bottom) anomalies for MEAN (A), INCR (B) and DECR (C) experiments. Units are °C, mm/day and ‰.

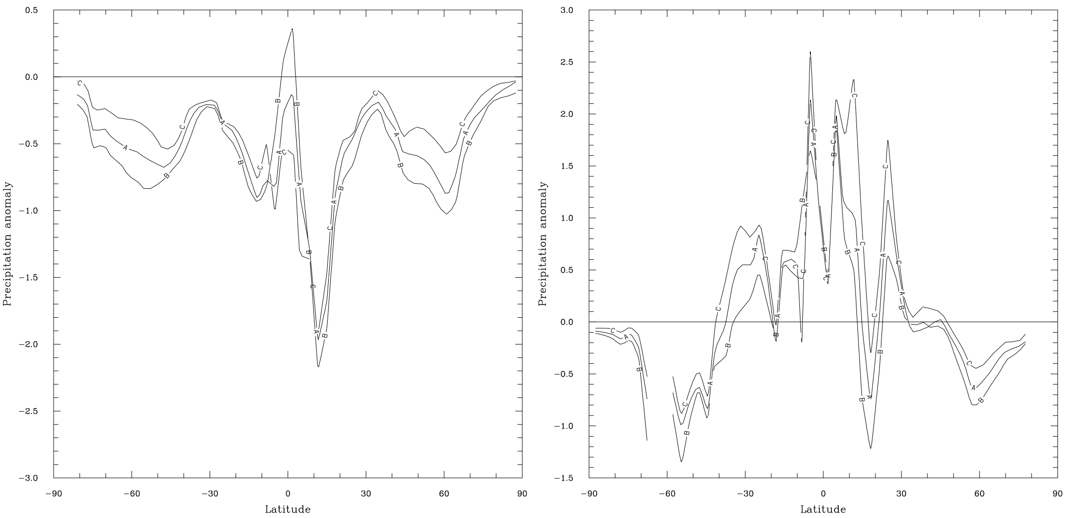

Figure 3.19: Zonal average precipitation anomaly over ocean (left) and land (right) for MEAN (A), INCR (B) and DECR (C) experiments. Units are mm/day.

mean cooling imposed. Small regions of enrichment are seen at high southern latitudes in DECR possibly due to the mid-latitude rainout and in the Northern Hemisphere subtropics in INCR where precipitation is reduced. The difference in the isotopic responses in the three experiments is not large in the tropics or subtropics, although isotopic anomalies at high latitudes differ by up to 2.5‰ due to the range of surface cooling.

The different responses to the SST gradients over ocean and land were compared by calculating the zonal average anomalies for the ocean and land components of precipitation and precipitation δ^{18}O. The precipitation response (Figure 3.19) differs greatly over ocean and land. The precipitation over ocean is generally decreased in response to SST cooling, with the only exception being at the equator in the INCR experiment. The zonal distribution is similar to that shown in Figure 3.18 with the largest decrease in the INCR experiment and the smallest in the DECR experiment.

Over land, there is an increase in precipitation over the tropics and subtropics, with the strongest increase generally seen in the DECR experiment where there is more moisture evaporated from the subtropical oceans and advected over land. The isotopic signal (Figure 3.20) is therefore also different over ocean and land, especially in the tropics where reduced precipitation leads to relative enrichment over ocean in all experiments. Over land, the increased

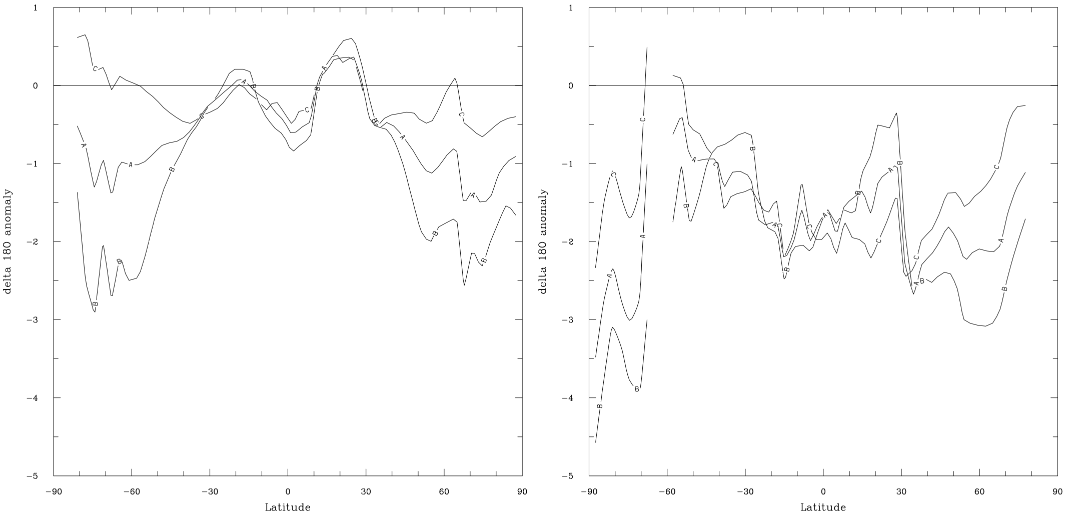

Figure 3.20: Zonal average precipitation δ^{18}O anomaly over ocean (left) and land (right) for MEAN (A), INCR (B) and DECR (C) experiments. Units are ‰.

precipitation produces relatively greater isotopic depletion than would occur with surface cooling alone. At high latitudes the isotopic depletion differs by up to 2‰ between the experiments over both ocean and land.

3.7 Summary

The MUGCM and isotopic tracer scheme were described and the modelled climate and isotopic distribution compared with observations. The isotopic tracer scheme was able to reproduce the main features of the spatial distribution of isotopes in precipitation, including the dependence on surface temperature, precipitation amount, altitude and continentality. The δ^{18}O–temperature slope produced by the model was within the range of observed slopes, while the model reproduced the main feature of the global δ^{18}O–δD relationship.

The variability of isotopes in precipitation on interannual time scales was found to be in agreement with observations. The interannual variability of tropical precipitation δ^{18}O was found to be negatively correlated with precipitation amount and temperature over ocean, while the correlation with temperature was positive over land via a relationship with precipitation amount.

Sensitivity experiments with altered continentality and SST gradients were carried out to examine the response of isotopes in precipitation to idealised changes in climate. The location of continents in the tropics with varying meridional extents was found to produce a change in the δ^{18}O–temperature relationship, with a reversal of the observed slope for the extreme case of polar oceans. Changes in SST gradients produced shifts in the meridional distribution of precipitation and δ^{18}O, with substantially different responses over ocean and land in the tropics and mid-latitudes.

Chapter 4

Modelling isotopes in the surface ocean, runoff and snow

4.1 Introduction

Surface ocean isotopic ratios vary on seasonal and interannual time scales in response to changes in local precipitation and evaporation, upwelling and advection as well as river and glacial runoff and sea ice formation. On glacial time scales, the effect of changes in global ice volume are significant. Modelling surface ocean isotopic ratios is of interest to determine the impact of variable isotopic evaporative fluxes on the isotopic content of atmospheric vapour and precipitation. The modelled surface ocean isotopic ratios can also be compared with observed ocean isotopic ratios and with proxies such as coral and foraminifera in order to test the palaeoclimate interpretation of marine isotopic records.

Simulations of water isotope tracers in atmospheric models have generally assumed a constant ocean surface isotopic ratio both spatially and temporally of either SMOW [eg. *Jouzel et al.*, 1987b] or slightly enriched values [eg. *Hoffmann and Heimann*, 1998]. As outlined in Chapter 2, studies of the ocean isotopic distribution have used atmospheric fluxes from isotopic GCMs or calculated isotopic ratios of precipitation via regressions with observed precipitation and temperature [eg. *Schmidt*, 1998; *Delaygue et al.*, 2000]. Other studies have employed offline calculations of surface ocean δ^{18}O from modelled atmospheric fluxes with empirically determined depth and mixing time scales [*Juillet-Leclerc et al.*, 1997].

An alternative approach which captures the interaction between surface ocean and atmospheric isotopic content is presented here. The surface ocean isotopic ratio is calculated directly from the atmospheric water and isotopic tracer fluxes, altering the isotopic ratio for oceanic evaporation accordingly. The surface ocean isotopic scheme is described and the surface ocean δ^{18}O distribution produced by the model is compared with observations. A river runoff scheme which includes isotopic tracers is developed, and the contribution of snow melt to the isotopic runoff signal is modelled using a prognostic snow scheme modified to include isotopic tracers. Finally, horizontal transport is included in the surface ocean isotopic scheme using upper ocean currents from an ocean GCM.

4.2 Spatially variable surface ocean δ^{18}O

In order to test the sensitivity of the atmospheric vapour and precipitation isotopic distribution to spatially variable surface ocean ratios, the MUGCM is modified to incorporate the annual average observed surface ocean isotopic distribution as the ocean boundary condition. The impact of the resulting change in isotopic evaporative fluxes on the atmospheric isotopic distribution is investigated. This approach is similar to that used in the GENESIS model where the atmospheric isotope tracer scheme uses different zonally averaged surface ocean δ^{18}O for each major ocean region [*Mathieu et al.*, 2002].

Surface ocean δ^{18}O data

The observed surface ocean δ^{18}O values from the NASA-GISS GSO database [*Schmidt*, 1999a; *Bigg and Rohling*, 2000] described in Chapter 2 were used to construct an annual surface ocean isotopic distribution. A Cressmann weighting function was used to replace missing values with a weighted average of surrounding data points. The GSO data set was then interpolated onto the MUGCM grid using a linear interpolation scheme, giving the distribution shown in Figure 4.1. The δD values were calculated assuming the relationship $\delta\text{D} = 8 \times \delta^{18}\text{O}$. Evaporation over the ocean therefore follows the formulation in Equations 3.4 and 3.5 with a prescribed value of R_{ocean} at each ocean grid point.

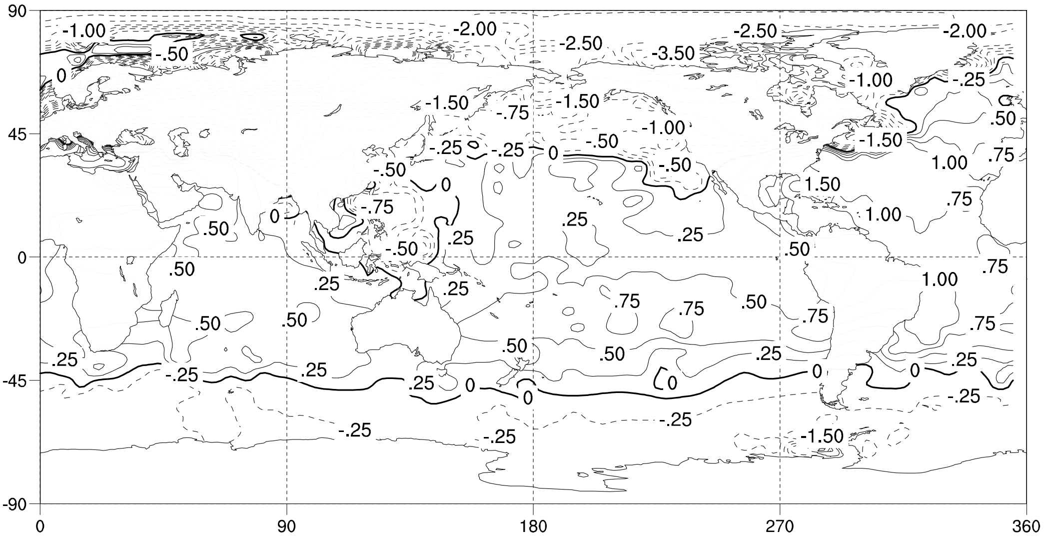

Figure 4.1: Observed (GSO) surface ocean δ^{18}O interpolated to MUGCM grid. Contour interval is 0.25‰ for values less than ±1‰ and 0.5‰ otherwise.

Atmospheric response

A 10-year model simulation was carried out to investigate the atmospheric response to spatially variable surface ocean δ^{18}O. The model run used the same surface ocean δ^{18}O for all months as the GSO data set consists of annual average values, with seasonal information only available at a small number of locations. The modelled δ^{18}O in precipitation and in atmospheric water vapour at the lowest atmospheric model level ($\sigma = 0.991$, approximately 75 m above the surface) was compared with the distributions from a control run with a uniform and constant surface ocean δ^{18}O value of 0‰. The differences between the δ^{18}O of vapour and precipitation of the two runs are shown in Figure 4.2.

It can be seen that the atmospheric vapour δ^{18}O values follow the changes in the ocean surface ratio closely although with a reduced magnitude (vapour δ^{18}O ranges from -1.2 to $+1.2$‰ compared with -6‰ to $+2$‰ for the surface ocean). It is suggested that vertical and horizontal atmospheric mixing may be responsible for the smaller anomalies in the atmosphere than in the surface ocean distribution. Feedbacks from reduced isotopic evaporation resulting from higher atmospheric isotopic ratios may also weaken the response.

Precipitation δ^{18}O also responds to the surface and atmospheric isotopic anomalies, however the signal is noisier than the atmospheric vapour anomalies due to atmospheric mixing and advection. The isotopic ratios over North Africa

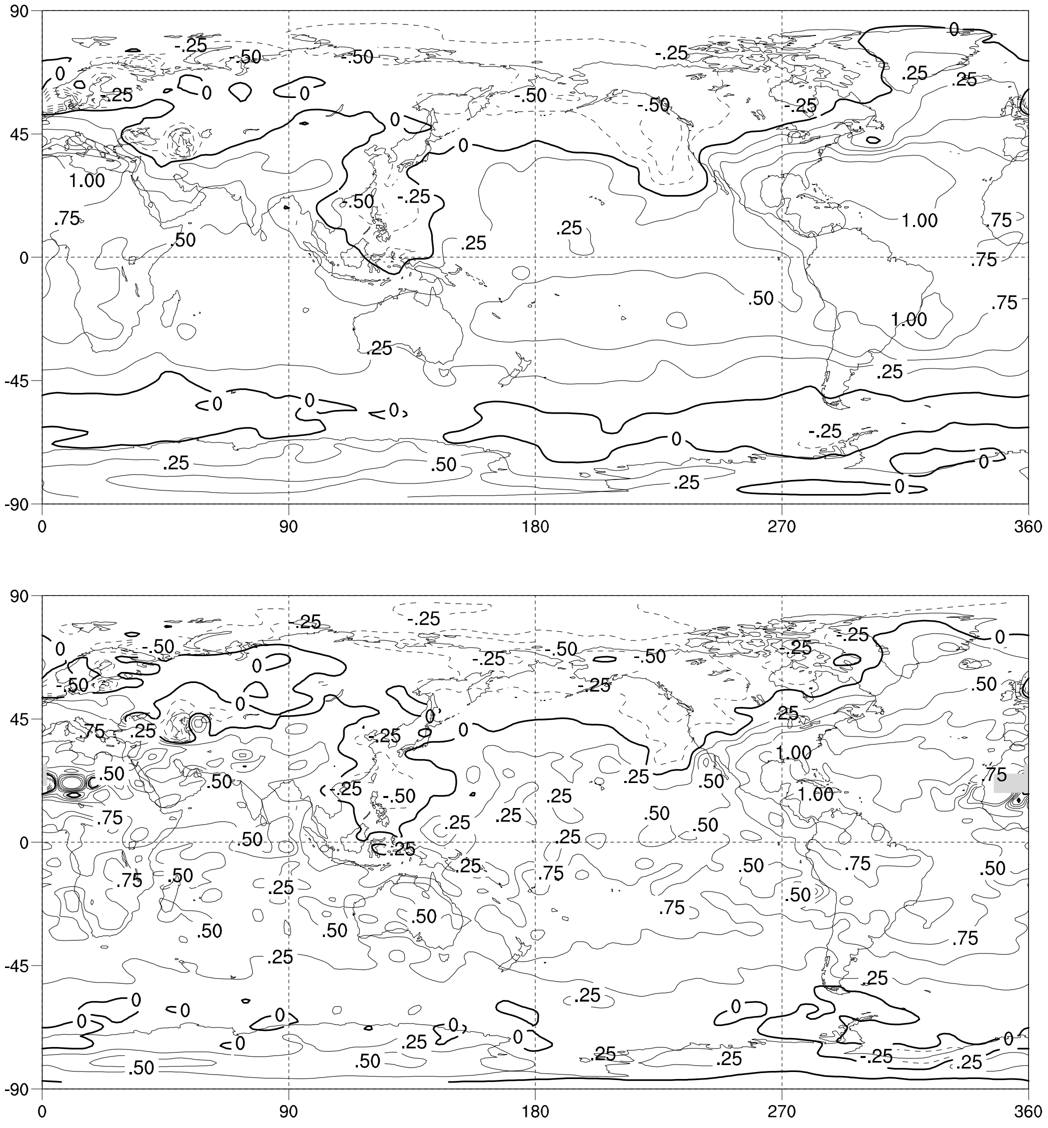

Figure 4.2: Difference between observed (GSO) surface ocean δ^{18}O run and control run: vapour δ^{18}O (top) and precipitation δ^{18}O (bottom). Contour interval is 0.25‰ for values less than ±1‰ and 0.5‰ otherwise.

are highly variable due to extremely small precipitation amounts, so that the apparently large δ^{18}O anomalies over this region may have little meaning. As the precipitation δ^{18}O anomalies are generally smaller than 0.5‰, responses to variation in surface ocean isotopic ratios are not likely to form a significant component of the precipitation δ^{18}O signal unless precipitation amount, temperature and other factors remain constant.

4.3 Surface ocean isotopic scheme

The implementation of an interactive, temporally variable representation of the upper ocean isotopic ratio is required to reproduce the isotopic response to changes in local precipitation and evaporation on time scales from individual precipitation events to seasonal and interannual changes. Such a scheme can also be used to simulate the surface ocean isotopic distribution under past climate conditions and compare the modelled response to changed hydrologic fluxes with evidence from marine palaeo-records.

4.3.1 Description of surface ocean isotopic scheme

A one-dimensional model of the ocean surface isotopic budget was constructed, similar to the "box model" of *Craig and Gordon* [1965]. In the model, the surface layer has a variable isotopic ratio while the deep water ratio remains constant. The depth of a surface or upper ocean layer of normal water Q and of the isotopic tracer Q_i is calculated from the difference between precipitation (P, P_i) and evaporation (E, E_i). A damping term relaxes Q back to a mean depth h and Q_i back to a mean depth hR (where R is the mean surface ratio) with a time scale determined by the coefficient k:

$$\frac{\partial Q}{\partial t} = (P - E) + k(h - Q) \tag{4.1}$$

$$\frac{\partial Q_i}{\partial t} = (P_i - E_i) + k(hR - Q_i) \tag{4.2}$$

The isotopic ratio of the surface layer is calculated from Q/Q_i, so that the ratio is damped towards the mean ocean ratio R. This damping term can be considered to represent vertical diffusion between the surface layer and the deep ocean.

Depth, h	**Damping, k**	**Average δ^{18}O**	**DJF – JJA δ^{18}O**
2.5 m	0.00028	−2.0 to +1.9	−1.8 to +1.7
5 m	0.00014	−2.1 to +1.9	−0.7 to +1.0
10 m	0.00007	−2.1 to +1.8	−0.3 to +0.4
50 m	0.000014	−2.1 to +1.9	−0.1 to +0.1
50 m	0.00014	−0.3 to +0.2	−0.1 to +0.1

Table 4.1: Tuning of surface ocean isotopic scheme: ranges of annual average and DJF – JJA surface ocean δ^{18}O produced for different combinations of layer depth h and damping coefficient k.

The dimensionless damping coefficient k is related to a relaxation time scale τ via $k = \tau/\Delta t$ where Δt is the model time step. Altering the value of k will change the magnitude of the isotopic response, as will altering the depth of the surface layer h. These parameters can be tuned to produce a surface ocean isotopic distribution and seasonal range which corresponds to the observed distribution.

In the case of a steady state where $\partial Q/\partial t = 0$ and $\partial Q_i/\partial t = 0$, the surface layer depth for normal water is given by:

$$Q = -\frac{(P - E) + kh}{k} \tag{4.3}$$

and equivalently the isotopic surface layer depth is given by:

$$Q_i = -\frac{(P_i - E_i) + khR}{k} \tag{4.4}$$

and the resulting surface layer isotopic ratio is given by:

$$\frac{Q_i}{Q} = \frac{(P_i - E_i) + khR}{(P - E) + kh} \tag{4.5}$$

Therefore for given values of the P, P_i, E, E_i and mean ocean ratio R, the magnitude of the resulting isotopic ratio will depend on the product of the layer depth, h, and the damping coefficient, k. The magnitude of the seasonal signal associated with changes in the hydrologic balance is also determined by the product of the layer depth and damping coefficient.

Different values of the parameters h and k were tested to tune the model. Values of h and k and the resulting ranges for the annual average and seasonal cycle of δ^{18}O are shown in Table 4.1. The model was tuned for the tropics and mid-latitudes only as this study is primarily concerned with the tropical isotopic signal. We therefore aimed to simulate an annual average spatial range of ±2‰ and a seasonal range (maximum DJF – JJA δ^{18}O) of ±1‰.

Values which are of the same order as the real ocean mixed layer depth and mixing time scale ($h = 50$ m and $\tau = 50$ days [*Paul et al.*, 1999], corresponding to $k = 0.00014$ for the model time step of 1200 seconds) produced a mean and seasonal range of tropical and mid-latitude surface ocean δ^{18}O which is much smaller than the observed range. A smaller value of depth, $h = 5$ m, with the same damping coefficient, $k = 0.00014$, was found to produce a mean and seasonal range of surface ocean δ^{18}O which were of the same magnitude as observations. These values were used for all subsequent simulations.

4.3.2 Validation of surface ocean isotopic scheme

Seasonal average DJF, JJA and DJF – JJA surface ocean δ^{18}O values from a 10-year climatological model run are shown in Figure 4.3. These are compared with the observed annual average values from the GSO data set (Figure 2.3). The model captures the enrichment in the subtropical Pacific, Atlantic and Indian Oceans due to the local excess of evaporation over precipitation. The response to tropical precipitation is also reproduced, with the western Pacific Warm Pool displaying the most depleted surface ocean isotopic values due to the high precipitation simulated in this region.

The model is unable to reproduce the most negative δ^{18}O values at high northern latitudes due to runoff of isotopically depleted continental precipitation, as the basic version of the model does not incorporate a runoff scheme. The consequence of the absence of horizontal and vertical mixing is also apparent in the localised nature of the precipitation and evaporation signals in the model compared with the smoother observed distribution.

While observed seasonal surface ocean δ^{18}O values are not available globally, local observational δ^{18}O timeseries are available for a number of tropical locations. In the Seychelles in the Indian Ocean the annual range is around 0.1‰ [*Charles et al.*, 1997], while the modelled range is of the same magnitude. The annual isotopic range is larger in the western Pacific, for example around 1‰ near Java and around 0.5‰ off the coast of Papua New Guinea [*Gagan et al.*, 2000] with similar ranges in the modelled isotopic ratios.

The seasonal range in the central Pacific reaches a maximum of around

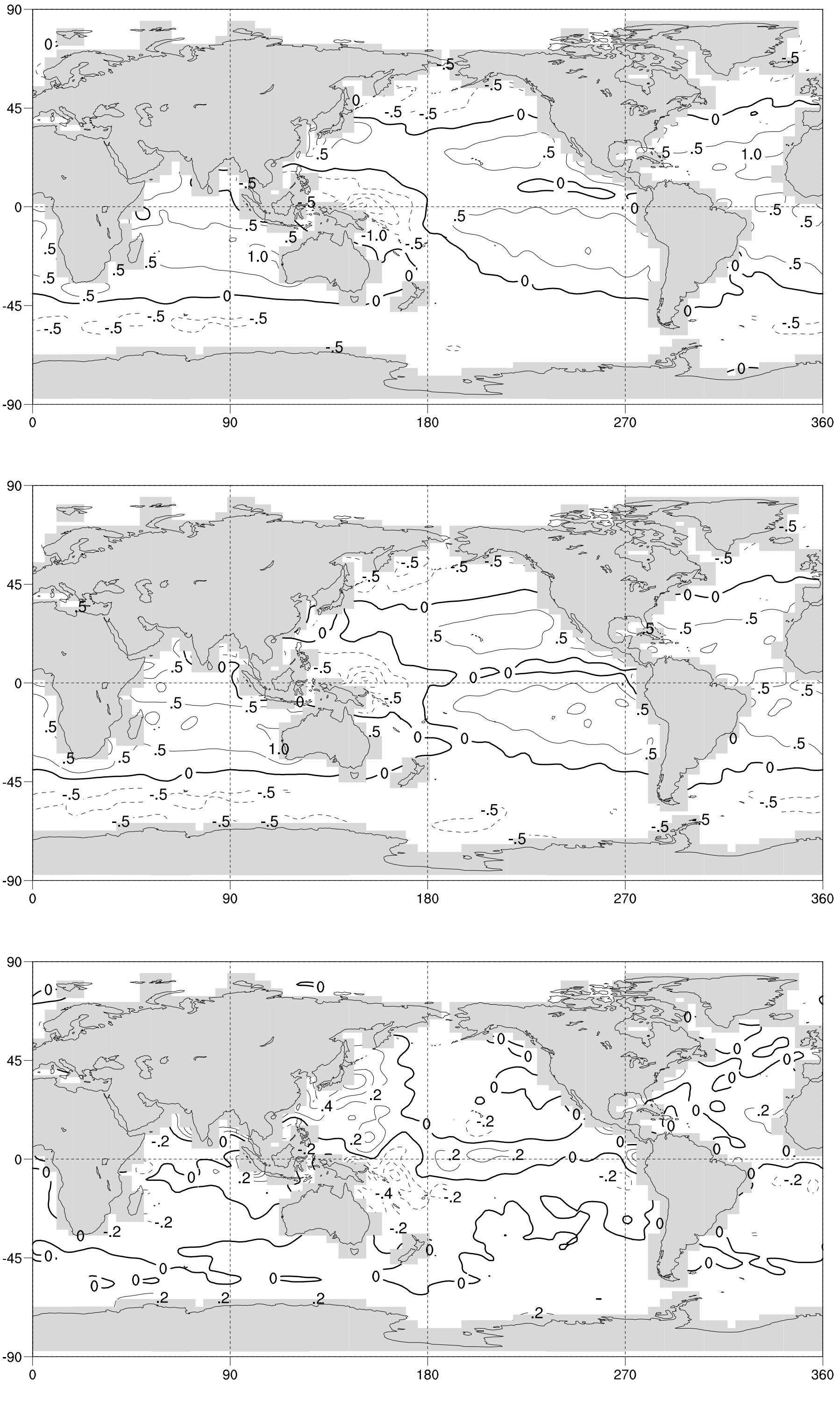

Figure 4.3: Modelled surface ocean δ^{18}O: DJF (top), JJA (middle) and DJF – JJA (bottom). Contour intervals are 0.5‰ and 0.2‰ for difference.

0.3‰ at Clipperton Atoll [*Linsley et al.*, 1994]. The modelled seasonal signal is between 0.2‰ and 0.4‰ in this region. The signal at the Galapagos Islands in the eastern Pacific is also small, with values ranging from 0.27‰ to 0.38‰ reported by *Wellington et al.* [1996]. The model simulates a larger seasonal range near the coast of tropical South America, but offshore the seasonal range is of the observed magnitude.

We have shown that a simple one-dimensional surface ocean isotopic scheme is able to simulate the main features of the zonal δ^{18}O distribution in the tropics and mid-latitudes, as well as the relative depletion in the regions of the ITCZ and western Pacific Warm Pool. In general the modelled surface ocean δ^{18}O values are within 0.5‰ of the observed values in the tropics and mid-latitudes. We now investigate the contribution to the surface ocean δ^{18}O signal from river runoff and snow melt and the inclusion of upper ocean horizontal transport. The temporal variability of surface ocean isotopic ratios in response to variable climate forcing is examined further in Chapter 5.

4.4 River runoff scheme

An important component of the freshwater budget at the ocean surface is continental river runoff. As runoff consists of isotopically depleted continental moisture, the influx of runoff into the ocean will alter the isotopic ratio of the surface ocean in coastal areas, for example producing the highly depleted values seen in the Arctic Ocean [*Schmidt*, 1999a]. The inclusion of runoff in the model will therefore provide a more physical representation of the influences on the surface ocean isotopic distribution, as well as providing a test of the modelled isotopic ratios in precipitation through comparison of modelled and observed river isotopic composition.

The inclusion of river runoff in the model also allows the change in runoff and its isotopic composition to be tested for different climate conditions. For example, ENSO produces a strong isotopic signal in runoff from north eastern Australia, which is captured by coral in the Great Barrier Reef area [*McCulloch et al.*, 1994]. Similarly, the changes in hydrology over glacial time scales could alter the isotopic composition of runoff. For example *Guilderson et al.* [2001] suggest that changes in Amazonian precipitation and runoff amounts during the LGM could produce a change in the surface ocean and coral δ^{18}O at nearby Barbados in the tropical Atlantic.

The accuracy of the simulation of river runoff will depend on the ability of the soil moisture scheme to correctly simulate local runoff due to saturation. While the two-layer soil moisture scheme of *Deardorff* [1977] is a relatively simple scheme, it has been shown to be able to reproduce the large-scale impact of soil moisture variability on the atmosphere, as discussed in Chapter 3. The soil moisture scheme coupled with a simple topographic runoff scheme is considered to be adequate for the purpose of investigating the sensitivity of coastal surface ocean isotopic ratios to changes in the volume and isotopic ratio of continental runoff.

4.4.1 Description of river runoff scheme

A river runoff transport scheme was developed to model the transport of excess soil moisture to the ocean via surface grid box to grid box transport. The scheme was based on that of *Sausen et al.* [1994] implemented in the ECHAM model. Runoff occurs when the moisture fraction in the upper or lower soil moisture layer exceeds the saturation value, as described in Section 3.2.3. The total volume of excess soil moisture is designated as runoff, with no representation of local runoff drainage.

The runoff is transported to adjacent grid boxes in a direction and at a rate dependent on the slope of the topography, with a flow rate u ms^{-1} calculated (in the zonal i direction) of:

$$u_{(i,j)} = c \left[\frac{h_{(i,j)} - h_{(i+1,j)}}{\Delta x} \right]^a \tag{4.6}$$

where c ms^{-1} is a constant which allows tuning of the rate of flow, h is the topographic height in metres, Δx is the horizontal distance between adjacent grid points in the zonal direction and a is a dimensionless constant allowing tuning of the dependence of the flow rate on slope. An equivalent formulation is used for the meridional flow rate, v.

The total runoff depth in each grid box reservoir is converted into volume in order to account for the differences in grid box surface area. The horizontally transported flux of water into each land grid box $A(i, j)$ at each time step is calculated from the slope in the four adjacent grid box and the volume of water in each grid box runoff reservoir $W(i, j)$:

$$A(i,j) = f_{(i-1,j)\rightarrow(i,j)} + f_{(i,j)\rightarrow(i+1,j)} + f_{(i,j-1)\rightarrow(i,j)} + f_{(i,j)\rightarrow(i,j+1)} \tag{4.7}$$

where $f_{(i,j)\rightarrow(i',j')}$ is the flux of water from box (i, j) to box (i', j') following the upstream formulation where flow into box (i, j) occurs when the upstream flow is positive or downstream flow negative:

$$f_{(i,j)\rightarrow(i+1,j)} = \begin{cases} u_{(i,j)}W_{(i,j)} & \text{if } u_{(i,j)} \geq 0 \\ u_{(i,j)}W_{(i+1,j)} & \text{if } u_{(i,j)} < 0 \end{cases} \tag{4.8}$$

$$f_{(i,j)\rightarrow(i,j+1)} = \begin{cases} v_{(i,j)}W_{(i,j)} & \text{if } v_{(i,j)} \geq 0 \\ v_{(i,j)}W_{(i,j+1)} & \text{if } v_{(i,j)} < 0 \end{cases} \tag{4.9}$$

The volume of water in each runoff reservoir, W, is calculated for each continental grid box at each timestep from the sum of local runoff, L (excess soil moisture), and transported runoff from adjacent grid boxes, A:

$$\frac{\partial W}{\partial t} = L + A + D \tag{4.10}$$

where the discharge term D is defined so that $D = A$ at coastal ocean grid points and $D = 0$ elsewhere.

The equivalent isotopic local runoff volume is calculated from the excess isotopic soil moisture, and runoff reservoir volumes are calculated for each tracer. The isotopic ratio of the local runoff, runoff reservoir storage and coastal discharge at each timestep can then be calculated directly. The coastal discharge volumes of both normal water (D) and isotopic tracers (D_i) are converted into a depth per area of surface ocean, and added to the surface ocean moisture flux budget so that Equation 4.1 becomes:

$$\frac{\partial Q}{\partial t} = (P - E + D) + k(h - Q) \tag{4.11}$$

and Equation 4.2 becomes:

$$\frac{\partial Q_i}{\partial t} = (P_i - E_i + D_i) + k(hR - Q_i) \tag{4.12}$$

4.4.2 Choice of topography and drainage scheme

Two topography datasets were used in testing the runoff scheme. The first was the standard MUGCM topography taken from the 1°× 1°data set of *Gates and Nelson* [1975] in grid point form, interpolated to the model resolution. The second was the spectral topography transformed back into grid point form. The two data sets differ because of the finite wavenumber truncation in the spectral representation which produces inland minima due to the Gibbs phenomenon, overshooting in the vicinity of steep mountains as well as small ripples in the ocean surface. The spectral and grid point topography is shown in Figure 4.4.

Sausen et al. [1994] recommend modifying the spectral topography via an algorithm which compares the spectral topography with real topography to remove inland minima. However this method includes subjective modification of the topography which limits its application to palaeo-epochs such as the LGM when topography and runoff drainage is not adequately known. It was decided to instead treat the inland minima in an objective manner, setting the volume of runoff in all isolated non-draining inland water reservoirs to zero and comparing the resulting runoff from the two topographic datasets. While some runoff schemes transport runoff from inland minima to the ocean as groundwater transport [eg. *Arora et al.*, 1999], this was not carried out for the current study as the proportion of moisture stored inland was generally small. In addition, the isotopic signal associated with runoff was not greatly affected by eliminating the contribution from a small fraction of inland grid boxes.

An additional consideration was the direction of runoff moisture transport over land. *Arora and Boer* [1999] note that topographic gradients over large areas (such as the MUGCM 5.6° × 3.3° grid boxes) may not represent the actual direction of flow of rivers, and so suggest the use of a high resolution flow routing scheme based on observational data. The 1° × 1° Total Runoff Integrating Pathways (TRIP) flow data set of *Oki and Sud* [1998] was obtained from http://EarthInteractions.org. The flow vectors were interpolated onto the MUGCM grid, and these directional unit vectors multiplied by the magnitude of the topographic slope to produce an alternative set of slopes.

The runoff storage and discharge amounts were compared for climatological simulations with each of the gridded, spectral regridded and TRIP interpolated flow velocities shown in Figure 4.5. It was found that the modelled discharge volume and distribution was similar for all three simulations. The extent of

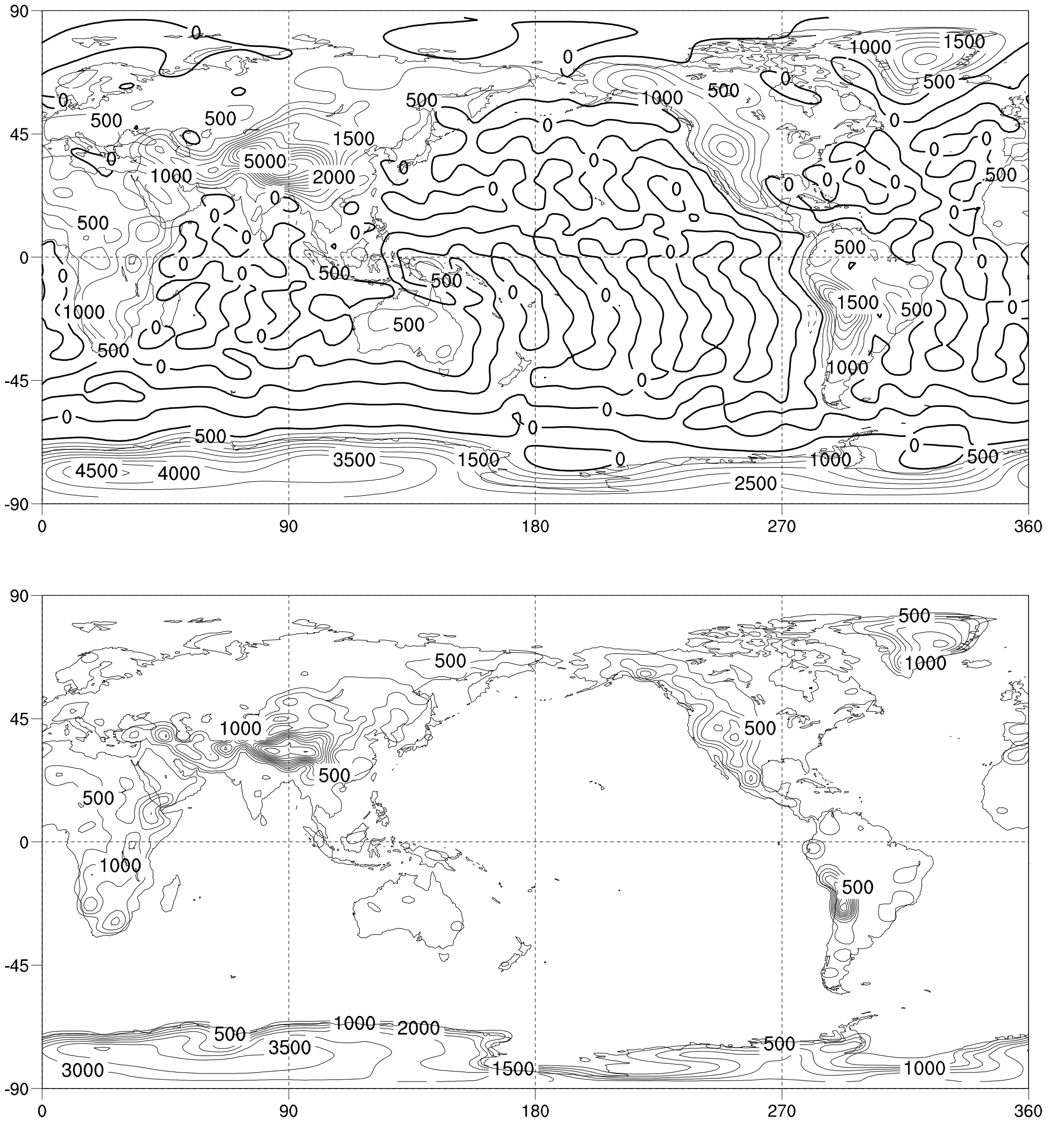

Figure 4.4: Spectral topography converted to grid form (top) and raw 1° × 1° topography interpolated to MUGCM resolution (bottom). Contour interval is 500 m.

inland minima was also similar for the gridded and spectral topography, while the TRIP interpolated topography produced more inland minima. As the results from all three topographic data sets were similar, it was decided to use the spectral regridded topography which is available as a model input data set, enabling the flow rates to be easily calculated for any specified topography.

The role of catchment basins was also explicitly considered. The isotopic signature of runoff from a particular river will depend on the location of the precipitation that flows into the river such as isotopically depleted inland or high altitude precipitation. It is therefore desirable that the discharge in a given coastal grid box should originate in the region corresponding to the observed catchment area.

Observational basin masks available from the National Geophysical Data Center (NGDC) database (http://www.ngdc.noaa.gov) were used to correct the flow directions to ensure that no water flowed across basin boundaries by reversing the direction of flow vectors where this occurred. However this was found to produce additional inland minima, as well as being limited to present day known catchment basins. For these reasons the use of explicit catchment basins was rejected and instead the uncorrected topographic slopes were used.

The flow constant (c in Equation 4.6) can be tuned to produce the observed river flow rates. *Arora et al.* [1999] compare the approaches used in a range of runoff models for the calculation of flow rates. The approach of *Sausen et al.* [1994] is more sophisticated than those formulations using a constant flow rate, but simpler than formulations such as Manning's equation in which flow rate depends on slope, hydraulic radius and the roughness coefficient of the river [*Arora et al.*, 1999]. As the flow rate does not influence the mean ocean discharge and surface ocean isotopic ratio, it was decided to use flow constants of the same magnitude as those chosen by *Sausen et al.* [1994], $c = 4.0$ ms^{-1} and $a = 0.2$.

4.4.3 Validation of runoff and river discharge

The modelled local runoff (excess soil moisture at each land grid box) in units of mm/day was compared with observed runoff amounts from the Global Runoff Data Center as presented in *Sausen et al.* [1994]. A quantitative comparison between modelled and observed runoff amounts was not carried out as the accurate representation of runoff amount is limited by the modelled precipitation distri-

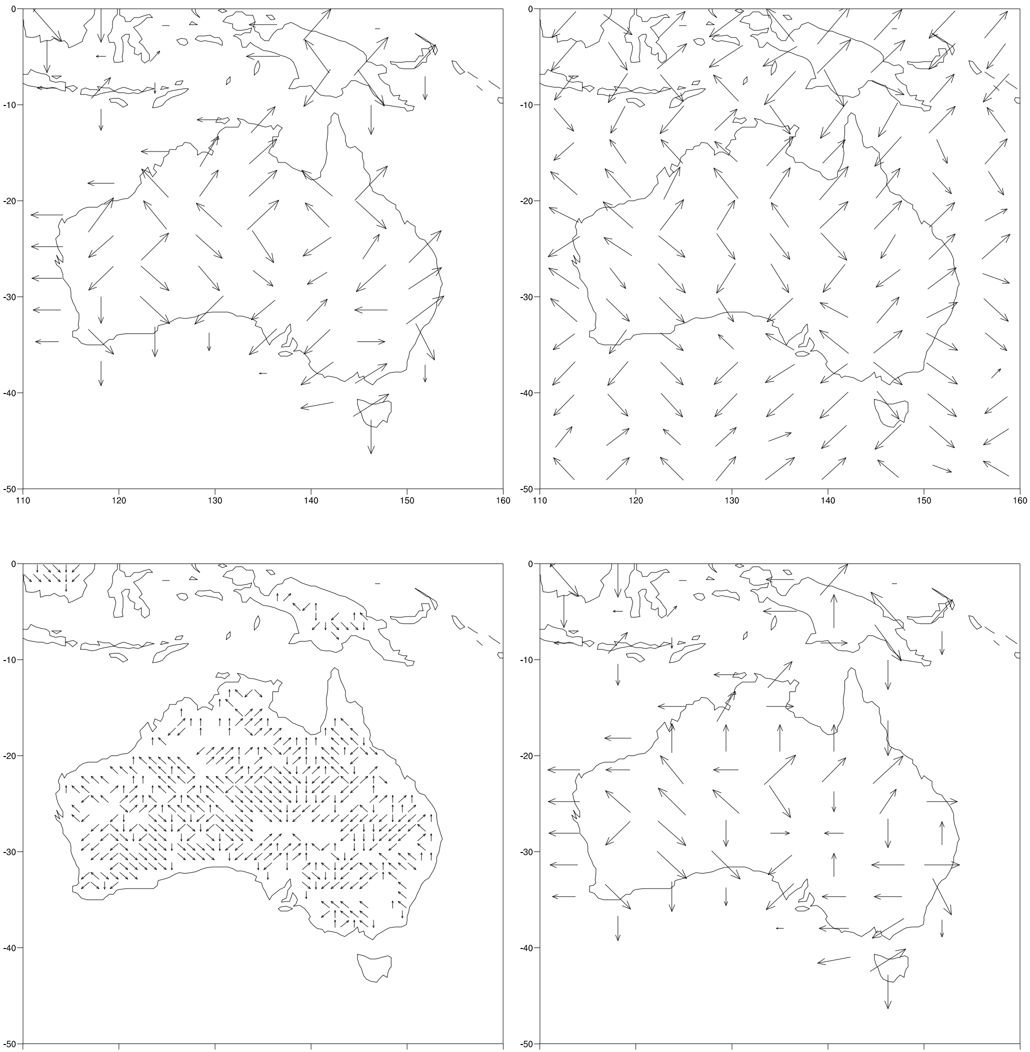

Figure 4.5: Flow vectors over the Australian region from gridded topography (top left), spectral topography (top right) and TRIP 1° × 1° (bottom left) and interpolated (bottom right) flow vectors. Note that the flow vectors are the flow rate between each grid box and the adjacent easterly and northerly grid boxes.

bution. Of more importance for the surface ocean isotopic contribution from runoff is the correct representation of the runoff flow direction and seasonality.

As shown in Figure 4.6, the modelled runoff varies from DJF to JJA, with maxima in the southern summer over tropical southern Africa and South America, northern Australia and the Indonesian region. Large amounts of runoff are simulated over Central America, tropical northern Africa and Asia in the northern summer.

The signal due to high latitude snow melt is absent in this version of the model as snow is not included as a separate precipitation type in the surface representation. The model also underestimates the observed runoff over the Amazon as modelled precipitation is too low in this region. Runoff over southeast Asia and northern Australia is overestimated due to the excessive precipitation simulated there.

The modelled ocean discharge (Figure 4.7) was also compared with the observed discharge from major rivers as listed in *Russell and Miller* [1990]. The ability of the model to simulate the correct average discharge depends both upon the correct representation of precipitation and local runoff as well as the correct flow direction and the absence of artificial inland storage basins created by the model topography. It should also be noted that the modelled discharge is an average over entire coastal grid boxes with a larger spatial scale than the corresponding river mouths.

Of the world's five largest rivers, the Yangtze, Brahmaputra-Ganges, Amazon, Congo and Orinoco [*Russell and Miller*, 1990], discharge is seen in the approximate location of the Yangtze and Brahmaputra-Ganges, while discharge corresponding to the Congo is modelled in the southern summer. The Amazon and Orinoco are absent due to the low precipitation and inland draining basins over tropical South America in the model. The model simulates large volumes of discharge in the regions of Asia and the Indian subcontinent corresponding to rivers such as the Indus, Brahmaputra-Ganges, Irrawaddy, Si, Mekong and Yangtze. Discharge from Indonesia, Papua New Guinea and northern Australia is overestimated as for runoff.

Discharge is also simulated in the approximate vicinity of the Columbia River on the east coast of Canada and in the region of La Plata in Argentina. The model simulates discharge along the west coasts of North and South America which is not observed, due to the lower elevation of model topography in these regions. The observed runoff and discharge into the Arctic Ocean from North

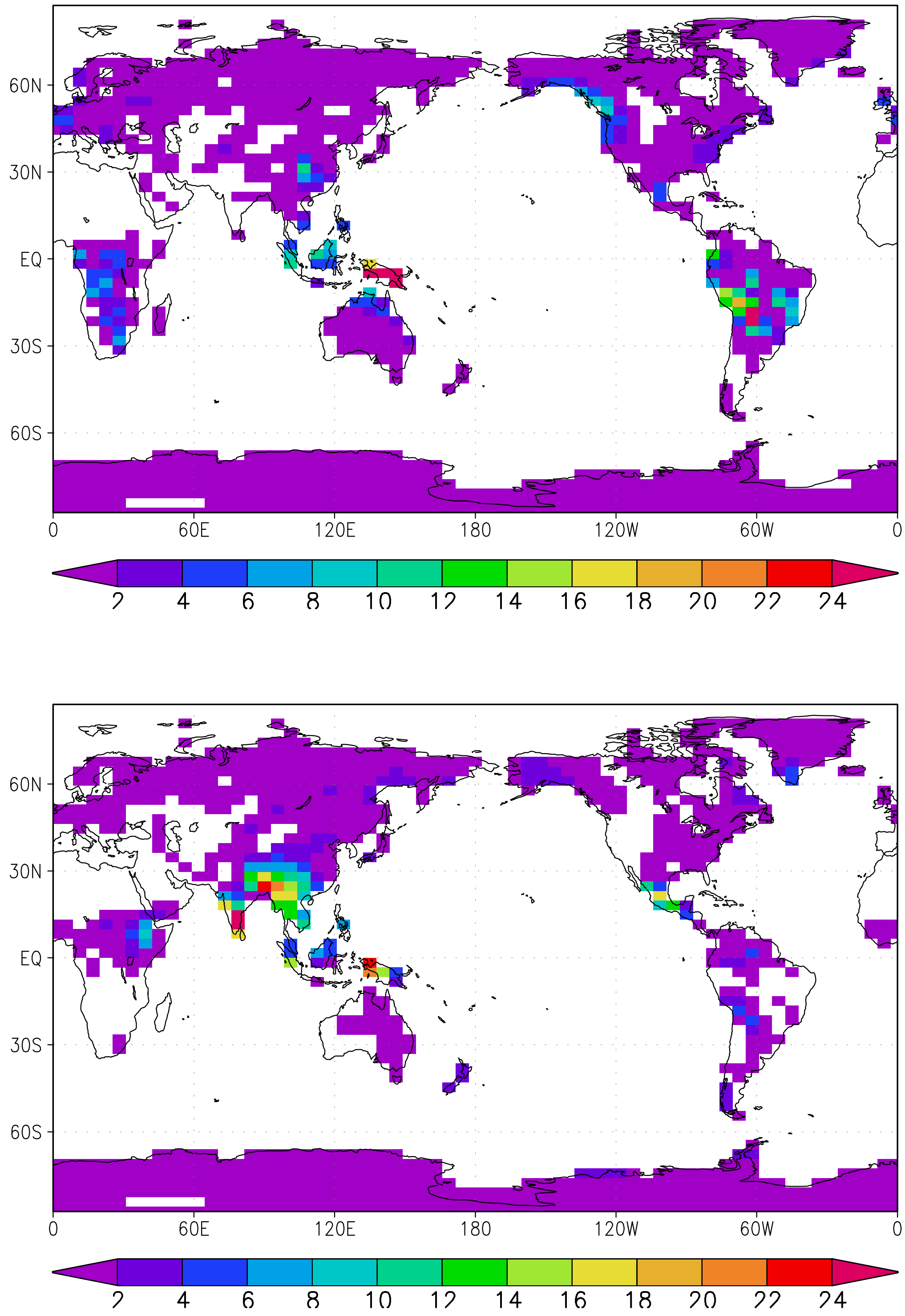

Figure 4.6: Modelled local runoff: DJF (top) and JJA (bottom). Unit is mm/day.

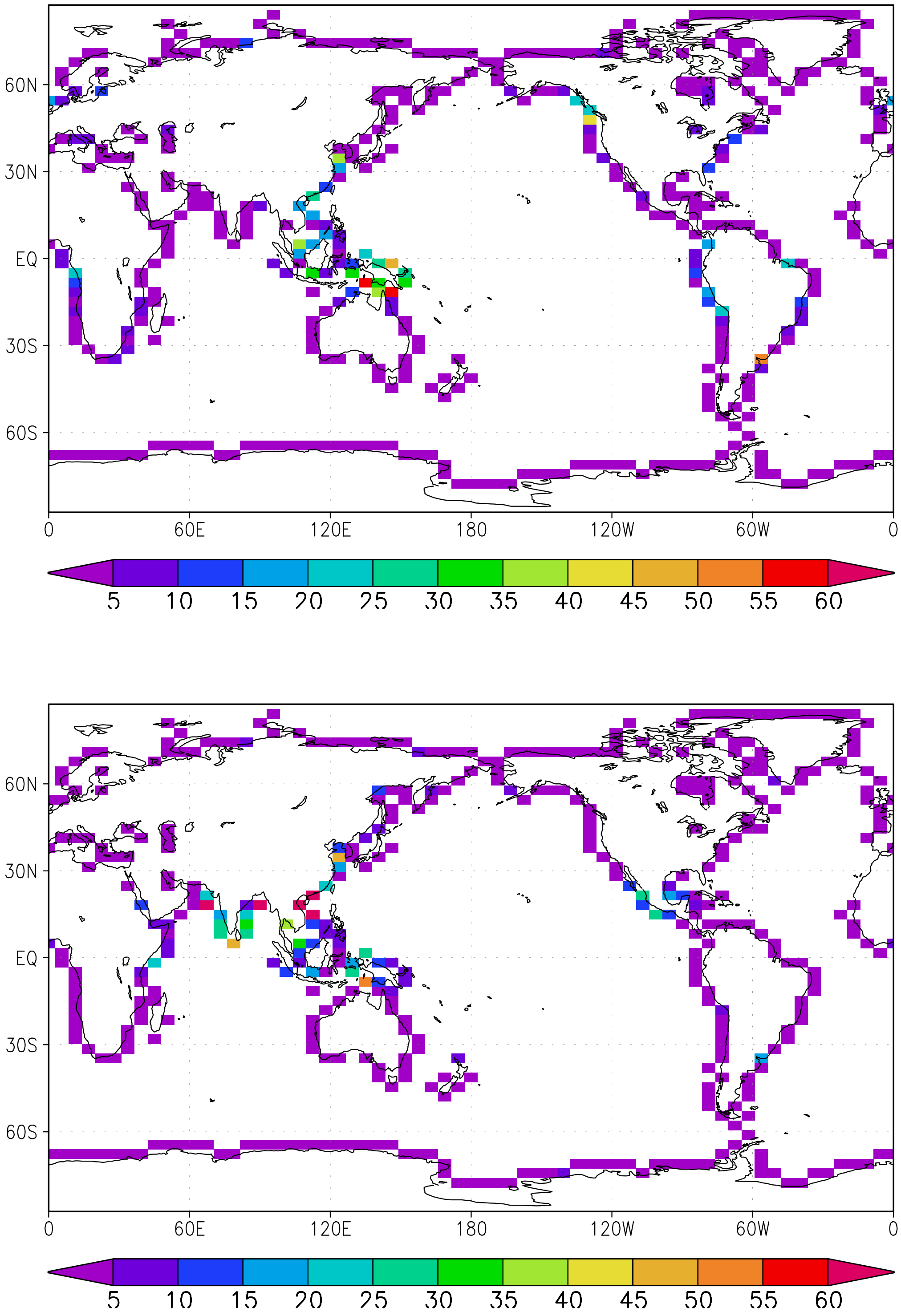

Figure 4.7: Modelled ocean discharge: DJF (top) and JJA (bottom). Unit is 10^3 m^3/s.

America and Europe is underestimated, due to the small precipitation amounts and the lack of a snow melt contribution to runoff in this version of the model.

4.4.4 Validation of runoff isotopic ratios

The isotopic composition of local runoff is determined by the soil moisture ratio at the location where excess precipitation occurs. After entering the runoff reservoir there is no further interaction with the modelled soil moisture, simulating the transport of runoff via localised river systems rather than flow over the entire land surface. There is therefore no isotopic exchange between the runoff and soil moisture. Isotopic enrichment due to evaporation of river runoff during transport is also not included, which may lead to overly depleted simulated runoff δ^{18}O values, as discussed by *Hoffmann and Heimann* [1998].

The isotopic ratio of modelled runoff (Figure 4.8) follows the balance between precipitation and evaporation, with the most isotopically depleted values at high elevations, inland, at high latitudes and in areas of high precipitation. The runoff and discharge δ^{18}O is generally lower than the mean precipitation δ^{18}O (Figure 3.7) over the same region. This is because runoff occurs only when the soil moisture reaches saturation during high precipitation events, weighting the runoff isotopic ratio towards the more depleted values associated with large precipitation amounts. *Hoffmann and Heimann* [1998] argue that a total separation of soil moisture and runoff is not realistic and that the representation of runoff isotopic content would be improved with the addition of diffusive exchange between the reservoirs before runoff transport occurs.

The isotopic ratio of river discharge for the Rhine, Mackenzie and Amazon Rivers is compared with the ratios simulated by the ECHAM model given in *Hoffmann and Heimann* [1998] and with observations cited therein, as summarised in Table 4.2. The discharge values were taken at the nearest coastal model grid point to the actual location of the river mouth.

The Rhine River runoff consists of water from two catchment basins, an Alpine basin and a lower altitude basin, with correspondingly different isotopic signatures. While the MUGCM simulates a mean runoff isotopic ratio of the same magnitude as the observed and ECHAM values, the model does not capture the observed seasonal cycle with more depleted summer runoff due to inflow of isotopically light snow melt from the Alpine catchment area. For the Mackenzie River, the model again simulates a mean runoff isotopic ratio which

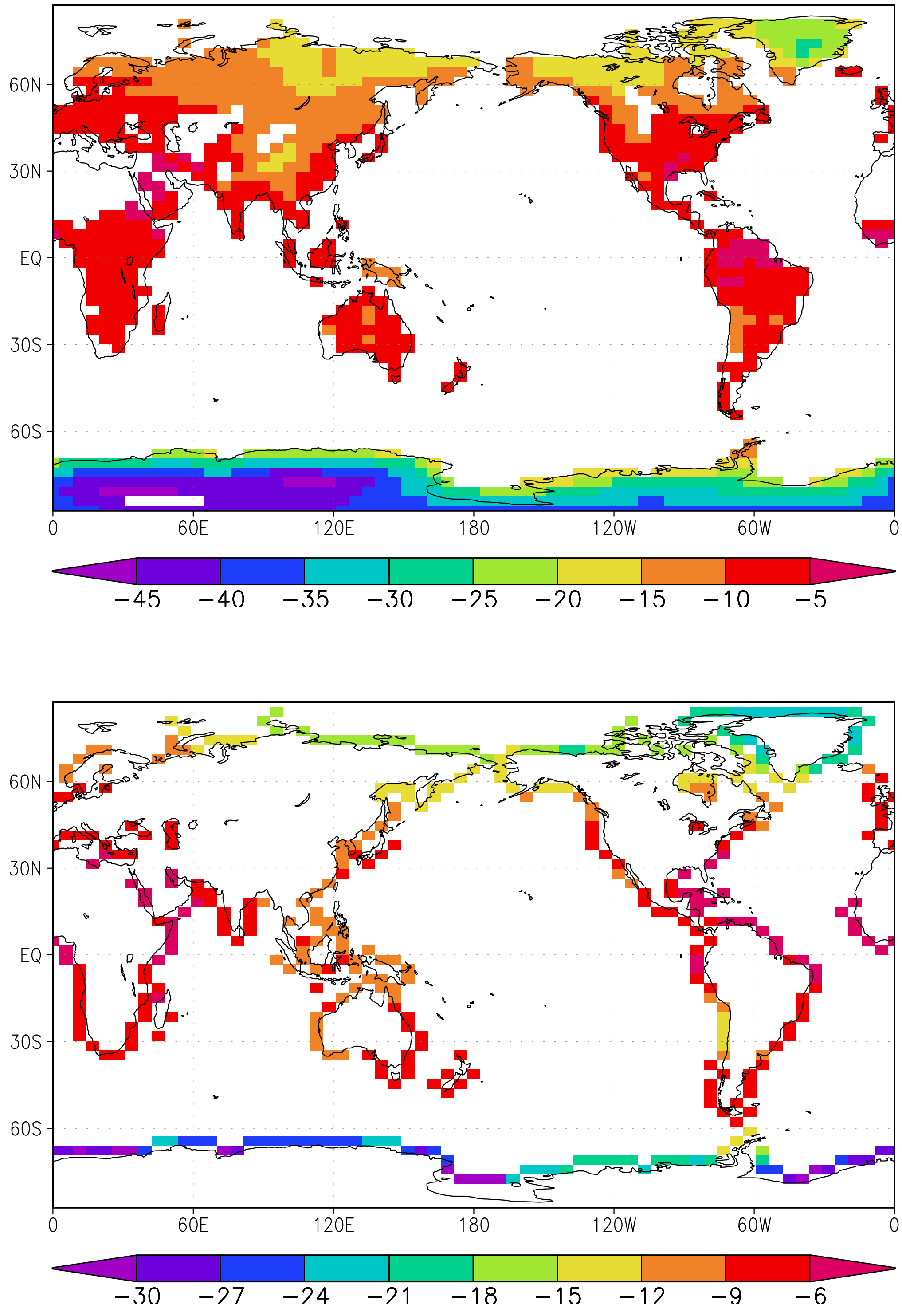

Figure 4.8: Modelled annual average local runoff δ^{18}O (top) and discharge δ^{18}O (bottom). Unit is ‰.

River runoff	**Observed**		**MUGCM**		**ECHAM**
	DJF	**JJA**	**DJF**	**JJA**	**Ave**
Rhine River	−8.8	−10.5	−8.1	−7.1	−8
Mackenzie River	−17	−21	−19.4	−17.6	−19
Amazon River	−5 to −6		−4.7	−4.3	−10 to −11
Ocean discharge					**GISS**
Arabian Sea	−9 to −11.5		−7.8	−8.2	−4.5
Bay of Bengal	−6 to −10		−9.3	−10.0	−4.5

Table 4.2: River runoff δ^{18}O for major rivers: observed, MUGCM, ECHAM and GISS values (‰). ECHAM values from *Hoffmann and Heimann* [1998], GISS values from *Delaygue et al.* [2001]. In some cases an annual range is given rather than DJF and JJA averages.

compares well with observed values, but fails to simulate the impact of summer snow melt on the runoff isotopic seasonal cycle.

The Amazon River has a small annual range of isotopic ratios, which is well simulated by the MUGCM isotopic runoff scheme. The ECHAM model produces runoff δ^{18}O values which are overly depleted due to the amount effect bias mentioned above, despite the model simulating the correct precipitation δ^{18}O over the Amazon. The closer match between the MUGCM modelled discharge and observations appears to be due to the cancellation of errors due to the amount bias and the underestimation of Amazonian precipitation and isotopic depletion.

The discharge into the Arabian Sea and Bay of Bengal is modelled using the GISS model by *Delaygue et al.* [2001] and the results compared with observations, as outlined in Table 4.2. In both cases, the summer monsoon runoff is more isotopically depleted than the winter runoff, while the total volume of runoff is greater for the Bay of Bengal which receives river discharge from the Brahmaputra-Ganges and Irrawaddy Rivers. In the Arabian Sea, the MUGCM simulates coastal discharge isotopic ratios which are slightly less depleted than observed, but closer to the observed range than those simulated by the GISS model. The modelled discharge into the Bay of Bengal is within the range of observed runoff δ^{18}O, while the GISS model again underestimates the isotopic depletion of runoff at this location.

The surface ocean δ^{18}O with the inclusion of runoff is shown in Figure 4.9 for

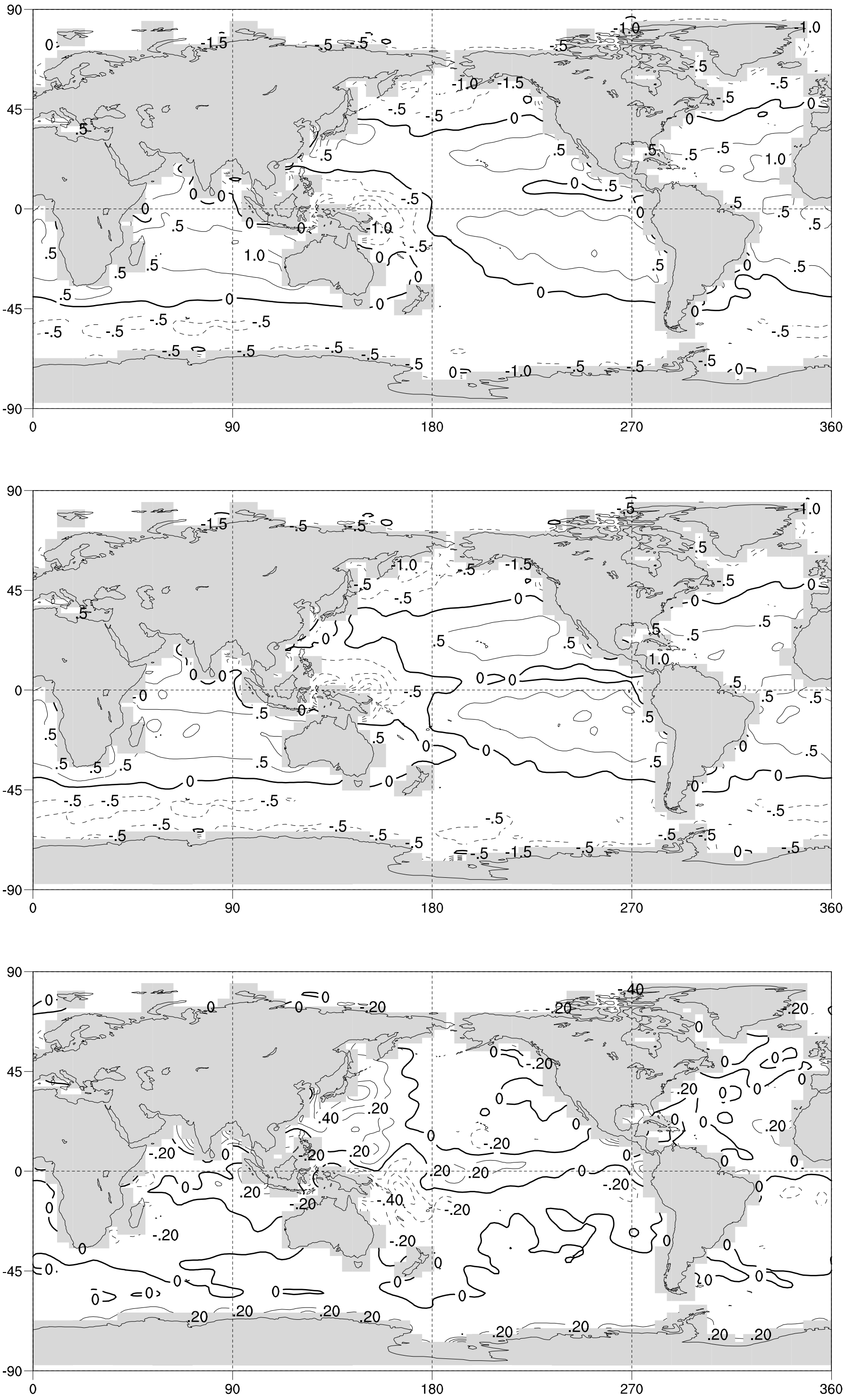

Figure 4.9: Modelled surface ocean $\delta^{18}O$ with runoff: DJF (top), JJA (middle) and DJF – JJA (bottom). Contour intervals are 0.5‰ and 0.2‰ for difference.

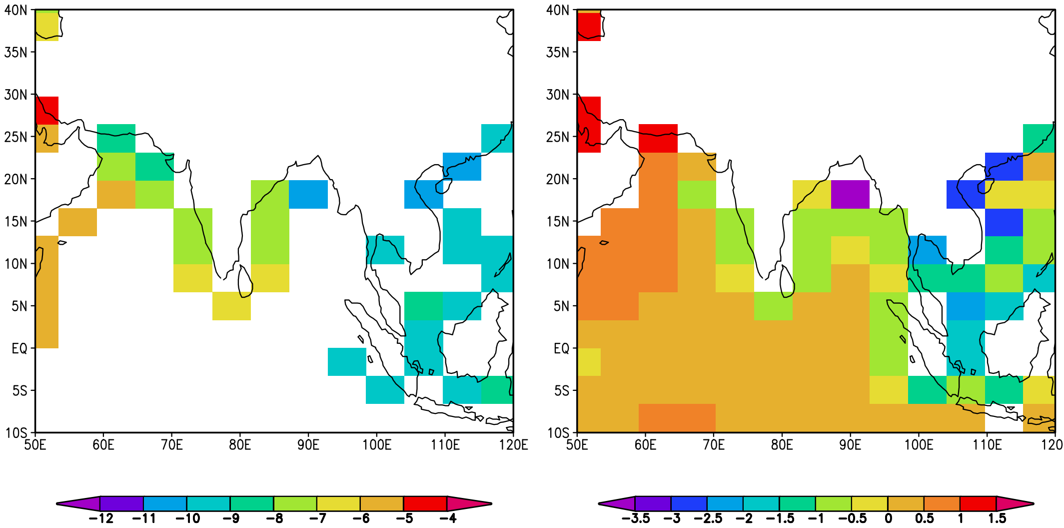

Figure 4.10: Modelled annual average discharge δ^{18}O (left) and surface ocean δ^{18}O (right) in the Arabian Sea and Bay of Bengal. Unit is ‰.

DJF, JJA and DJF – JJA. The minimum modelled δ^{18}O is −4.5‰ compared with −3‰ for the ocean scheme without runoff, indicating that the impact of isotopically depleted continental runoff is captured by this scheme. The seasonality of the runoff isotopic signal is seen in the tropics where the coastal discharge from Asia, India and Central America reduces the surface δ^{18}O values in JJA and the discharge from Indonesia, Papua New Guinea and northern Australia produces more depleted DJF surface ocean δ^{18}O values. At high northern and southern latitudes the seasonality of the runoff isotopic signal is reversed due to the greater isotopic depletion of winter precipitation and runoff.

The modelled discharge and surface ocean isotopic ratios with the inclusion of runoff are shown for the Arabian Sea and Bay of Bengal in Figure 4.10. The Arabian Sea is the source of a large proportion of monsoon precipitation over India, with high evaporation rates producing high salinity and surface isotopic enrichment. The observed Arabian Sea surface ocean δ^{18}O has values of up to +0.9‰ with a range of around 0.5‰*Delaygue et al.* [2001]. The MUGCM simulates surface isotopic values of around +0.5 to +1.0‰ with negative values at the coast.

The Bay of Bengal by contrast to the Arabian Sea does not experience high evaporation rates, while receiving a large influx of continental runoff from monsoon precipitation via the Brahmaputra-Ganges River. The surface ocean is therefore less saline and has observed surface δ^{18}O of 0‰ to 0.5‰ at the equator and more depleted values of around −2‰ in the north *Delaygue et al.* [2001]. The modelled δ^{18}O are also neutral or positive at the equator in the Bay and increasingly depleted to the north.

4.5 Isotopic snow scheme

An additional component of the runoff and surface ocean isotopic signal is the influx of continental runoff from snow melt, which is strongly isotopically depleted compared with the surface ocean. The isotopic signal of snow melt in the surface ocean incorporates a seasonal delay with the influx of snow melt adding an isotopically depleted winter precipitation signal in the spring and summer months. In order to incorporate the effects of snow melt in the modelled surface ocean isotopic distribution, the volume of both normal water and isotopic snow melt is required.

The basic version of the MUGCM does not include a separate budget of snow in the surface hydrologic calculations. Snow is designated as a land surface type for the purposes of albedo calculations while the surface water budget for “snow” grid points is calculated using the soil moisture scheme just as for bare soil. The model also includes the option of a prognostic snow scheme developed by *Walland and Simmonds* [1996]. The snow scheme calculates the snow depth and snow fraction and incorporates the effect of sub-gridscale topography with a statistical parameterisation. The scheme was modified to incorporate isotopic tracers as well as normal water in the snow depth calculation in order to produce the required isotopic snow melt quantities.

4.5.1 Prognostic snow scheme

The prognostic snow scheme calculates the snow depth, D:

$$\frac{\partial D}{\partial t} = P_{snow} - E - M \tag{4.13}$$

where P_{snow} is the precipitation rate falling as snow, E is the rate of moisture loss due to sublimation and M is the melt, which occurs when the surface temperature rises above the freezing temperature (T_f).

The model uses the temperature at the second sigma level ($\sigma = 0.92$), approximately 800 to 1000 m, to determine the form of precipitation. If the temperature at this level is below T_f then precipitation is in the form of snow; otherwise precipitation is considered to be liquid.

Using the mean grid box temperature and assuming a moist adiabatic lapse rate, the freezing level for each grid box is calculated. The sub-gridscale topography is then used to calculate the proportion of the grid box which lies above the freezing level (non-ablating) and below (ablating). When precipitation occurs, the snow depth is calculated for the grid box fraction above the freezing level. For the fraction below the freezing level, the surface moisture budget is calculated according to the model's soil moisture scheme. The energy budget is also calculated separately for the snow covered and non-snow covered fraction of the grid box.

The model represents the effect of vegetation cover on snow coverage via a surface roughness parameterisation. Over a surface with rough vegetation (eg. forest) more snow is required to achieve the same fractional coverage. This is parameterised following *Pitman et al.* [1991] with a scaling for the snow depth according to the surface canopy roughness, taken from the data of *Wilson and Henderson-Sellers* [1985].

The modelled 10-year average DJF and JJA snow fraction and snow depth are shown in Figures 4.11 and 4.12. The snow fraction reproduces the observed distribution well, as described by *Walland and Simmonds* [1996]. The modelled snow depth over the Northern Hemisphere is also compared by *Walland and Simmonds* [1996] with the limited observations available, who conclude that the model appears to simulate snow depth adequately. Accumulation of unphysically large depths such as 15 m over the Andes suggests that there may be limitations to the modelled representation of snow depth in regions where precipitation exceeds evaporation and melting.

4.5.2 Isotopes in snow and snow melt

The representation of isotopic fractionation during the formation of solid condensate in this version of the model is the same as that described in Chapter 3. The condensate is assumed to be solid below $-10°C$ and kinetic effects occur below $-20°C$, with no fractionation or kinetic effects during reevaporation from solid precipitation. The MUGCM does not contain a separate budget for solid and liquid condensate, but simply calculates the net changes in water content and isotopic ratios of vapour and precipitation for an assumed solid/liquid ratio

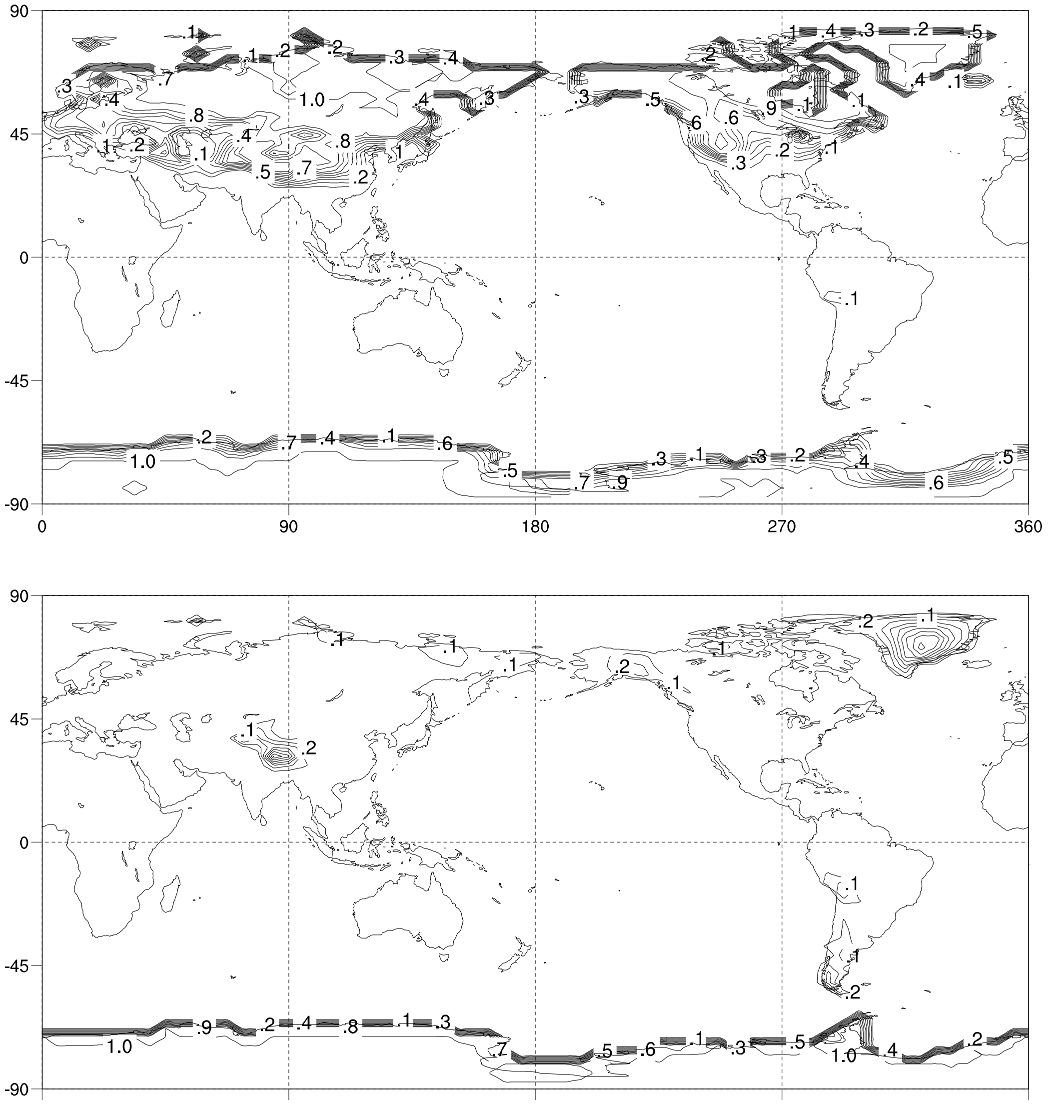

Figure 4.11: Modelled snow fraction: DJF (top) and JJA (bottom). Contour interval is 0.1.

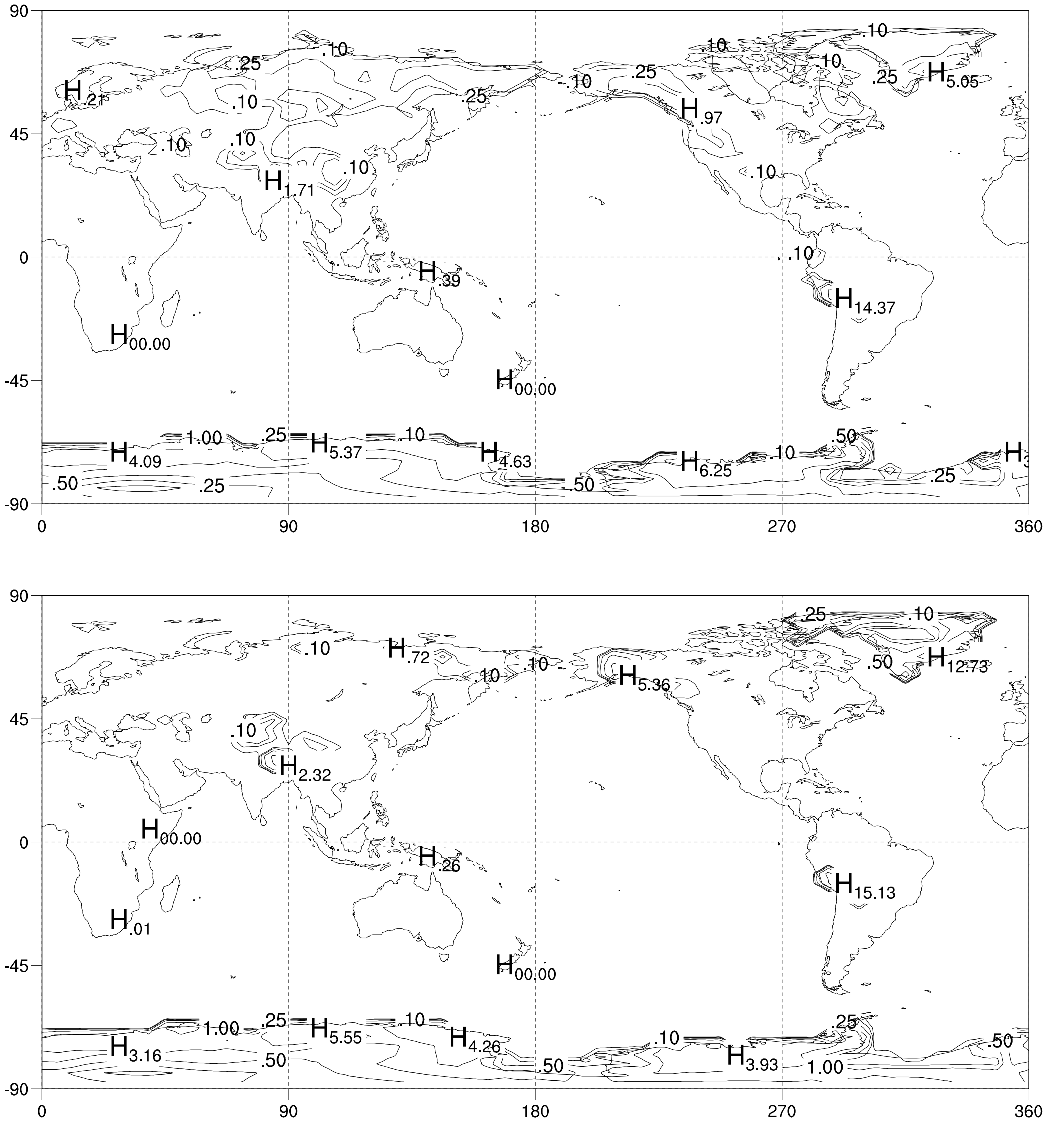

Figure 4.12: Modelled snow depth: DJF (top) and JJA (bottom). Contours are 0.1, 0.25, 0.5, 1, 2, 5, 10 m.

determined from the temperature of the saturated atmospheric layers.

It should be noted that the formation of solid condensate in an atmospheric column in the convective adjustment scheme (with the appropriate fractionation factor and kinetic effects) will not necessarily correspond to the precipitation designated as snow by the snow scheme criteria of sub-freezing temperatures at the second atmospheric level. This may be considered to represent the conditions where solid condensate is formed within a cloud but melts before reaching the ground. The converse case where liquid condensate forms within the convective scheme while the snow scheme diagnoses solid condensate may lead to errors in the extent of fractionation and kinetic effects undergone by the precipitation.

The formulation of fractionation during condensation in the MUGCM is similar to that used in other isotopic tracer schemes in the LMD, GISS, ECHAM and GENESIS GCMs which follow the suggested parameterisations of *Merlivat and Jouzel* [1979] and *Jouzel and Merlivat* [1984]. In order to include separate budgets of solid and liquid precipitation, a more complex cloud model is required. An alternative approach is to model the full mixed cloud processes, accounting for the Bergeron-Findesein process whereby simultaneous undersaturation with respect to liquid and supersaturation with respect to ice occurs, as in the mixed cloud isotopic model of *Ciais and Jouzel* [1994]. However the implementation of such a scheme was not considered necessary for this study.

During evaporation from snow (sublimation) and melting, fractionation is not included, as for all other isotopic GCM tracer schemes. This is because the low diffusivity of the isotopes in ice makes fractionation during evaporation from snow, frozen soil or ice negligible [*Jouzel et al.*, 1987b]. However in the case of dew and frost formation, fractionation is included, with kinetic effects for frost formation as described in Chapter 3.

The normal and isotopic snow melt is added to the upper layer of the soil scheme in the model where melting occurs, producing the possibility of runoff in the case of excess soil moisture. Thus the isotopic ratio of the snow will contribute to the isotopic ratio of runoff and coastal discharge into the surface ocean. This scheme does not allow for the effects of layering in the snow whereby only upper layers of the snow pack undergo melt, and so may lead to a smoothing of the isotopic signal of snow melt in runoff.

4.5.3 Validation of isotopic snow scheme

The DJF and JJA distributions of snow δ^{18}O and snow melt δ^{18}O are shown in Figures 4.13 and 4.14. Those grid boxes with extremely small snow depths ($\leq$ 0.1 m) are excluded from the calculation of snow δ^{18}O. The isotopic ratios of snow are similar to those for precipitation, as expected. The snow melt δ^{18}O values follow those of the snow from which the melt derives as there is no fractionation during the melting process.

The modelled surface ocean isotopic distribution produced with the inclusion of isotopic snow is shown in Figure 4.15. It can be seen that the range of surface ocean δ^{18}O values is slightly increased compared with the surface scheme with runoff only. The seasonal signal (DJF – JJA) is also increased substantially in polar regions. The Antarctic DJF coastal ocean δ^{18}O values are now more negative with the influx of summer snow melt, whereas in the model without snow the seasonal signal was positive in this region due to the seasonal signal of δ^{18}O in precipitation (more depleted precipitation and runoff δ^{18}O in JJA). Similarly the Arctic Ocean coastal δ^{18}O values are now more depleted in JJA whereas the seasonal signal without snow was reversed.

4.6 Ocean horizontal transport scheme

The observed surface ocean isotopic signal is influenced by horizontal transport due to ocean currents as well as the vertical surface flux balance. For example, *Delaygue et al.* [2000] compared the modelled distribution from a one-dimensional box model with that produced by an ocean GCM, and found that the ocean model was better able to reproduce the observed distribution (actually a comparison between observed and modelled "salinity" tracers). They found that tropical gyres smooth and displace the subtropical maxima with transport from the equator poleward along the western side of ocean basins and from high latitudes on the eastern side. The resulting upwelling also acts to smooth the signal.

4.6.1 Description of transport scheme

The importance of horizontal transport was investigated with the addition of a horizontal transport term in the surface scheme using ocean currents from the ocean component of the CSIRO Mark 2 Coupled GCM [*Gordon and O'Farrell*,

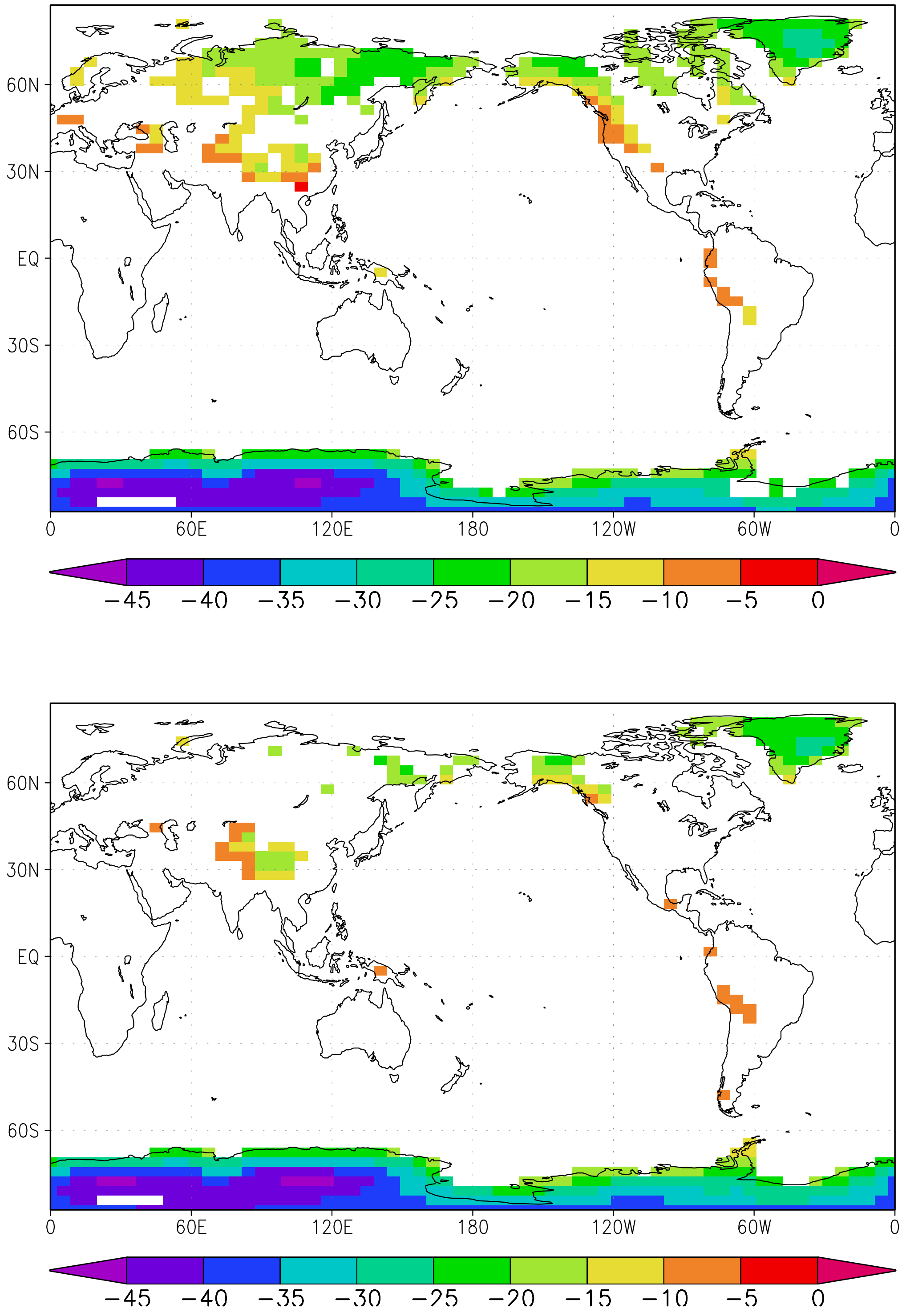

Figure 4.13: Modelled snow δ^{18}O: DJF (top) and JJA (bottom).

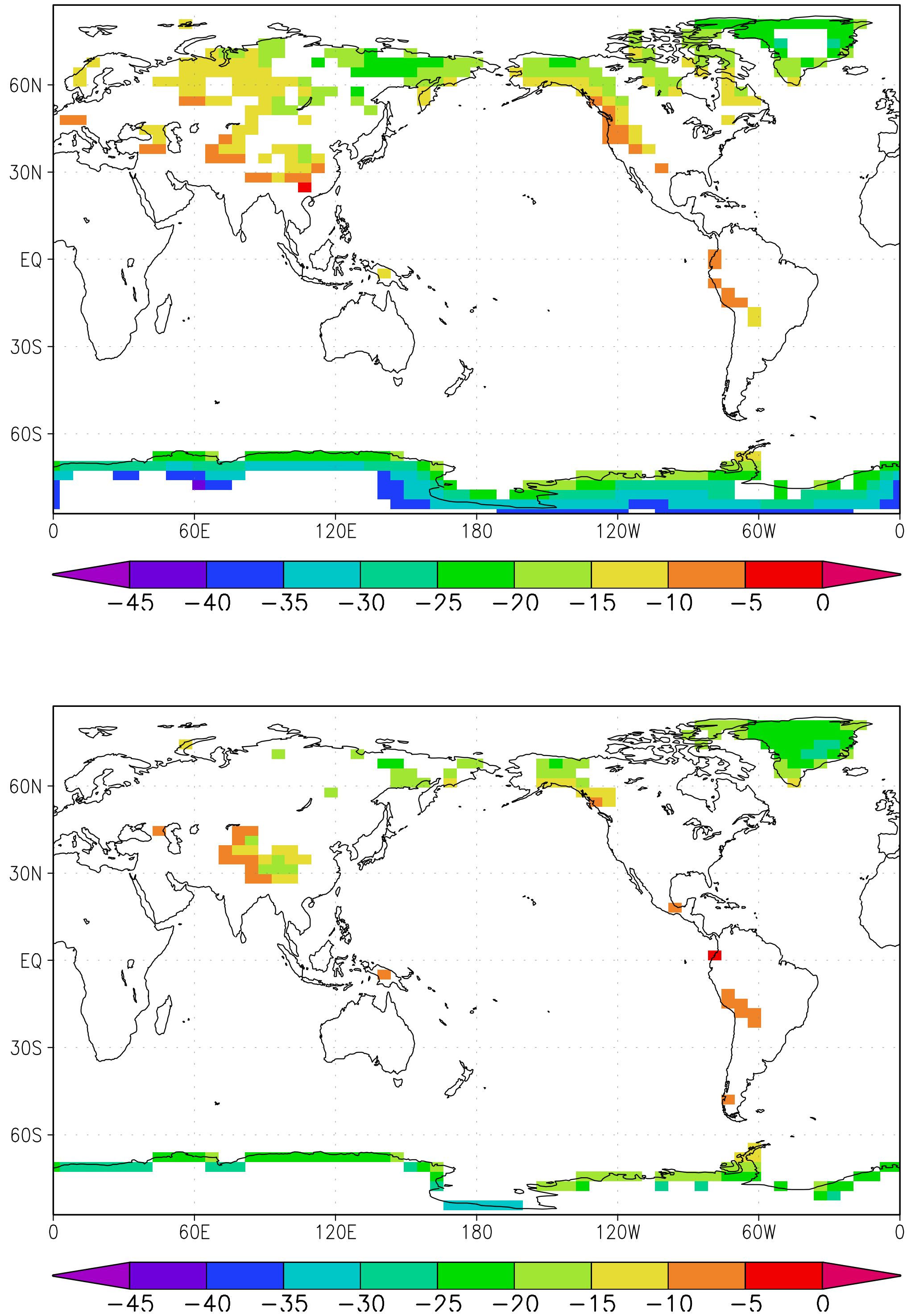

Figure 4.14: Modelled snow melt δ^{18}O: DJF (top) and JJA (bottom).

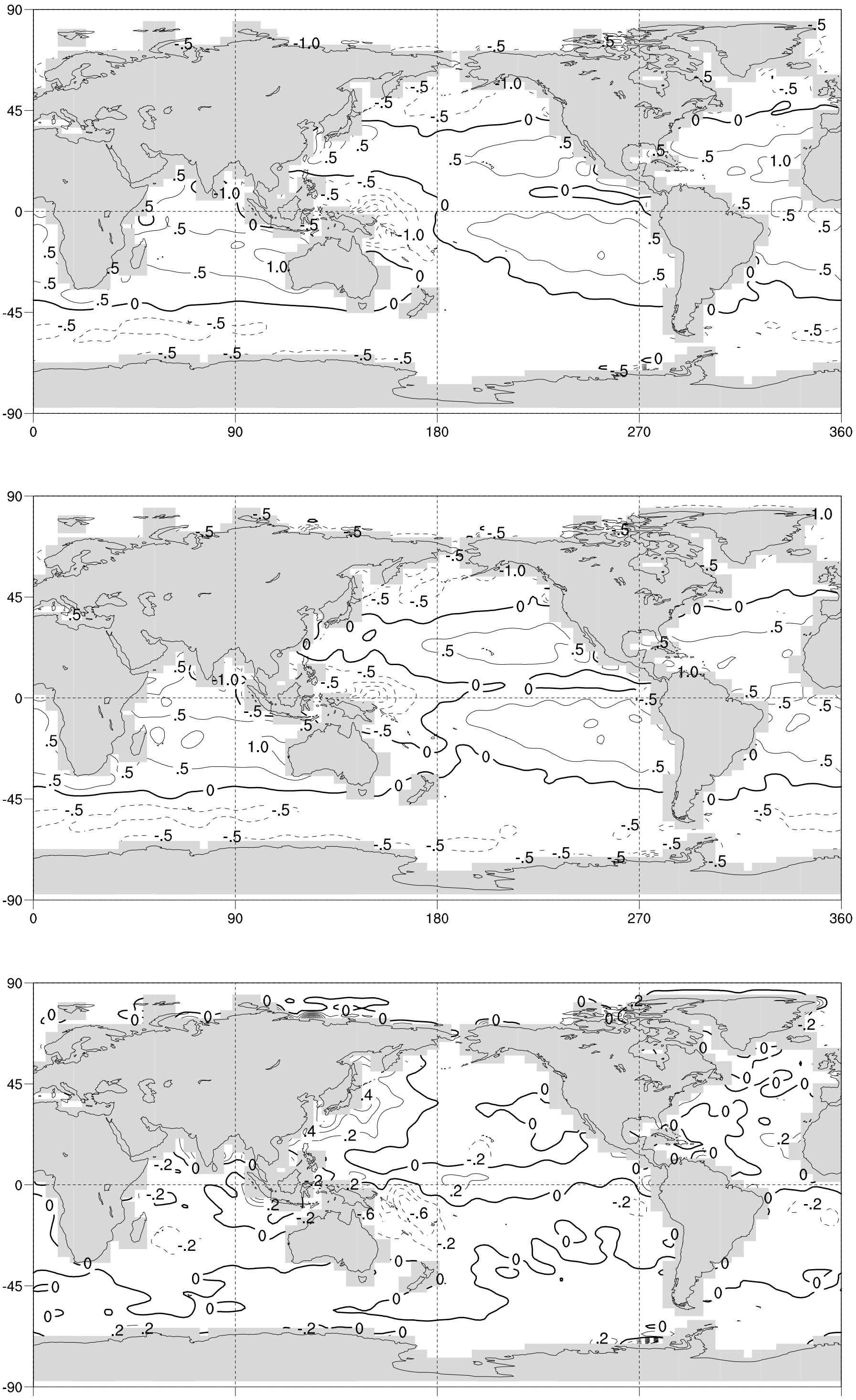

Figure 4.15: Modelled surface ocean δ^{18}O with runoff and snow melt: DJF (top), JJA (middle) and DJF – JJA (bottom). Contour intervals are 0.5‰ and 0.2‰ for difference.

1997]. Monthly average currents were obtained from a climatological run of the ocean model with present day boundary conditions [*Hirst et al.*, 2000]. Three different sets of currents were compared: those from the top four levels of the model (depths of 12, 37, 65 and 98 m), those from the top two levels and from the upper level only. As the land masks of the CSIRO and MUGCM models are slightly different, the missing coastal ocean values were filled with the average of adjacent values.

As for the river runoff scheme, water depths are converted to volume to account for grid box surface area before transport occurs. The normal water and isotopic water volumes are transported horizontally at each timestep to adjacent grid boxes according to the magnitude of the u and v components of the currents at each grid point in an equivalent manner to the river runoff scheme (Equations 4.7, 4.8 and 4.9). The surface normal water budget therefore becomes:

$$\frac{\partial Q}{\partial t} = (P - E + D) + adv(Q) + k(h - Q) \tag{4.14}$$

with the equivalent isotopic budget:

$$\frac{\partial Q_i}{\partial t} = (P_i - E_i + D_i) + adv(Q_i) + k(Rh - Q_i) \tag{4.15}$$

where $adv(Q)$ and $adv(Q_i)$ are the sum of the transports from the adjacent ocean grid boxes.

Comparison of the modelled surface δ^{18}O distribution simulated using the three different current data sets indicated that the averaged 12 m and 37 m currents produced a surface isotopic distribution which corresponded most closely with the observed distribution, and so these values were adopted for the model simulation. As these two upper layers correspond to the depth of the ocean mixed layer (about 50 m) this is not surprising, although the depth of the surface layer in the isotopic scheme is only 5 m as outlined in Section 4.3.

The mean DJF and JJA currents averaged over the 12 m and 37 m levels are shown in Figure 4.16. It can be seen that the north- and south-easterly equatorial currents are strongly present in both seasons, with the Kurishio and Gulf Stream western boundary currents also reproduced. The equatorward eastern boundary currents are less well represented, and the equatorial countercurrent is not reproduced at this resolution. The Antarctic circumpolar current is also seen, with a weak equatorward flow in the South Atlantic sector.

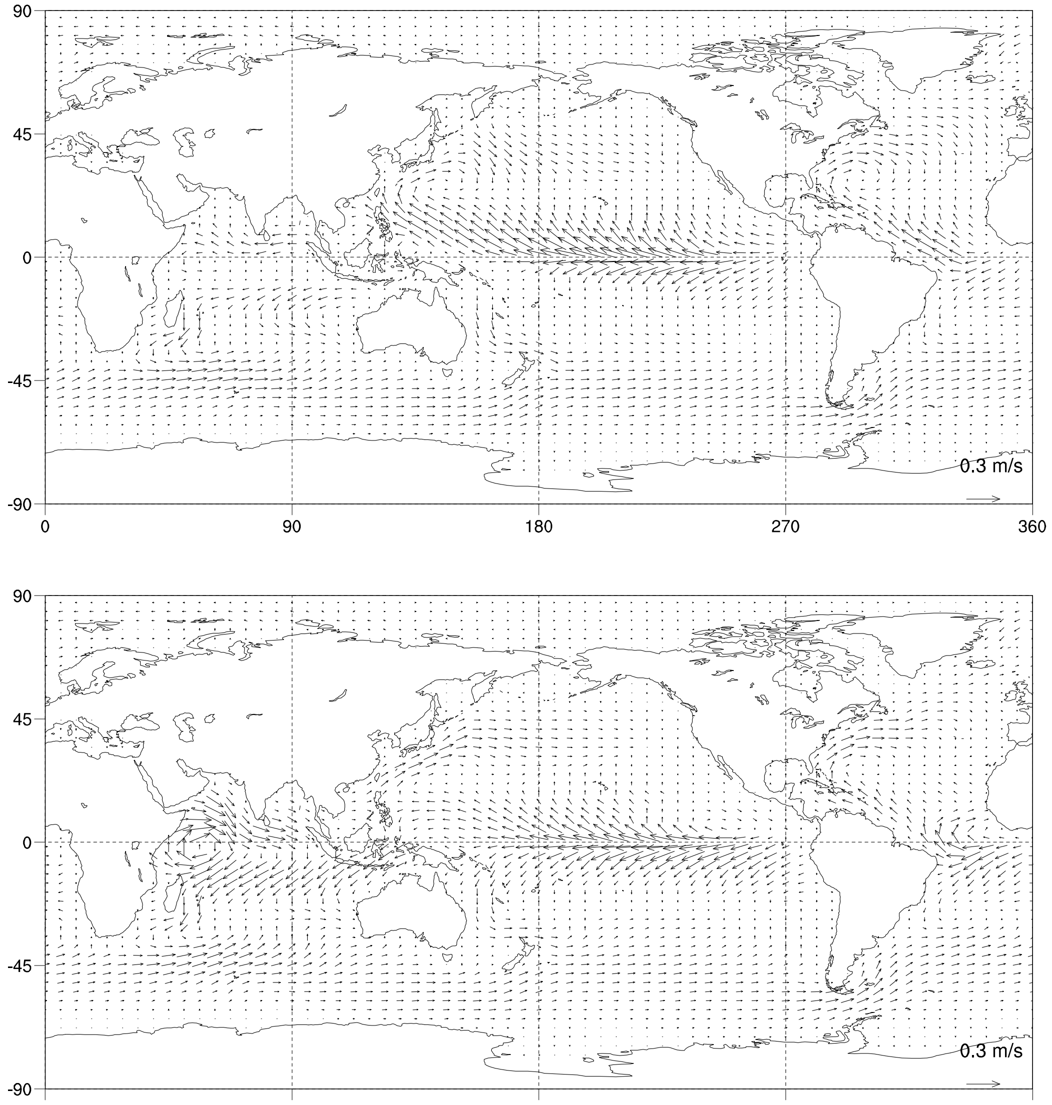

Figure 4.16: Average currents from upper two layers (12 m and 37 m) of the CSIRO Mark 2 ocean model: DJF (top) and JJA (bottom).

4.6.2 Validation of transport scheme

The modelled surface ocean isotopic distribution with the inclusion of horizontal transport, shown in Figure 4.17, is compared with the distribution from the surface scheme with runoff but without transport (4.9). It can be seen that the surface isotopic distribution is altered with the addition of horizontal transport. The poleward currents on the western side of the ocean basins transport the relatively enriched tropical surface waters to high latitudes while the equatorward currents on the east side bring isotopically depleted waters from high latitudes towards the tropics.

The largest difference between the surface distribution with and without transport is the displacement of isotopically enriched central Pacific surface water towards the western Pacific where high precipitation amounts lead to relatively isotopically light surface waters in the basic version of the model. The net result of this transport is to make the central Pacific equatorial surface waters isotopically lighter and the western Pacific isotopically heavier. The role of surface currents in transporting runoff discharge from coastal areas into the ocean basins is also seen, with slight increases in coastal isotopic δ^{18}O values and decreases in adjacent regions away from the coast, for example in the Antarctic and Arctic regions.

An additional method of validation of the surface ocean δ^{18}O distribution is the calculation of a modelled "salinity" in parallel to the isotopic tracers to permit comparison with the observed upper ocean salinity distribution from *Levitus* [1982], which is more spatially complete than the observed δ^{18}O distribution. As salinity is also influenced by precipitation, evaporation, runoff and vertical and horizontal ocean transport, the modelled δ^{18}O would be expected to match the observed distribution if this is the case for modelled salinity.

The salinity of the surface ocean layer was calculated as for the isotopic tracers via a "salt content" term S (where salinity is S/Q):

$$\frac{\partial S}{\partial t} = adv(S) + k(hS_{mean} - S) \tag{4.16}$$

where $adv(S)$ is the transported salt content from adjacent grid boxes, h is the mean depth, k is the relaxation coefficient and S_{mean} is the mean salinity (set to 34.6‰ for the present day). In this formulation, the precipitation, runoff and evaporation balance alters the fresh water depth Q from Equation 4.14 so that ratio S/Q representing salinity is altered in the equivalent manner to the

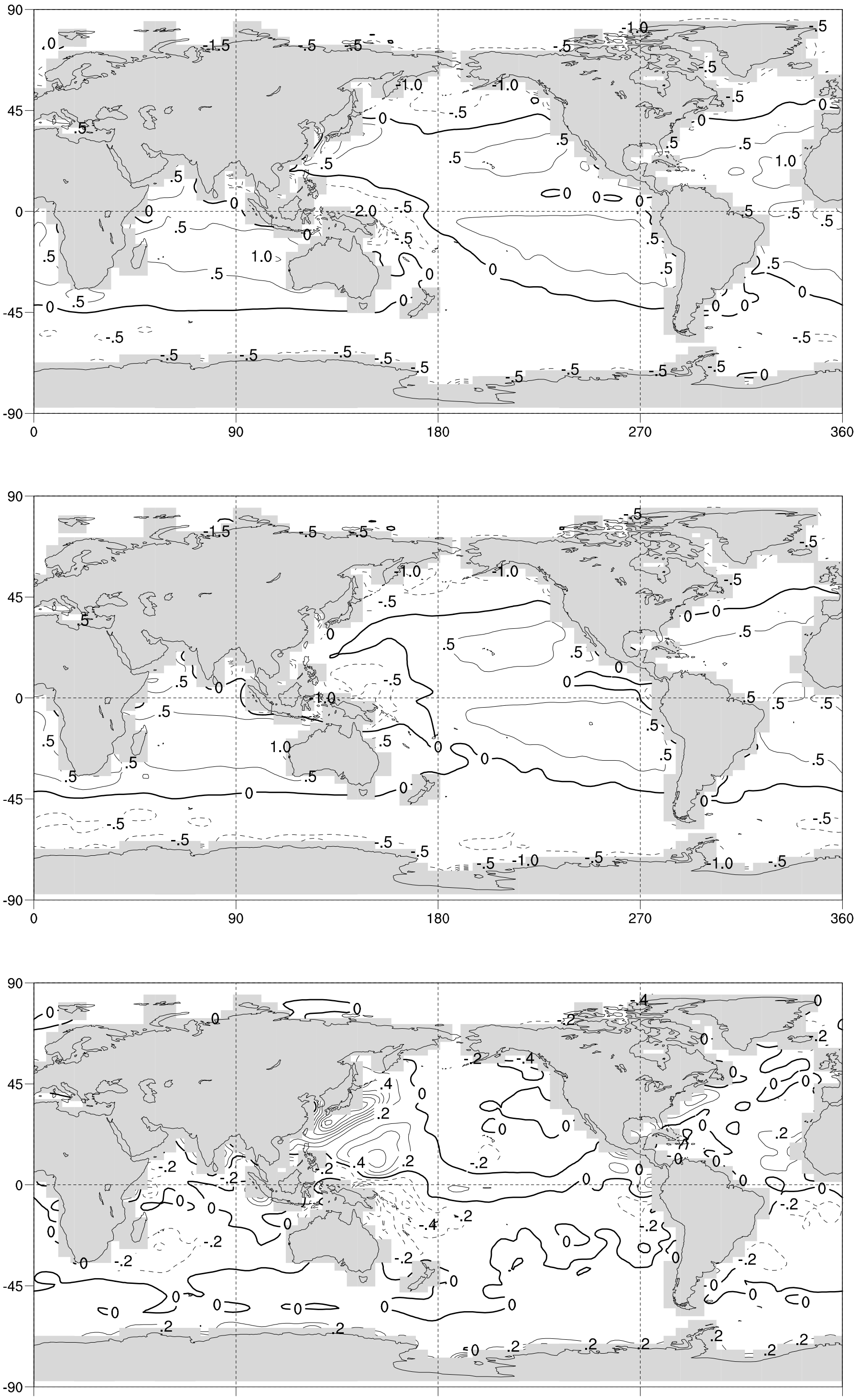

Figure 4.17: Modelled surface ocean δ^{18}O with runoff and horizontal transport: DJF (top), JJA (middle) and DJF – JJA (bottom). Contour intervals are 0.5‰ and 0.2‰ for difference.

variation of the isotopic ratio Q_i/Q.

The modelled salinity distribution for the basic surface scheme without runoff or horizontal transport and the salinity distribution for the surface scheme with runoff and transport is compared with the annual average surface ocean salinity from *Levitus* [1982] in Figure 4.18. The salinity distribution in the basic version of the surface scheme captures the subtropical regions of high salinity with the global maxima in the Mediterranean and Red Seas and the low salinity in the western Pacific and at high latitudes. However the gradients of the modelled salinity distribution are stronger than the observed gradients.

The version of the model which incorporates horizontal transport is better able to reproduce the observed salinity distribution with greater smoothing due to the poleward transport of surface water on the western basin boundaries and equatorward transport on the eastern boundaries, as described above. The modelled salinity for this version of the model also has a larger range of 17.1–41.5‰ compared with 25.3–41.6‰ for the basic surface scheme which compares better with the range of 6.4–39.2‰ for the observed distribution. The lower salinity values simulated by this version of the model are likely to be due to the contribution of fresh water from river runoff.

4.7 Summary

The use of prescribed spatially varying surface ocean δ^{18}O for ocean evaporative fluxes was found to produce a close to linear response in the atmospheric vapour isotopic ratios, which in turn produced a noisier but similarly largely linear response in the precipitation δ^{18}O. A simple one-dimensional interactive surface isotopic scheme was then implemented to investigate the temporal variability of the surface ocean δ^{18}O signal and the atmospheric response. The depth of the modelled surface ocean layer and the damping time scale were tuned to produce an average modelled surface ocean δ^{18}O and seasonal δ^{18}O range which matched observations for the tropics and mid-latitudes.

The incorporation of a river runoff scheme enabled the contribution of river discharge to the surface ocean isotopic distribution to be included. The river runoff scheme captured the large scale distribution of local runoff and discharge within the limitations of the model topography and precipitation distribution. Improvements to the representation of runoff and discharge would require a subgridscale river flow scheme. An alternative approach consists of the modification

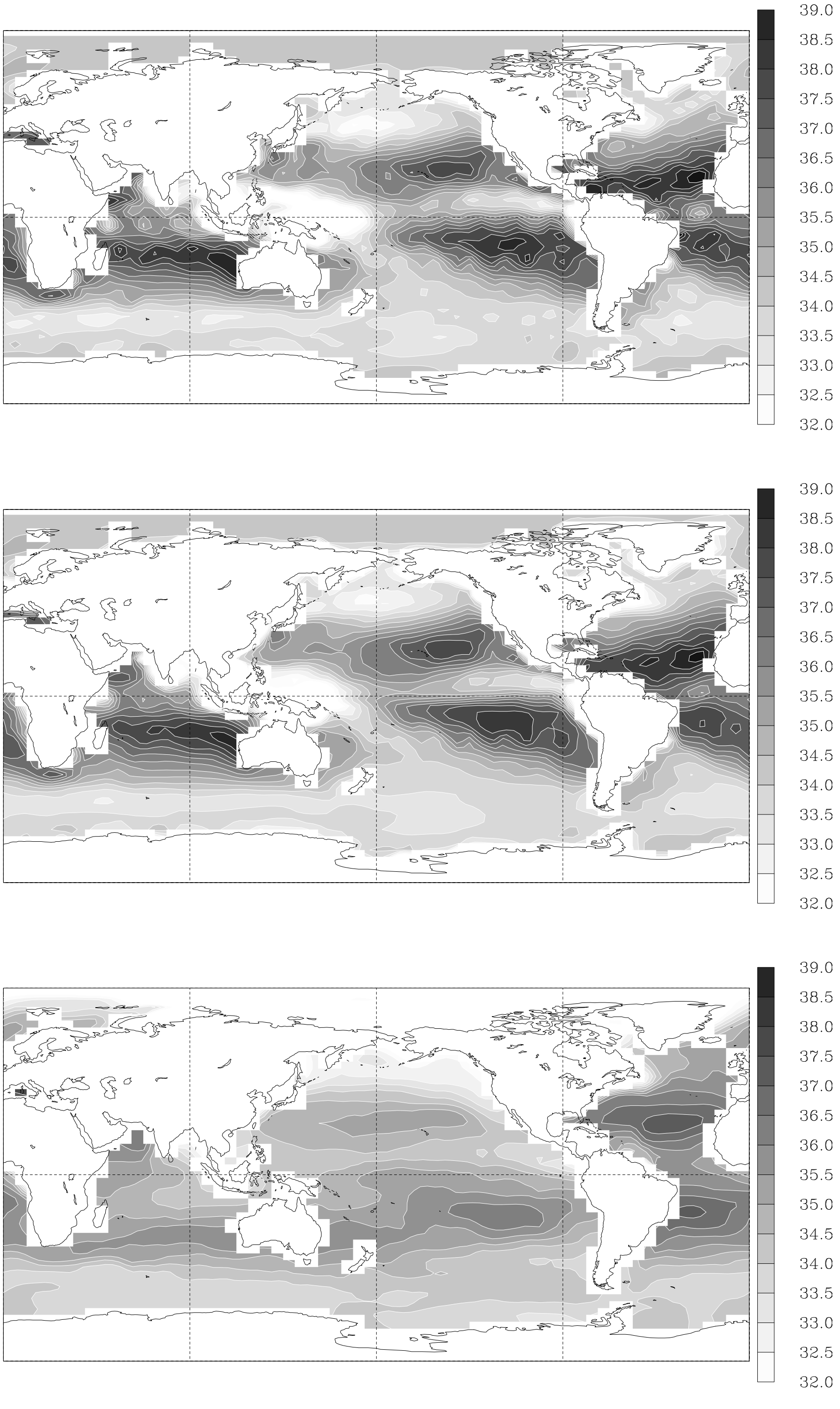

Figure 4.18: Modelled annual average salinity for basic surface ocean scheme (top), scheme with horizontal transport and runoff (middle) and observed annual average surface ocean (0 m) salinity (bottom).

of topographically calculated slopes to reproduce observed flow directions and catchment basins, although such an approach would limit the model to simulations of present day runoff.

The isotopic content of modelled river runoff and discharge was found to reproduce the observed $\delta^{18}O$ values for the Rhine, McKenzie, Amazon and Brahmaputra-Ganges Rivers and the Bay of Bengal and Arabian Sea as well or better than the GISS and ECHAM modelled isotopic runoff. The inclusion of runoff produced more isotopically depleted surface ocean values in coastal regions as seen in observations. Thus the basic surface ocean isotopic scheme and river runoff scheme may confidently be used for sensitivity tests of the isotope hydrologic cycle, such as simulations of the LGM.

Another component of the isotopic hydrologic cycle which was incorporated into the model was snow and the contribution of snow melt to soil runoff. The optional prognostic snow scheme in the MUGCM was modified to include both normal water and isotopic tracers. Such a model could potentially be used to assist the interpretation of ice core isotopic records which consist of accumulated snow in regions such as Antarctica and the Andes, for example in separating the mean isotopic signal in precipitation from that stored in accumulated snow. However such a study would require a more complex glaciological model and higher model resolution to capture the response at the scale of individual ice core sites.

The isotopic snow model was able to improve the representation of the seasonality of runoff at high latitudes (and therefore the contribution to the surface ocean) by introducing a delay between isotopically depleted winter precipitation falling as snow and then contributing to runoff when snow melting occurs in the spring and summer months. However as some tuning of the snow and soil isotopic ratios was still required to prevent unphysical isotopic ratios developing due to evaporation feedbacks in the model, this scheme was not included in subsequent climate simulations.

The addition of horizontal transport in the surface ocean scheme simulated the role of horizontal currents in smoothing the surface $\delta^{18}O$ signal, with transport of isotopically enriched surface waters from the tropics polewards, and transport of isotopically depleted high latitude waters towards the equator. As seen in a comparison between modelled “salinity” with and without horizontal transport and the observed surface salinity, the inclusion of horizontal transport improved the representation of the surface salinity (and $\delta^{18}O$) signal.

In order to extend this approach to the simulation of different climates, the appropriate surface ocean currents are required. Coupled model simulations of LGM climate are still in the validation and testing stage [eg. *Bush and Philander*, 1998; *Hewitt et al.*, 2001], and the next phase of the Paleoclimate Modeling Intercomparison Project will involve the use of coupled models to simulate LGM climate. Alternatively, simulated lower atmospheric winds from an atmospheric GCM may be used to calculate surface ocean stresses. However such an approach is beyond the scope of this study, and therefore the horizontal transport scheme was not adopted for simulations of interannual variability (Chapter 5) or LGM climate (Chapter 6).

Chapter 5

Present day tropical climate and isotopes

5.1 Introduction

Continental and marine isotopic records from the tropics have been used to reconstruct extended histories of tropical climate variability prior to instrumental records, as well as to reconstruct the tropical climate of periods such as the mid-Holocene and LGM. In order to use our model to test the reconstruction of climate from isotopic records on such time scales, we must first validate the model for present day climate. If the model is able to reproduce the main features of the present day tropical isotope signal, then we can more confidently apply the model to the simulation of the isotopic response to the climate conditions of the LGM.

We also use the simulation of present day climate to examine tropical isotope-climate relationships on seasonal and interannual time scales. As outlined in Chapter 2, previous modelling studies have identified strong correlations between tropical precipitation and δ^{18}O on seasonal and interannual time scales, while *Cole et al.* [1993b] found that interannual temperature–δ^{18}O correlations were relatively weak in the tropics. *Hoffmann and Heimann* [1998] and *Cole et al.* [1999] also identified a strong ENSO signal in tropical isotopic ratios, while *Hoffmann and Heimann* [1997] identified an isotopic response to the monsoon due to changes in moisture source and rainout.

This study includes a longer (50-year) climate simulation than previous studies. This study also extends previous work with the inclusion of a detailed comparison of the modelled isotopic signal with marine and continental isotopic records and observations over the modelled period. The inclusion of a surface ocean isotopic tracer scheme provides the ability to the simulate the interaction of surface ocean and atmospheric isotopic content, whereas previous studies have simulated only one component of the system.

A simulation of climate for the period 1950–1999 is carried out and the main features of present day tropical climate variability on seasonal and interannual time scales are identified. The modelled simulation of the monsoon, ENSO and longer term variability is described and compared with observations, and the isotopic response in precipitation and the surface ocean is outlined. The modelled isotopic variability for 1950–1999 is compared with the isotopic ratios in tropical ice cores and marine isotopic records for the same period. The extent to which the model can be confidently applied to simulations of past climate–isotope relationships is then addressed.

5.1.1 Boundary conditions

The GISST2.3b SST and sea ice coverage monthly data [*Rayner et al.*, 1996] were used to force a 50-year simulation of climate from 1950–1999. The SSTs and sea ice gridded data were first interpolated onto the MUGCM R21 grid. The surface masks for the model were then constructed using land and snow coverage for the standard MUGCM seasonal run. All ocean grid boxes in the standard MUGCM mask where filled with the GISST SST values unless the GISST sea ice coverage was greater than zero, in which case the grid box was designated as sea ice with fractional coverage from the GISST sea ice data.

The atmospheric carbon dioxide concentration was modified, using observed annual average concentrations from the IPCC website (www.ipcc.ch) to produce a new set of radiation transfer coefficients for each year 1950–1999. The concentrations increased linearly from 312 ppmv in 1950 to 367 ppmv in 1999. The standard MUGCM ozone concentrations from the TOMS satellite observations of the 1970s and 1980s were used. The model was run with the surface ocean isotopic scheme, using a deep ocean isotopic ratio of R_{SMOW}, and incorporating isotopic river runoff. The horizontal ocean transport and isotopic snow schemes were not used for the reasons outlined in Chapter 4.

The model was initialised from a climatological state from a previous simulation and boundary conditions from 1940–1949 were used to spin-up the model for the 50-year simulation. The simulation is similar to the 1979–1995 AMIP-style run carried out by *Noone and Simmonds* [2002] but covers a longer period, allowing an examination of the decadal variability in both climate and isotopes. Their simulation also did not include a surface ocean isotopic scheme and used a constant atmospheric carbon dioxide concentration.

As the modelled atmosphere does not respond linearly to the imposed SST and sea ice forcing, the model may produce a different climate state for different initial conditions. In order to reduce the effect of internal variability of the model, an ensemble of model runs from different initial conditions may be compared, as for example *Kang et al.* [2002b] for a study of the 1997/1998 El Niño. Such an ensemble approach was not employed for this study due to the length of model integration time required to carry out multiple 50-year transient simulations.

5.2 Main modes of tropical climate variability

The prescription of observed monthly SSTs and sea ice coverage from 1950–1999 is expected to force the atmospheric model to simulate atmospheric circulation, pressure, temperature and hydrologic conditions resembling those observed for the period. However the atmospheric model will also produce internal climate variability unrelated to the boundary conditions. The comparison of modelled and observed seasonal and interannual variability of the climate therefore allows the extent to which the model responds to external forcing to be determined. In addition the relationship between the various climate parameters and the isotopic ratios in precipitation and the surface ocean can be examined for the simulated climate regardless of the similarity of modelled and observed climate variability.

The main modes of seasonal and interannual tropical climate variability are identified in this Section using Empirical Orthogonal Function (EOF) analysis. EOF analysis is a technique for identifying spatially coherent patterns of variability commonly employed in the atmospheric sciences [eg. *Peixoto and Oort*, 1992]. While some caution is required in the physical interpretation of the statistically derived modes resulting from EOF analysis [*Dommenget and Latif*, 2002], the technique may be of use in combination with other approaches to compare spatial patterns associated with known modes of variability.

The average monthly and annual fields are analysed to determine the spatial patterns associated with the main modes of seasonal and interannual variability in the modelled temperature, pressure, precipitation, evaporation and isotopic fields. The spatial patterns and time series of the amplitudes of the interannual modes are also compared to identify common variability between climate and isotopic ratios. The variability associated with the monsoon and ENSO as well as decadal and longer term trends are discussed in more detail in later Sections.

5.2.1 EOF analysis: seasonal variability

EOF analysis was performed on the monthly averages of surface temperature, MSLP, precipitation, evaporation, precipitation δ^{18}O and surface ocean δ^{18}O to identify the seasonal cycle of the variables. EOF analysis is used to examine the seasonal cycle as it reveals the spatial pattern of those regions which vary in phase regardless of the magnitude of the values, whereas a simple difference of seasonal averages is dominated by regions with larger signals.

Unrotated EOF analysis was carried out for fields within the latitude range 45°S–45°N in order to isolate the tropical and subtropical components of the seasonal cycle. The data were detrended to remove any long term linear trends such as those due to anthropogenic warming over the modelled period. The mean of the timeseries at each grid point was subtracted and the data normalised before the EOF analysis was carried out.

The first EOF of monthly data for all the variables analysed is shown in Figure 5.1. Values represent the correlation between the amplitude of the component and the original variable. The spatial distribution of EOF1 of surface temperature, MSLP, precipitation and evaporation is compared with those for precipitation δ^{18}O and surface ocean δ^{18}O to determine the main controls on seasonal isotopic variability in each case.

Precipitation δ^{18}O follows the seasonal cycle of precipitation in the tropics with increased isotopic depletion associated with the summer monsoon in both hemispheres. In the tropics and subtropics EOF1 of precipitation δ^{18}O corresponds with EOF1 of precipitation but with a smaller variance explained and a noisier distribution, indicating the role of other factors such as atmospheric circulation in seasonal isotopic variability. In mid-latitudes the signal is reversed with increased precipitation in winter producing isotopic depletion associated with both precipitation amount and cooler temperatures, as seen over central Asia and south of Australia.

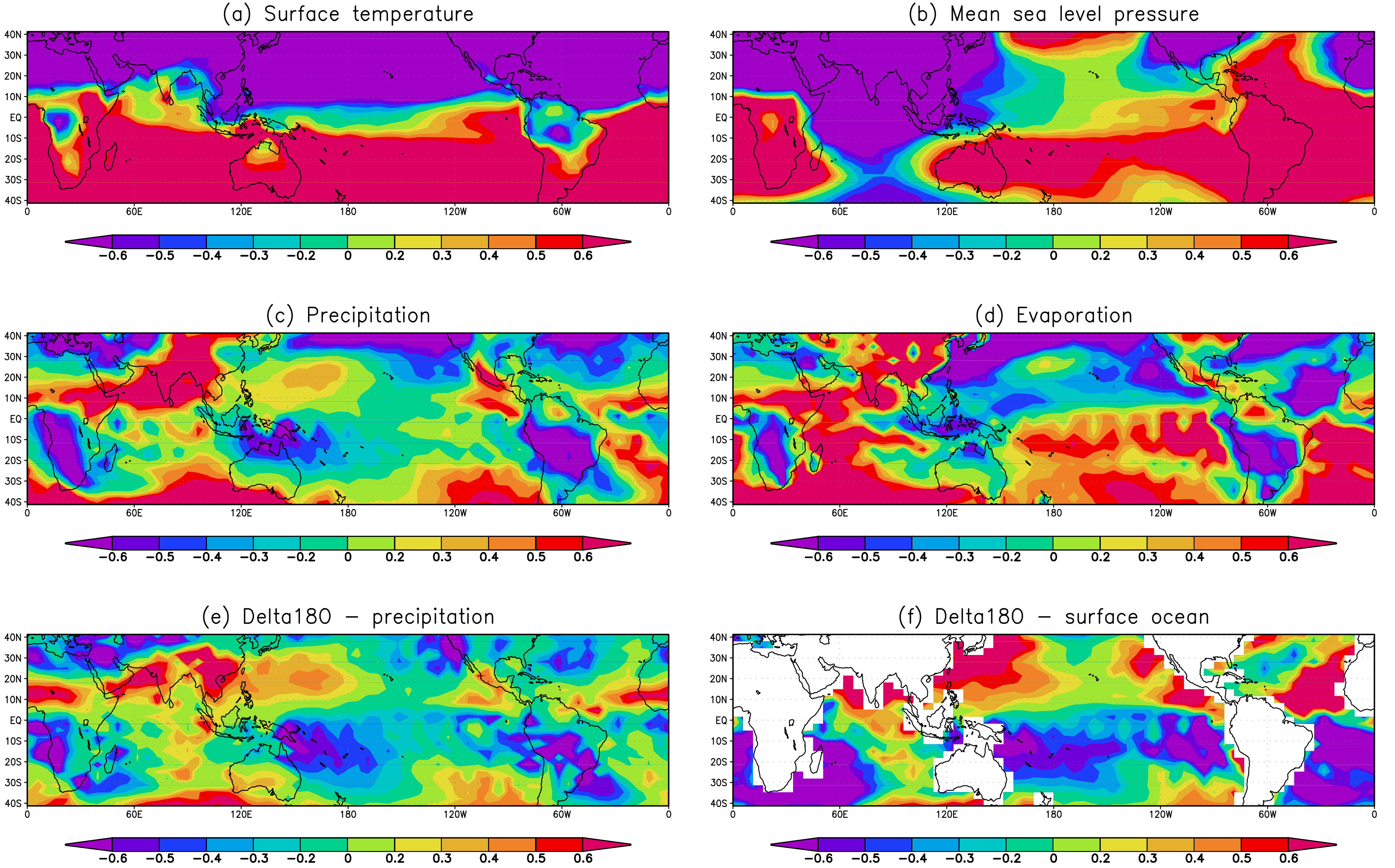

Figure 5.1: EOF1 of monthly surface temperature (a), MSLP (b), precipitation (c), evaporation (d), precipitation δ^{18}O (e) and surface ocean δ^{18}O (f). Values represent the correlation between the amplitude of the component and the original variable.

The surface ocean δ^{18}O seasonal signal is both smoother and stronger than the precipitation δ^{18}O signal due to the simplified one-dimensional nature of the surface ocean isotopic scheme. The simulated surface ocean δ^{18}O seasonal cycle is determined by the balance between precipitation and evaporation at each grid box. The surface ocean δ^{18}O seasonal cycle appears to be dominated by evaporation over the ocean basins, except in regions of large precipitation variability such as the equatorial western Pacific. The strongest seasonal signals are seen where the precipitation and evaporation contributions reinforce each other, such as in the North Atlantic and north-western Pacific where decreased precipitation and increased evaporation act to enrich the surface ocean isotopic ratio.

5.2.2 EOF analysis: interannual variability

The unrotated EOFs were also calculated for annual averages of SST, MSLP, precipitation, precipitation δ^{18}O and surface ocean δ^{18}O to identify the main modes of interannual variability in the tropical climate. The fields were again detrended and normalised before the EOF analysis was carried out.

The timeseries of the amplitudes of the first two principal components were subjected to spectral analysis to determine the main periods of variability of the components. The variance explained (VE) by the first two EOFs of each variable and their main periods of variability (listed in order of decreasing power) is given in Table 5.1. The periods listed exceed a red noise spectrum, although not all exceed the 95% significance level.

The main periods of the first EOF of the variables analysed largely fall within the range of observed ENSO variability (3–7 years). The spatial distribution of the first EOFs of SST, precipitation and MSLP (Figure 5.2) are similar to ENSO SST, precipitation and pressure anomalies identified by others [eg. *Philander*, 1990; *Dai and Wigley*, 2000]. The correspondence between EOF1 of the prescribed GISST SSTs and EOF1 of modelled pressure and precipitation confirms that the model simulates ENSO as the strongest interannual mode of tropical climate. The ENSO signal in the model is discussed further in Section 5.4.

The first EOF of precipitation δ^{18}O has a similar distribution to the first EOF of precipitation amount, with maximum variance and opposite signs in the tropical central and western Pacific associated with ENSO-related precipitation

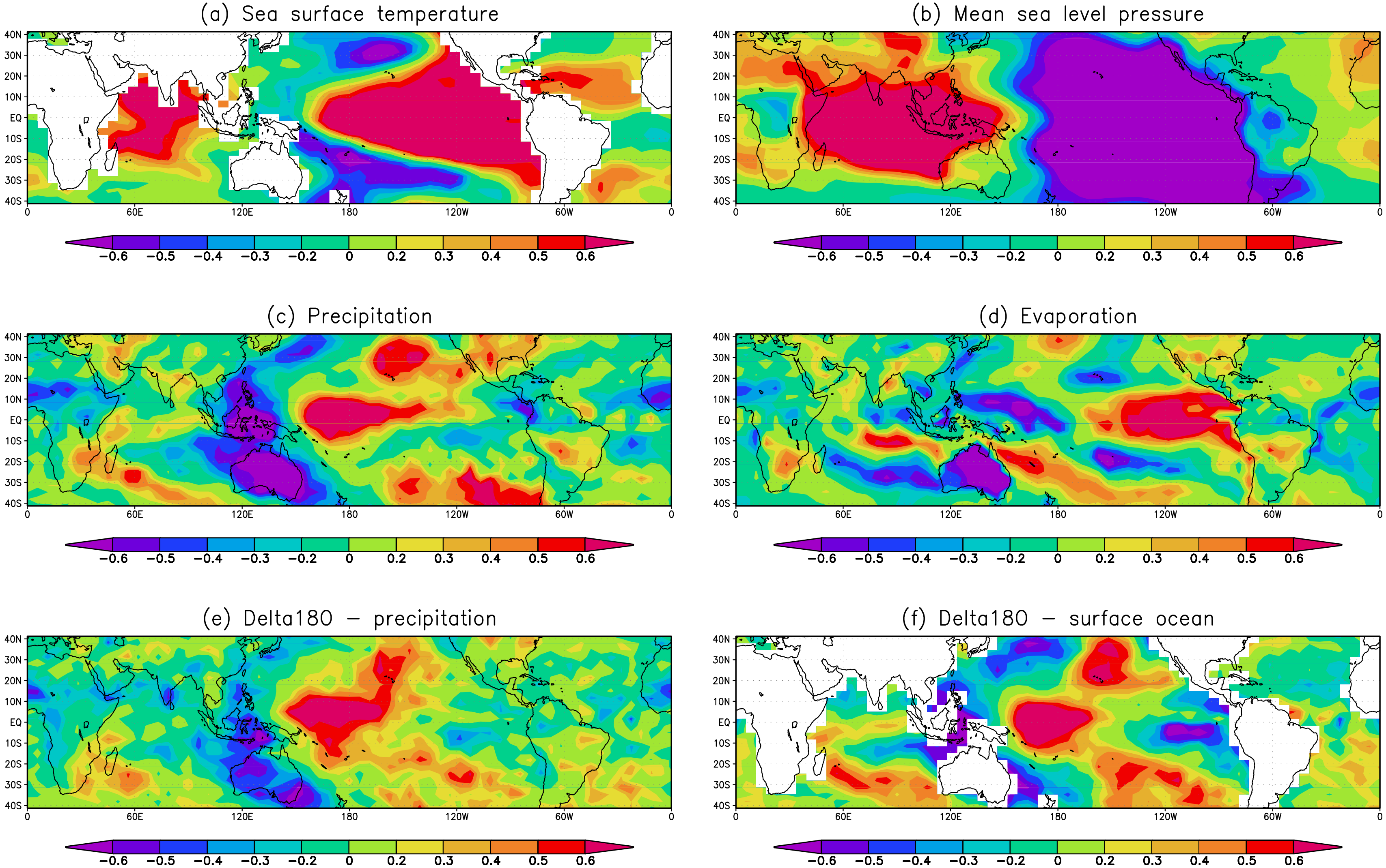

Figure 5.2: EOF1 of annual average SST (a), MSLP (b), precipitation (c), evaporation (d), precipitation δ^{18}O (e) and surface ocean δ^{18}O (f).

Variable	EOF	VE	Main periods (years)
SST	1	14.4%	5.0, 3.6, 12.5
MSLP	1	28.0%	12.5, 5.0, 3.6
Precipitation	1	10.0%	5.0, 3.6, 12.5
Evaporation	1	9.0%	5.0, 3.6, 12.5
Precipitation δ^{18}O	1	7.2%	3.3, 6.25, 2.5
Surface ocean δ^{18}O	1	8.2%	5.0, 3.3, 12.5
SST	2	10.4%	10.0, 3.6, 5.0
MSLP	2	13.2%	8.3, 3.1
Precipitation	2	6.9%	5.5, 2.5
Evaporation	2	6.5%	12.5, 3.6, 2.5
Precipitation δ^{18}O	2	6.2%	6.3, 3.3, 12.5, 2.4
Surface ocean δ^{18}O	2	6.7%	5.5, 3.6

Table 5.1: Variance explained (VE) and main periods of amplitude of EOF1 and EOF2 of annual SST, MSLP, precipitation, evaporation, precipitation δ^{18}O and surface ocean δ^{18}O.

anomalies. The first EOF of surface ocean δ^{18}O is closely related to the precipitation EOF1 pattern, with large variance in the central and western Pacific. There is also an equatorial eastern Pacific signal associated with the change in evaporation due to ENSO-related SST variability.

The magnitudes of the correlations between the amplitudes of the first EOFs of each of the variables as well as the modelled Southern Oscillation Index (SOI) (see Section 5.4) are shown in Table 5.2. The sign of the correlations is not given as the sign of the amplitudes calculated by the EOF routine is arbitrary. The correlations between SST, MSLP, precipitation and evaporation are all large, and these variables are strongly correlated with the SOI, confirming that the first EOF represents the ENSO response in the model. The surface ocean δ^{18}O amplitude also has a strong correlation with all the variables due to its direct dependence on precipitation and evaporation.

EOF1 of precipitation δ^{18}O has a correlation of less than $r = 0.5$ with each of the other variables. However the similarity between the main features of the spatial EOF1 δ^{18}O pattern and the precipitation EOF1 pattern suggests that the isotopic signal does represent a response to ENSO. The weak correlation between precipitation δ^{18}O and SOI suggests that the interannual isotopic response to ENSO is not uniformly strong over the tropics and mid-latitudes.

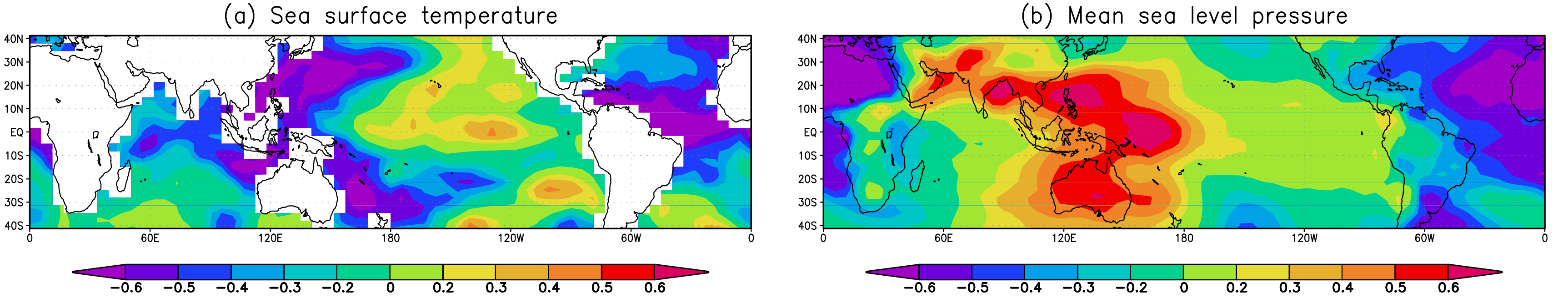

(a) Sea surface temperature

(b) Mean sea level pressure

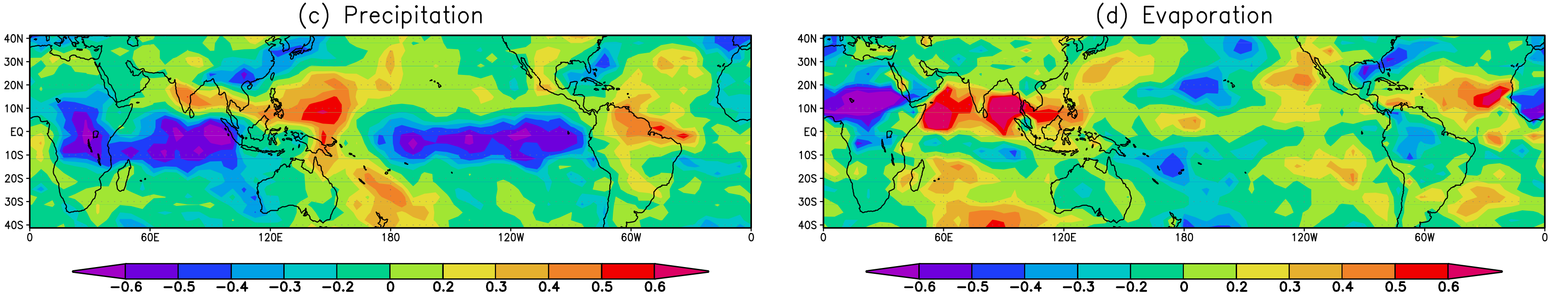

(c) Precipitation

(d) Evaporation

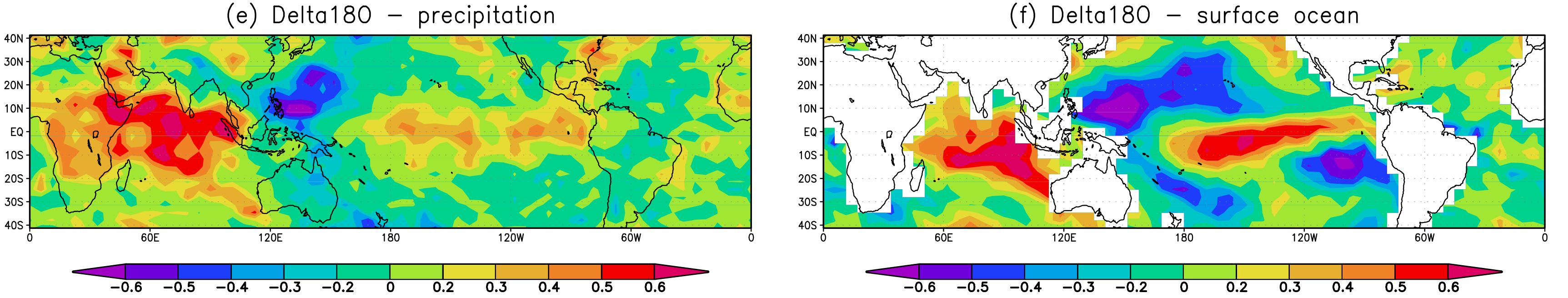

(e) Delta180 − precipitation

(f) Delta180 − surface ocean

Figure 5.3: EOF2 of annual average SST (a), MSLP (b), precipitation (c), evaporation (d), precipitation δ^{18}O (e) and surface ocean δ^{18}O (f).

Variable	SST	MSLP	P	E	$\delta^{18}O_p$	$\delta^{18}O_o$	SOI
SST	1.00						
MSLP	0.68	1.00					
P	0.68	0.90	1.00				
E	0.73	0.87	0.95	1.00			
$\delta^{18}O_p$	0.36	0.47	0.38	0.37	1.00		
$\delta^{18}O_o$	0.78	0.76	0.84	0.87	0.34	1.00	
SOI	0.76	0.83	0.91	0.89	0.33	0.86	1.00

Table 5.2: Magnitude of correlations between EOF1 of annual SST, MSLP, precipitation (P), evaporation (E), precipitation $\delta^{18}O$ ($\delta^{18}O_p$), surface ocean $\delta^{18}O$ ($\delta^{18}O_o$) and modelled SOI. All correlations are significant at 98% confidence level.

The second EOFs of each of the variables are shown in Figure 5.3. EOF2 of SST appears to consist of an ENSO-like pattern with a larger northward extent, possibly associated with ENSO-like decadal variability, as supported by spectral analysis of the amplitude of the EOF which shows the strongest period at 10 years. The cross-correlations (not shown) between EOF2 of SST and each of the other EOF2 timeseries are weak ($r < 0.2$) except for surface ocean $\delta^{18}O$ and no other EOF2 spectra shows a strong peak at 10 years, indicating that SST variability on this time scale does not produce a strong signal in the modelled climate.

The second EOFs of MSLP, precipitation, evaporation and precipitation $\delta^{18}O$ are strongly cross-correlated ($r > 0.5$) and are also strongly correlated with an index of interannual Asian monsoon variability (see next Section). It is suggested that the second EOFs of these variables may be interpreted as representing interannual monsoon variability, although the requirement of orthogonality with EOF1 (ENSO) will exclude the component of the variability due to ENSO–monsoon interaction. The isotopic response to the monsoon on seasonal and interannual time scales is discussed in the next Section.

5.3 Monsoon

The term “monsoon” describes the seasonal reversal of winds and strong seasonality of precipitation experienced over much of the tropics. Regional monsoons can be identified, including the Asian, Indian, African and Australian-

Indonesian monsoons, although there is interaction between these regional systems. As the monsoon dominates the seasonal precipitation cycle in these regions, it will strongly influence the isotopic signal in precipitation and the surface ocean over the tropics. The interannual variability of the monsoon will also produce a response in the isotopic record corresponding predominantly to changes in precipitation amount but also atmospheric circulation and moisture source region changes.

Seasonal and interannual monsoon signals have been identified in isotopic records from Tibetan ice cores and corals in the western Pacific and Indian Oceans. Such records promise to contribute to the reconstruction of monsoon variability over centuries in order to better understand the sensitivity of the monsoon system. Variation in monsoon strength is also believed to have occurred under glacial conditions, with the cooling of the Asian continent leading to a weakening of the Asian summer monsoon [eg. *Hoffmann and Heimann*, 1997] as explored in Chapter 6.

The seasonal climatology of the monsoon as simulated by the MUGCM is presented and the main components of the African, Australian-Indonesian, Asian and Indian monsoons described. The isotopic signal associated with the seasonal precipitation cycle is also outlined. The interannual variability of the monsoon reproduced in the 1950–1999 climate simulation is then discussed and compared with observed variability over the same period via indices of monsoon precipitation and circulation strength. The isotopic response to interannual monsoon variability is identified and compared with observational records.

5.3.1 Seasonal monsoon climatology

Examination of the seasonal climatology of the simulated monsoon is of interest in determining the extent to which the isotopic signal in monsoon regions can be expected to match the observed response. As the isotopic response in the tropics is closely related to the spatial and temporal representation of precipitation, the ability of the model to reproduce the observed monsoon is a basic precondition for a realistic isotopic distribution.

The MUGCM seasonal precipitation cycle associated with the monsoon was compared with observed precipitation from Xie and Arkin from 1979–2000 [*Xie and Arkin*, 1996]. The climatology of monsoon precipitation in the model was also compared with that simulated by other atmospheric models as described by *Gadgil and Sajani* [1998] for AMIP (1979–1988) model runs and by *Kang et al.* [2002a] as part of the CLIVAR GCM Monsoon Intercomparison Project.

The ability of atmospheric GCMs to represent the seasonal and interannual monsoon may depend on a number of factors. For example, *Kang et al.* [2002a] suggested that the use of the Arakawa-Schubert convection scheme improved the representation of monsoon precipitation. *Slingo et al.* [1994] also found that convective parameterisation influenced the representation of the monsoon. However *Gadgil and Sajani* [1998] compared 30 AMIP simulations with different GCMs and found no connection between convective parameterisation and monsoon simulation. Other possible causes for the variable representation of the monsoon in different models include horizontal resolution [*Sperber et al.*, 1994], the representation of orography [*Fennessy et al.*, 1994] and hydrological parameterisations [*Laval et al.*, 1996].

The observed and modelled precipitation for the peak austral summer monsoon (January–February, JF) and peak boreal summer monsoon (July–August, JA) was compared. The precipitation distributions are shown in Figure 5.4, and the simulated regional monsoons (African, Australian-Indonesian, Asian and Indian) are compared below with observations as described in *Gadgil and Sajani* [1998]. The isotopic responses to the regional precipitation cycle is also briefly discussed to provide a basis for later examination of interannual monsoon precipitation and isotopic variability.

African monsoon

The main observed precipitation band over Africa for JF is in the region 10°–20°S, and shifts northward to 0°–10°N in JA. The MUGCM is able to reproduce the observed meridional shift in the convergence zone as well as the amount of precipitation, as are most of the models in the *Gadgil and Sajani* [1998] study. The model shows some minima in the precipitation distribution over the east coast of the African continent which are not observed, a similar problem occurring in several other models discussed. In the MUGCM it appears that this is related to the underestimation of southern Indian Ocean precipitation in the austral summer.

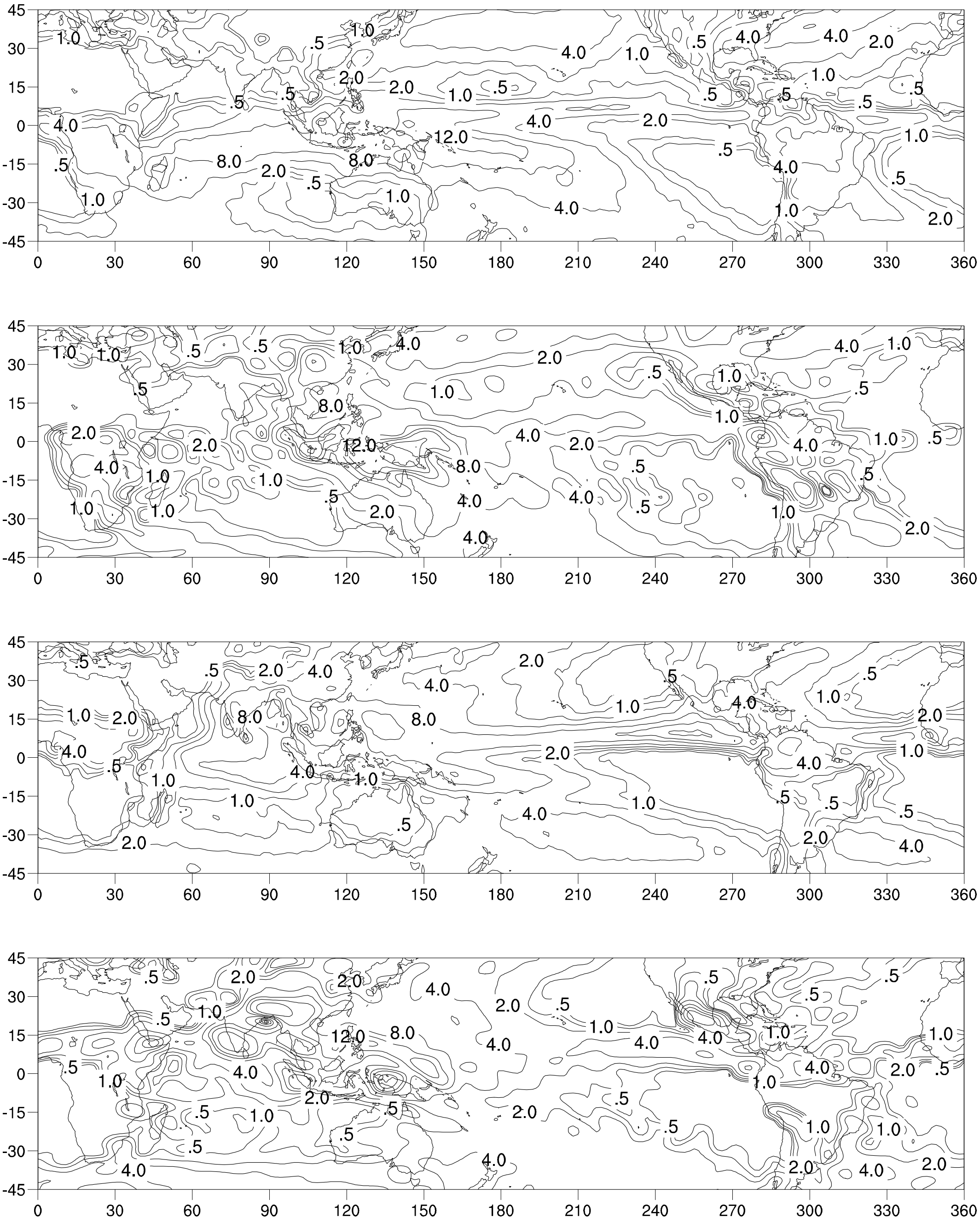

Figure 5.4: JF precipitation: observed (Xie and Arkin)(top) and modelled (upper middle), JA precipitation: observed (lower middle) and modelled (bottom). Contours are 1, 2, 4, 8, 12, 16 and 24 mm/day.

Australian-Indonesian monsoon

The observed summer monsoon over Australia and Indonesia consists of a rainband oriented south-east from the equator to northern Australia. During JA the convergence zone moves north of the equator. The MUGCM simulates the northward shift of the ITCZ correctly, and for the most part reproduces the observed amount of precipitation over northern and central Australia.

However the model greatly overestimates the amount of summer monsoon precipitation over Indonesia (Sumatra and Kalimantan) and Papua New Guinea due to rainout over topography in the model convection scheme. This excess precipitation is also observed in JA although of smaller magnitude than in JF. The models surveyed in *Gadgil and Sajani* [1998] generally have difficulties simulating precipitation over this region.

Asian monsoon

The main precipitation band of the Asian (or Asia-Pacific) monsoon is located over the equatorial ocean during the austral summer (JF), and then migrates northward over the Asian continent during the boreal summer (JA). The MUGCM captures this northward shift, which *Gadgil and Sajani* [1998] argue is the most important aspect of simulating the Asian monsoon.

However, like some other models which capture the meridional shift of the ITCZ, the precipitation distribution in the MUGCM does not closely match observations. There is an underestimation of precipitation over the Indian Ocean in JF and too much precipitation over the South China Sea and East Asia. The model generally lacks the observed zonal structure of tropical precipitation, with a weak ITCZ maximum in the central Pacific and Atlantic and the lack of a clear SPCZ.

The MUGCM can be loosely classified according to the scheme of *Kang et al.* [2002a] as one of those models which simulate more equatorial precipitation and less subtropical western Pacific precipitation than observed. The other class of models which they identify tend to overestimate the Indian monsoon and shift the subtropical western precipitation maximum to the north of the observed location.

Indian monsoon

The precipitation distribution over India is connected to that over the Asia-Pacific region, with the southern limit of the precipitation band extending over the equatorial region during JF and the majority of precipitation for the Indian subcontinent falling during JA. The precipitation consists of four main bands: a continental band, an oceanic band and two bands related to orographic lifting over the Himalayan and Ghat mountains.

The MUGCM captures the northward shift of the precipitation band but simulates too much precipitation over the Himalayas (and other nearby elevated areas such as Sumatra). The model also fails to simulate the oceanic band in JF or the northward extent of the continental band in JA.

Overall the MUGCM is able to simulate the main features of the seasonal monsoon precipitation distribution in the tropics as well as other state-of-the-art atmospheric models [*Gates et al.*, 1999]. The main limitation of the modelled precipitation distribution is the simulation of excessive precipitation over elevated topography. The seasonal migration of tropical convergence zones is well reproduced, which constitutes the crucial test for the simulation of seasonal monsoon precipitation by GCMs according to *Gadgil and Sajani* [1998].

5.3.2 Isotopic response to monsoon

The isotopic ratio in precipitation responds to the seasonal variation of precipitation amount associated with the monsoon in each region as shown in Figure 5.5. Over Africa, isotopic depletion is greatest to the south of the equator in JF and to the north in JA. Over Indonesia and northern Australia the southern summer monsoon produces strong isotopic depletion in JF which may be overestimated due to the excessive precipitation over Papua New Guinea. The northern summer monsoon produces isotopic depletion over Sumatra extending north into Asia in JA.

The meridional shift of the convergence zone produces isotopic depletion over Asia and India in the northern summer due to changes in moisture rainout over the continent. The northern extent of the monsoon is represented by the boundary between positive and negative JF–JA isotopic anomalies at around 30°N over central Asia.

Surface ocean isotopic ratios are also influenced by the seasonal variation of precipitation amount over the tropics, with large JF–JA isotopic differences in

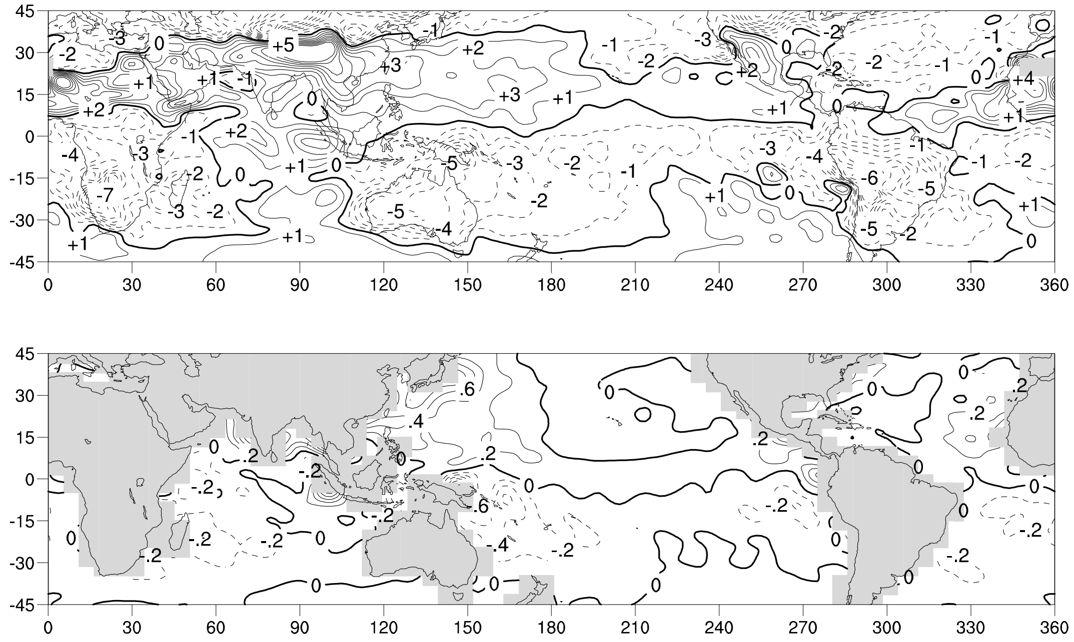

Figure 5.5: JF – JA modelled precipitation δ^{18}O (top) and surface ocean δ^{18}O (bottom). Contour intervals are 1‰ and 0.2‰.

the tropical Indian and western Pacific Oceans. In the Indian Ocean, the African monsoon is associated with depletion to the south in JF. The Indian monsoon produces isotopic depletion in the Arabian Sea and Bay of Bengal associated with the northern summer monsoon. The southern summer monsoon produces isotopic depletion in the western Pacific to the north of Australia.

5.3.3 Interannual monsoon variability

Interannual variability of the regional monsoons is an important component of interannual precipitation variability in the tropics [eg. *Sperber and Palmer*, 1996]. Interannual monsoon variability is not independent of other tropical modes of variability such as ENSO, but is known to interact selectively with ENSO so that many years of excess monsoon precipitation are associated with cold (La Niña) events, and vice versa [eg. *Webster and Yang*, 1992].

The interannual variability of the monsoon is also associated with changes in ocean and land surface temperatures and the strength of atmospheric circulation over the tropics. The ability of the MUGCM to simulate aspects of the interannual variability of the Indian and Asian monsoons is examined using two

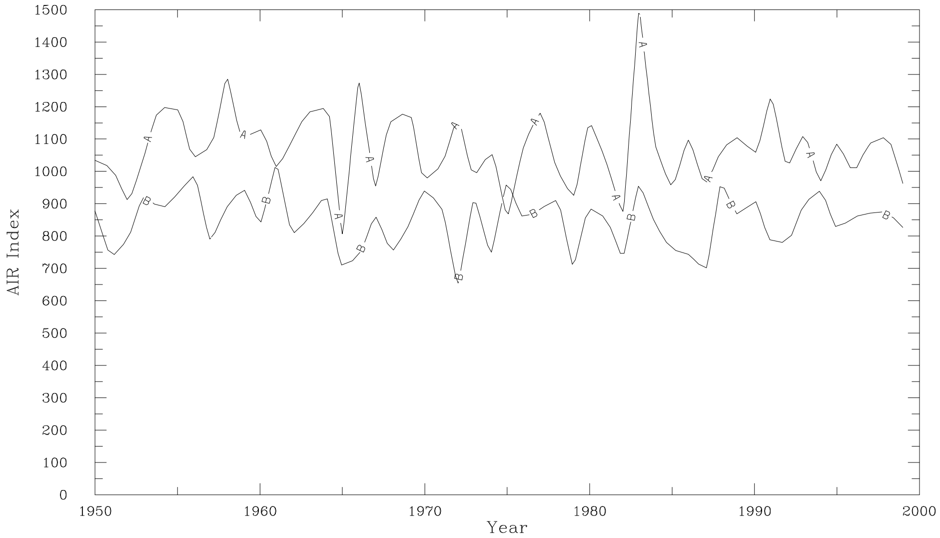

Figure 5.6: All India Rainfall index: modelled (A) and observed (B).

commonly employed indices of monsoon strength: the All India Rainfall (AIR) index and the zonal wind shear index of *Webster and Yang* [1992].

All India Rainfall index

One measure of the interannual variability of the monsoon is the AIR index. This index is the sum of precipitation over the Indian continent for June–September, reflecting the strength of the Indian monsoon [eg., *Wang and Fan*, 1999]. The modelled AIR index was calculated from the sum of all precipitation over land between 5°–30°N and 65°–90°E during June–September for each year of the simulation. This index was compared with the observed AIR index of *Parthasarathy et al.* [1994] available from the IGES database (grads.iges.org/india/allindia.html).

The observed and modelled AIR indices are shown in Figure 5.6. The correlation between the observed and modelled indices is only $r = +0.17$, indicating that the modelled interannual monsoon variability is not strongly forced by the imposed SSTs. *Sperber and Palmer* [1996] compare the modelled AIR indices from a range of models for 1979–1988 AMIP simulations and find that most models are unable to fully capture the interannual variability of monsoon precipitation over this period. For the decade 1979–1988, the MUGCM correctly reproduces the sign of the AIR index anomaly for seven out of ten years which is similar to other models. The MUGCM is able to reproduce the reduced Indian monsoon in 1982 and 1987 El Niño years but does not simulate the increased precipitation during the 1988 La Niña.

Previous studies [*Sperber and Palmer*, 1996; *Gadgil and Sajani*, 1998] have found that the ability to correctly reproduce the teleconnection between Pacific Ocean SSTs and Indian monsoon precipitation is central to the correct simulation of interannual monsoon variability. Global temporal correlations between annual SST and observed and modelled AIR indices (Figure 5.7) show that the MUGCM simulates the incorrect relationship between Pacific SSTs and Indian precipitation, with positive correlations in the equatorial eastern Pacific compared with negative observed correlations. This limitation is common to approximately half of the models examined in the study of *Sperber and Palmer* [1996].

The modelled AIR index was correlated with the modelled annual precipitation, precipitation δ^{18}O and surface ocean δ^{18}O as shown in Figure 5.8. Correlations with precipitation amount are generally low except locally over India. A significant negative precipitation δ^{18}O–AIR index correlation is seen over this region while a positive correlation over the tropical southern Indian Ocean is due to the amount effect. Surface ocean δ^{18}O is positively correlated with AIR over much of the Indian Ocean and north-western Pacific Ocean as well as the eastern equatorial Pacific where the (incorrect) positive SST–AIR index correlation occurs.

Zonal wind shear index

The zonal wind shear index of Webster and Yang [*Webster and Yang*, 1992] (WY index) is a measure of the Asia-Pacific monsoon and convective activity over the western Pacific as distinct from the AIR index which is a measure of the Indian monsoon [*Wang and Fan*, 1999]. The WY index was calculated for the model and compared with that calculated from NCEP reanalysis [*Kalnay et al.*, 1996] winds for the same period.

The WY index is the westerly wind shear anomaly between 850 hPa and 200 hPa pressure surfaces for May–August calculated over the area 0°–20°N, 40°–110°E:

$$\text{WY index} = U^*_{850} - U^*_{200} \tag{5.1}$$

where U^*_{850} and U^*_{200} are the anomalies of the 850 hPa and 200 hPa zonal

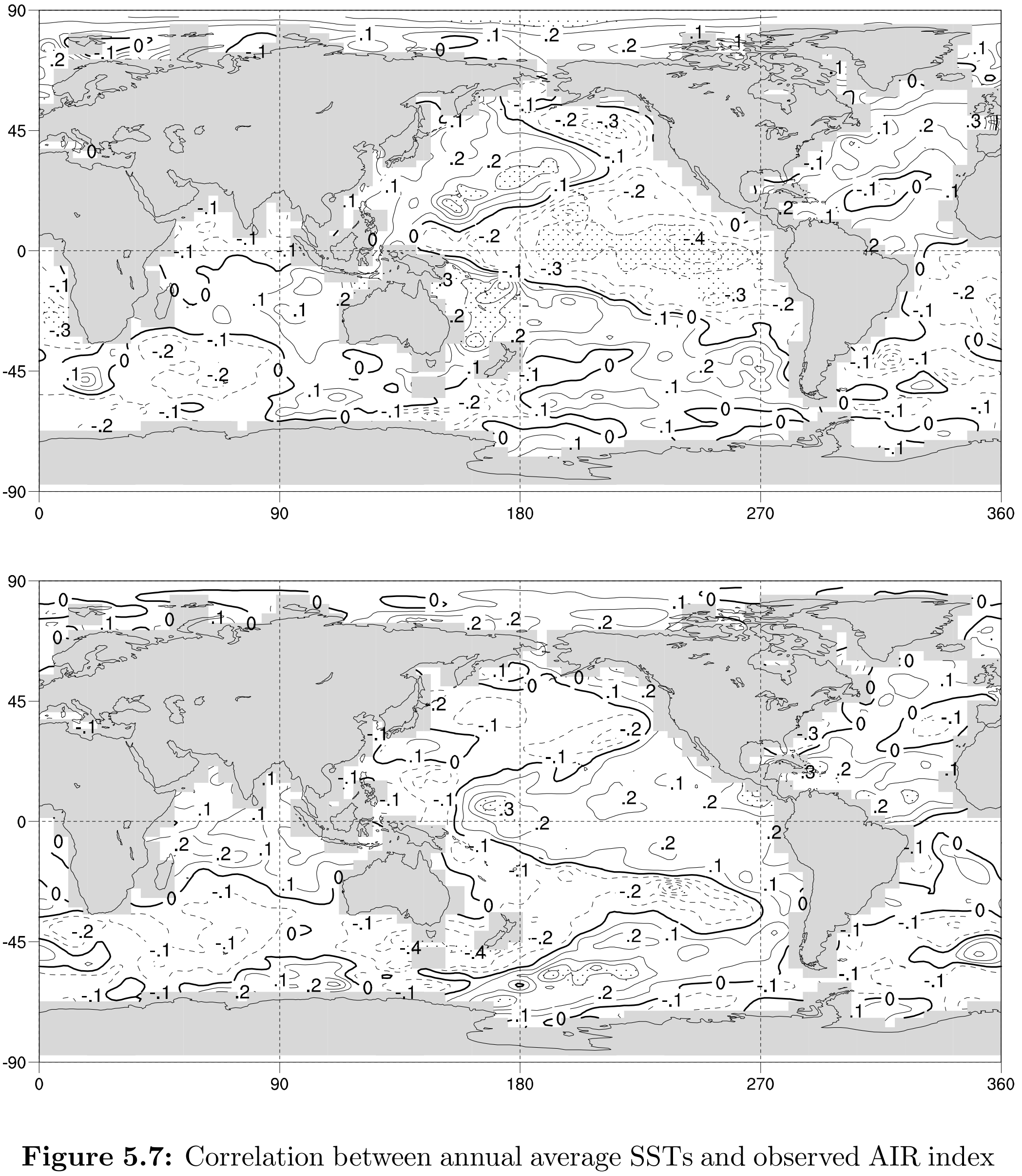

Figure 5.7: Correlation between annual average SSTs and observed AIR index (top) and modelled AIR index (bottom). Contour interval is 0.1. Stippled correlations are significant at 95% confidence level.

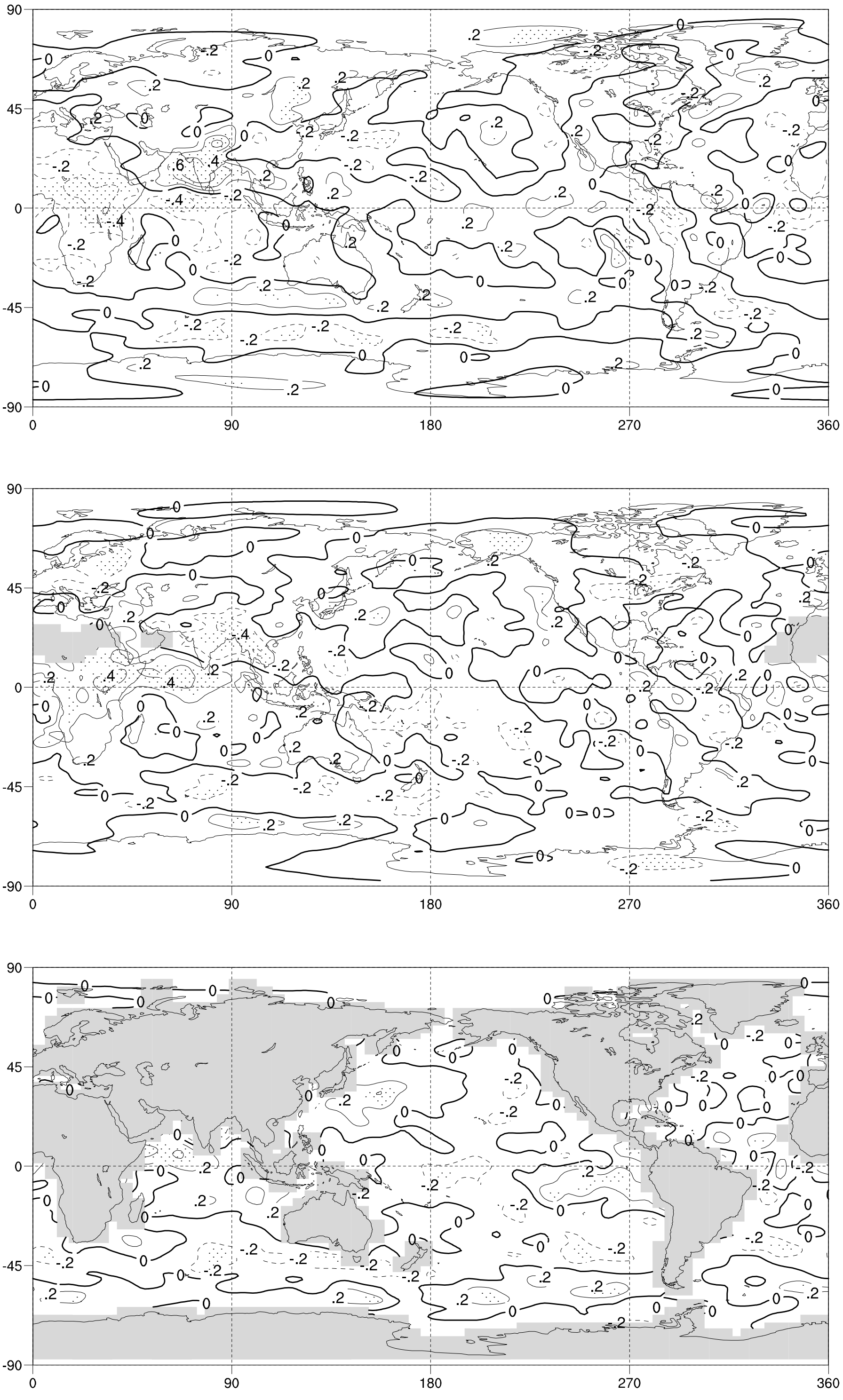

Figure 5.8: Correlation between AIR index and precipitation (top), precipitation δ^{18}O (middle) and surface ocean δ^{18}O (bottom). Contour interval is 0.2. Stippled correlations are significant at 95% confidence level.

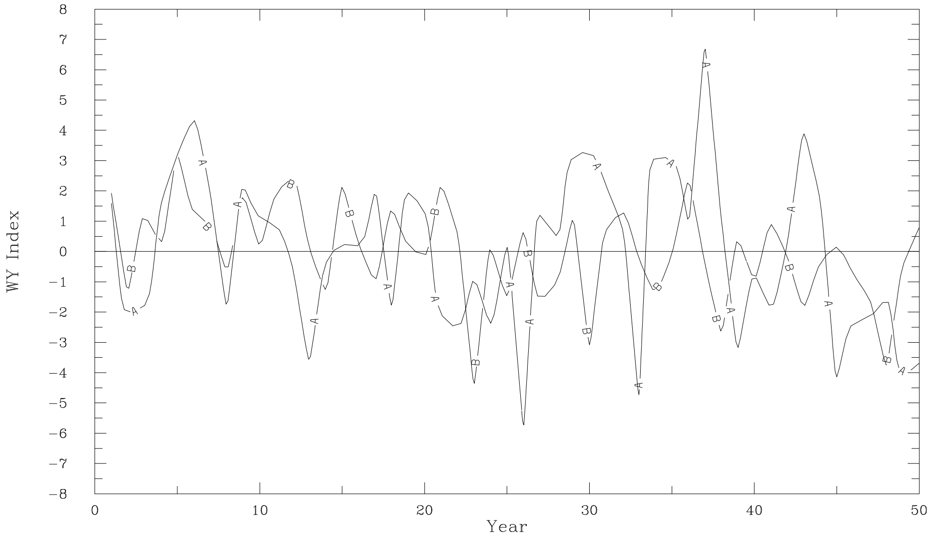

Figure 5.9: Zonal wind shear index: modelled (A) and observed (B).

winds. The WY index is significantly (at 99% confidence level) correlated with the AIR index for observations ($r = +0.44$) and for the modelled values ($r = +0.42$), indicating that the Indian monsoon precipitation and the wind shear over the Asia-Pacific region are physically related, and that the model is able to reproduce this relationship.

The modelled WY index and that calculated from NCEP winds are of the same order of magnitude, with the modelled index in the range −5.7 to +6.7 compared with the observed index in the range −3.5 to +2.5 (see Figure 5.9). The two series are not significantly correlated ($r = +0.02$) indicating that the modelled variability is not directly forced by SSTs, as for the AIR index, but instead represents internal atmospheric variability in the model.

The correlation between the modelled WY index and precipitation, precipitation δ^{18}O and surface ocean δ^{18}O is shown in Figure 5.10. The correlation between modelled WY index and modelled precipitation is strongest over the region of the index, with a negative correlation to the south-west in the summer monsoon moisture source region over the Indian Ocean. The precipitation δ^{18}O response differs from the AIR signal with only a weak negative correlation over continental East Asia and a stronger positive correlation over the Indian Ocean extending inland over much of India.

Significant positive correlations between the WY index and surface ocean δ^{18}O also exist over the tropical Indian Ocean. As for precipitation δ^{18}O, these appear to be a response to reduced precipitation over the Indian Ocean during

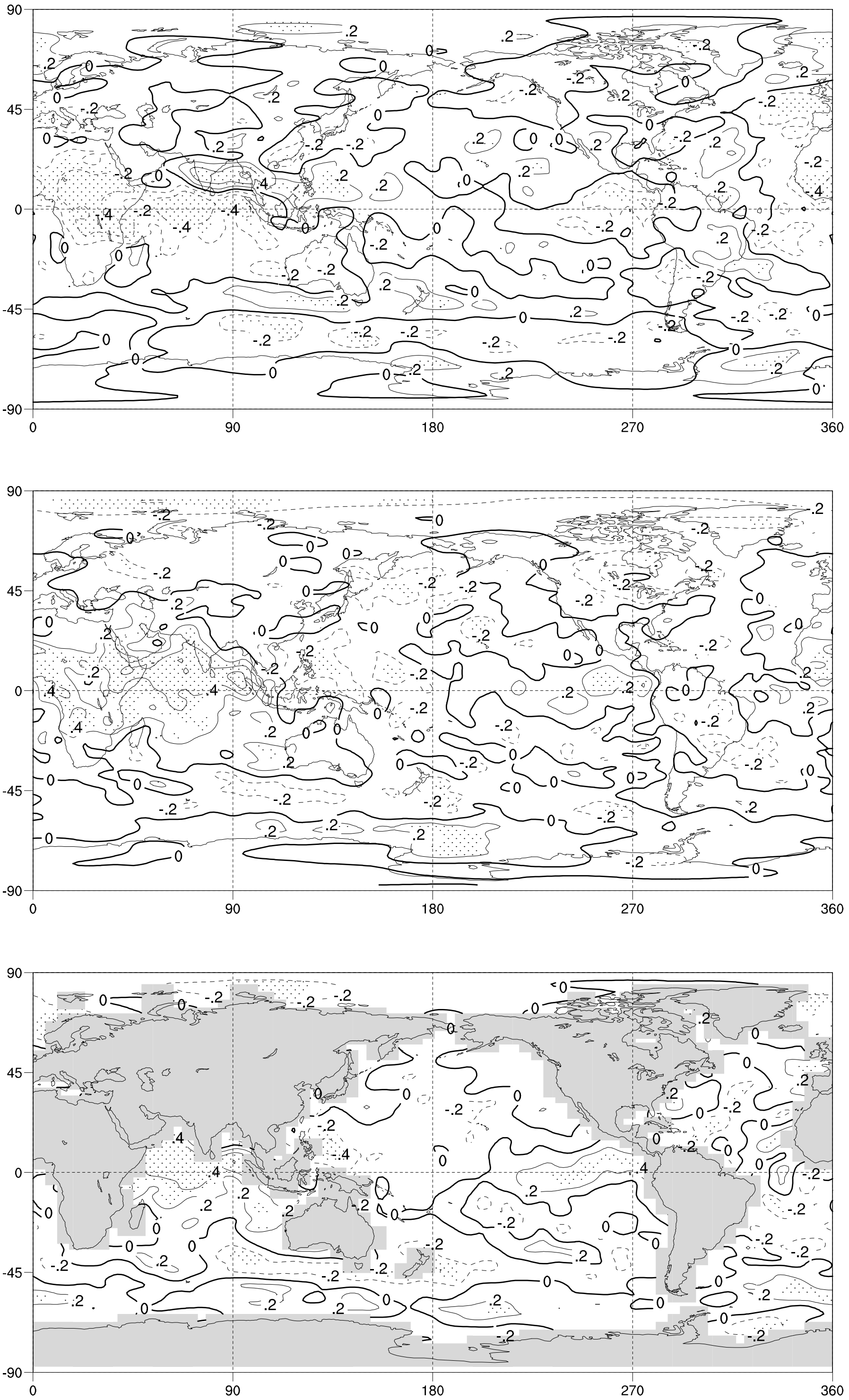

Figure 5.10: Correlation between zonal wind shear index and precipitation (top), precipitation δ^{18}O (middle) and surface ocean δ^{18}O (bottom). Contour interval is 0.2. Stippled correlations are significant at 95% confidence level.

years of stronger Asia-Pacific monsoon circulation. Significant negative correlations are seen for precipitation, precipitation δ^{18}O and surface ocean δ^{18}O in the equatorial eastern Pacific indicating that a weak teleconnection exists between eastern Pacific precipitation and monsoon circulation strength.

5.4 El Niño-Southern Oscillation

As discussed in Chapter 2, ENSO is the strongest mode of interannual variability in the tropical climate system, dominating observed interannual temperature, pressure and precipitation variability in the tropics. While ENSO is known to be driven by atmosphere-ocean interaction in the real climate system, the forcing of an atmospheric GCM with observed SSTs will produce pressure, surface temperature, circulation and precipitation anomalies which resemble the observed ENSO anomalies. The ability of the MUGCM to simulate the ENSO climate response is examined for the modelled 1950–1999 climate.

The strength of the correlation between modelled and observed ENSO phases represents the extent to which the modelled climate is driven by the imposed SSTs, as for the interannual monsoon variability discussed in the previous Section. As the model produces an ENSO-like atmospheric oscillation which is not entirely forced by the prescribed SSTs but resembles the physical ENSO mode, the sensitivity of isotopic ratios to ENSO is examined in relation to the modelled ENSO rather than the observed.

The isotopic response in tropical precipitation and the surface ocean is identified over the large scale and at individual locations in comparison with observations. The ENSO signal in high latitude precipitation δ^{18}O is also examined to determine whether the model reproduces the observed ENSO signal in Antarctic isotopic ratios. The ENSO signal in tropical ice cores and coral isotopic records is examined in Section 5.6.

5.4.1 Modelled ENSO

One method of comparison between the modelled and observed ENSO is via indices of ENSO strength such as the SOI and Nino SST anomaly indices. Recent studies have discussed the relative merits of different indices, and concluded that the Nino3.4 index (SST anomaly in the region 5°N–5°S, 190°E–240°E) is the most consistent measure of ENSO strength [*Trenberth*, 1997]. However the

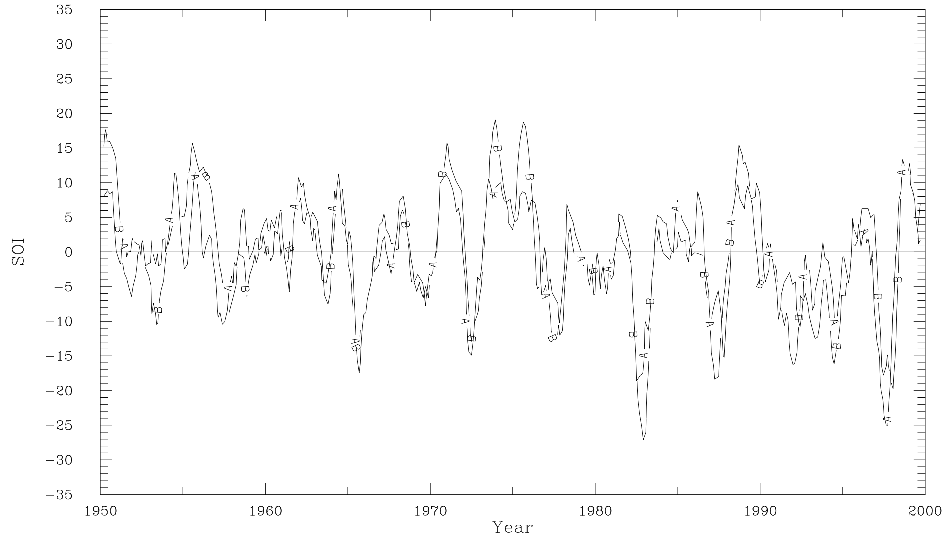

Figure 5.11: Modelled monthly SOI (A) and observed monthly SOI (B).

Nino SST index will be identical for model and observation as the SSTs are imposed boundary conditions, whereas the SOI measures the response of the modelled atmosphere to the SST forcing. For this reason, the SOI is used here to characterise the modelled ENSO response.

The Troup SOI [*Troup*, 1965] is the standardised anomaly of the MSLP difference between Tahiti and Darwin:

$$\mathrm{SOI} = 10 \times \frac{P_{diff} - <P_{diff}>}{\sigma_{Pdiff}} \tag{5.2}$$

where P_{diff} is the average Tahiti – Darwin MSLP difference for a given month, $<P_{diff}>$ is the long term average of P_{diff} for that month, and σ_{Pdiff} is the long term standard deviation of P_{diff} for the same month. In determining the modelled SOI, the location of Darwin and Tahiti was taken to correspond to the closest model grid points. The monthly SOI was calculated from the modelled MSLP and compared with the observed SOI available from the Australian Bureau of Meteorology (www.bom.gov.au) over the same period.

The correlation between the observed and modelled SOI timeseries shown in Figure 5.11 is $r = +0.46$ (significant at 99% confidence level), which increases to $r = +0.70$ after filtering using a six month window. These correlations are similar to those obtained by *Smith* [1995] using the CSIRO4 R21 atmospheric GCM ($r = +0.54$ to $+0.57$ and around $r = +0.7$ for five-month running mean values). The strength of the correlation indicates that although the model responds to

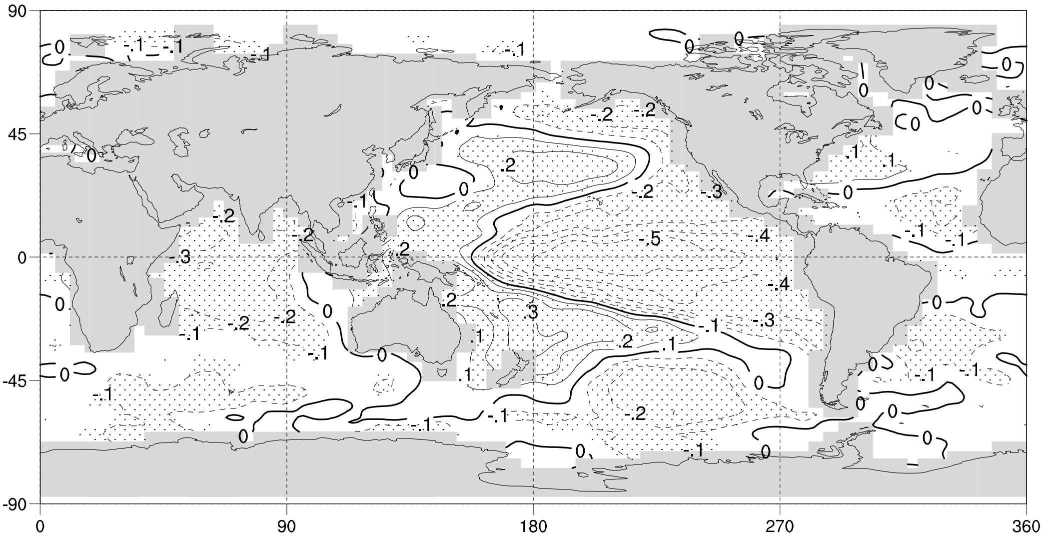

Figure 5.12: Correlation between monthly anomalies of GISST2.3b SSTs and modelled SOI. Contour interval is 0.1. Stippled correlations are significant at 95% confidence level.

the SST forcing to produce pressure anomalies resembling those observed during ENSO events, the atmospheric response is not strongly constrained by the forcing. In part this is because the ocean surface forcing does not respond to the atmosphere, as occurs in the real climate system.

In order to identify the modelled SST, MSLP and precipitation anomalies associated with typical El Niño and La Niña events, the monthly anomalies were correlated with the modelled SOI. The correlations with modelled pressure were compared with correlations between the observed NCEP MSLP and the observed SOI for 1949–2001, while the correlations with modelled precipitation were compared with correlations between observed Xie and Arkin precipitation and observed SOI for 1979–2000.

The correlation between monthly anomalies of the prescribed SSTs and the observed SOI is shown in Figure 5.12. The correlation pattern resembles the classical ENSO wedge-shaped SST anomaly in the eastern tropical Pacific, and is also similar to EOF1 of annual SSTs seen in Section 5.2. The observed and modelled MSLP–SOI correlations are shown in Figure 5.13. The modelled MSLP–SOI correlation strongly resembles the observed correlation, with a similar pressure dipole between the eastern and western Pacific. The negative correlations between the modelled fields do not extend into the tropical Atlantic Ocean as seen in the observed correlations. As expected, the correlation between the modelled fields resembles EOF1 of modelled annual MSLP.

The correlations between modelled and observed precipitation and SOI are shown in Figure 5.14. The observed precipitation covers a shorter time period (1979–2000) resulting in a noisier correlation pattern. The modelled El Niño precipitation maximum is located correctly in the western-central Pacific, but does not extend across the ITCZ to the eastern Pacific. The minimum in the western Pacific over Indonesia and Australia is also correctly located and extends to the SPCZ as observed. Over the tropical Atlantic the model does not simulate the increased precipitation during El Niño events seen in observations, which may related to the different pressure anomalies simulated in this region. Again, the spatial pattern of the correlation is similar to EOF1 of annual precipitation.

5.4.2 Tropical isotopic response to ENSO

The correlations between modelled and observed precipitation δ^{18}O and SOI are shown in Figure 5.15. The precipitation-weighted monthly δ^{18}O anomalies from all GNIP stations with more than 36 months of data are correlated with the observed monthly SOI values for the same months. The observed correlations are smoothed to provide an average value over regions with a high density of data as in Chapter 3.

The observed correlations between SOI and δ^{18}O values include positive correlations of up to +0.4 in the central equatorial Pacific and negative correlations over the Indonesian and western Pacific regions, as well as over northern and central Australia. Moderate correlations (± 0.1–0.2) are seen in parts of Europe, Africa and North America. However the main regions of spatially coherent correlations are found over the central and western Pacific, southeast Asia and tropical South America.

The modelled correlations are strongest over the central equatorial Pacific where the model reproduces a strong ENSO precipitation response, in agreement with the isotopic modelling studies of *Cole et al.* [1993b] and *Hoffmann and Heimann* [1998]. The observed negative correlations over the western tropical and subtropical Pacific are also reproduced by the model. Observed strong negative correlations over tropical South America are not seen in the model, as are strong positive correlations in the northern Pacific and Alaska. Significant

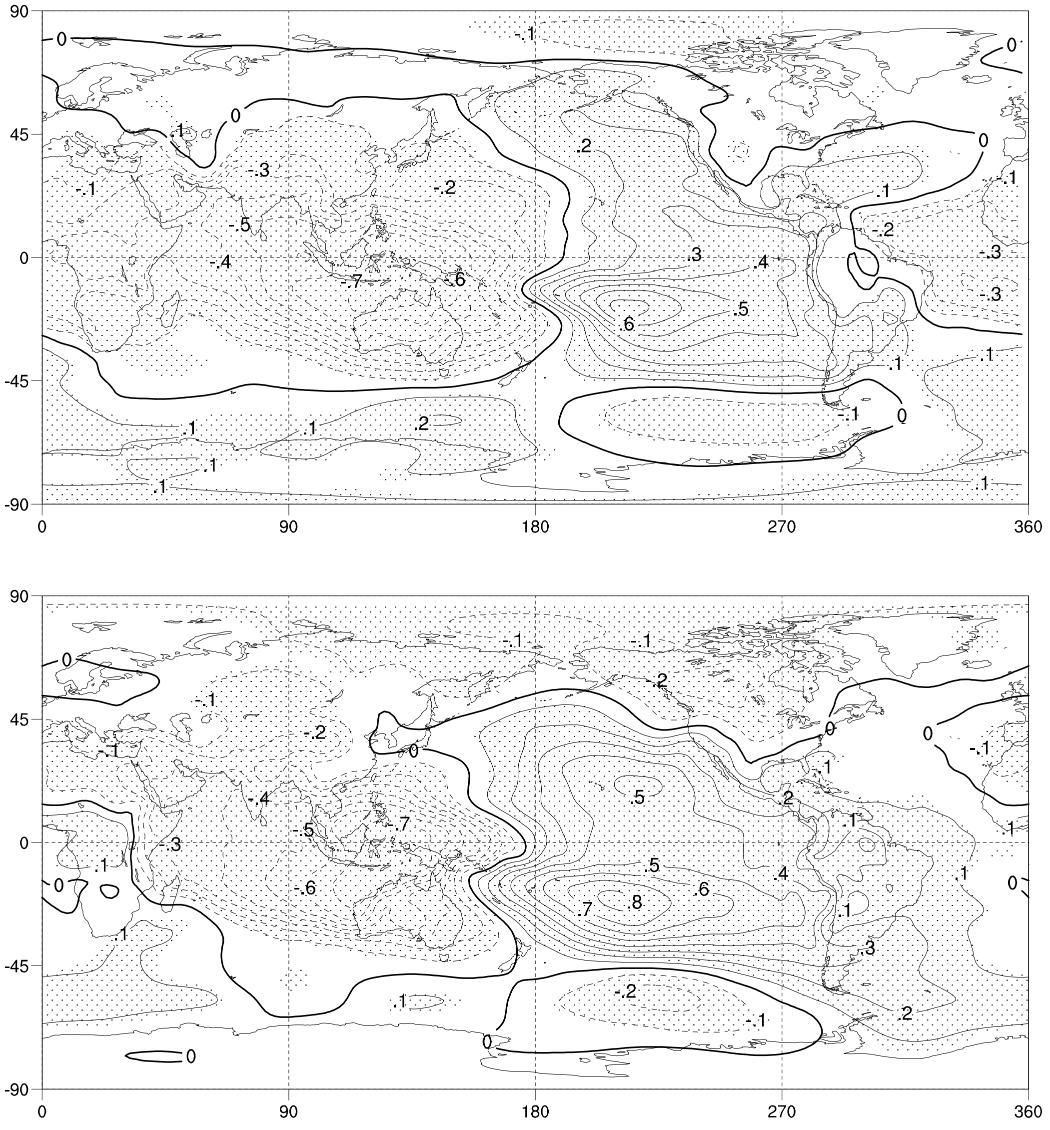

Figure 5.13: Correlation between monthly anomalies of observed (1949–2001) MSLP and SOI (top) and monthly anomalies of modelled (1950–1999) MSLP and SOI (bottom). Contour interval is 0.1. Stippled correlations are significant at 95% confidence level.

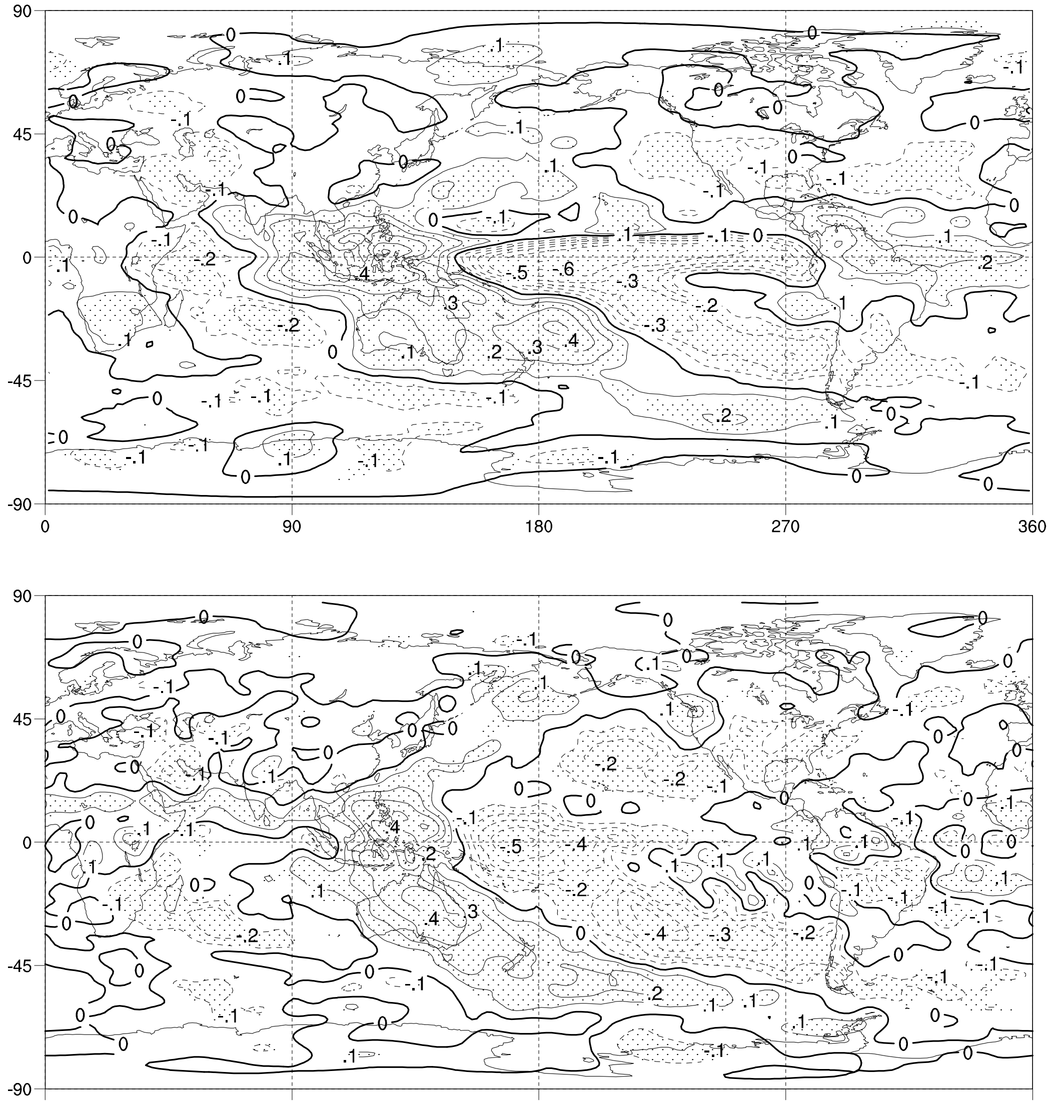

Figure 5.14: Correlation between monthly anomalies of observed (1979–2000) precipitation and SOI (top) and monthly anomalies of modelled (1950–1999) precipitation and SOI (bottom). Contour intervals is 0.1. Stippled correlations are significant at 95% confidence level.

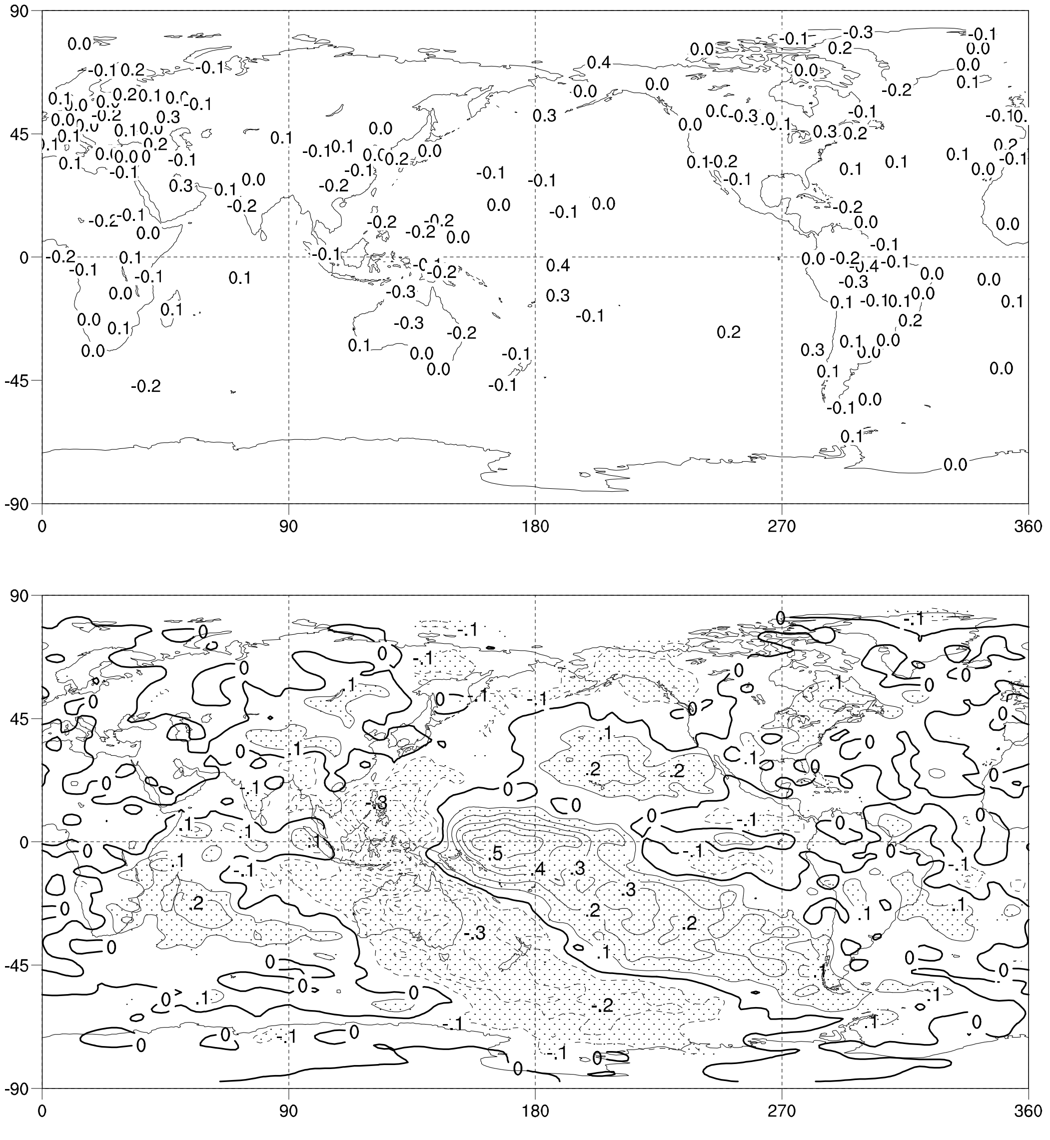

Figure 5.15: Correlation between monthly anomalies of observed (GNIP) precipitation δ^{18}O and SOI (top) and monthly anomalies of modelled precipitation δ^{18}O and SOI (bottom). Contour interval is 0.1 for latter. Stippled correlations are significant at 95% confidence level.

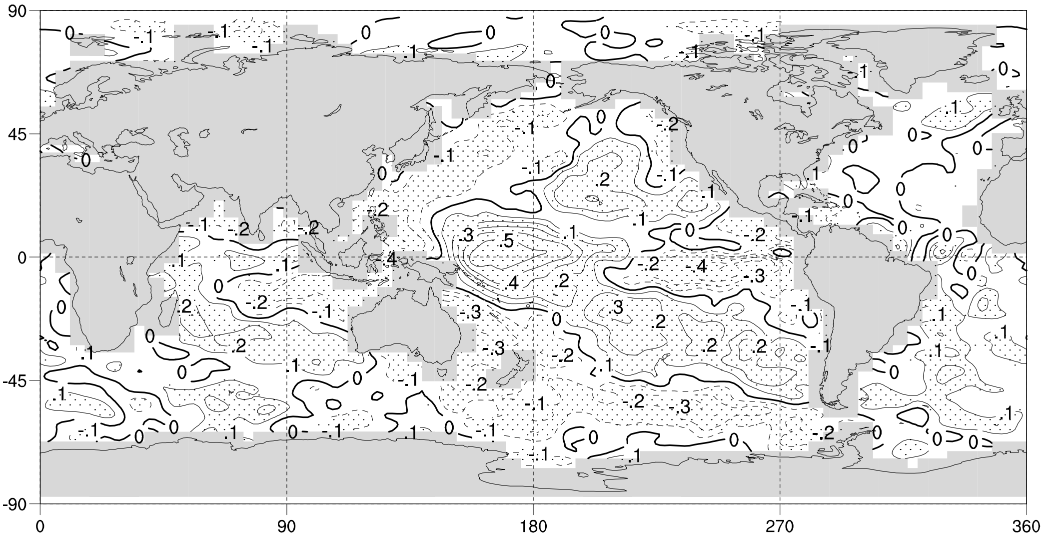

Figure 5.16: Correlation between monthly anomalies of modelled surface ocean δ^{18}O and SOI. Contour interval is 0.1. Stippled correlations are significant at 95% confidence level.

correlations extend via atmospheric teleconnections from the tropical central and western Pacific to high southern latitudes. While GNIP observations are limited in the Southern Hemisphere oceans, the Antarctic ENSO–isotope response is discussed briefly below.

The surface ocean δ^{18}O also responds to changes in precipitation and evaporation associated with ENSO. While monthly or annual surface ocean isotopic measurements are not generally available for comparison with the modelled signal, annually resolved coral records of local ocean δ^{18}O and SST variability will be compared with the model in Section 5.6. The modelled correlation between surface ocean δ^{18}O and SOI is shown in Figure 5.16.

The correlation between modelled δ^{18}O and SOI is strongly positive in the central Pacific in the region of enhanced precipitation during El Niño events, with positive correlations extending to the mid-latitudes in the eastern Pacific. Over the equatorial western Pacific and Indian Ocean negative correlations indicate the inverse precipitation–ENSO relationship. In the eastern Pacific Ocean, warmer SSTs during El Niño events lead to increased evaporation and relatively enriched surface ocean δ^{18}O values producing a strong negative correlation between ocean δ^{18}O and SOI in this region.

GNIP station	Length record	r(δ^{18}O, SOI)$_{obs}$	r(δ^{18}O, SOI)$_{mod}$
Darwin	1962–1998	−0.26	−0.18
Alice Springs	1962–1987	−0.27	−0.31
Apia Island	1962–1977	+0.28	+0.34
Canton Island	1962–1966	+0.41	+0.37
Manaus	1965–1990	−0.37	−0.01
Porto Velho	1965–1983	−0.29	−0.05

Table 5.3: Correlations between observed and modelled precipitation δ^{18}O and SOI at selected GNIP stations. All correlations are statistically significant at 99% confidence level except for Manaus and Porto Velho modelled values.

ENSO influences at individual GNIP stations

The ability of the model to simulate the observed interannual precipitation and isotopic variability due to ENSO was tested by comparison with records from several GNIP stations. Stations were chosen with relatively strong observed ENSO signals in the isotopic record as indicated by a correlation between GNIP δ^{18}O monthly anomalies and SOI of magnitude at least 0.3. The stations chosen were Darwin and Alice Springs, Australia; Apia and Canton Islands in the central Pacific and Manaus and Porto Velho in central Brazil.

The observed and modelled correlations for each location are listed in Table 5.3. The modelled correlations were calculated for the entire period of the simulation (1950–1999) whereas the observed correlations were calculated for variable periods given in the Table, which may limit the validity of direct comparison between the correlations.

At Darwin (12.4°S, 130.8°E) in northern Australia and Alice Springs (23.8°S, 133.9°E) in central Australia, precipitation is reduced during El Niño events [eg. *McBride and Nicholls*, 1983]. Rainout of moisture during transport from oceanic source regions will also be reduced for Alice Springs during El Niño. We therefore expect to observe corresponding positive anomalies in local precipitation δ^{18}O due to the amount effect. The model is able to reproduce the sign and magnitude of the observed negative correlations between precipitation δ^{18}O and SOI at these locations, due to the correct simulation of the precipitation response to ENSO in this region.

At Apia Island (13.8°S, 188.2°E) in the southern central Pacific and Canton Island (2.7°S, 188.2°E) in the central equatorial Pacific, El Niño events are associated with increased precipitation [eg. *Dai and Wigley*, 2000]. The modelled precipitation response to ENSO is strong in this region, and therefore the model reproduces the positive SOI–δ^{18}O correlation in the central Pacific.

At Manaus (3.12°S, 60.02°W) and Porto Velho (8.77°S, 63.92°W) in tropical central Brazil, precipitation is reduced during El Niño events [eg. *Bradley et al.*, 1987]. The model does not produce a strong ENSO precipitation response over tropical South America, and therefore does not simulate the observed relationship between precipitation δ^{18}O and SOI at these locations. The modelled response to ENSO over tropical South America is discussed further in Section 5.6 in relation to Andean ice core records.

5.4.3 ENSO signals in Antarctic isotopic ratios

Studies have shown that ENSO influences mass transport to the Antarctic continent [*Bromwich et al.*, 2000] as well as being associated with variability of sea ice extent [*Simmonds and Jacka*, 1995] and pressure, temperature and precipitation anomalies over regions of Antarctica [eg. *Smith and Stearns*, 1993; *Harangozo*, 2000]. The relationship between ENSO phases and Antarctic climate also appears to vary over time and to depend on interactions with other aspects of climate variability such as the Semiannual Oscillation [*Meehl*, 1991].

The presence of ENSO signals in precipitation δ^{18}O from Antarctica has been identified in observational records from Argentine Island on the western side of the Antarctic Peninsula [*Ichiyanagi et al.*, 2002]. ENSO variability has also been identified in the precipitation record over West Antarctica, including isotopic ratios in an ice core from Siple Dome [*Bromwich et al.*, 2000].

The physical mechanisms which produce high latitude ENSO–isotope signals are not predominantly local temperature or amount effects. Instead, isotope–ENSO relationships may involve a response to local changes in sea ice coverage, circulation, temperature and precipitation as well as the influence of changes upstream in mid-latitude moisture source regions.

The observed correlations between the SOI and monthly anomalies of δ^{18}O in Antarctic precipitation are relatively weak, as seen in Figure 5.15. Argentine Island (65.25°S, 64.27°W) GNIP station on the Antarctic Peninsula records a correlation of $r = +0.12$ between δ^{18}O and SOI from 1964–2001, while the correlation at Halley (75.5°S, 26.65°W) for 1965–1991 observations is $r = -0.04$. The shorter observational record at Rothera (67.57°S, 68.13°W) consists of only

18 months of data with a correlation between δ^{18}O and SOI of $r = -0.33$ (which is only significant at the 85% confidence level).

The modelled high latitude response to ENSO was investigated for Antarctica via correlations between SOI and annual surface temperature, precipitation amount, precipitation δ^{18}O and deuterium excess (Figure 5.17). Annual averages of the modelled fields and SOI were used rather than monthly anomalies in order to obtain a smoother signal, which is also more appropriately compared with the annual resolution of (high accumulation) ice core records.

The strongest correlations between SOI and δ^{18}O are seen over coastal East Antarctica, and inland towards the location of the Vostok drill site. *Werner and Heimann* [2002] identified the strongest correlation between modelled precipitation δ^{18}O and the Nino3 index for 1950–1994 in this region also, while they found that correlations for the period 1970–1994 were stronger and extended to the area west of the Antarctic Peninsula and Dronning Maud Land.

There is a strong SOI–δ^{18}O correlation in the Pacific sector to the north of Antarctica, associated with both precipitation (wetter during La Niña) and SST (cooler during La Niña) anomalies. However this does not produce a strong correlation over coastal West Antarctica. In general the modelled SOI–δ^{18}O correlations do not follow local surface temperature or precipitation ENSO signals, suggesting that factors such as increased rainout of source moisture, sea ice extent changes and circulation changes may be responsible for the ENSO signal in modelled δ^{18}O.

The modelled deuterium excess is also positively correlated with SOI in the Pacific and Atlantic sectors and negatively correlated in the Indian Ocean sector. The strongest positive correlations are seen over inland East Antarctica. Positive correlations between deuterium excess and SOI indicate that cool (warm) ENSO events lead to either an increase (decrease) in SST or decrease (increase) in relative humidity over the source region, assuming kinetic effects during condensation processes are unchanged.

5.5 Decadal variability and long term trends

The strongest modes of interannual tropical climate variability, ENSO and monsoon variability, have been identified in isotopic records and in the modelled isotopic distribution. While these components of climate variability will dominate the observed and modelled tropical isotopic record, decadal and longer

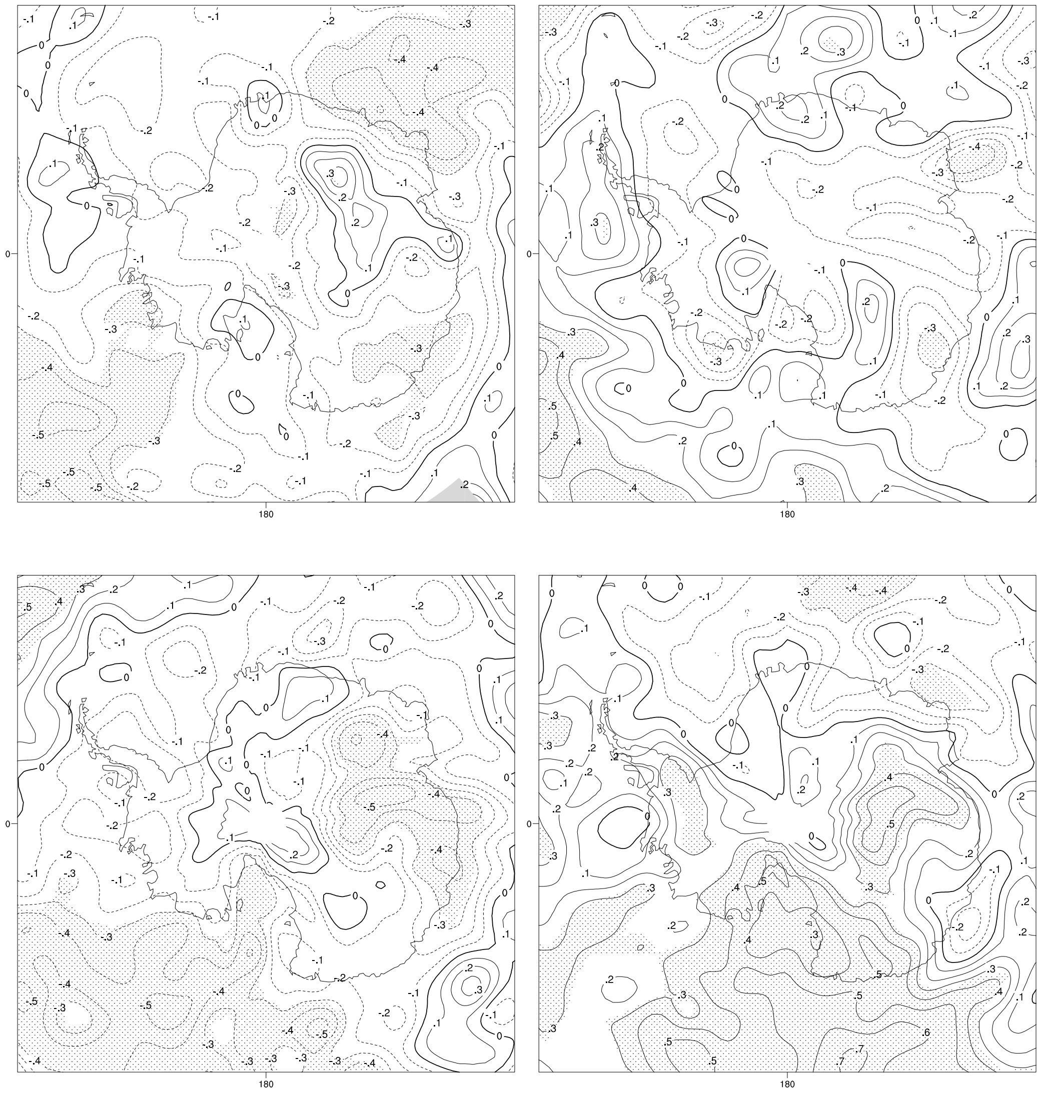

Figure 5.17: Correlation between SOI and modelled annual surface temperature (top left), precipitation (top right), precipitation $\delta^{18}O$ (bottom left) and deuterium excess (bottom right) in the Antarctic region. Contour interval is 0.1. Stippled correlations are significant at 95% confidence level.

term variability may also influence isotopic ratios in precipitation and the surface ocean. As discussed in Chapter 2, marine and continental isotopic records may be used to extend limited observational records of tropical climate in order to investigate decadal climate variability, linear warming trends and other low frequency components of climate variability. The modelled decadal variability and linear trends over the period 1950–1999 are examined below.

5.5.1 Tropical decadal variability

Tropical climate variability includes decadal variability of the monsoon, as discussed in Chapter 2. Here, decadal variability is examined in relation to an observed decadal tropical mode, the PDO. The PDO is an ENSO-like interdecadal mode in SST and pressure [*Zhang et al.*, 1997] which is defined as the leading EOF of mean November to March SST anomalies for the Pacific Ocean north of 20°N [*Mantua et al.*, 1997]. The observed PDO index for 1950–2000 was obtained from the JISAO database (www.tao.atmos.washington.edu) and annual averages of the index were calculated.

The PDO index was correlated with annual average modelled precipitation and observed Xie and Arkin precipitation, as shown in Figure 5.18. The observed precipitation–PDO correlation shows a wedge shaped ENSO-like pattern, as does the modelled correlation. The modelled distribution has larger values in the subtropics and in the northern Pacific than the ENSO precipitation correlation, as expected for the PDO. The modelled precipitation is also strongly correlated with the PDO over the Asian monsoon region, suggesting that decadal variability over the Pacific interacts with the monsoon in the model, whereas such a correlation is not seen in the observed distribution.

The correlation between the PDO index and modelled δ^{18}O is shown in Figure 5.19, while the equivalent correlation was not calculated for the observed GNIP δ^{18}O values as few GNIP station records are longer than a decade. The modelled isotopic response to the PDO is dominated by the amount effect in the tropics, with negative correlations in the tropical Pacific corresponding to increased precipitation during positive PDO phases. A region of strong negative correlation is also seen over the Asian monsoon region corresponding to the modelled precipitation anomaly in this region.

Surface ocean δ^{18}O follows the precipitation δ^{18}O response to increased precipitation over the tropical Pacific, producing negative correlations over the

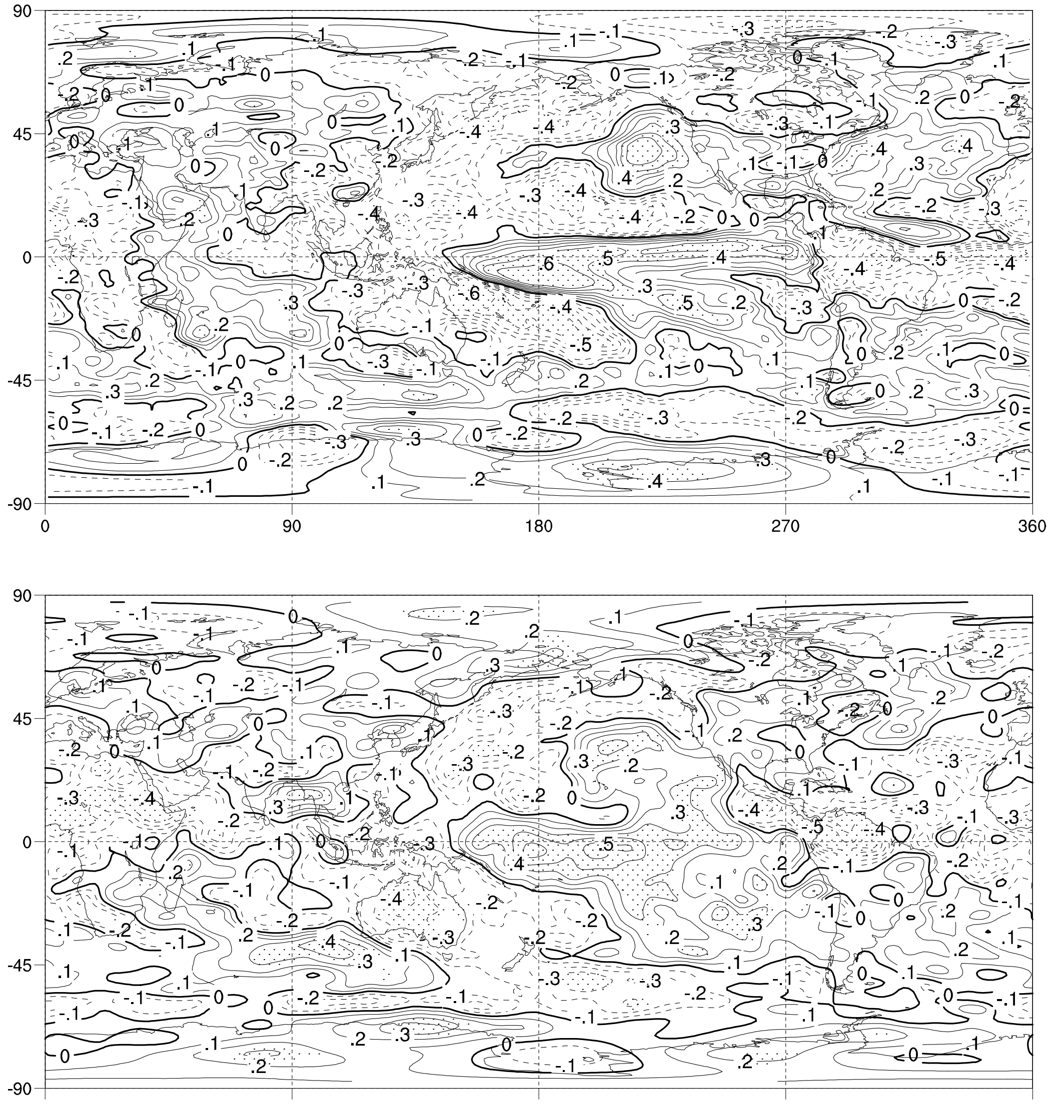

Figure 5.18: Correlation between PDO index and annual average observed precipitation (top) and modelled precipitation (bottom). Contour interval is 0.1. Stippled correlations are significant at 95% confidence level.

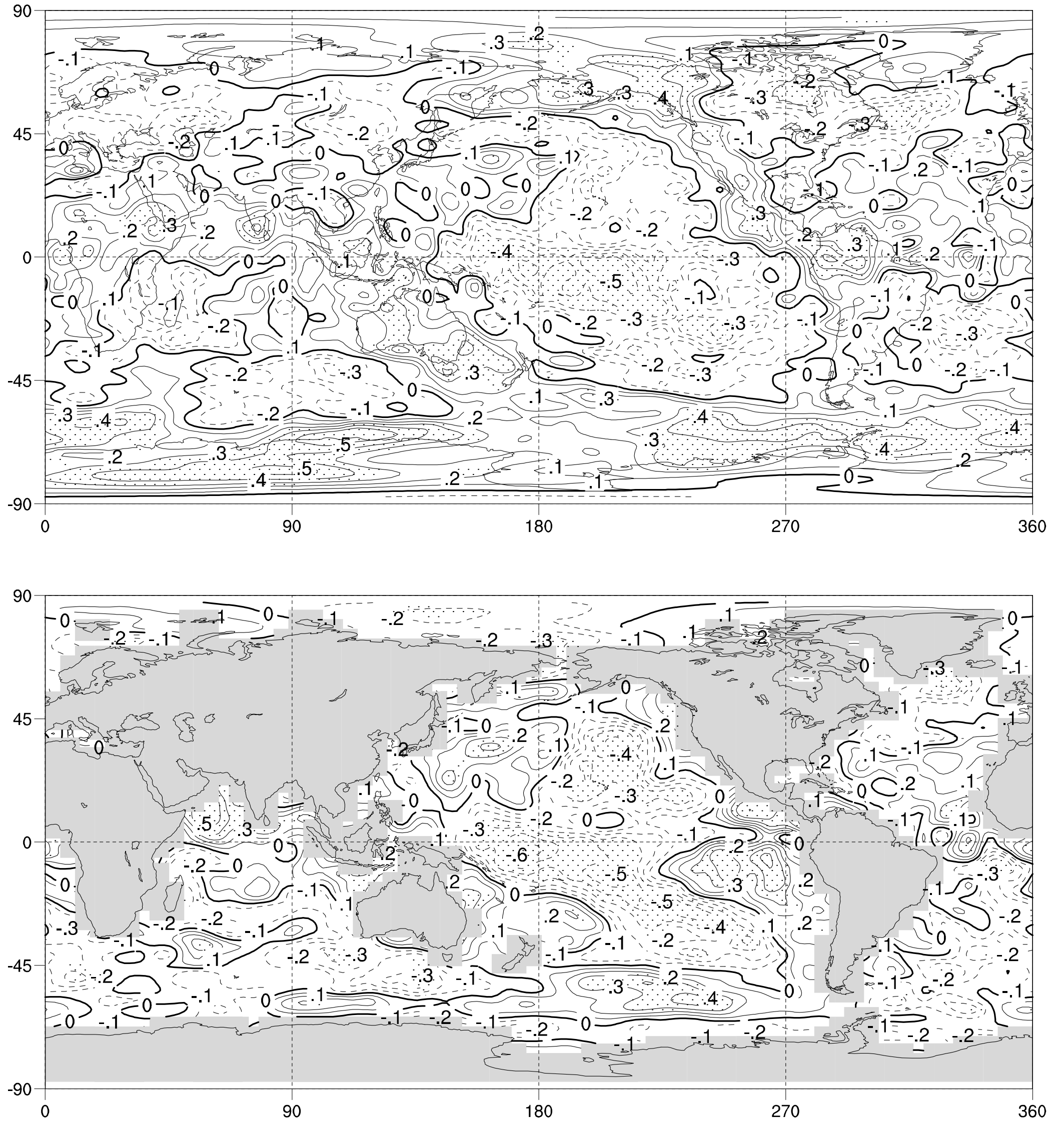

Figure 5.19: Correlation between PDO index and annual average modelled precipitation δ^{18}O (top) and modelled surface ocean δ^{18}O (bottom). Contour interval is 0.1. Stippled correlations are significant at 95% confidence level.

tropical western Pacific and eastern mid-latitudes. In the eastern equatorial Pacific, the evaporation response to the PDO SST anomalies leads to positive correlations between surface ocean δ^{18}O and the PDO index.

5.5.2 Fifty-year trends

The linear trends in annual average GISST2.3b SSTs and modelled precipitation are shown in Figure 5.20. The SST trend appears to consist of both a mean warming over much of the ocean and a trend to more El Niño-like conditions over the model simulation period, as discussed by *Hurrell and Trenberth* [1999]. An increase in precipitation is seen over the central Pacific, southern Africa and East Asia, while precipitation is reduced over the western Pacific and tropical South America. This response differs from the linear trend in annual observed precipitation over 1900–1988 identified by *Dai et al.* [1997]. They identified precipitation increases over North America, Eurasia and Australia using EOF analysis of land surface observations.

The precipitation δ^{18}O and surface ocean δ^{18}O trends are shown in Figure 5.21, while the trend in observed GNIP precipitation δ^{18}O is not calculated due to the short and discontinuous nature of the majority of the GNIP records. Precipitation δ^{18}O responds primarily to precipitation amount changes over the tropics, with depletion over most of the tropical ocean and enrichment over southern Africa, tropical South America and East Asia, consistent with observed isotopic enrichment in Andean ice cores over the late twentieth century. The precipitation isotopic response is also consistent with more El Niño-like conditions. A strong isotopic enrichment is seen at high latitudes in response to the enhanced warming in these regions.

The surface ocean δ^{18}O signal largely follows precipitation changes in the central and western Pacific, with the largest response in the region of increased precipitation in the central Pacific. Enhanced signals are seen where precipitation is reduced and evaporation increased with warmer SSTs, such as in the tropical eastern Pacific and to the north of Papua New Guinea in the western Pacific Warm Pool. The increased depletion of surface ocean δ^{18}O in regions of increased precipitation is likely to enhance isotopic enrichment in coral and foraminifera due to SST warming.

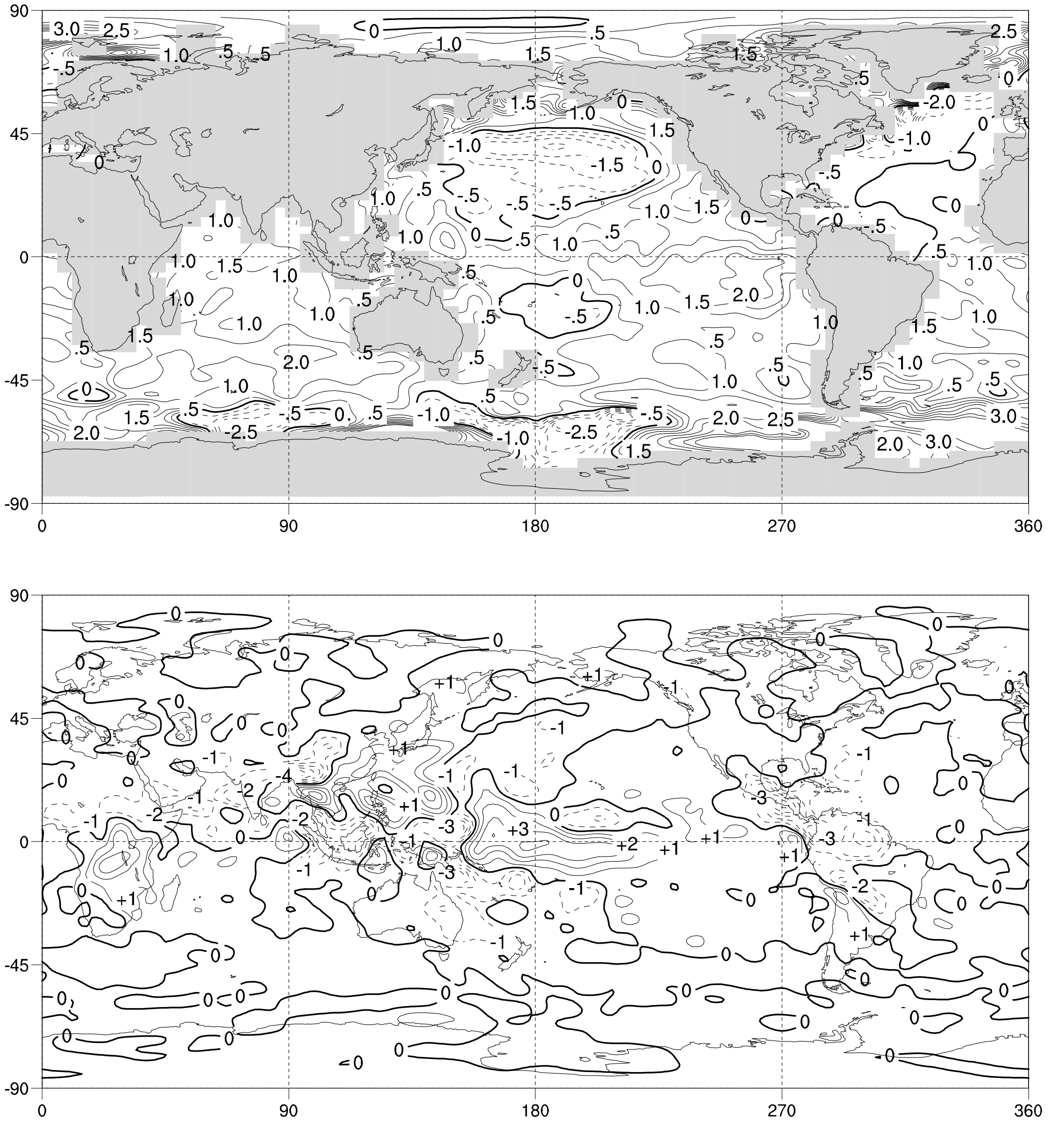

Figure 5.20: 1950–1999 trend of annual SST (top) (°C per year × 100) and modelled precipitation (bottom) (mm/day per year × 100). Contour intervals are 0.5°C and 1 mm/day respectively.

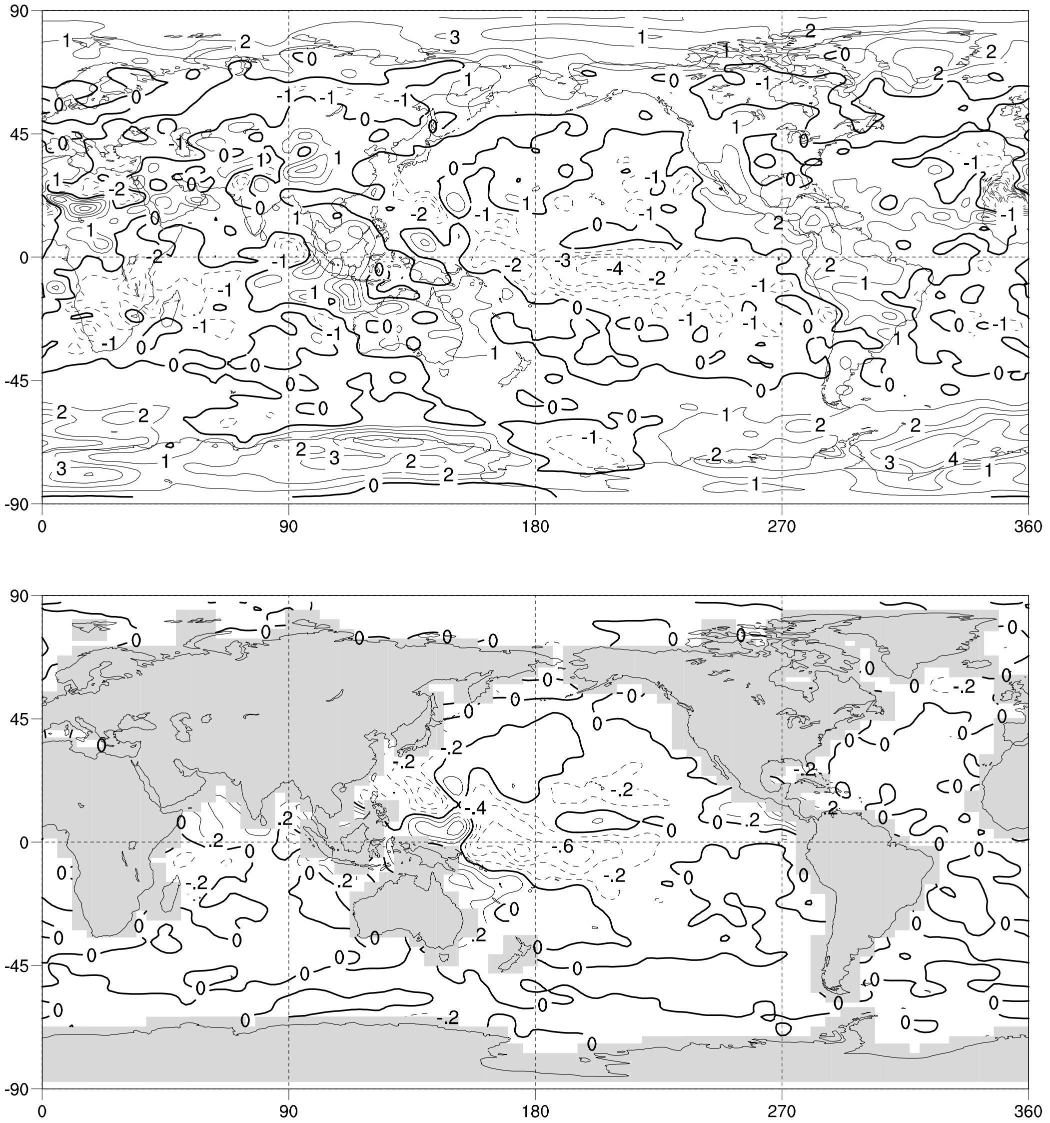

Figure 5.21: 1950–1999 trend of modelled annual precipitation δ^{18}O (top) (‰ per year × 100) and surface ocean δ^{18}O (bottom) (‰ per year × 100). Contour intervals are 1‰ and 0.2‰ respectively.

5.6 Comparison with ice core and coral records

5.6.1 Tropical ice core records: Andes

As outlined in Chapter 2, a number of tropical ice core δ^{18}O records have been retrieved from the tropical Andes with annual resolution covering the last century. Two of these, Huascaran and Quelccaya in Peru, are available from the NGDC database (www.ngdc.noaa.gov/paleo). Two cores from Huascaran [*Thompson et al.*, 1995] cover the modelled period until 1992 and 1993 respectively. A single high resolution record from Quelccaya [*Thompson et al.*, 1984, 1985] extends into the modelled period until 1984.

Previous observational and modelling studies of seasonal and interannual variability of isotopic ratios in precipitation over the Andes were outlined in Chapter 2. We compare the modelled seasonal and interannual precipitation δ^{18}O signal over the ice core sites with the observed ice core isotopic records. We also compare the δ^{18}O variability simulated by the MUGCM with the results of *Vuille et al.* [2003a, b] using the ECHAM and GISS models, and assess the ability of the MUGCM to reproduce the observed seasonal and interannual relationships between temperature, precipitation and δ^{18}O at the Andean ice core sites.

The modelled precipitation δ^{18}O values are interpolated using cubic interpolation to the locations of the ice core sites. While *Vuille et al.* [2003a] calculate average δ^{18}O values within a specified radius, the use of interpolation produces a similar result. Direct comparison between the interpolated model δ^{18}O values and δ^{18}O within individual ice cores is limited as the model does not fully resolve the steep localised topography of the Andes. However such a comparison provides the basis for an assessment of the regional controls on the isotopic signal.

Seasonal controls on δ^{18}O

The relationship between precipitation δ^{18}O and temperature and precipitation is compared on seasonal time scales. The modelled δ^{18}O values at both sites are much less depleted than the observed ice core values due to the lower model topography (1488 m at Huascaran compared with the real elevation of 6050 m; 2757 m at Quelccaya compared with the real elevation of 5670 m). The mean modelled δ^{18}O at Huascaran is $-6.0‰$, compared with the mean ice core values of −17.2‰ and −17.3‰. At Quelccaya the mean modelled δ^{18}O is −7.6‰ while the mean ice core δ^{18}O is −17.5‰.

The seasonal cycles of modelled surface temperature, precipitation and precipitation δ^{18}O for the Huascaran and Quelccaya sites using monthly averages from the 1950–1999 simulation are shown in Figure 5.22. The modelled seasonal cycles at the two sites are very similar, although the higher elevation of Quelccaya than Huascaran in the model results in cooler surface temperatures. The modelled seasonal δ^{18}O cycle corresponds to the seasonal cycle of precipitation amount, leading to a negative correlation with temperature as most of the precipitation falls in the warmer summer months. The modelled seasonal δ^{18}O–climate relationships are in agreement with the results of *Vuille et al.* [2003a] who also simulated a positive correlation with local precipitation amount and negative correlation with temperature at the Andean ice core sites.

Interannual controls on δ^{18}O

The modelled annual average δ^{18}O values at the ice core sites are compared with local temperature and precipitation, as well as the net precipitation minus evaporation averaged over the Amazon basin (0–10°S, 280–325°E). Correlations with the Nino3.4 index of ENSO activity are calculated to allow comparison with the correlations of *Vuille et al.* [2003a] for the ECHAM and GISS models. As described in Section 5.4, the Nino3.4 index is the SST anomaly calculated over the region 5°N–5°S, 190°E–240°E. The modelled precipitation δ^{18}O at the ice core sites is also correlated with the observed ice core δ^{18}O values for the corresponding years for the two Huascaran records and single Quelccaya record. The correlations are given in Table 5.4.

The model reproduces the observed positive correlation of Andean δ^{18}O with local temperature, and negative correlation with local precipitation, although only the correlation between modelled δ^{18}O and local precipitation at Quelccaya is significant at the 95% confidence level. The strongest correlations for both sites are with average precipitation minus evaporation over the Amazon basin, indicating that the model reproduces the observed relationship between Andean ice core δ^{18}O and rainout over the Amazon described in Chapter 2.

The correlations between modelled precipitation δ^{18}O and ice core δ^{18}O at both sites are small and not statistically significant, compared with correlations of +0.49 for ECHAM and +0.65 for the GISS model for the Huascaran record (correlations are not given for Quelccaya) [*Vuille et al.*, 2003a]. The inability of

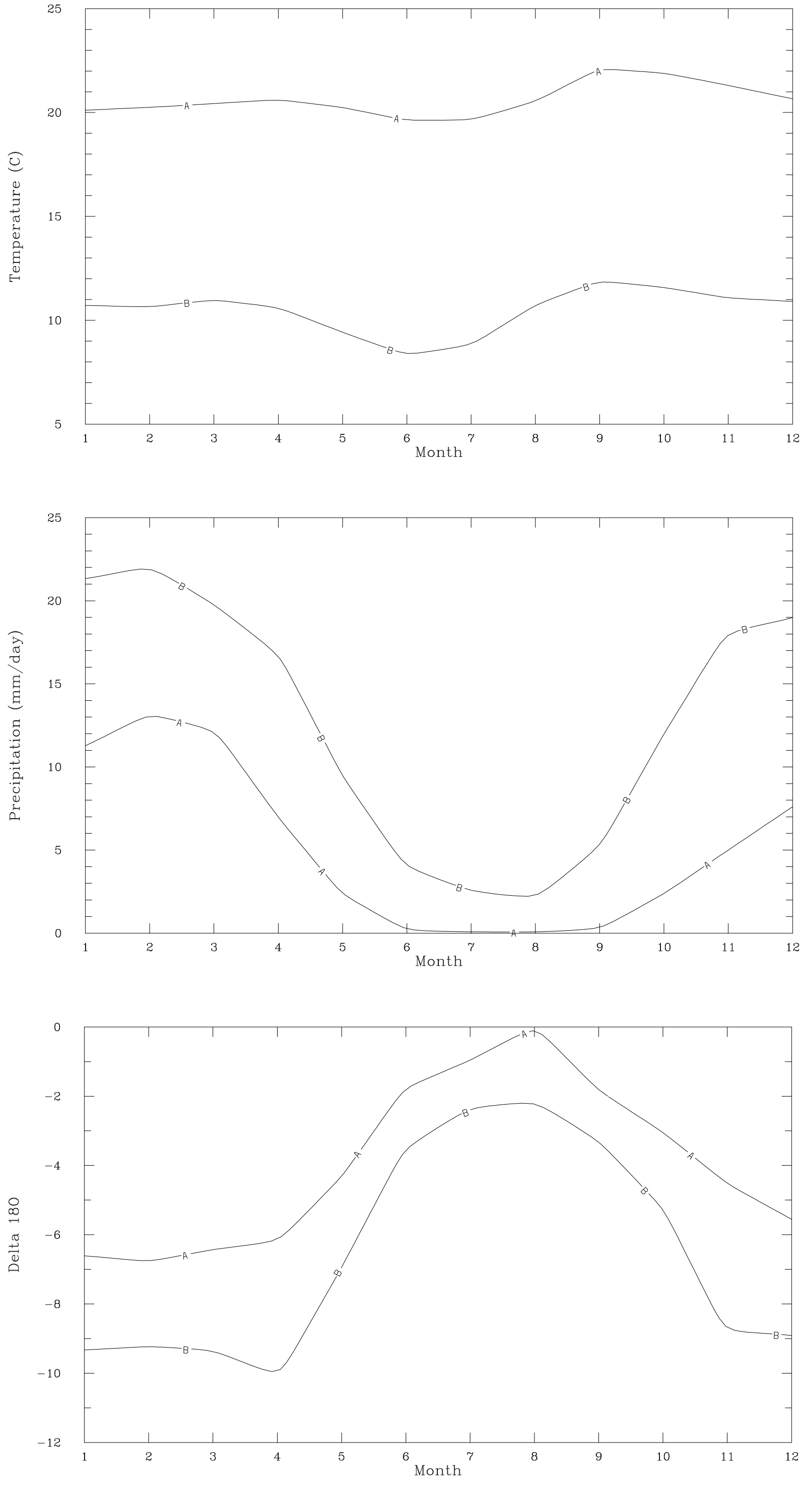

Figure 5.22: Huascaran (A) and Quelccaya (B) modelled seasonal cycles of surface temperature (top), precipitation (middle), and precipitation δ^{18}O (bottom).

Location	**Local T**	**Local P**	**Amazon P–E**	**Nino3.4**	**Ice core δ^{18}O**
Huascaran	+0.21	−0.19	−0.49*	+0.11	−0.09, 0.00
Quelccaya	+0.25	−0.51*	−0.52*	−0.02	+0.16

Table 5.4: Correlations between annual modelled δ^{18}O and local temperature (T), precipitation (P), Amazon precipitation minus evaporation, Nino3.4 and observed ice core δ^{18}O at Huascaran and Quelccaya core sites. Values marked * are significant correlations at 95% confidence level.

the MUGCM to simulate the observed interannual variability of precipitation δ^{18}O over the ice core sites appears to be due to the weak ENSO response in modelled precipitation over tropical South America, as identified in Section 5.4 for GNIP stations in Brazil. The correlation between modelled δ^{18}O and the Nino3.4 index is weak, whereas the ECHAM and GISS models simulate larger positive correlations.

The modelled surface temperature, precipitation and δ^{18}O response to ENSO over South America is illustrated in Figure 5.23, again using correlations with the Nino3.4 index to facilitate comparison with the results of *Vuille et al.* [2003a, b]. The model simulates the observed positive correlation between temperature and Nino3.4 over tropical South America, and the observed negative correlation between Amazon precipitation and Nino3.4. However the Amazon precipitation response to ENSO is relatively weak, while the model simulates a negative correlation locally over the Andes. As a result, the local relationship between δ^{18}O and Nino3.4 over the Andes consists of regions of weak positive and negative correlations.

The limitations of the modelled precipitation and isotopic response to ENSO are likely to be related to the lower Andean topography in the MUGCM compared to the ECHAM and GISS models. As *Valdes* [2000] comments, the resolution of Andean topography in climate models limits the simulation of atmospheric blocking and the relative contribution of Pacific and Atlantic moisture sources to Andean precipitation. While the ability of the MUGCM to reproduce the observed interannual δ^{18}O response over the Andes is limited, the large scale isotope–climate relationships are relatively well simulated by the model, including the dependence of Andean isotopic ratios on rainout over the Amazon.

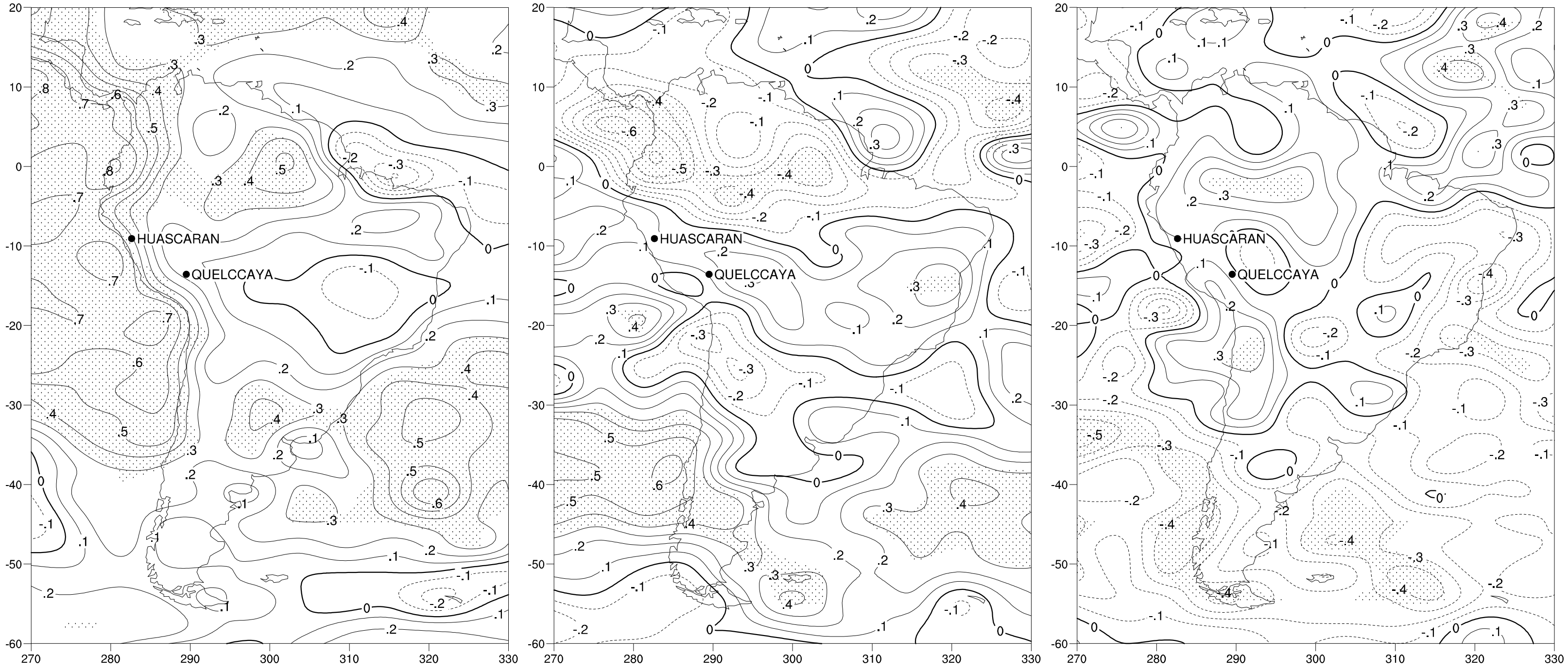

Figure 5.23: Correlation between Nino3.4 and modelled annual surface temperature (left), precipitation (centre) and precipitation δ^{18}O (right). Contour interval is 0.1. Stippled correlations are significant at 95% confidence level.

5.6.2 Tropical ice core records: Tibetan Plateau

Observed ice core δ^{18}O records from the Tibetan Plateau are not available for comparison with simulated interannual variability as only the Dasuopu core contains annual resolution, and this data is not publicly available. The modelled seasonal and interannual isotopic precipitation signal at the three sites (Guliya, Dunde and Dasuopu) is presented here for comparison with the qualitative discussion in Chapter 2. As the Tibetan ice core sites are located on the edge of the region influenced by the Asian monsoon, the relationship between local precipitation δ^{18}O and interannual monsoon variability is discussed. The presence of ENSO signals in modelled Tibetan Plateau δ^{18}O is also investigated.

Seasonal controls on δ^{18}O

The seasonal cycle of modelled surface temperature, precipitation and δ^{18}O interpolated to the sites of the three Tibetan ice cores is shown in Figure 5.24. The Guliya and Dunde sites are located to the north of the furthest extent of the ITCZ. The winter temperatures are similar in both locations but Dunde experiences warmer summers and greater precipitation associated with an influx of moisture from the south-west. The Dasuopu site is further south and experiences a monsoonal influence on temperature and precipitation, with the arrival of the summer monsoon during June associated with a strong precipitation maximum.

The modelled surface temperature at Dasuopu is warmer than that at the other sites as the elevation in the model is lower, whereas the observed elevation is higher resulting in cooler surface temperatures. The lower elevation of the Dasuopu site in the model may also lead to an overestimation of precipitation and the influence of the monsoon.

The observed isotopic records at Guliya and Dunde are correlated with temperature on seasonal time scales, as discussed in Chapter 2. The simulated isotopic seasonal cycle at these locations produces the most depleted values associated with the winter months, with secondary isotopic minima during the summer wet season. The Dasuopu isotopic signal has a seasonal cycle directly related to precipitation amount, with the lowest δ^{18}O values in the summer months.

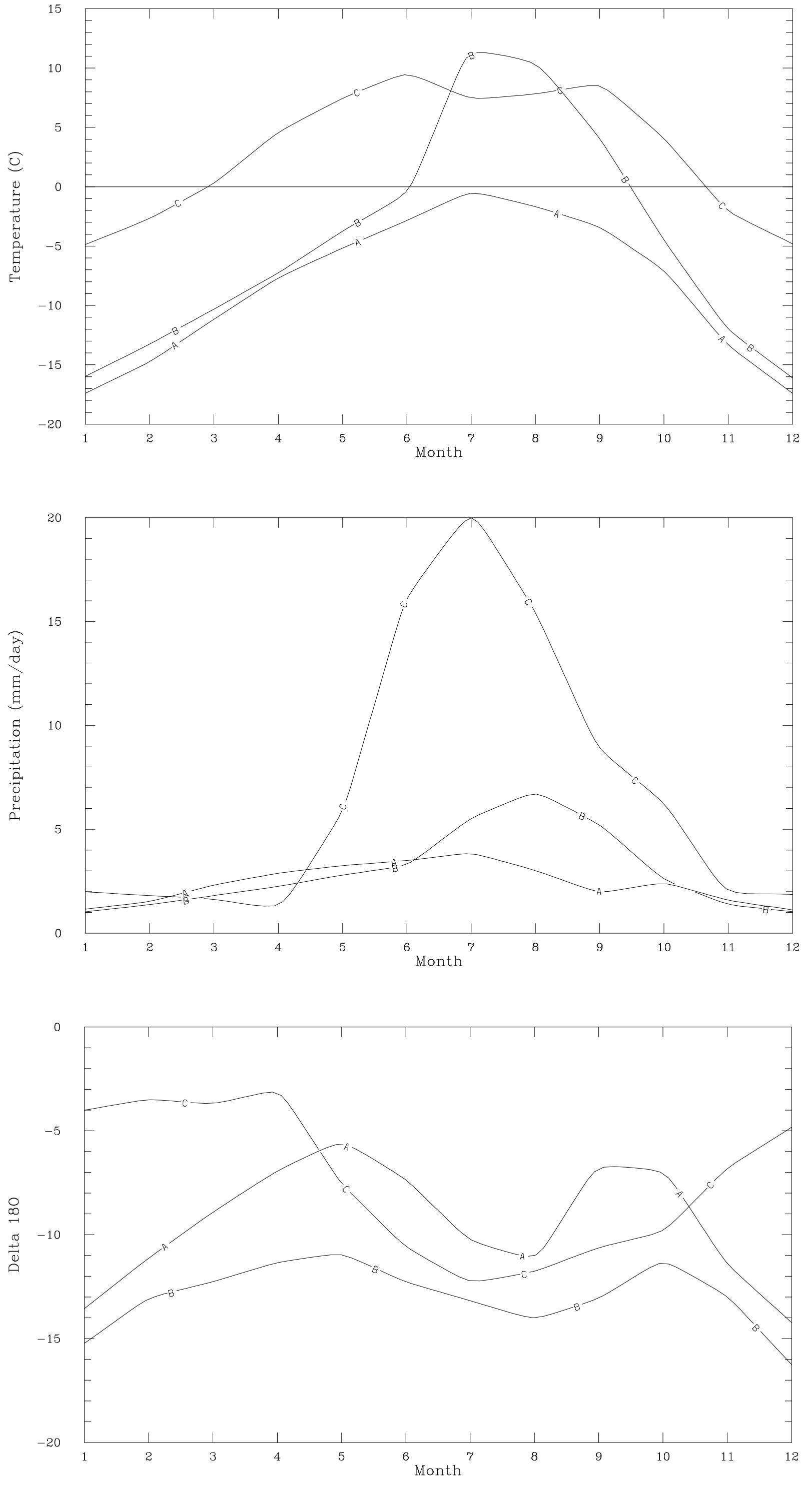

Figure 5.24: Guliya (A), Dunde (B) and Dasuopu (C) modelled seasonal cycle of surface temperature (top), precipitation (middle), and precipitation δ^{18}O (bottom).

Location	Temperature	Precipitation	AIR index	SOI
Guliya	−0.15	−0.62*	−0.06	+0.17
Dunde	+0.12	−0.45*	+0.13	+0.02
Dasuopu	−0.11	−0.17	−0.24	−0.31*

Table 5.5: Correlations between modelled annual δ^{18}O and temperature, precipitation, AIR index and SOI at Guliya, Dunde and Dasuopu core sites. Values marked * are significant correlations at 95% confidence level.

Interannual controls on δ^{18}O

The relationship between simulated δ^{18}O over the Tibetan ice core sites and climate parameters was also investigated on interannual time scales. Correlations were calculated between the modelled annual average δ^{18}O and local temperature and precipitation, as well as the AIR monsoon index and SOI (Table 5.5). The correlations with AIR and SOI represent the influence on Tibetan Plateau δ^{18}O values of isotopic rainout of moisture during transport inland from Indian and Pacific Ocean source regions.

The modelled δ^{18}O at Guliya and Dunde sites is significantly correlated with local precipitation amount, but not with local temperature or indices of monsoon or ENSO variability. The weak temperature correlations are in contradiction with the interpretation of these records as proxies for temperature on interannual time scales [*Thompson*, 2000]. The Dasuopu δ^{18}O record is not strongly correlated with local precipitation or temperature, while the strongest correlation is with the SOI, indicating either the direct influence of Pacific moisture or indirect interaction between ENSO and the monsoon. The moderate correlation with AIR monsoon index (significant at 90% confidence level) suggests that the isotopic signal at this location is partially determined by the extent of rainout of monsoonal moisture.

The temporal correlations between simulated annual δ^{18}O and surface temperature, precipitation and AIR index over the region centred on the Tibetan Plateau are shown in Figure 5.25. The local temperature–δ^{18}O relationship is positive over most of the Asian and Indian continental area with significant correlations over India and West China indicating a local temperature control over isotopic depletion. A band of negative correlations inland may be due to the association of cooler continental temperatures with a weaker summer monsoon and therefore less isotopic rainout of moisture.

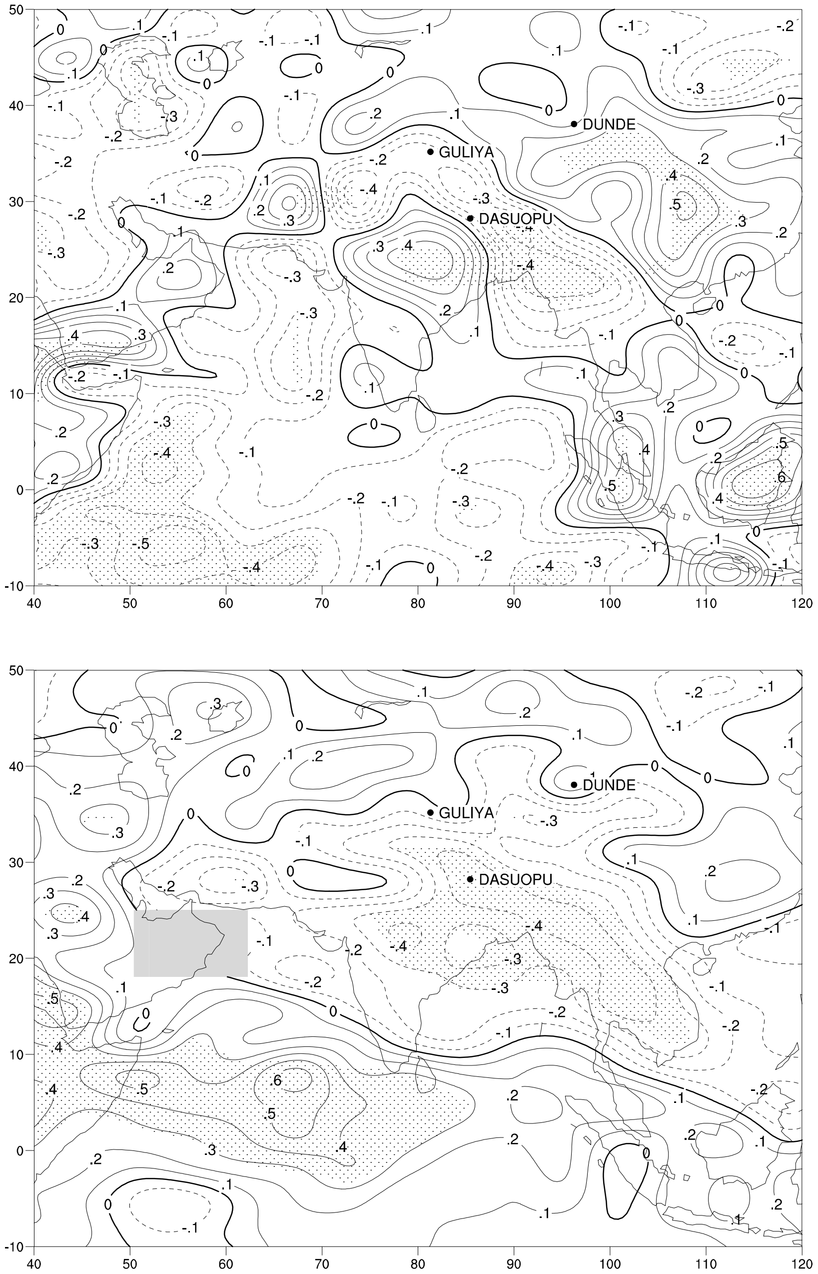

Figure 5.25: Temporal correlation between modelled annual δ^{18}O and surface temperature (top) and δ^{18}O and All India Rainfall index (bottom). Contour interval is 0.1. Stippled correlations are significant at 95% confidence level.

The correlation between δ^{18}O and the AIR index is negative over India and central Asia, where a stronger monsoon leads to more isotopic rainout. This relationship extends inland to the northward limit of the summer monsoon and the meridional extent of the ITCZ. The model simulation suggests that information about interannual monsoon strength may be extracted from isotopic records at Dasuopu but that the isotopic records at Dunde and Guliya reflect local precipitation variability on interannual time scales.

5.6.3 Coral isotopic records

The oxygen isotope ratio in coral carbonate skeletons records information about both local SST and ocean δ^{18}O, as described in Chapter 2. As coral δ^{18}O records are available for a large number of sites across the tropics [*Gagan et al.*, 2000], many having monthly sampling resolution, they provide an ideal comparison with the modelled surface ocean δ^{18}O as direct surface ocean δ^{18}O measurements are unavailable with the same spatial or temporal coverage.

The surface ocean isotopic scheme in the model outputs monthly average surface ocean δ^{18}O values, which are used to calculate a modelled "coral" δ^{18}O signal using the prescribed GISST2.3b SSTs. Empirical relationships between surface ocean δ^{18}O, SST and coral δ^{18}O have been determined for a range of massive coral species in different locations and for different sampling resolutions [eg., *McConnaughey*, 1989; *Gagan et al.*, 1994; *Wellington et al.*, 1996; *Juillet-Leclerc and Schmidt*, 2001]. The following linear relationship is used here:

$$\delta^{18}\mathrm{O}_{coral} = \delta^{18}\mathrm{O}_{ocean} + a(SST) + b \tag{5.3}$$

where a and b are empirical species-dependent constants, and SST is given in °C. A particular set of empirical constants ($a = -0.2 \pm 0.02‰/°\mathrm{C}$, $b = 0.45‰$) are taken from *Juillet-Leclerc and Schmidt* [2001] for *Porites Lutea* coral. These values are similar to those given in other studies for a range of *Porites* corals.

This linear relationship constitutes an estimate of the dependence of coral isotopic ratios on SST and local ocean δ^{18}O. In this study, biological and environmental factors such as changes in foraminiferal ecology, secondary calcification and dissolution are not considered, unlike the approach of *Schmidt* [1999b] who calculated planktonic foraminiferal isotopic ratios from ocean model isotopic output. The use of simplified linear fractionation with SST is justified as we wish to validate the ability of the model to reproduce the SST and local ocean δ^{18}O components of the coral signal only.

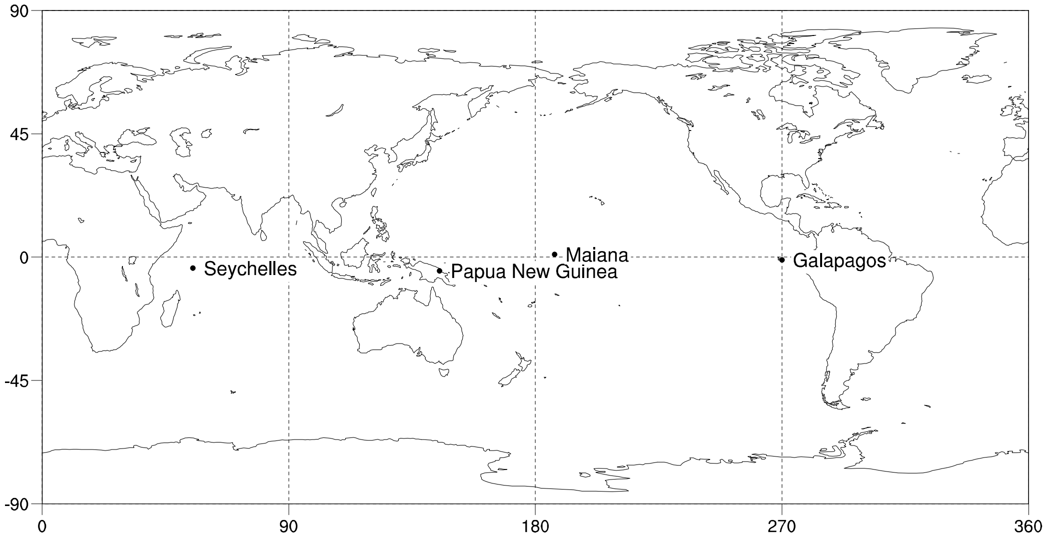

Figure 5.26: Locations of coral isotopic records: Mahe Island, Seychelles; Madang and Laing Islands, Papua New Guinea; Maiana Island, Kiribati; Bartolome, Champion and Urvina Islands, Galapagos.

The NGDC database (www.ngdc.noaa.gov/paleo) includes coral isotopic records for recent periods extending back more than five centuries. A range of records were chosen for the period of the model simulation to compare with the modelled "coral" signal, at location shown in Figure 5.26. Records were chosen from the Seychelles in the Indian Ocean, Papua New Guinea in the tropical western Pacific, Kiribati in the central Pacific and Galapagos in the eastern Pacific covering regions influenced by precipitation, evaporation and SST variability associated with the monsoon and ENSO.

Seychelles, Indian Ocean

Coral records from Mahe Island, Seychelles (4°S, 55°E) from *Porites Lutea* coral have a monthly resolution covering the period 1846–1995 [*Charles et al.*, 1997]. The modelled and observed coral δ^{18}O monthly and annual values are compared for 1950–1999. The seasonal cycle of coral δ^{18}O is controlled by SST in both observed and modelled records. The observed interannual coral isotopic signal follows SST, while the modelled surface ocean component is larger than the SST component (expressed as $-0.2(SST)$ for comparison with δ^{18}O) due to the high simulated precipitation variability (Figure 5.27). The modelled annual coral δ^{18}O is moderately correlated with the observed record (r = +0.35).

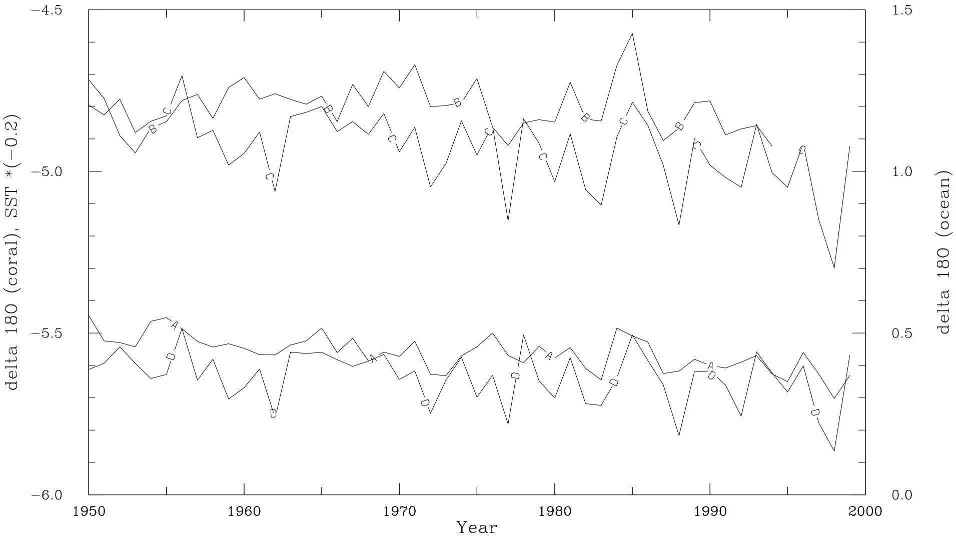

Figure 5.27: Seychelles: annual SST (× − 0.2) (A), observed coral δ^{18}O (B), modelled coral δ^{18}O (C) and modelled surface ocean δ^{18}O (D).

Interannual variability of Seychelles coral δ^{18}O is associated with both ENSO and monsoon variability via a dependence on SST [*Charles et al.*, 1997]. The amplitude of the ENSO signal in the modelled record is weaker than that observed due to the competing influence of precipitation variability. The modelled correlation between annual coral δ^{18}O and SOI is $r = +0.29$, while the observed correlation is $r = +0.49$. *Charles et al.* [1997] find that the Seychelles coral record captures decadal-scale variability associated with the Asian monsoon. For the period of the simulation, both the modelled and observed coral δ^{18}O are only weakly correlated with the WY monsoon circulation index ($r = +0.36$ for model, $r = +0.31$ for observations) and show no significant correlation with the AIR monsoon index.

Papua New Guinea, western Pacific Ocean

A composite of two coral records from the western Pacific Warm Pool is compared with the modelled coral δ^{18}O. Records of *Porites* coral from Madang (5°S, 145°E) and Laing (4°S, 144°E,) Papua New Guinea, sampled at four times annual resolution from 1884–1993, are compared with fossil corals from the same location in the study of *Tudhope et al.* [2001]. The present day coral δ^{18}O shows a dependence on both SST and precipitation, producing combined interannual variability associated with ENSO.

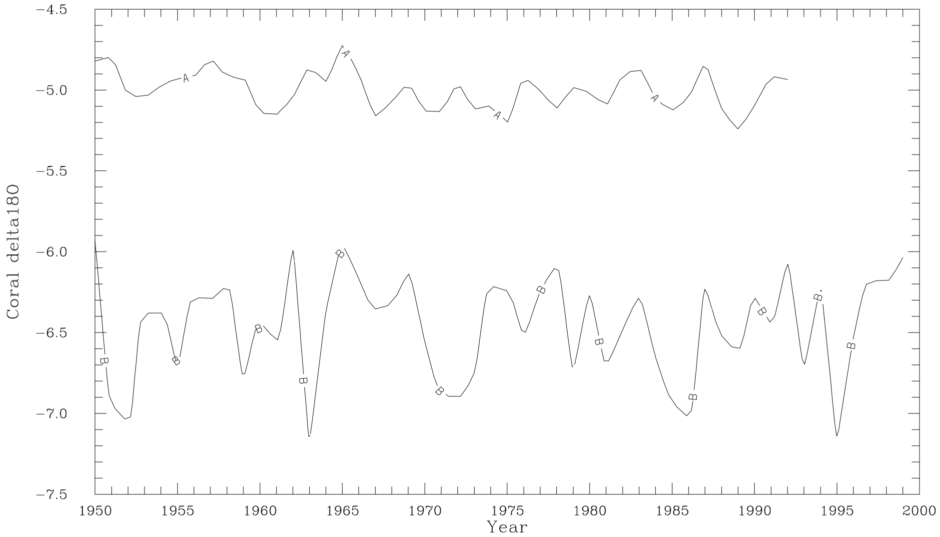

Figure 5.28: Papua New Guinea: annual observed (A) and modelled (B) coral δ^{18}O

The comparison with modelled coral δ^{18}O in this region illustrates several of the limitations of the modelled surface ocean isotopic signal. The modelled coral δ^{18}O averages −6.5‰ compared with −5.0‰ for observed coral (Figure 5.28), due to the overly depleted ocean δ^{18}O values (modelled value of −0.8‰ compared with +0.3‰ from the GSO ocean δ^{18}O database). The overly strong ocean δ^{18}O depletion is due to the excessive precipitation simulated by the model in this region. The interannual range of precipitation, ocean δ^{18}O and coral δ^{18}O is also overestimated by the model.

The interannual signal in the observed coral δ^{18}O is associated with ENSO, with r(δ^{18}O, SOI) = −0.43, while the modelled correlation with SOI is weak ($r = -0.05$). This is due to the position of the site at the edge of the central Pacific precipitation anomaly associated with ENSO, which extends further west in the MUGCM than in observations. The weak correlation between modelled and observed annual coral δ^{18}O ($r = +0.17$) confirms that the model does not closely reproduce observed precipitation anomalies associated with the dominant ENSO signal at this location.

Maiana Island, central Pacific Ocean

Monthly coral records from 1950–1993 from Maiana Island (1°N, 173°W) Republic of Kiribati in the central Pacific [*Urban et al.*, 2000] are compared with the modelled isotopic signal. Coral δ^{18}O values in the central Pacific are primar-

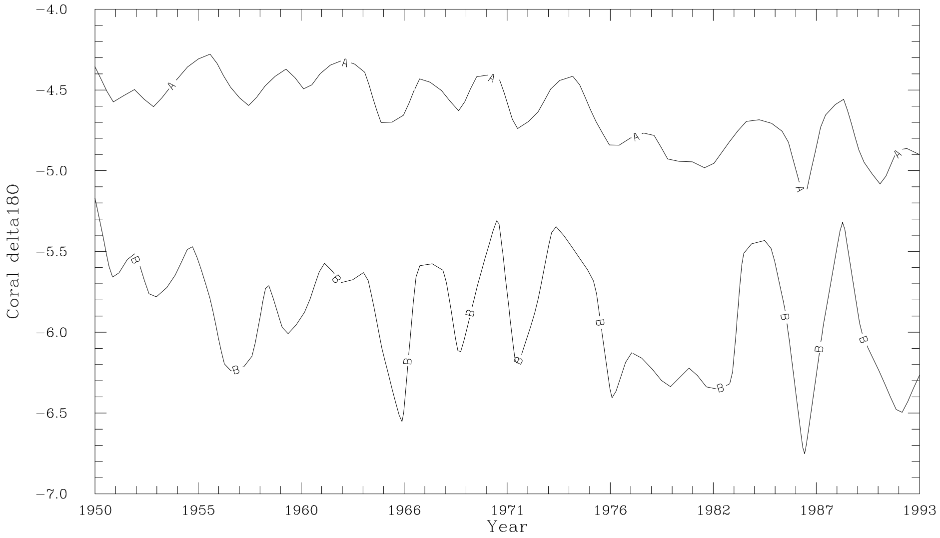

Figure 5.29: Maiana Island: annual observed (A) and modelled (B) coral δ^{18}O

ily controlled by variation in surface ocean δ^{18}O associated with precipitation amount changes. As the strong central Pacific ENSO precipitation and isotopic response is reproduced by the MUGCM, the modelled ocean δ^{18}O and coral δ^{18}O correspond well with observations in this region. The modelled and observed coral δ^{18}O at Maiana are strongly correlated ($r = +0.73$).

The modelled surface ocean δ^{18}O reproduces the large interannual ENSO signal, producing strong correlations with SOI for modelled coral δ^{18}O (r = +0.83) compared with the observed coral δ^{18}O–SOI correlation (r = +0.73). The model overestimates precipitation at this location, resulting in a mean modelled coral δ^{18}O which is around 1.5‰ more depleted than observed, as well as simulating a larger than observed interannual precipitation and δ^{18}O range, as shown in Figure 5.29.

Galapagos, eastern Pacific Ocean

In the eastern Pacific, eight monthly coral δ^{18}O records from Bartolome (0°, 270°E), Champion (1°S, 270°E) and Urvina Islands (0°, 269°E) in the Galapagos, Ecuador, cover the period 1993–1995. Local SST, salinity and ocean δ^{18}O measurements are also available for the same period [*Wellington et al.*, 1996]. The eight records were averaged and compared with the modelled coral and ocean δ^{18}O and salinity (calculated as described in Chapter 4) averaged over the grid points 2°N and 2°S, 270°E, as shown in Figure 5.30.

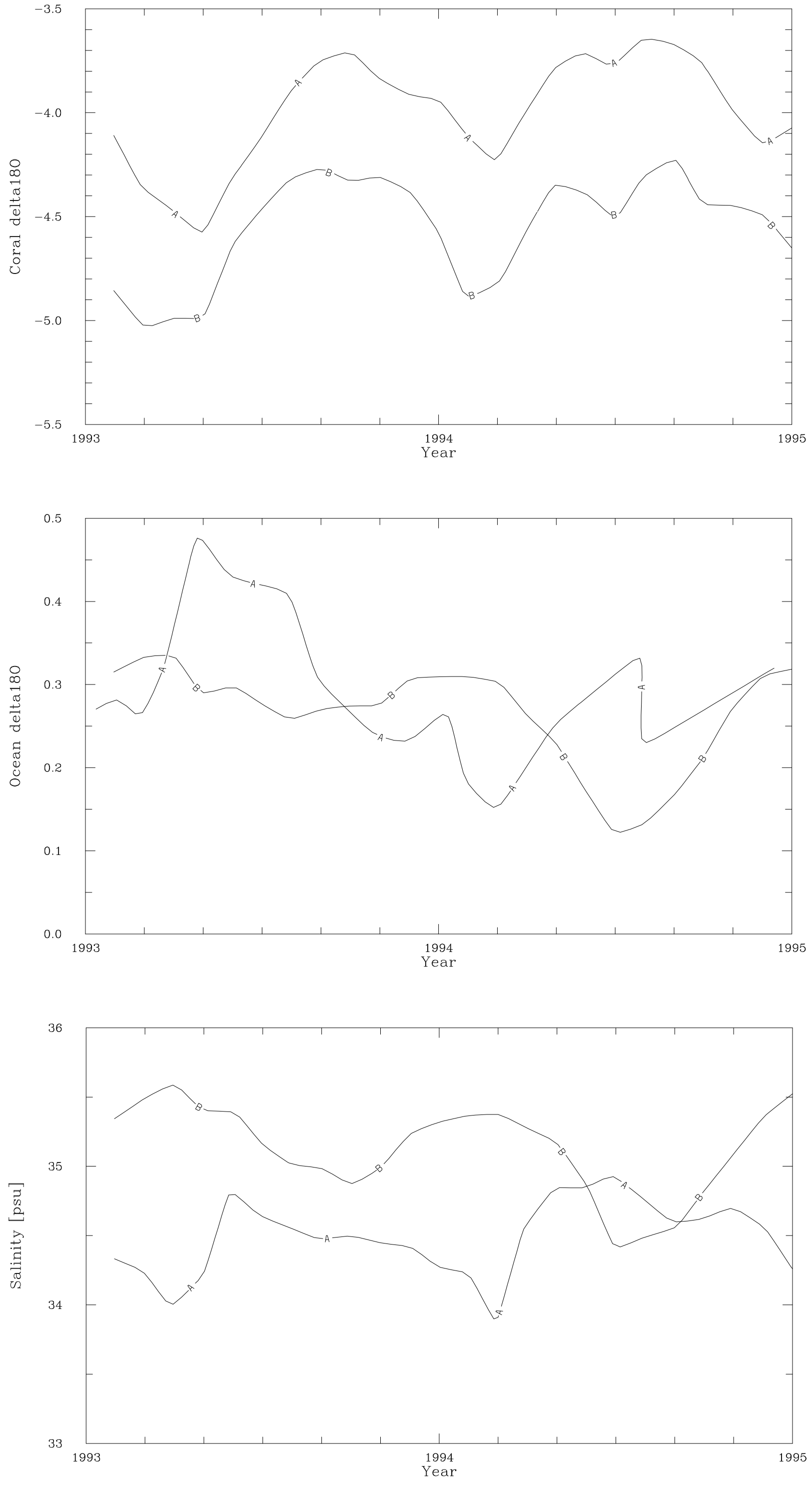

Figure 5.30: Galapagos: monthly observed (A) and modelled (B) coral δ^{18}O (top), ocean δ^{18}O (middle) and salinity (bottom).

Wellington et al. [1996] found that the Galapagos coral δ^{18}O records are mainly controlled by SST which explains 90% of the variance in the coral isotopic signal, while the local ocean δ^{18}O variability is associated with changes in ocean currents rather than precipitation. The modelled coral δ^{18}O matches the observed well for this region ($r = +0.86$) due to the dominance of the SST signal, with the observed SST and observed coral δ^{18}O being highly anticorrelated ($r = -0.96$).

The annual cycle of observed salinity and ocean δ^{18}O has a minimum in the early months of the year believed to be associated with southerly flow of low salinity, isotopically depleted water from the Gulf of Panama as the ITCZ migrates south [*Wellington et al.*, 1996]. The modelled salinity is negatively correlated with observed salinity ($r = -0.66$) and the modelled and observed ocean δ^{18}O are also not visibly correlated, indicating that important processes influencing local salinity and δ^{18}O at this location are not captured by the one-dimensional surface isotopic scheme.

5.7 Summary

The ability of the MUGCM to simulate the main feature of seasonal and interannual climate variability in the tropics was examined for a simulation of climate from 1950–1999. The isotopic response to variability of temperature, precipitation and evaporation and atmospheric circulation was examined and the simulated isotopic ratios in precipitation and the surface ocean were compared with isotopic records in tropical ice cores and marine coral records.

On seasonal time scales, the model reproduces the circulation and precipitation variability associated with the monsoon and seasonal migration of the ITCZ in the tropics. The model also reproduces the strong observed dependence of tropical isotopic ratios on precipitation amount, although overestimating precipitation amount and isotopic depletion over continental topography. The dominance of precipitation amount controls on seasonal precipitation δ^{18}O is observed to produce negative correlations with temperature as the most depleted δ^{18}O values are associated with the summer wet season.

On interannual time scales the model is able to simulate ENSO variability in precipitation, pressure and circulation, and ENSO is correctly simulated as the strongest interannual mode in the tropics. The modelled ENSO precipitation δ^{18}O response generally corresponds to that seen in observed GNIP δ^{18}O records, with the strongest signals in the central and western tropical Pacific where large precipitation anomalies are associated with ENSO. The model surface ocean isotopic scheme simulates δ^{18}O anomalies in response to changes in precipitation and evaporation due to ENSO. In the central and western Pacific the surface ocean isotopic ratio responds to precipitation variability, whereas in the eastern equatorial Pacific, evaporation variability produces surface ocean δ^{18}O anomalies.

On smaller spatial scales, the model is able to reproduce the sign and magnitude of the observed δ^{18}O–SOI correlations at the location of GNIP stations in northern and central Australia and the central Pacific. Over tropical South America the model does not reproduce the observed correlation between precipitation δ^{18}O and ENSO, due to the weak ENSO precipitation response over this region. The model also simulates moderate correlations between Antarctic precipitation δ^{18}O and ENSO, which appear to be due to changes in rainout and isotopic depletion in mid-latitude source regions rather than local precipitation or temperature anomalies.

The ability of the MUGCM to reproduce observed interannual monsoon variability is limited, in common with many other atmospheric GCMs. The magnitude of interannual precipitation and wind shear variability is reproduced, indicating that the model generates substantial interannual monsoon variability independently of SST forcing. Correlations between indices of interannual monsoon variability and precipitation and isotopic ratios are strong locally over the monsoon moisture source region and over continental India, but elsewhere the model does not simulate strong teleconnections with monsoon variability.

The modelled isotopic signal was also compared with isotopic records in tropical ice cores and marine coral records. The model correctly simulates the positive temperature–isotope and negative precipitation–isotope correlations over tropical South America on interannual time scales, and the dependence of Andean δ^{18}O on rainout over the Amazon. However the precipitation response to ENSO over the Amazon and Andes does not match observations, preventing the model from correctly simulating the influence of ENSO on interannual variability of ice core δ^{18}O.

Over the Tibetan Plateau the modelled seasonal and interannual variability of δ^{18}O was identified at locations corresponding to ice core sites. The variability of the isotopic record at northern locations is found to be most closely correlated with local precipitation, whereas in the south the influence of ENSO and monsoon variability is identified. Correlations with local temperature on interannual time scales are not observed in disagreement with previous interpretations of the Tibetan Plateau ice core records.

The ability of the model to reproduce the observed surface ocean $\delta^{18}O$ signal was tested by a comparison between observed coral $\delta^{18}O$ and a modelled "coral" $\delta^{18}O$ response to SST and surface ocean $\delta^{18}O$ variability. The model captures the interannual coral $\delta^{18}O$ signal in the Indian Ocean and eastern Pacific following the prescribed SST variability. In the central Pacific, the strong modelled precipitation response to ENSO allows the model to closely reproduce the observed coral $\delta^{18}O$ signal. In the western Pacific Warm Pool, limitations to the modelled precipitation–ENSO response lead to an overestimation of surface ocean isotopic depletion and incorrect ENSO–isotope relationship.

It is shown that the model captures the main features of the tropical isotope–climate relationship on seasonal and interannual time scales. The model reproduces the large scale precipitation amount dependence of isotopic ratios in tropical precipitation, and the interannual signals associated with ENSO and monsoon variability. Limitations of the modelled representation of precipitation at a regional scale over tropical South America and the western Pacific prevent the model from capturing the interannual signal in specific isotopic records.

Despite these limitations the large scale temperature–$\delta^{18}O$ and precipitation-$\delta^{18}O$ response appears to be adequately represented by the model for use in palaeoclimate simulations. As argued by *Cole et al.* [1999], the isotopic signal associated with present day–glacial climate changes is likely to consist of a response to large scale temperature and precipitation changes produced by global forcing. The modelled distribution and variability of present day tropical precipitation $\delta^{18}O$ and surface ocean $\delta^{18}O$ validates the ability of the model to simulate isotopic sensitivity to large scale climate change.

Chapter 6

Sensitivity of isotopes to LGM tropical climate

6.1 Introduction

Modelling the climate of the LGM, 21,000 years BP, provides an opportunity to test the sensitivity of isotopes in the global climate system to conditions which differ greatly from the present day. Changes in sea ice coverage, the presence of extensive Northern Hemisphere ice sheets and the resulting change in sea level all contribute to changes in the climate. The changes in SST distribution and zonal mean SST values also substantially alter the atmospheric circulation and hydrologic cycle.

Isotopic ratios in precipitation and the surface ocean respond to changes in temperature, precipitation and evaporation and atmospheric circulation on present day seasonal and interannual time scales, as discussed in the previous Chapter. We now examine the isotopic response to large scales changes in climate between the LGM and present day, with a particular focus on tropical isotope–climate relationships. The existence of a large set of marine and continental palaeoclimate proxy records from the LGM period allows a comparison between the modelled isotopic ratios in precipitation and the surface ocean and isotopic palaeoclimate records.

As the extent of cooling of tropical SSTs at the LGM remains the subject of debate, the sensitivity of isotopes in precipitation and the surface ocean to tropical SST forcing under LGM conditions is investigated by comparing the results of two simulations with different tropical SST boundary conditions. A simulation using the standard CLIMAP SSTs (see Section 6.2) with largely unchanged tropical SSTs is compared with a simulation with cooled tropical SSTs. The isotopic response to each set of SST boundary conditions is compared with continental and marine isotopic records to determine which simulation is more consistent with the proxy evidence. This comparison focuses on continental records from Andean and Tibetan ice cores and marine records from coral and foraminifera in the tropical eastern and western Pacific Ocean.

A brief description is given below of the reconstruction of tropical SSTs from marine records including isotopic ratios in coral and foraminifera, and of the boundary conditions used to simulate LGM climate with our model. The modelled climates including surface temperature, MSLP, surface winds, precipitation, evaporation and atmospheric circulation for both CLIMAP and cooled tropical SST simulations are described. The precipitation and the surface ocean isotopic response is then compared with the climate anomalies and with observational records, and the implications for the reconstruction of tropical climate at the LGM are discussed.

6.2 LGM reconstructions

6.2.1 Reconstructions of SSTs

The CLIMAP SST reconstruction [*CLIMAP Project Members*, 1976] used the faunal assemblage technique of *Imbrie and Kipp* [1971] to determine LGM SSTs via comparison between modern planktonic core-top assemblages and LGM assemblages. The relationship between the distribution of species and SST was assumed to be unchanged for glacial conditions. The reconstruction calculated a 1–2°C cooling of tropical SSTs at the LGM, with warming in the region of the subtropical gyres.

Questions were raised about this reconstruction by *Rind and Peteet* [1985] who found that such small tropical cooling could not produce the observed lowering of snow levels in Papua New Guinea, Hawaii, Columbia and East Africa at the LGM. Alternatively, *Webster and Streten* [1978] suggested that changes in atmospheric circulation with increased cold air incursions from high latitudes may explain lowering of snow levels. *Broecker* [1997] calculated that the mean snowline change implied by the sea level fall at the LGM would require SST cooling of 4°C assuming a constant atmospheric lapse rate.

Additional questions were raised by the analysis of LGM groundwater noble gas compositions from tropical Brazil [*Stute et al.*, 1995]. The noble gas concentrations are primarily a function of local mean temperature, which the analysis estimated to be 5°C cooler than present day temperatures. The increased isotopic depletion at the LGM in ice cores from the Andes also appear to require cooling of tropical Pacific and Atlantic SSTs to alter the climate of tropical South America [*Thompson*, 2000].

Some marine palaeoclimate evidence, as described in Chapter 2, also suggests that the CLIMAP reconstruction may have underestimated the cooling of tropical SSTs at the LGM. Coral δ^{18}O and Sr/Ca anomalies provide evidence for tropical ocean cooling of the order of 5°C in the tropical Atlantic and western tropical Pacific [*Guilderson et al.*, 1994; *Beck et al.*, 1997]. There is also evidence that SSTs were cooler in the Coral Sea [*Anderson et al.*, 1989] and the northern tropical Indian Ocean [*Sonzogni et al.*, 1998] than the CLIMAP reconstructions suggest.

Hostetler and Mix [1999] recalibrated the CLIMAP faunal assemblage data, and produced greater tropical cooling in the equatorial Pacific and Atlantic Oceans than the original CLIMAP values. Recent work by *Crowley* [2000] suggests an intermediate level of cooling of 2–3°C for tropical SSTs based on a reconsideration of the available proxy data using the CLIMAP reconstruction technique. Previous modelling studies have also found that the disagreement between LGM SSTs computed with a thermodynamic slab ocean and the prescribed CLIMAP SSTs was greatest in the tropics [eg. *Dong and Valdes*, 1998; *Pinot et al.*, 1999].

Given these conflicting reconstructions of LGM tropical SSTs, it is of interest to simulate the climate and isotopic response to two possible extreme scenarios: the largely unchanged tropical SSTs of the CLIMAP reconstruction and substantially cooled tropical SSTs. The use of CLIMAP SSTs for one simulation is also desirable in order to provide a basis for comparison with the range of other climate modelling studies which have used the CLIMAP boundary conditions.

6.2.2 Boundary conditions

The climate of the LGM was simulated using the sea ice, topography, insolation and atmospheric composition boundary conditions specified by the Paleoclimate Modeling Intercomparison Project (PMIP) [*Joussaume and Taylor*, 1995].

Standard CLIMAP SSTs were used to carry out the first simulation of LGM climate ("CLIMAP" run). A second LGM simulation is carried out with cooled tropical SSTs ("COOL" run). We chose to impose large values for the tropical SST cooling and to remove the zonal SST gradient across the Pacific in order to produce a strong climate and isotope response. It is expected that a smaller cooling would produce a response of the same nature but with smaller magnitude, although the extent of changes in zonal and meridional SST gradients may also be important, as suggested by *Rind* [2000].

The two sets of prescribed SSTs are described and seasonal DJF and JJA averages for CLIMAP and COOL simulations compared with the present day ("PD" run) SST boundary conditions described in Chapter 3. The sea ice, topography, insolation and atmospheric composition boundary conditions common to both simulations are then outlined.

CLIMAP SSTs

The SSTs for the CLIMAP run consist of monthly SST distributions constructed from February and August data available from the CLIMAP project [*CLIMAP Project Members*, 1976, 1981]. The differences from the present day for these months were interpolated assuming a sinusoidal variation between February and August maximum anomalies to produce an annual cycle of anomalies. The monthly CLIMAP SST anomalies were then added to the present day monthly SST distributions to produce the SST boundary conditions for the LGM simulation.

The DJF and JJA CLIMAP – PD SST anomalies are shown in Figures 6.1 and 6.2, with sea ice regions excluded. The SST values are generally cooler in the mid- and high latitudes than the present day for both DJF and JJA. The largest SST anomalies are seen at high latitudes, with cooling of up to 6°C at the edge of the extended LGM sea ice regions. Regions of tropical warming are most pronounced in DJF, with much of the tropical and subtropical Pacific being warmer than the present day. In JJA, regions of warmer SSTs are seen in the subtropics as well as off the east coast of Australia.

The western Pacific Warm Pool is only slightly cooler (less than 1°C) than present day, while on average the zonal SST gradient across the Pacific is similar, with slightly warmer SSTs in both the eastern and western Pacific for CLIMAP data, as shown in Figure 6.3. The zonal SST forcing on the atmospheric Walker circulation is therefore similar to the present day, although the

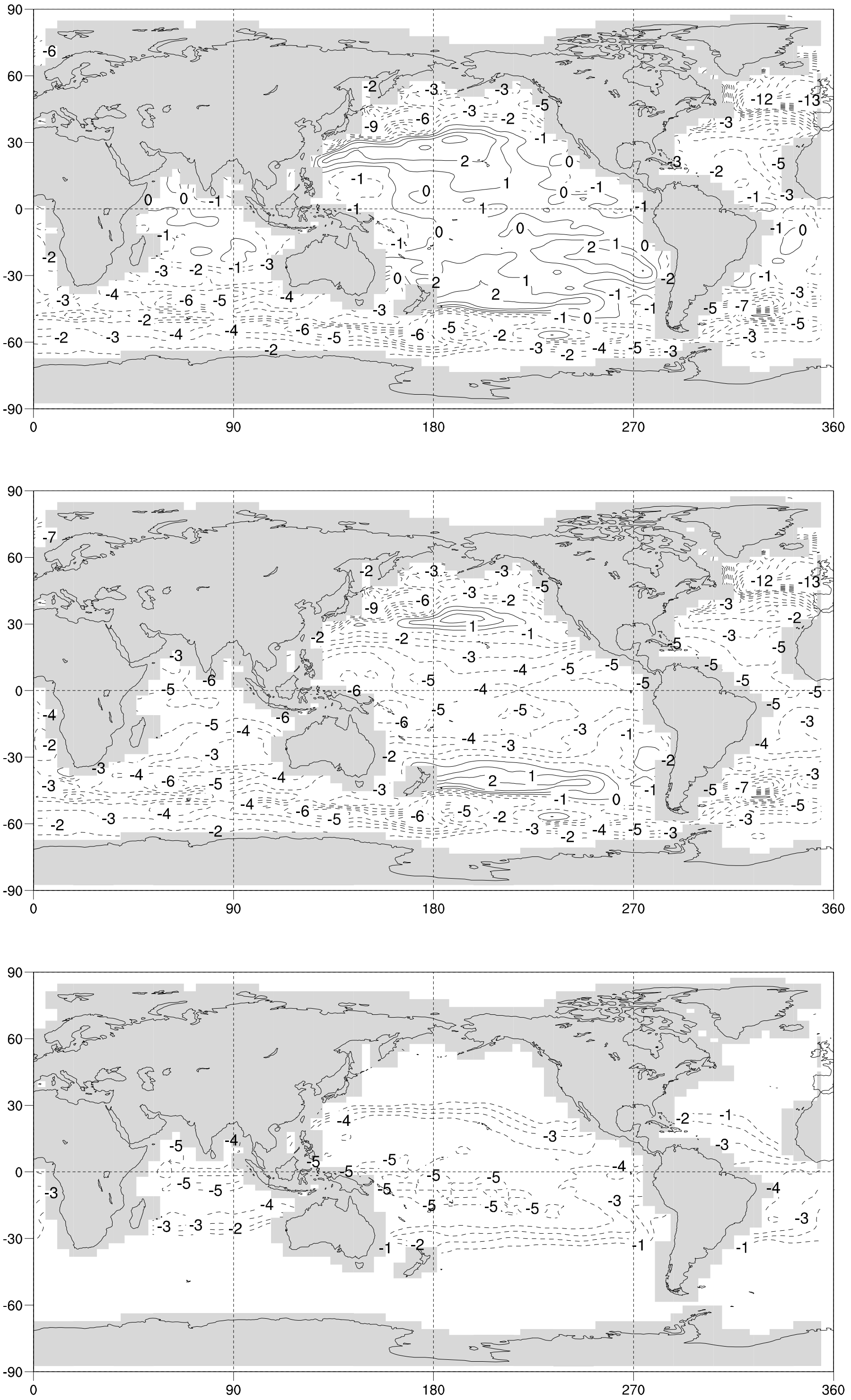

Figure 6.1: DJF SST anomalies: CLIMAP – PD (top), COOL – PD (middle) and COOL – CLIMAP (bottom). Contour interval is 1°C.

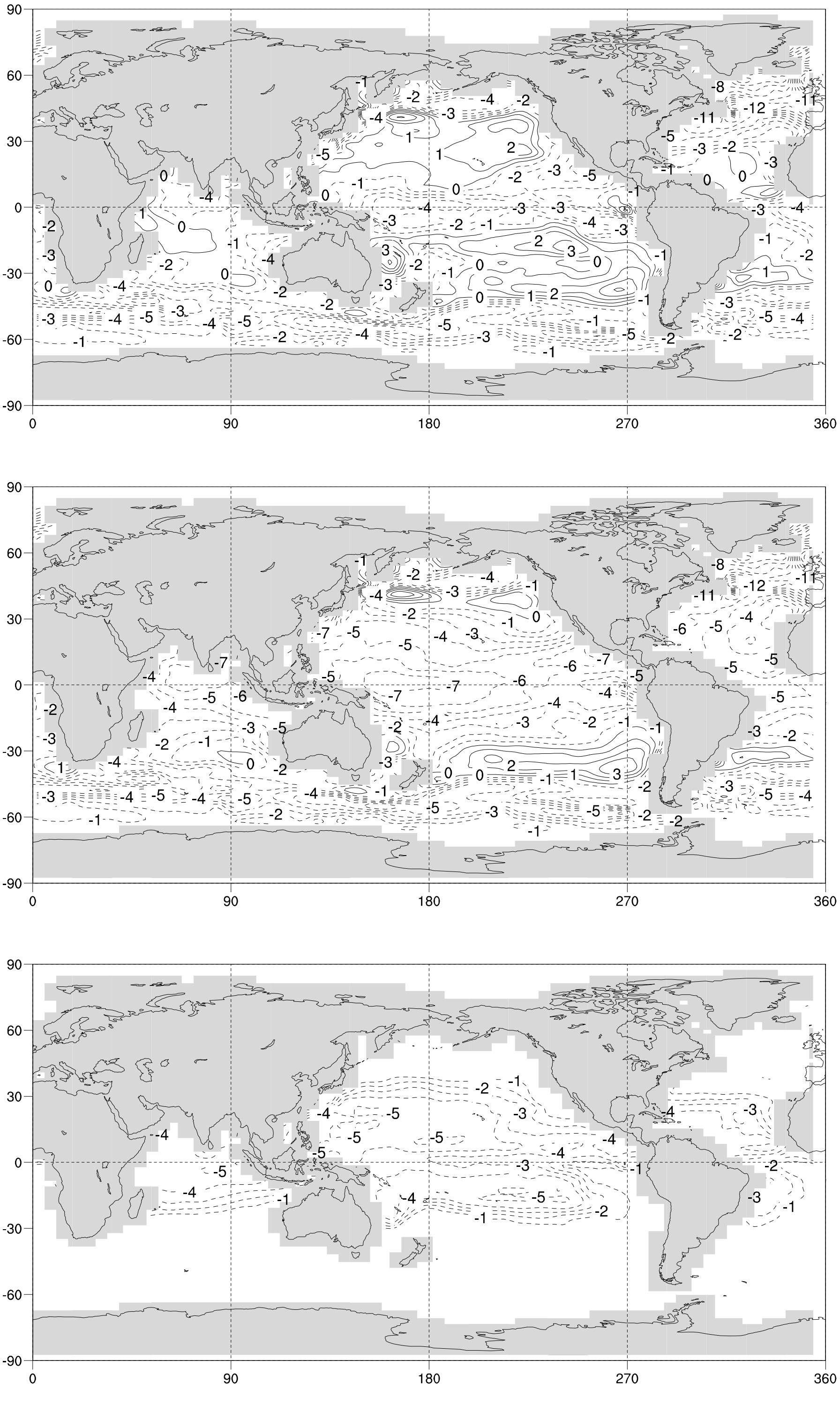

Figure 6.2: JJA SST anomalies: CLIMAP – PD (top), COOL – PD (middle) and COOL – CLIMAP (bottom). Contour interval is 1°C.

change in meridional SST gradients (Figure 6.4) due to slightly warmer tropical SSTs and cooler high latitude SSTs may alter the meridional atmospheric heat transport.

Cooled tropical SSTs

The SST boundary conditions for the COOL simulation were constructed following the approach of *Charles et al.* [2001] by cooling the tropical SSTs of the CLIMAP reconstruction. A maximum cooling of 5°C was imposed where the CLIMAP SSTs were greater than 28°C. To produce a smooth SST distribution, values greater than 20°C and less than 28°C were cooled linearly (ie by 0.625°C for each °C above 20°C). The resulting seasonal SSTs anomalies relative to PD and CLIMAP are also shown in Figures 6.1 and 6.2.

These adjusted SSTs are cooler than the present day everywhere except for two regions in the mid-latitudes in the Pacific Ocean. The largest tropical cooling is seen in the western Pacific for JJA where SSTs are more than 6°C cooler than present day. The imposed cooling was sufficient to remove the western Pacific Warm Pool and the zonal SST gradient across the Pacific (see Figure 6.3). The SSTs outside the cooled tropical region are identical to CLIMAP, so that the meridional temperature gradient beyond approximately 30° latitude in both hemispheres is unchanged. The equator to pole temperature difference is substantially reduced however, as can be seen in Figure 6.4.

Sea ice

The monthly sea ice concentration files were constructed differently to the suggested PMIP procedure as the MUGCM includes the parameterisation of sea ice leads. The seasonal cycle of sea ice extent was constructed from interpolation between the February and August CLIMAP reconstructed sea ice extent, representing annual extremes. The fraction of ice coverage was estimated from the sea ice extent by assuming 98% concentration at the coast linearly decreasing to 85% half way to the ice edge and 50% at the limit of the ice extent as described by *Noone* [2001].

Topography and land mask

The increase in terrestrial ice volume at the LGM led to a lowering of the sea level of 120±5 m [*Fairbanks*, 1989]. The changes in model topography

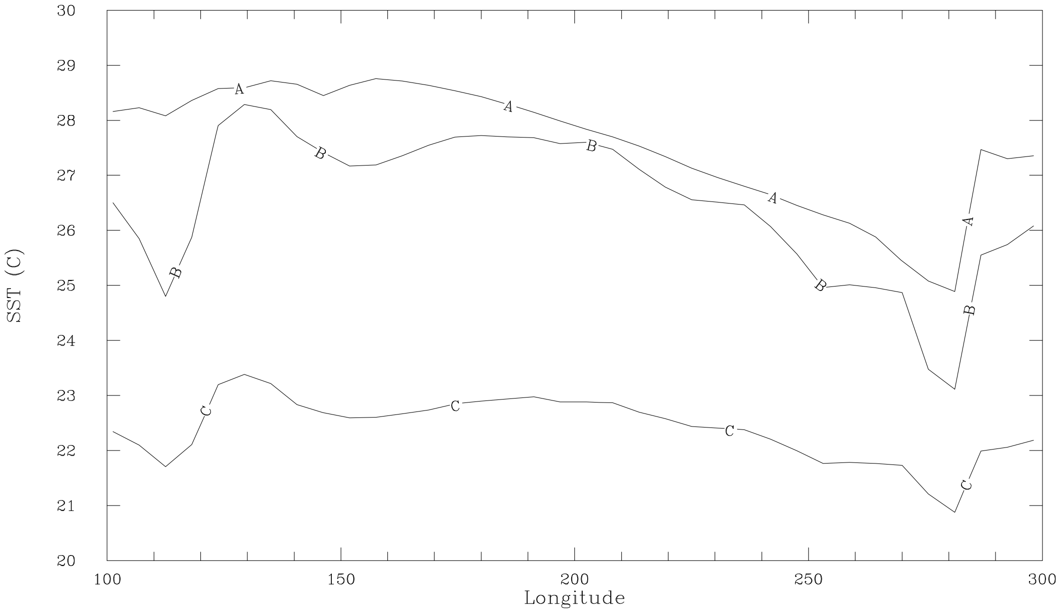

Figure 6.3: Meridional average SSTs between 15°S–15°N: PD (A), CLIMAP (B) and COOL (C).

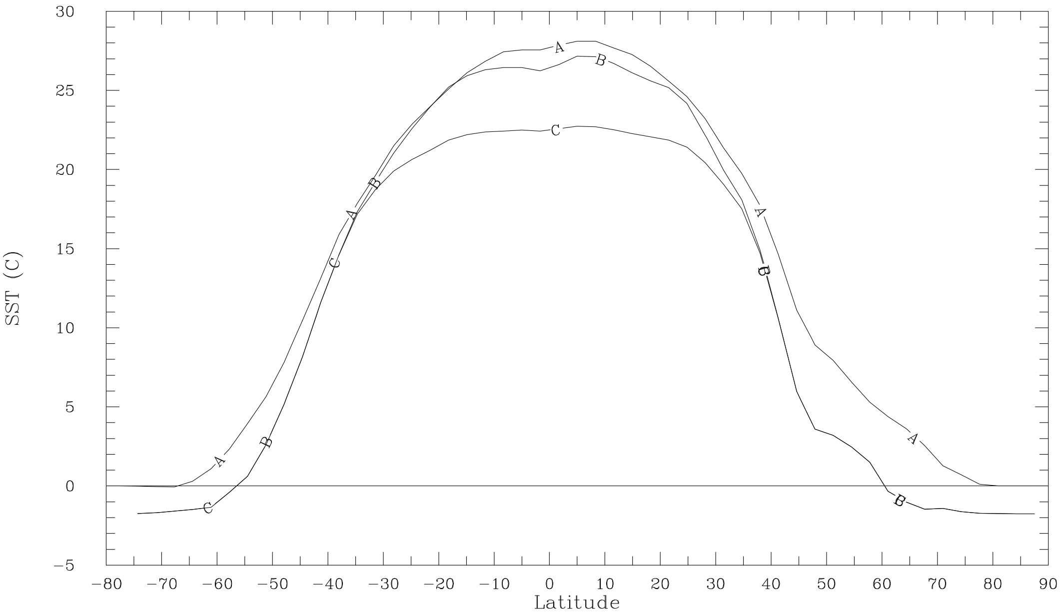

Figure 6.4: Zonal average SSTs: PD (A) CLIMAP (B) and COOL (C).

take account of the sea level change as well as the increased height of the Northern Hemisphere continental ice sheets. The LGM topography of *Peltier* [1994] was converted to the MUGCM grid and the land type masks constructed as described by *Noone* [2001]. The topography for the LGM and the difference between LGM and present day are shown in Figure 6.5.

The land mask for the LGM was constructed so that all points with more than 35% snow coverage in the NIMBUS 7 microwave observations are designated as snow, compared with the criteria of 50% for the present day land masks. The resulting increase in snow coverage represents the expected response to LGM ocean and land surface cooling.

Insolation

The orbital parameters were calculated for 21,000 years BP within the model based on the scheme of *Berger* [1978]. The vernal equinox was fixed at March 21. The LGM orbital eccentricity is 0.0190 compared with 0.0167 for the present day. The LGM date of perihelion was set to 12 days later in January. The LGM obliquity is 22.95° compared to 23.45° for the present day.

The net result of these changes in the orbital parameters is a small change in the insolation, with a reduction in winter insolation at high latitudes and changes in the seasonality of insolation. It should also be noted that the use of fixed SSTs in the simulation greatly reduces the direct impact of changes in insolation, although the SSTs used are assumed to represent the glacial state of the ocean, including the response to solar forcing.

Atmospheric composition

The atmospheric carbon dioxide concentration was decreased from the present day (1995) value of 345 ppmv to the LGM value of 200 ppmv as measured in ice core records [*Raynaud et al.*, 1993]. The atmospheric absorption spectra coefficients for the model radiation parameterisation were recalculated for the reduced atmospheric carbon dioxide concentration. The concentration of ozone is unchanged from present day. The changes in atmospheric composition produce a net change in radiative forcing of -3.4 W/m^2, as specified by PMIP.

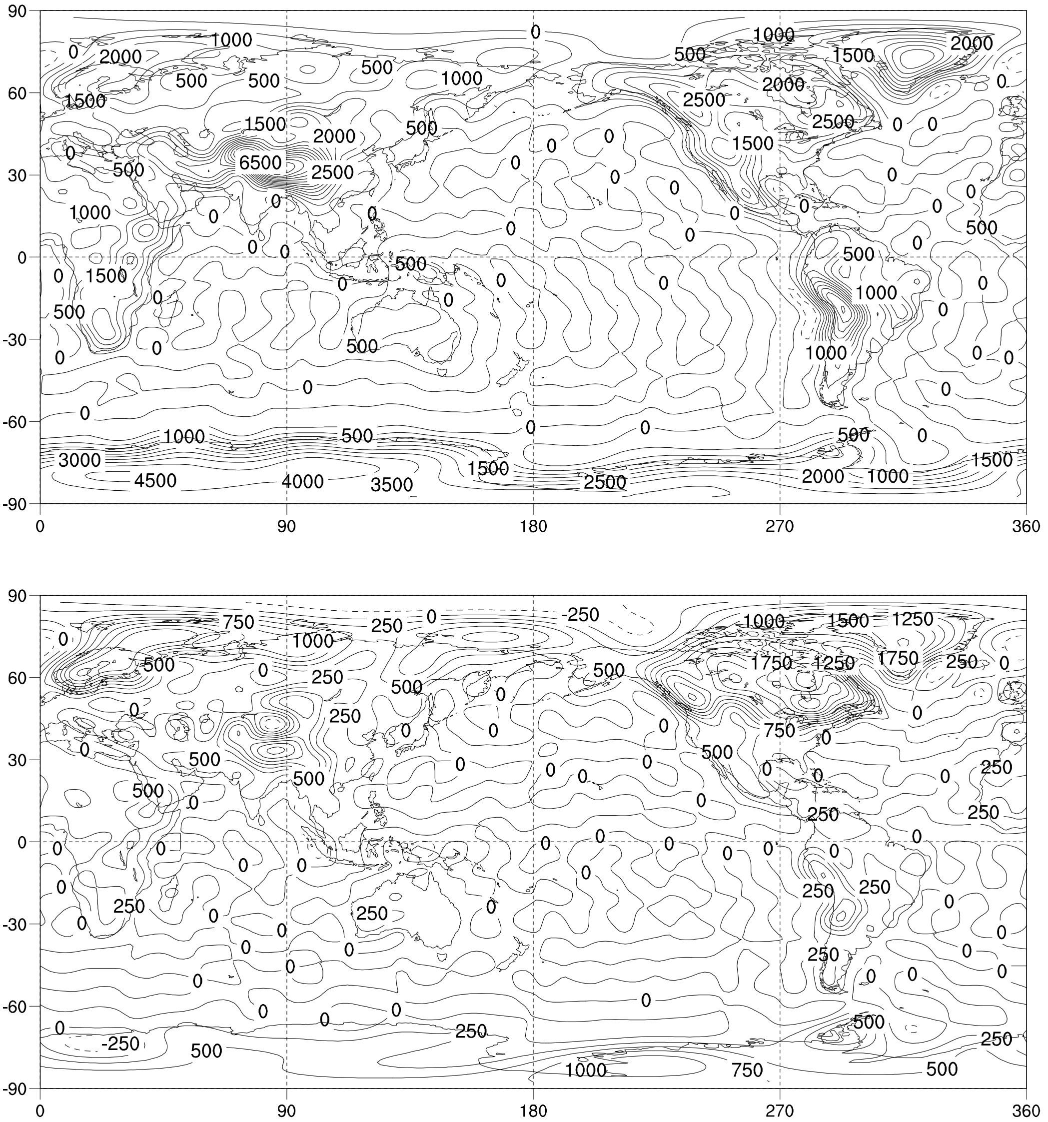

Figure 6.5: Topography for LGM (top) and difference from present day (bottom). Contour intervals are 500 m and 250 m respectively.

Ocean isotopic ratio

The mean isotopic ratio of the ocean changes with the increase in global ice volume at the LGM. As the terrestrial ice sheets contain water which is isotopically depleted relative to the ocean, conservation requires that the ocean becomes enriched in $H_2^{18}O$ and HDO. Previous modelling studies of water isotopic ratios at the LGM (see Chapter 2) have commonly used an oxygen isotope ocean enrichment of +1.6‰ following *Duplessy* [1981].

However more recent calibration of the isotope–sea level relationship using fossil coral records from Huon Peninsula in the western Pacific [*Chappell et al.*, 1996] gave an $H_2^{18}O$ isotopic enrichment of only +1.2‰ for an estimated sea level change of 120 m. As this study includes comparison with a range of marine proxy data, it was decided to use this enrichment value which is more commonly employed in marine palaeoclimate reconstruction [eg. *Martinez et al.*, 1997; *De Deckker et al.*, 2003]. The LGM ocean isotopic δ value is enriched by +1.2‰ for $H_2^{18}O$ and +9.6‰ for HDO. This enrichment alters the mean ocean isotopic ratio towards which the surface ratio is relaxed in the surface ocean isotopic scheme.

6.3 Modelled LGM climate

Simulations of LGM climate were carried out using the CLIMAP and COOL boundary conditions outlined above. The model was run with the surface ocean isotopic scheme and river runoff scheme, but without horizontal ocean transport or isotopic snow, as for the simulation of present day climate described in Chapter 5. The model was initialised using a present day climatological state and 15-year model integrations were carried out, with the last 10 years of the integration included in the analysis. The LGM simulations required the specification of higher horizontal diffusion than the standard values used in the model in order to prevent atmospheric dynamical instability developing. A 15-year present day control run was therefore carried out with the same increased horizontal diffusion to allow a consistent comparison with the simulated LGM climate.

The modelled LGM climate from the CLIMAP and COOL simulations is compared with the present day climate from the seasonally repeating control run. Seasonal average anomalies (CLIMAP – PD, COOL – PD) of surface temperature, MSLP, precipitation, evaporation, surface wind and atmospheric transport fields are constructed for DJF and JJA. The climate for the CLIMAP and COOL simulations is also compared (COOL – CLIMAP anomalies) in order to determine how the different tropical SST boundary conditions influence the simulated climate.

6.3.1 Surface temperature, mean sea level pressure

Surface temperature

The LGM surface temperature anomalies for DJF and JJA are shown in Figures 6.6 and 6.7. While the surface temperatures over ocean are set by the SST boundary conditions shown in Figures 6.1 and 6.2, the continental response to SST forcing is discussed here. The cooler LGM SSTs produce extensive cooling over land which reaches a maximum over the Laurentide and Fennoscandian ice sheets in the Northern Hemisphere where increased elevation and snow coverage contribute to strong surface cooling.

Substantial cooling is seen in both simulations over tropical and mid-latitude continental areas including Europe and North America, with the largest cooling over elevated regions such as the Andes and the Tibetan Plateau. Land surface cooling exceeds that over ocean in both CLIMAP and COOL simulations in agreement with other simulations of LGM climate [eg. *Dong and Valdes*, 1998; *Pinot et al.*, 1999].

The surface temperatures in the COOL simulation are cooler than those in CLIMAP over all continental areas for both DJF and JJA in response to the reduction in tropical SSTs. Although SSTs in the mid-latitudes are the same as for the CLIMAP simulation, the relative continental cooling extends to mid- and high latitudes with temperature anomalies as large as $-9°$C relative to CLIMAP simulated over North America and Greenland in the boreal summer.

Mean sea level pressure

In order to compare pressure fields from the present day and LGM with different topographic elevations, the simulation data are adjusted to a standard topographic height as described by *Walsh et al.* [2000]. This is necessary in order that the total atmospheric mass is conserved to allow comparison of momentum and atmospheric circulation statistics.

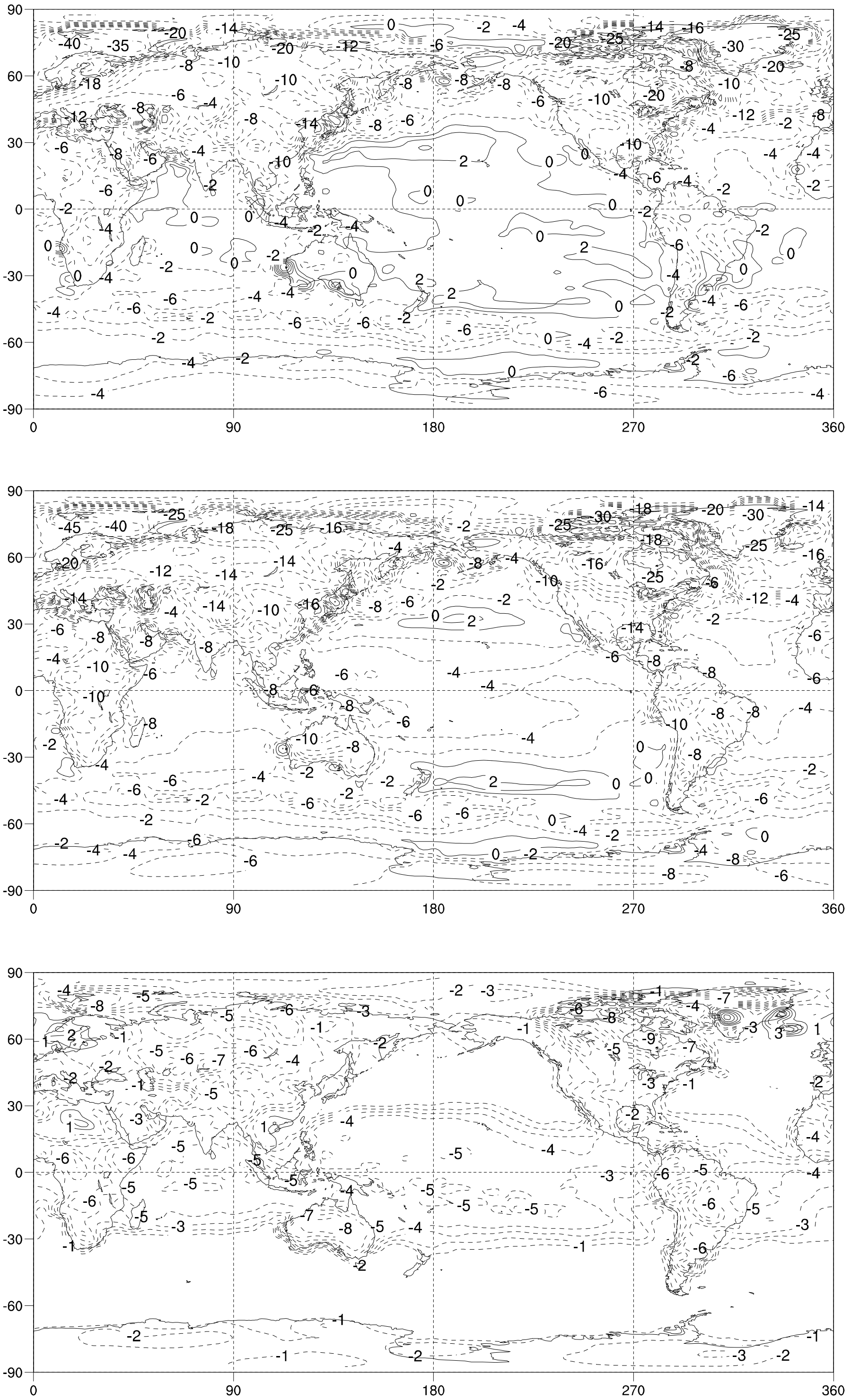

Figure 6.6: DJF surface temperature anomalies: CLIMAP – PD (top), COOL – PD (middle) and COOL – CLIMAP (bottom). Contour interval is 2°C for less than 20°C, 5°C otherwise (top, middle) and 1°C (bottom).

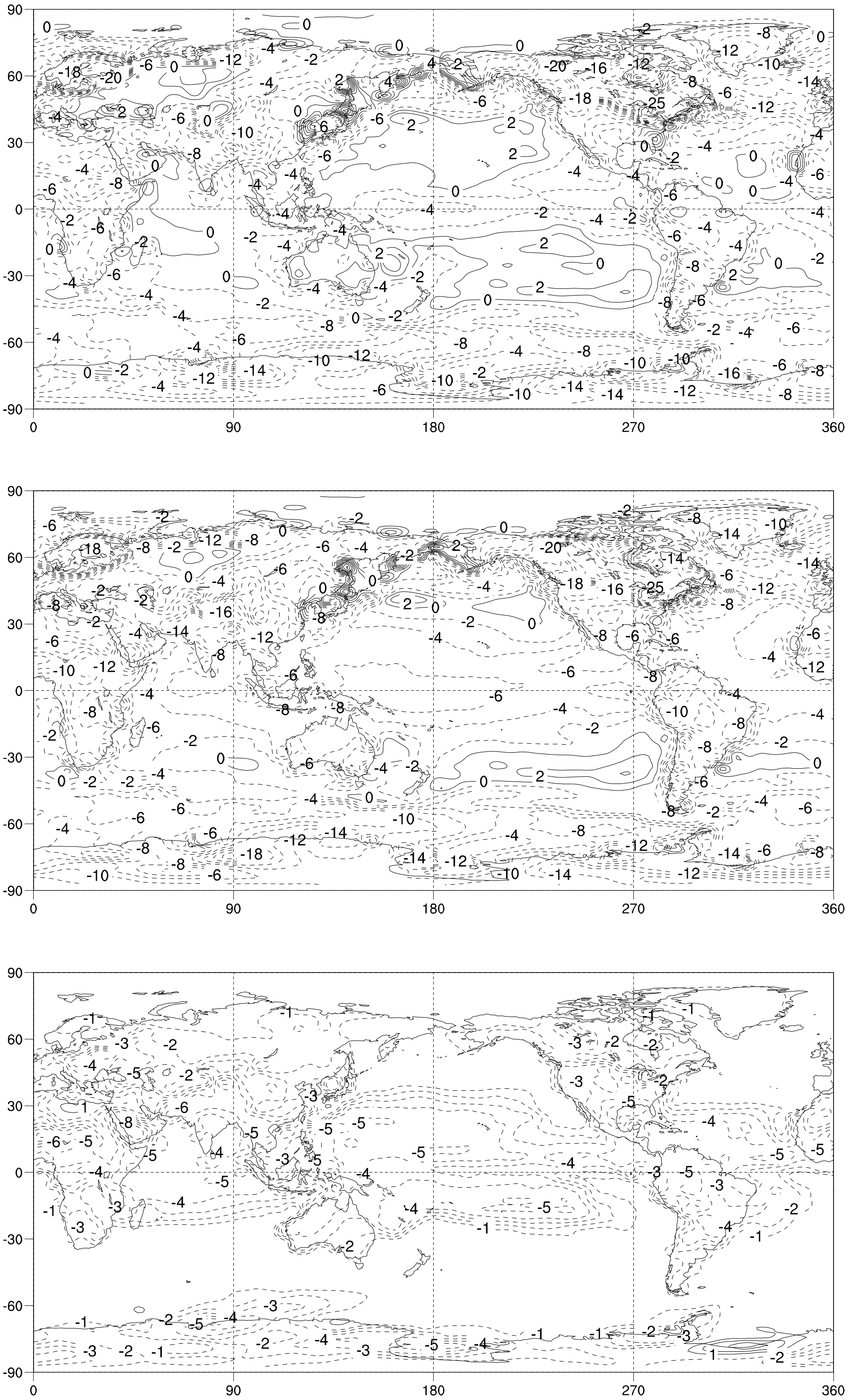

Figure 6.7: JJA surface temperature anomalies: CLIMAP – PD (top), COOL – PD (middle) and COOL – CLIMAP (bottom). Contour interval is 2°C for less than 20°C, 5°C otherwise (top, middle) and 1°C (bottom).

Figures 6.8 and 6.9 show the MSLP anomalies for the CLIMAP and COOL simulations. The modelled pressure anomalies for both runs are similar to those described by *Noone* [2001] for a simulation of LGM climate with CLIMAP SSTs using the same model. In DJF, the Northern Hemisphere continents are cooler producing higher surface pressure, with an intensified effect in COOL. The Aleutian low is strengthened and pressure is reduced across the northern and tropical Pacific Ocean in response to the SST warming in CLIMAP. In the Southern Hemisphere the circumpolar trough is weakened except to the west of the Antarctic Peninsula.

In JJA, negative pressure anomalies are seen in the Indian and Atlantic Oceans, with a strong positive anomaly in the region to the south of Australia extending into the central Pacific and Indian Oceans. A reduction in the heat low over southern Asia is seen in both CLIMAP and COOL simulations, implying a weakened Asian summer monsoon. Positive pressure anomalies over southeast Asia and the western equatorial Pacific, which are larger in COOL, also suggest a weakening of the Walker circulation as discussed below in relation to changes in atmospheric circulation.

6.3.2 Atmospheric circulation

Surface winds

The changes in DJF and JJA wind at the lowest atmospheric level (approximately 75 m above the surface) are shown in Figures 6.10 and 6.11. In DJF both the CLIMAP and COOL simulations produce a strengthening of the circulation associated with the Aleutian Low, a weakened North Atlantic circulation and anticyclonic flow due to the high pressure anomaly to the south of Australia. In the COOL simulation, there is a strengthening of the trade winds in the western Pacific and weakening in the eastern Pacific. The CLIMAP run produces a strengthened north-easterly winter monsoon circulation, while this is weakened in the COOL simulation as the winter land–ocean temperature contrast is enhanced in CLIMAP and reduced in COOL relative to the present day.

In JJA, the CLIMAP simulation produces a weakened south-westerly summer monsoon flow from the Indian Ocean and Arabian Sea to East Asia due to the reduced continental summer heat low. The reduced Asian summer monsoon circulation is also seen in the COOL run as the relative cooling of both land and ocean for this simulation leads to a similar net change in the land–ocean

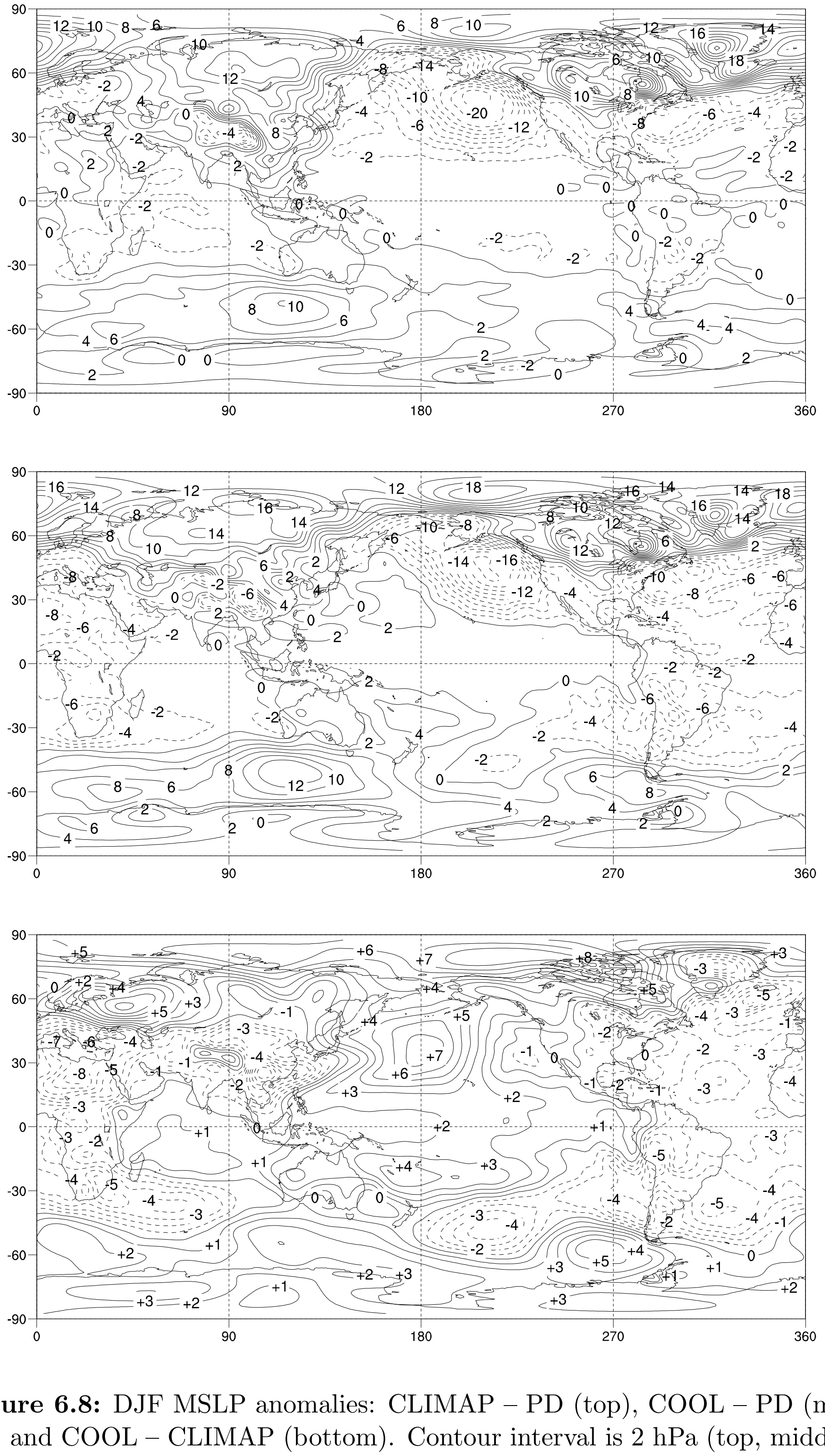

Figure 6.8: DJF MSLP anomalies: CLIMAP – PD (top), COOL – PD (middle) and COOL – CLIMAP (bottom). Contour interval is 2 hPa (top, middle), 1 hPa (bottom).

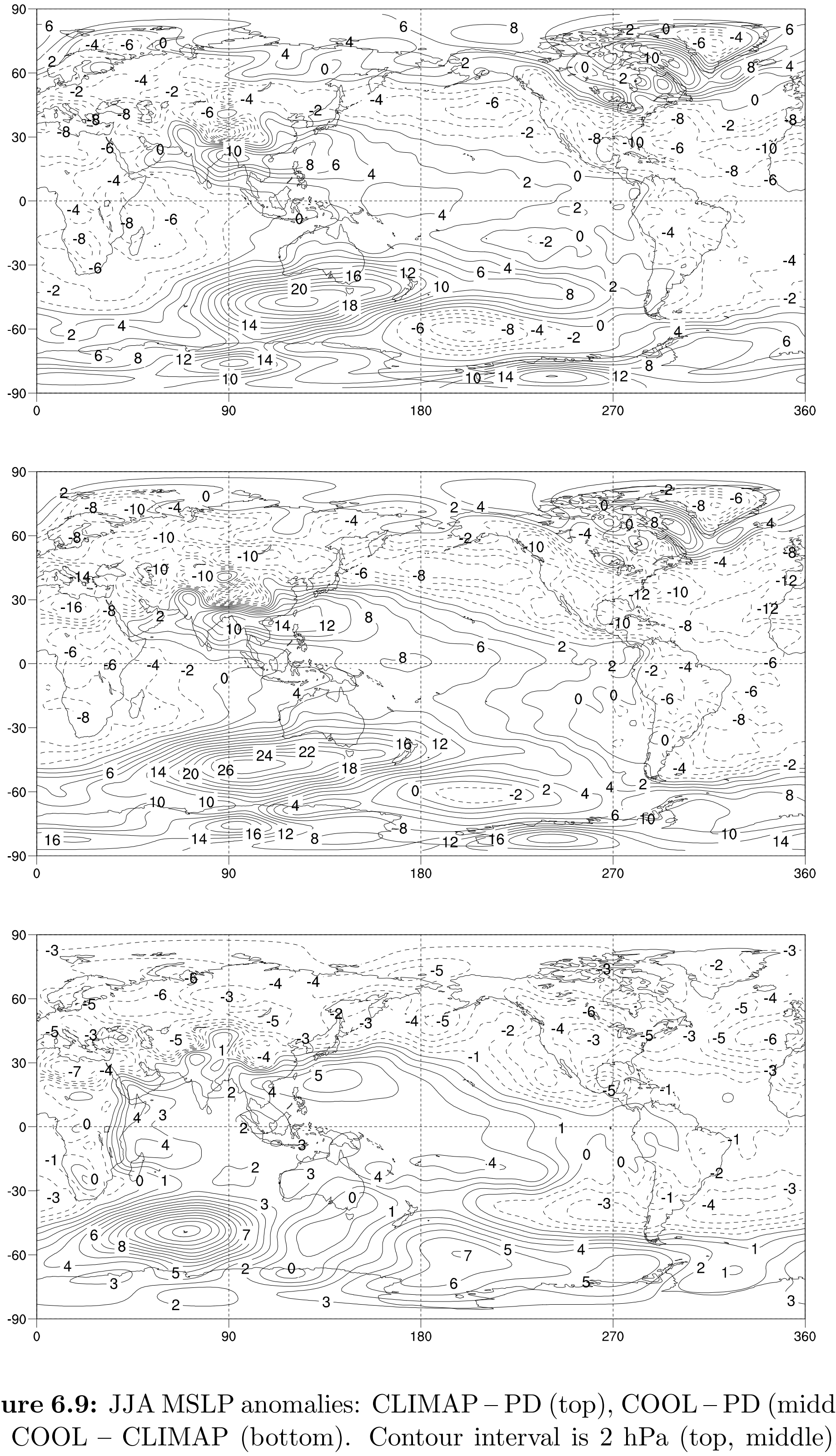

Figure 6.9: JJA MSLP anomalies: CLIMAP – PD (top), COOL – PD (middle) and COOL – CLIMAP (bottom). Contour interval is 2 hPa (top, middle), 1 hPa (bottom).

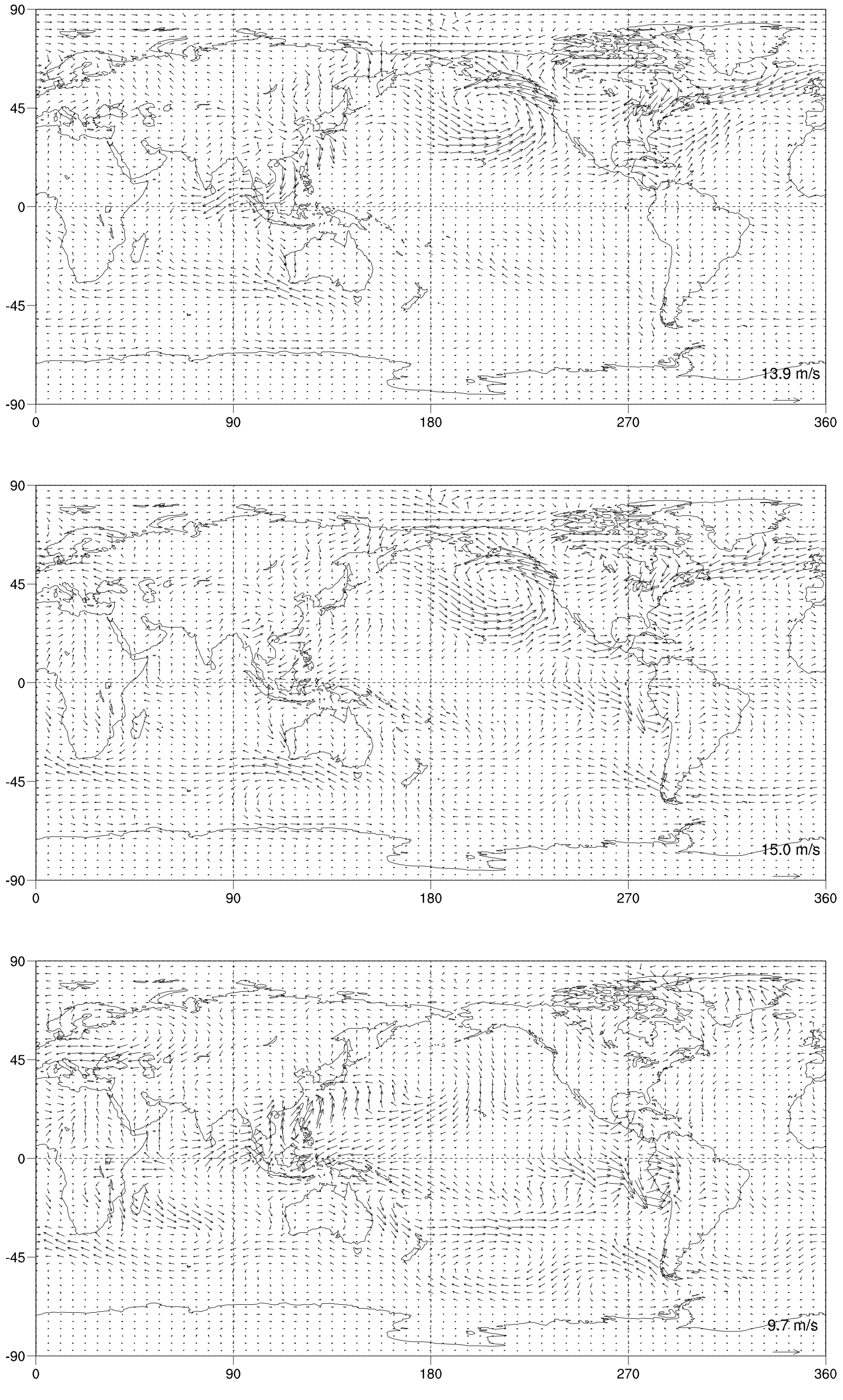

Figure 6.10: DJF wind anomalies at lowest atmospheric level: CLIMAP – PD (top), COOL – PD (middle) and COOL – CLIMAP (bottom). Note different vector scales (bottom right of plots).

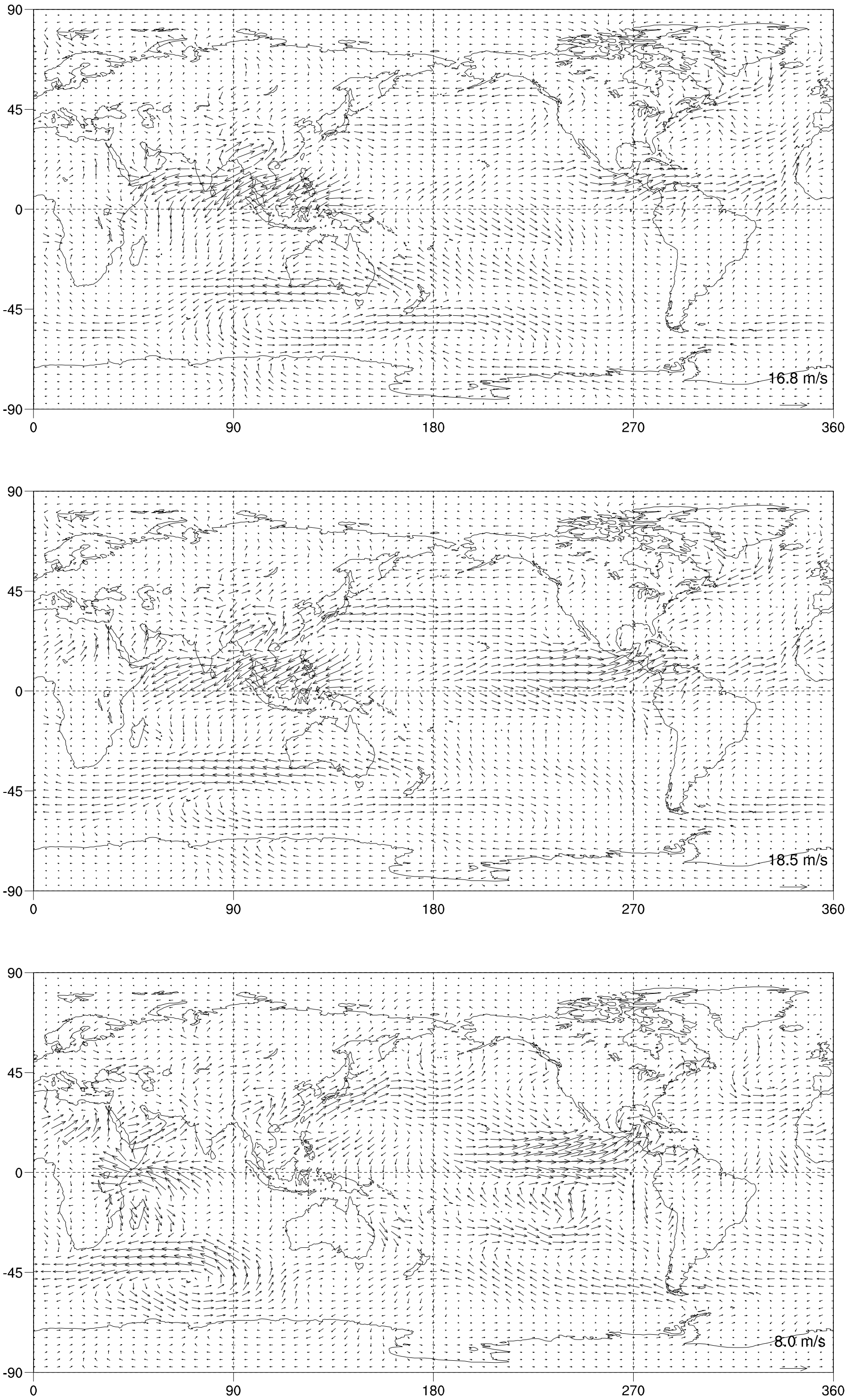

Figure 6.11: JJA wind anomalies at lowest atmospheric level: CLIMAP – PD (top), COOL – PD (middle) and COOL – CLIMAP (bottom). Note different vector scales (bottom right of plots).

temperature gradient. In the CLIMAP simulation, easterly trade winds are weakened in the central Pacific in JJA while the weakening is more pronounced in the eastern Pacific for COOL. While *Noone* [2001] found an overall increase in the trade winds, this is only seen in the western Pacific during JJA, and is associated with the weakening of the south-westerly monsoon flow into the Northern Hemisphere.

Zonal wind cross section

The response to changes in the zonal SST gradient across the tropical Pacific can be seen in changes to the strength of the Walker circulation comprised of the lower level easterly flow and upper level return westerly flow in the zonal wind cross section (Figures 6.12 and 6.13). The COOL SSTs remove the zonal SST gradient across the Pacific, while the CLIMAP zonal SST gradient in the tropical Pacific is similar to the present for both DJF and JJA, as discussed in the previous Section.

The Walker circulation differs from the present day for both CLIMAP and COOL simulations. In DJF, CLIMAP produces a weakened upper level westerly wind and slight weakening of the surface easterlies in the eastern Pacific. In COOL, the Walker circulation appears to almost divide into two cells with the upper and lower level winds reversing direction in the eastern Pacific, and the lower level easterlies strengthening in the western Pacific. The CLIMAP response in JJA is similar to DJF with a weakening of upper level flow in the western Pacific and reversal in the eastern Pacific. In the COOL simulation, the surface easterly flow shifts to the west and extends into the Indian Ocean while the Walker circulation is again divided into two cells with a reversal of the eastern Pacific winds.

The weakening and reorganisation of the Walker circulation in the COOL simulation occurs in response to the reduced zonal SST gradient, as seen in previous studies with zonally average SSTs in which the Walker circulation is weakened or disrupted [*Simmonds and Smith*, 1986; *Simmonds et al.*, 1989]. The disruption of the Walker circulation in the CLIMAP simulation implies that changes in meridional SST gradients may influence the zonal wind structure over the tropical Pacific, as suggested by *Rind* [2000].

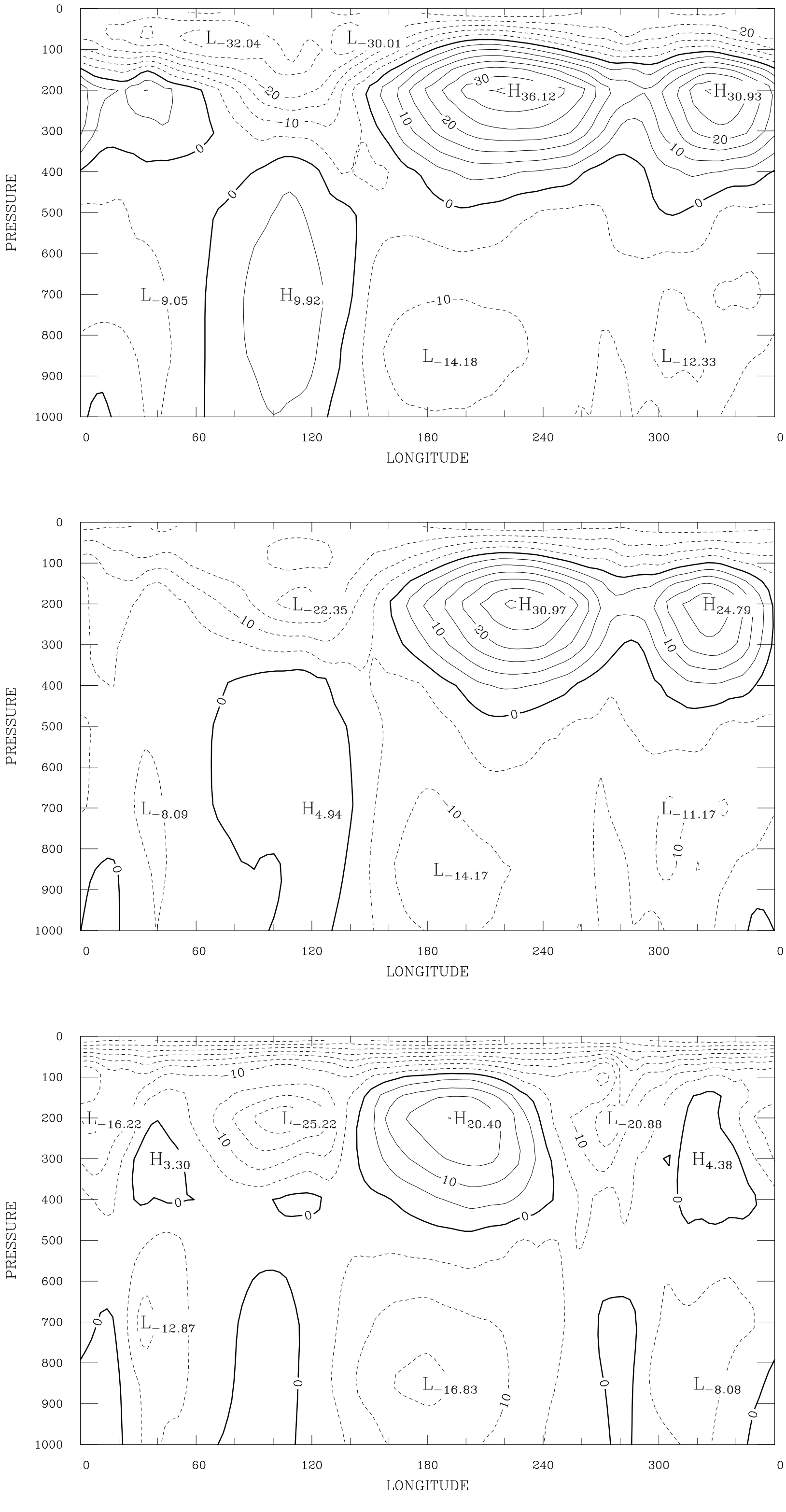

Figure 6.12: DJF average (10°S–10°N) westerly wind zonal cross section: PD (top), CLIMAP (middle) and COOL (bottom). Contour interval is 5 m/s.

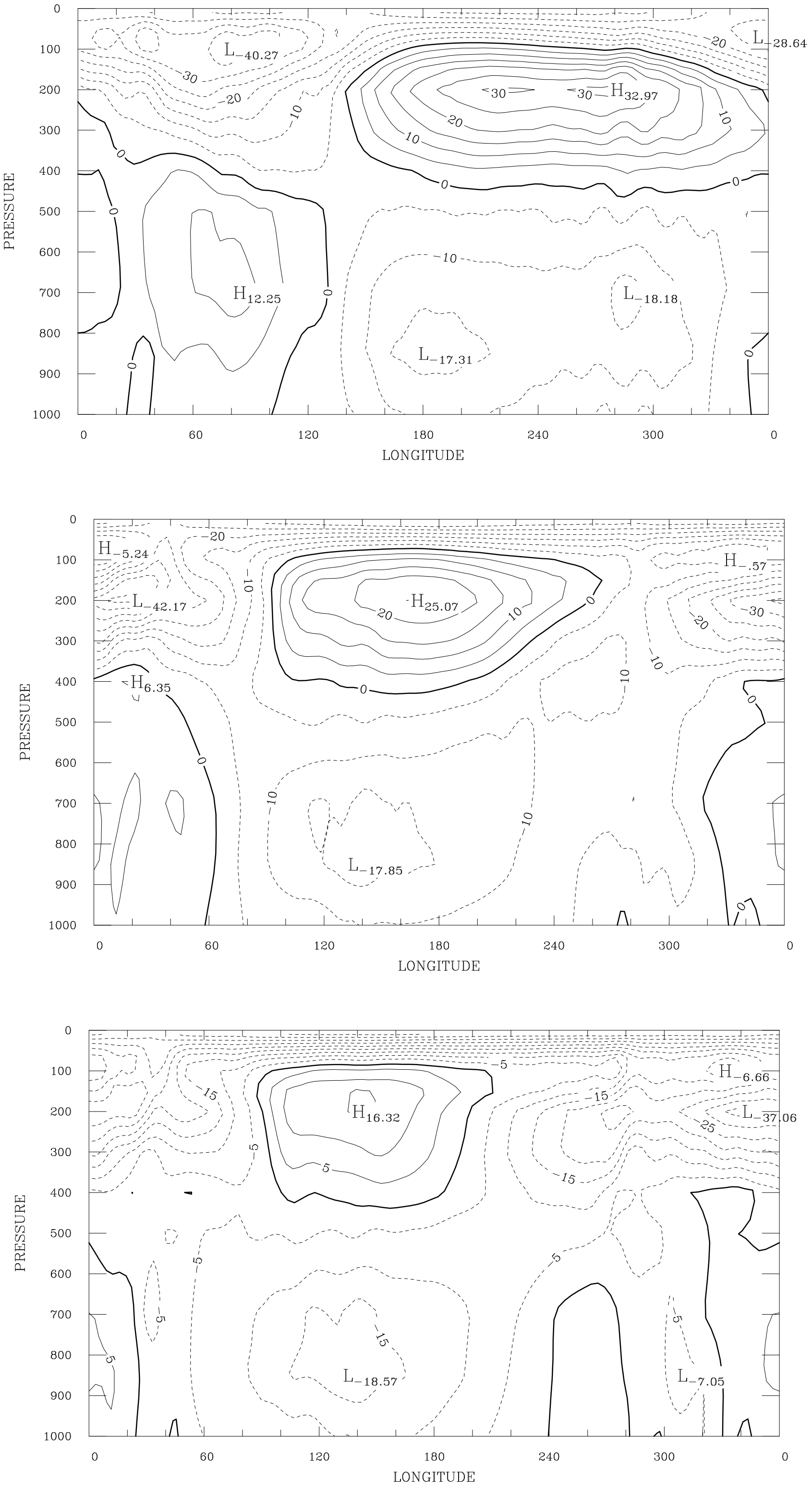

Figure 6.13: JJA average (10°S–10°N) westerly wind zonal cross section: PD (top), CLIMAP (middle) and COOL (bottom). Contour interval is 5 m/s.

Meridional mass flux transport

The meridional mass flux streamfunction cross section is also examined for each LGM simulation and compared with the present day in order to identify changes in meridional atmospheric transport (Figures 6.14 and 6.15). In the CLIMAP simulation a strengthening of the Northern Hemisphere Hadley cell in DJF and a weakening of the northern Ferrell cell is produced, with an increase in the northerly extent of the Hadley cell. The same response is seen in the COOL run, with greater strengthening of the northern Hadley cell. The strengthening of the northern winter Hadley cell may be associated with the strengthened Asian winter monsoon circulation described above.

In JJA, the southern Hadley cell is weakened in both CLIMAP and COOL simulations, although this effect is greatest in CLIMAP, where the southern Ferrell and Polar cells are also strengthened. The northerly extent of the southern Hadley cell is also extended in both simulations. This result agrees with the modelling study of *Rind* [1987], who simulated a weakened southern Hadley cell in July at the LGM due to decreased tropical convergence and precipitation. This may also be associated with the weakening of the Northern Hemisphere summer monsoon under LGM conditions.

6.3.3 Hydrologic cycle

Precipitation

The precipitation anomalies for both simulations are shown in Figures 6.16 and 6.17. There is an overall decrease in precipitation over the tropics (30°S–30°N) in CLIMAP and COOL, with a larger decrease in COOL. Precipitation over the tropical oceans is decreased in both simulations (-0.11 mm/day for CLIMAP, -0.84 mm/day for COOL) in response to cooler mean SSTs. However precipitation over land is increased in both simulations ($+0.16$ mm/day for CLIMAP, $+1.25$ mm/day for COOL). This is in disagreement with the LGM simulations with prescribed CLIMAP and computed SSTs of *Dong and Valdes* [1998] and *Pinot et al.* [1999] who found that precipitation over tropical continents decreased. However *Charles et al.* [2001] found an increase in tropical continental precipitation for an LGM simulation with cooled tropical SSTs.

In DJF, there is an increase in northern Pacific precipitation associated with the deepened Aleutian Low. Precipitation is reduced over southeast Asia and

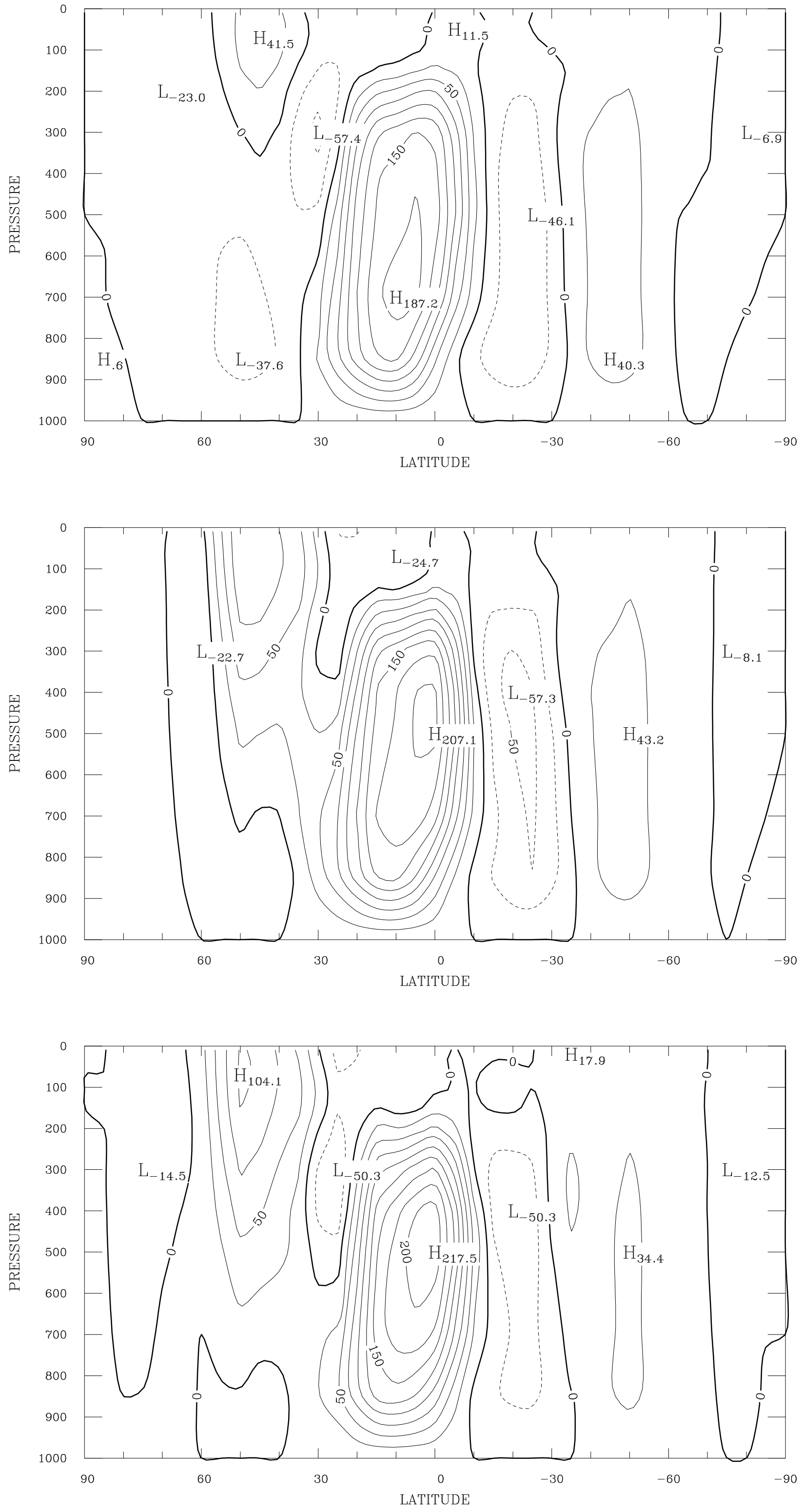

Figure 6.14: DJF zonally average meridional mass flux streamfunction cross section: PD (top), CLIMAP (middle) and COOL (bottom). Units are 10^9 kg/s.

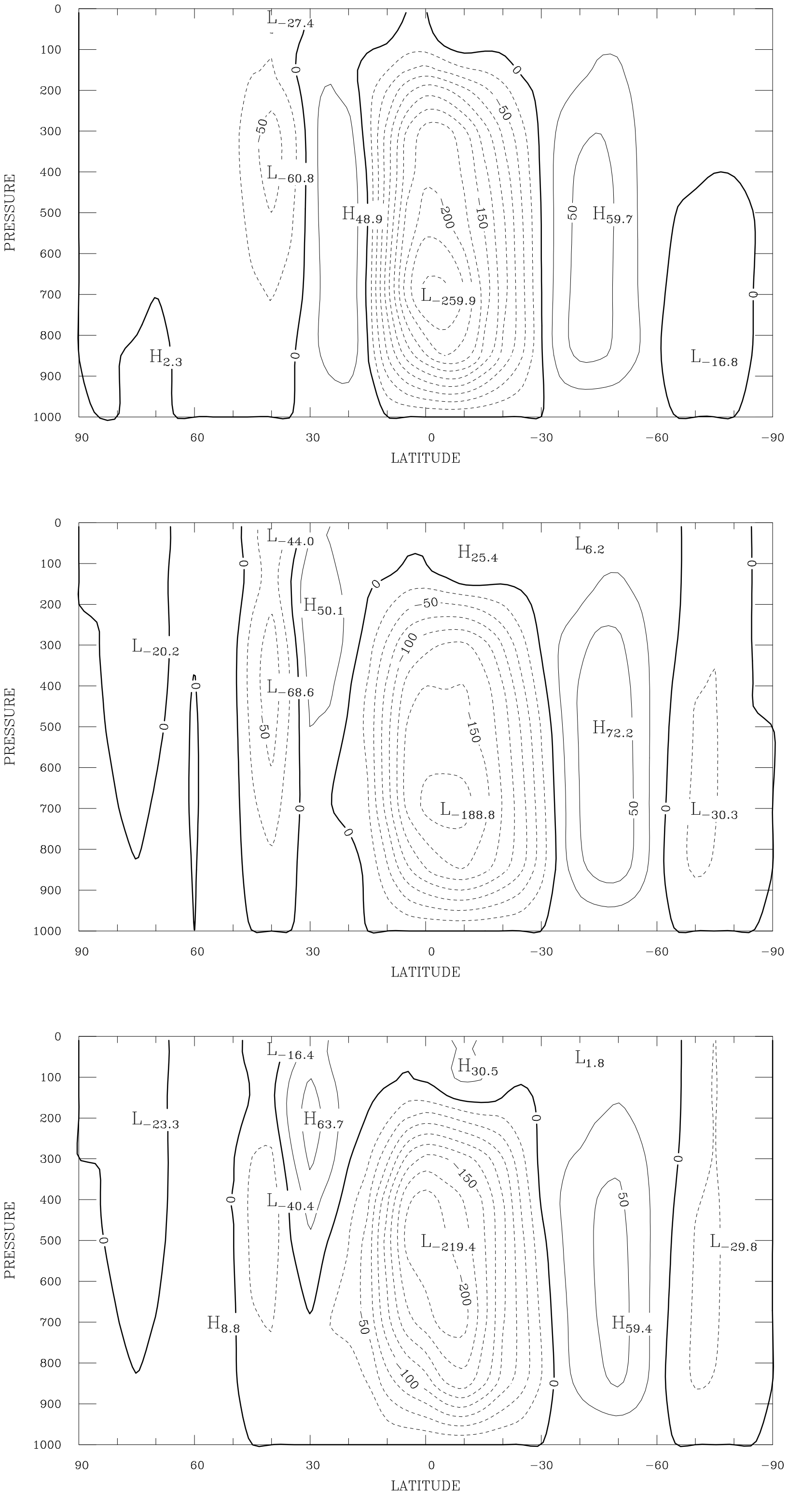

Figure 6.15: JJA zonally average meridional mass flux streamfunction cross section: PD (top), CLIMAP (middle) and COOL (bottom). Units are 10^9 kg/s.

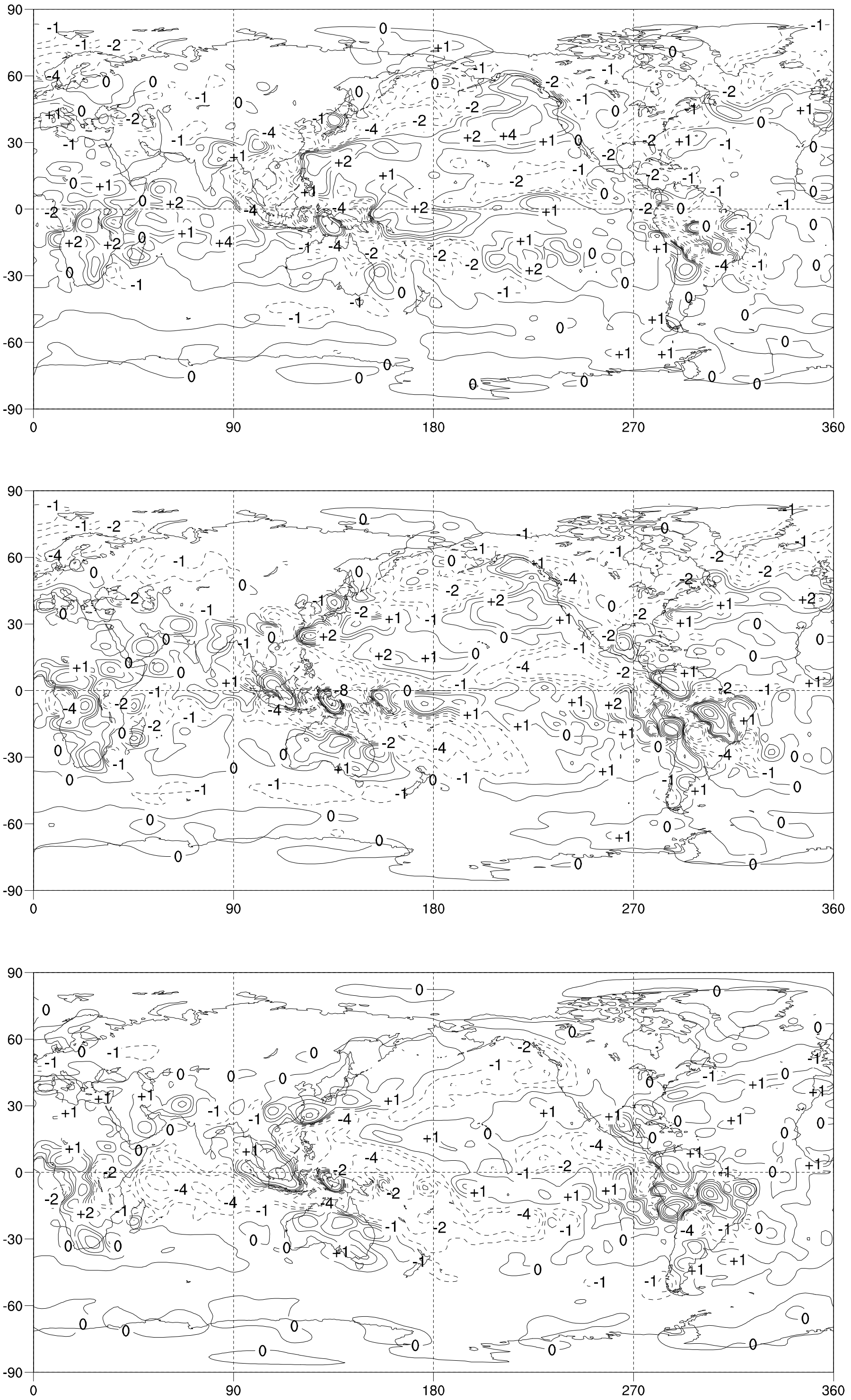

Figure 6.16: DJF precipitation anomalies: CLIMAP – PD (top), COOL – PD (middle) and COOL – CLIMAP (bottom). Contours are ± 0, 1, 2, 4, 8, 12, 16 mm/day.

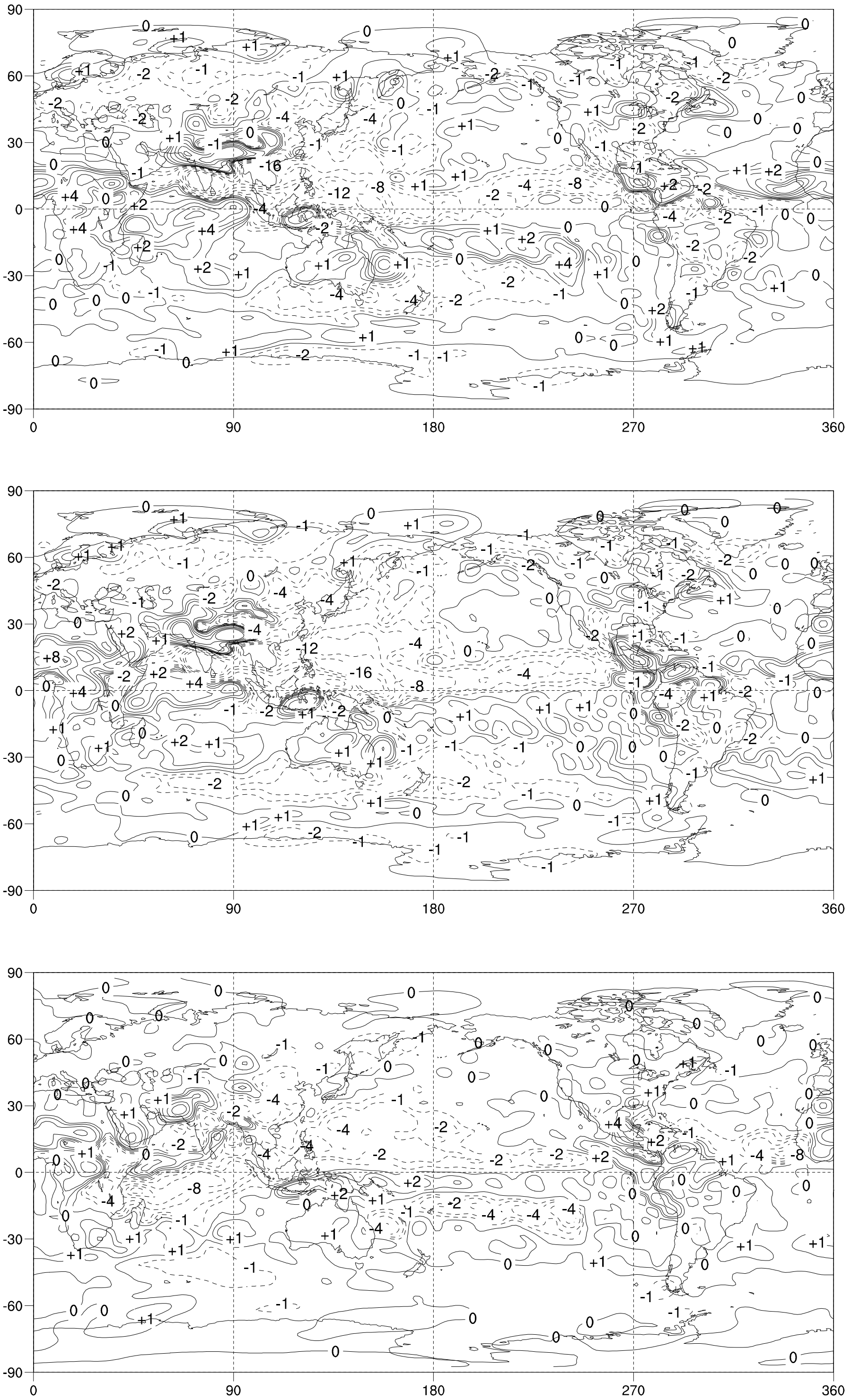

Figure 6.17: JJA precipitation anomalies: CLIMAP – PD (top), COOL – PD (middle) and COOL – CLIMAP (bottom). Contours are ± 0, 1, 2, 4, 8, 12, 16 mm/day.

increased in the central Pacific, consistent with a weakened Walker circulation, in agreement with the LGM simulation of *Rind* [1987] with CLIMAP SSTs. The strengthening of the north-easterly Asian winter monsoon flow in CLIMAP appears to be associated with increased precipitation in the equatorial Indian Ocean. Increased tropical precipitation and slight decreases in the subtropics are consistent with a stronger winter Hadley cell in DJF.

In JJA, there is a reduction in precipitation over East Asia and coastal regions of the Indian subcontinent associated with the weakened Indian and Asian summer monsoons. Convergence in the Pacific sector of the ITCZ is greatly reduced as a result of cooler equatorial SSTs in both simulations, while convergence in the northern tropical Atlantic is increased. The reduction in equatorial precipitation and increase in subtropical precipitation in the Pacific and Indian Oceans is consistent with a weakening of the winter Hadley cell. The reduction in precipitation over the Indonesian region in JJA, despite the strengthened north-easterly flow, may be the result of a decrease in available moisture as the ocean surface area is reduced due to the lower sea level.

The COOL simulation produces an increase in continental precipitation relative to CLIMAP over Australia, South America, South Africa and parts of southeast Asia. There is a relative reduction in precipitation over the western Pacific Ocean, and over much of the tropical ocean where cooler SSTs lead to reduced evaporation and convective activity. Exceptions to this are seen in the southern equatorial Pacific in both seasons, indicating a southward shift in the ITCZ which is also observed in the simulations of *Dong and Valdes* [1998] with computed slab ocean SSTs.

The difference in precipitation anomalies over ocean and land is consistent with the idealised experiments carried out in Chapter 3 with altered mean SSTs and SST gradients under present day conditions. As in those simulations, cooler tropical SSTs lead to reduced precipitation over ocean and increased precipitation over land. Where meridional SST gradients are increased, such as in the DJF CLIMAP simulation, precipitation increases at the equator and decreases in the subtropics. Decreased meridional SST gradients such in the JJA COOL distribution lead to reduced tropical precipitation. The precipitation response to SST forcing in the CLIMAP and COOL simulations may therefore be interpreted as a response to both mean SST changes and changes in the meridional SST gradient.

Evaporation

The anomalies of evaporation for CLIMAP and COOL simulations are shown in Figures 6.18 and 6.19. The mean tropical (30°S–30°N) evaporation is decreased in both CLIMAP and COOL simulations relative to the present day due to cooler average SSTs. As was seen for precipitation, evaporation is increased over tropical land areas in both simulations (+0.07 mm/day for CLIMAP, +0.30 mm/day for COOL), while evaporation is reduced over tropical oceans (−0.37 mm/day for CLIMAP, −1.13 mm/day for COOL).

The spatial distribution of evaporation anomalies follows changes in SSTs and surface winds. In CLIMAP increased evaporation is seen over the tropical and subtropical Pacific, Atlantic and Indian Oceans. Increased evaporation in DJF in particular is associated with the strengthened Aleutian Low, while a local SST maximum in the East China Sea results in a large increase in evaporation. Evaporation over land is reduced over tropical South America and East Asia where precipitation is lower in the CLIMAP simulation.

In the COOL simulation evaporation from tropical oceans decreases relative to CLIMAP in all ocean basins. There is an increase in evaporation over land in the tropics and subtropics over the same regions which experience increased precipitation, suggesting that a larger proportion of local precipitation results from recycled continental moisture. This is consistent with the study of *Charles et al.* [2001] who found a substantial increase in continental moisture recycling in their simulation with cooled tropical SSTs. The relative decrease in tropical oceanic evaporation and increase in precipitation over land in the tropics also implies a greater transport of mid-latitude moisture equatorward.

6.4 Isotopes in precipitation

The response of isotopes in precipitation to simulated LGM climate is examined globally and in comparison with ice core records from the Andes and Tibetan Plateau. The modelled LGM precipitation δ^{18}O anomalies are compared with changes in surface temperature, local precipitation and rainout in order to identify the controls on the LGM isotopic response. The simulated LGM isotopic distribution is also compared with the results of the previous modelling studies of isotopes in the LGM climate which were outlined in Chapter 2.

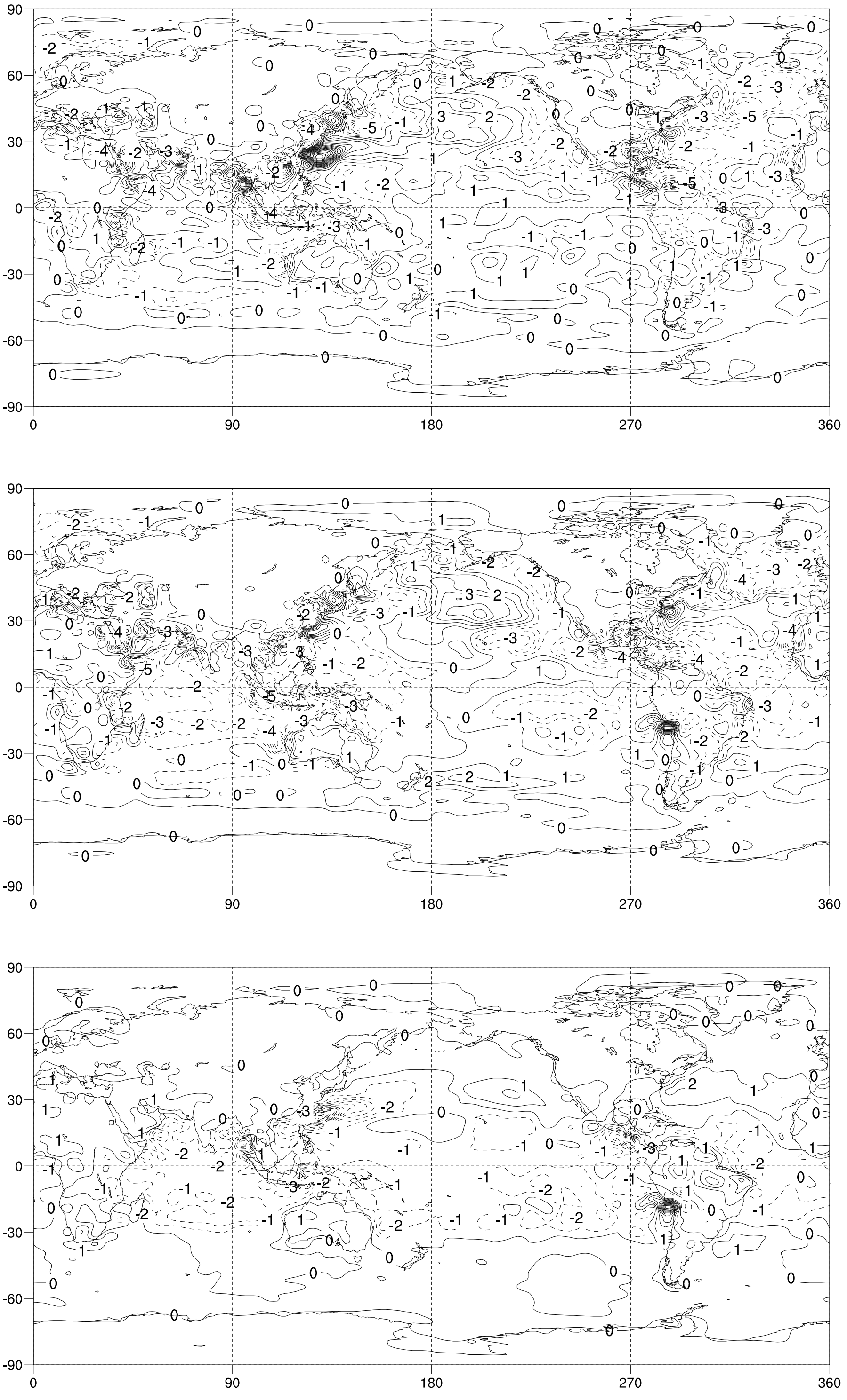

Figure 6.18: DJF evaporation anomalies: CLIMAP – PD (top), COOL – PD (middle) and COOL – CLIMAP (bottom). Contour interval is 1 mm/day.

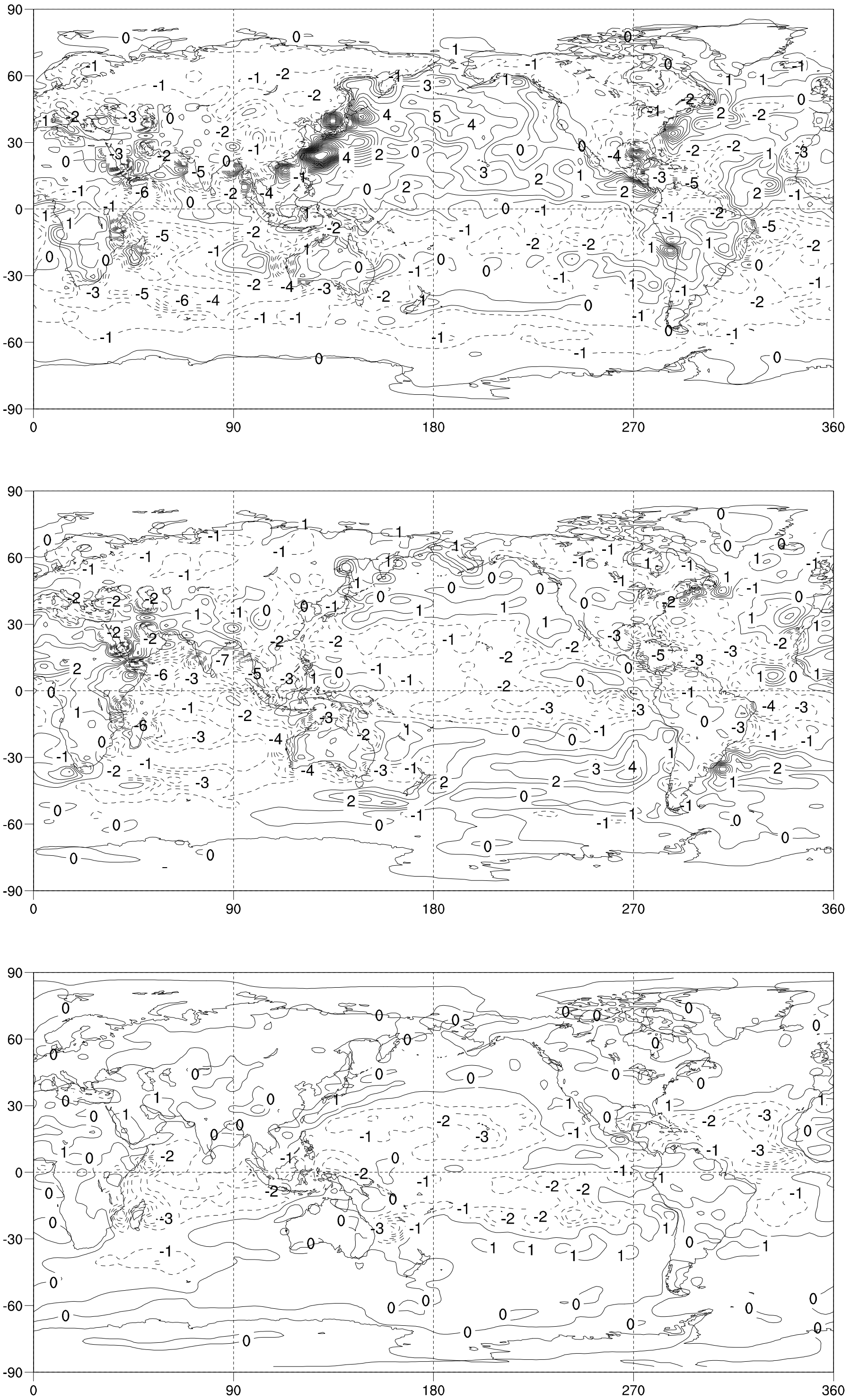

Figure 6.19: JJA evaporation anomalies: CLIMAP – PD (top), COOL – PD (middle) and COOL – CLIMAP (bottom). Contour interval is 1 mm/day.

6.4.1 Precipitation isotopic ratios

Precipitation δ^{18}O for CLIMAP and COOL simulations is compared with the present day DJF and JJA seasonal averages (Figures 6.20 and 6.21). For both simulations the mean δ^{18}O values over tropical and mid-latitude ocean basins are enriched by 1–2‰ in response to the mean ocean enrichment in both DJF and JJA, in agreement with previous isotopic modelling studies of the LGM [eg. *Jouzel et al.*, 1994; *Hoffmann and Heimann*, 1997]. Positive precipitation δ^{18}O anomalies are seen in the western Pacific, especially in the COOL simulation, in response to reduced precipitation. Regions of greater isotopic depletion over ocean are seen in the Indian Ocean for both COOL and CLIMAP simulations and in the northern tropical Atlantic in JJA for CLIMAP.

Over tropical continents the slight weakening of the Southern Hemisphere summer monsoon in both simulations produces positive isotopic anomalies over northern Australia and Indonesia. In JJA reduced Asian and Indian summer monsoon precipitation and weaker transport of maritime moisture inland results in positive isotopic anomalies over East Asia and parts of India. Increased isotopic depletion is seen over West Asia and equatorial Africa, with greater depletion over the Tibetan Plateau and tropical South America and Central America in the COOL simulation.

Large increases in isotopic depletion are seen over mid-latitude regions of Europe and North America in DJF. At high latitudes the increased elevation of the Northern Hemisphere ice sheets results in large negative isotopic anomalies, while large negative anomalies are also seen over Antarctica and the Southern Hemisphere sea ice regions. The relatively greater isotopic depletion over mid-latitude and polar continents in the COOL simulation is in agreement with the isotopic response to cooled tropical SSTs in the study of *Charles et al.* [2001].

In the COOL simulation, the greater reduction in tropical precipitation than in CLIMAP results in less depleted precipitation δ^{18}O values in the northern equatorial Pacific and western Pacific Warm Pool in particular. The relative enrichment of precipitation δ^{18}O in COOL despite stronger surface cooling confirms that precipitation amount rather than surface temperature determines the isotopic signal over the tropical oceans even on glacial time scales. In the eastern equatorial Pacific, a relative increase in precipitation in COOL is associated with increased isotopic depletion.

The COOL – CLIMAP precipitation δ^{18}O anomaly over land is generally

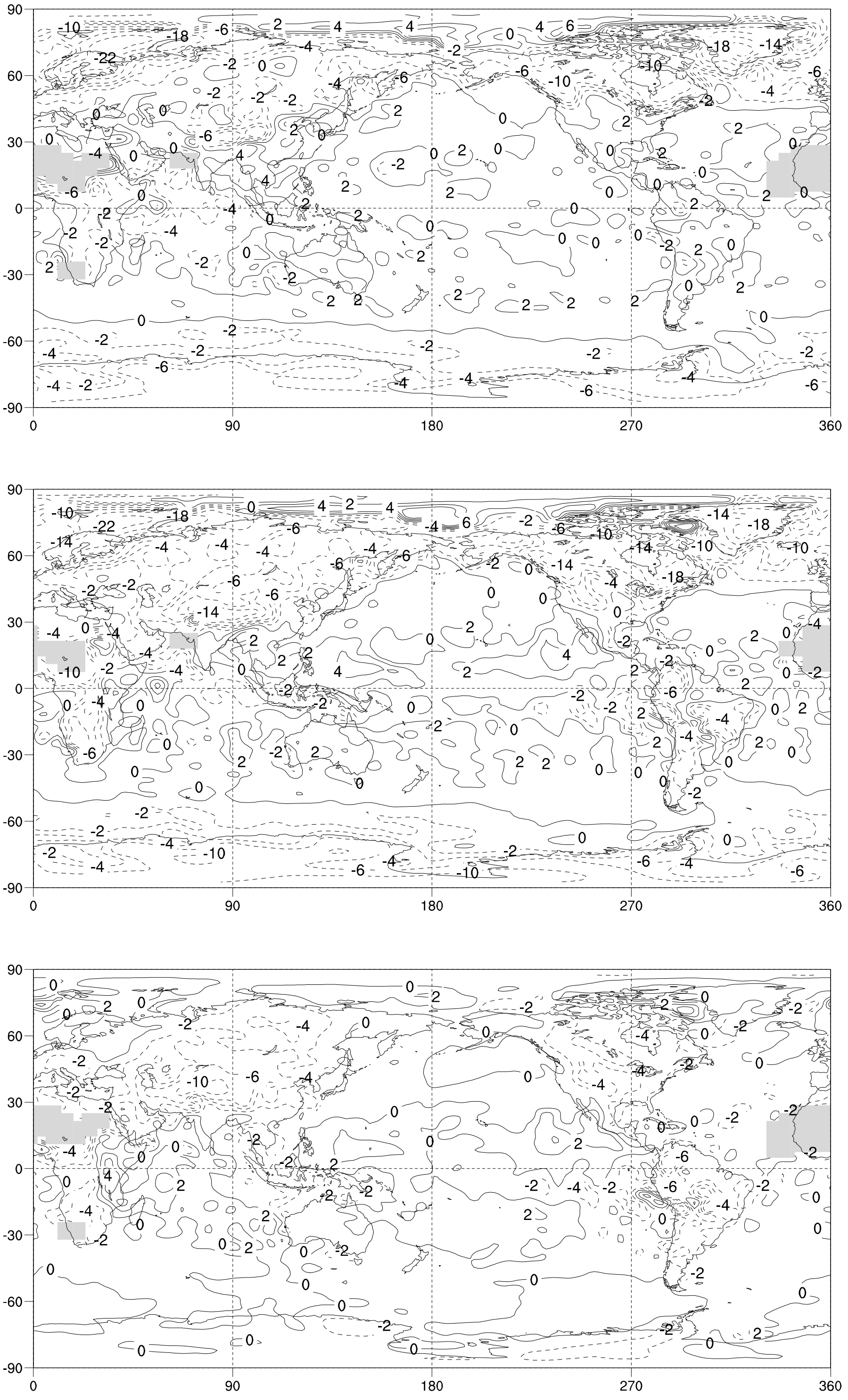

Figure 6.20: DJF precipitation δ^{18}O anomalies: CLIMAP – PD (top), COOL – PD (middle) and COOL – CLIMAP (bottom). Contour interval is 4‰ for differences larger than 6‰ and 2‰ otherwise.

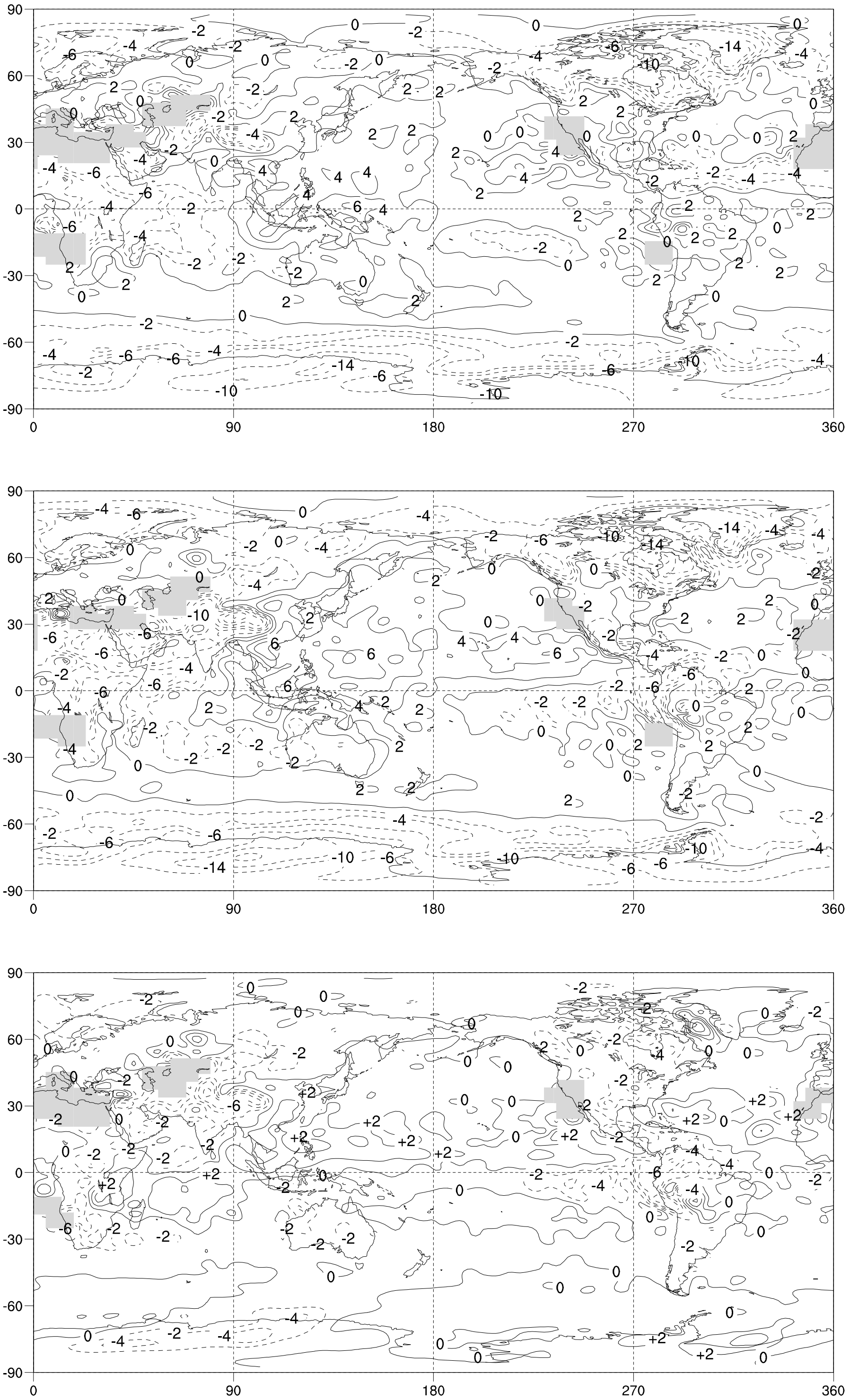

Figure 6.21: JJA precipitation δ^{18}O anomalies: CLIMAP – PD (top), COOL – PD (middle) and COOL – CLIMAP (bottom). Contour interval is 4‰ for differences larger than 6‰ and 2‰ otherwise.

negative at all latitudes, including over tropical continents. This may be partly due to the cooler land surfaces in COOL producing greater isotopic depletion. Greater precipitation over most tropical continental areas in COOL also contributes to the more depleted precipitation δ^{18}O. The greater importance of precipitation amount than temperature for the isotopic response over tropical continents is seen over East Asia and tropical East Africa, where reduced precipitation in COOL is associated with positive δ^{18}O anomalies relative to CLIMAP despite greater land surface cooling.

Charles et al. [2001] suggests that the greater continental isotopic depletion in LGM simulations with cooled tropical SSTs may result from increased recycling of continental moisture. As described in Chapter 2, the increase in precipitation and evaporation over land in the tropics results in a greater proportion of moisture originating from more isotopically depleted continental sources [*Koster et al.*, 1993]. However our results suggest that cooling of land surfaces and increased precipitation over tropical continents may be sufficient to explain the greater isotopic depletion in COOL, although the role of continental recycling may also be important in some regions such as tropical South America. This effect is discussed further below in reference to the isotopic signal in Andean ice cores.

6.4.2 Comparison with ice core records

The modelled isotopic signal in precipitation is examined in more detail over the regions of the Andes in South America and the Tibetan Plateau in Asia where ice core records from the LGM can be compared with the modelled δ^{18}O in precipitation. The regional climate and isotope anomalies are briefly described before comparing the isotopic ratios at the ice core sites.

Andes

As shown in Figures 6.22 and 6.23, surface temperatures are cooler over South America in CLIMAP and COOL than the present day, with the greatest cooling found along the west coast in the region corresponding to the Andes. The 850 hPa winds anomalies indicate a weaker easterly flow across tropical South America, which is more pronounced in COOL than CLIMAP. Precipitation over South America shows a non-uniform response to glacial conditions, with positive and negative anomalies in both simulations. The precipitation and

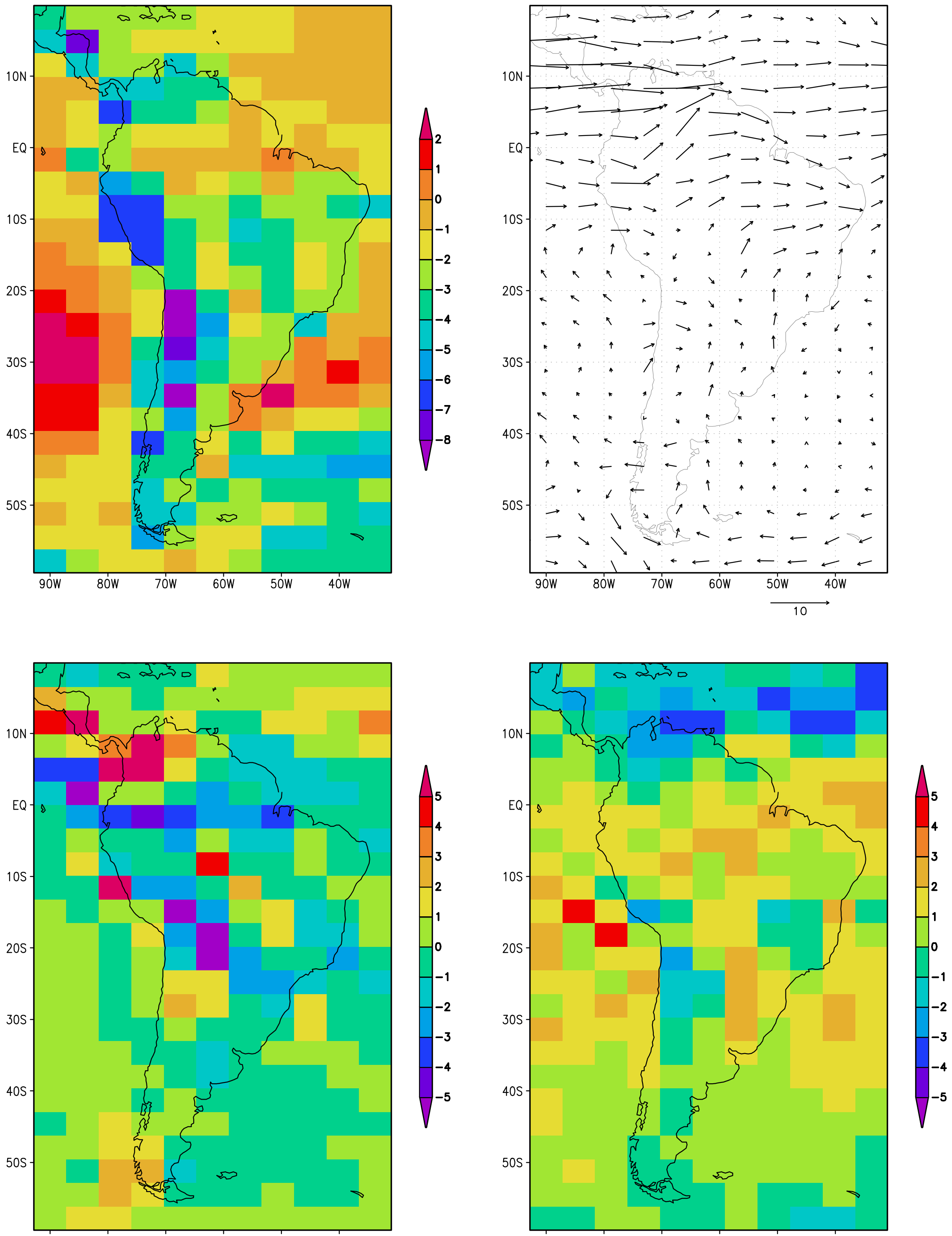

Figure 6.22: CLIMAP surface temperature (top left), 850 hPa wind (top right), precipitation (bottom left) and δ^{18}O (bottom right) anomalies over South America. Units are °C, m/s, mm/day and ‰ respectively.

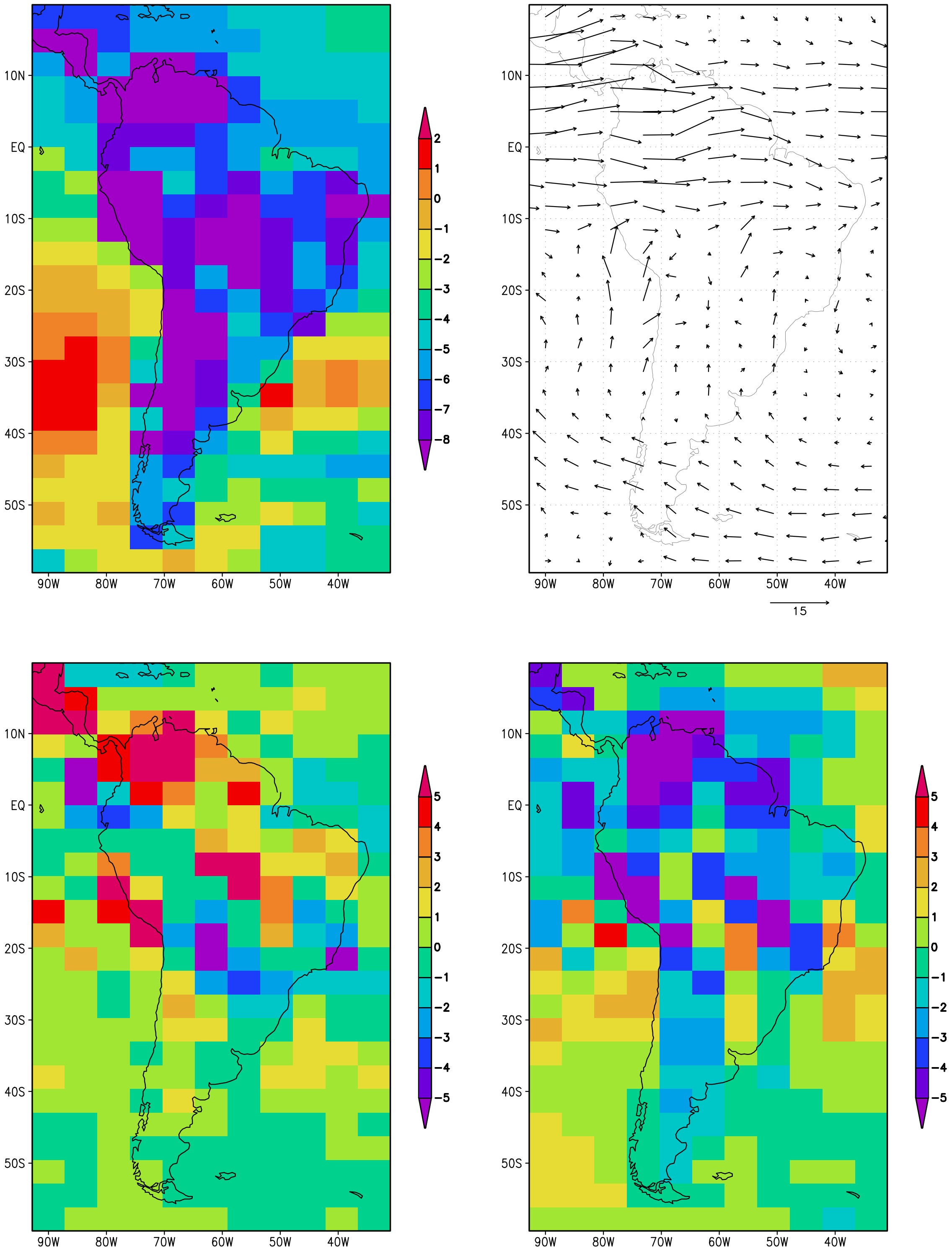

Figure 6.23: COOL surface temperature (top left), 850 hPa wind (top right), precipitation (bottom left) and $\delta^{18}O$ (bottom right) anomalies over South America. Units are °C, m/s, mm/day and ‰ respectively.

temperature anomalies in COOL are larger than in CLIMAP, and there is an overall increase in precipitation over tropical South America in COOL which is not seen in CLIMAP.

The modelled precipitation δ^{18}O anomalies over this region show considerable spatial variability. Most of tropical South America, including the Amazon basin, displays positive isotopic anomalies in CLIMAP whereas the isotopic anomalies in COOL are mostly negative over land. The more isotopically depleted precipitation over the Amazon in COOL is consistent with both cooler land surface temperatures and increased precipitation amounts as well as increased recycling of continental moisture.

Locally over the Andes, land surface temperatures are reduced in both CLIMAP and COOL simulations, with a greater reduction in COOL. Precipitation in the region of the Huascaran and Sajama ice core sites, indicated on Figures 6.22 and 6.23, is reduced in CLIMAP at both sites and increased at both sites in COOL. The increased Andean precipitation in the COOL simulation is in agreement with palaeo-evidence of higher lake levels on the Altiplano at the LGM [*Farrera et al.*, 1999].

The observed LGM δ^{18}O anomalies in the Huascaran and Sajama ice cores are -4.4‰ and -5.4‰ respectively [*Thompson et al.*, 1995, 1998], as described in Chapter 2. The modelled CLIMAP anomalies interpolated to the ice core locations are $+1.5$‰ and $+0.6$‰, while the modelled COOL anomalies are -6.5‰ and -8.6‰, in better agreement with the observed values. The modelled isotopic anomalies suggest a local precipitation amount control on δ^{18}O rather than a local temperature control, as temperatures are cooler in both simulations.

In addition to local climate influences, we consider the change in rainout over the Amazon basin which constitutes the strongest influence on present day observed and modelled Andean ice core δ^{18}O, as discussed in Chapter 5. The net change in precipitation minus evaporation over the Amazon basin (0°– 10°S, 280°– 325°E) is -0.24 mm/day for CLIMAP and $+1.29$ mm/day for COOL, despite a decrease in average evaporation over the basin in both simulations. The positive Andean precipitation δ^{18}O anomaly in CLIMAP and the negative anomaly in COOL are therefore also consistent with the modelled change in rainout over the Amazon basin.

While *Charles et al.* [2001] identified a strong spatial correlation between precipitation δ^{18}O anomalies and the extent of continental recycling, our results indicate that the extent of rainout is a more important control on local and downstream precipitation δ^{18}O. The increased proportion of moisture originating from continental evaporation is likely to result from increased precipitation over land, while the extent of recycling itself only constitutes a second order control on precipitation δ^{18}O, as discussed in Chapter 2.

An additional consideration is the role of changes in moisture source regions for Andean precipitation in the modelled LGM climate. The reverse trajectories of moisture from precipitation events over four grid points in the region of the Andean ice core sites were tracked using a three-dimensional Lagrangian tracking scheme [*Noone*, 2001]. The scheme uses six-hourly instantaneous wind fields to calculate back-trajectories from a specified pressure sigma level above the grid points ($\sigma = 0.75$ or approximately 500 hPa, corresponding to the average condensation level above the tropical Andes). The trajectories were traced to their location four days prior to the precipitation events.

The trajectories for present day, CLIMAP and COOL simulations for the upper quartile of precipitation totals during DJF (the summer wet season) are shown in Figure 6.24. The upper quartile of DJF precipitation days represents high precipitation events which are likely to contribute a large proportion of the annual snow accumulation at the Andean ice core sites. It is noted that such high precipitation events may not be representative of the average precipitation conditions, and that the seasonal distribution of precipitation may have varied from the LGM to the present day.

The density of the four-day reverse trajectory origin points was also calculated in order to estimate the moisture source regions for Andean precipitation in each simulation (Figure 6.25). The density was normalised by dividing all values by the total number of trajectories in the upper quartile in order to allow the PD, CLIMAP and COOL density distributions to be compared without bias due to the different number of trajectories for each simulation.

In the present day, both Pacific and Atlantic Ocean moisture sources contribute to precipitation over the Andean ice core sites. The trajectory origin point density distribution indicates that approximately half of the moisture originates in each source region for the upper quartile of summer precipitation events. A similar distribution is seen for the CLIMAP simulation, with a reduction in the distance from the Atlantic source due to the weaker easterly flow over the Amazon basin, and a slightly greater contribution from Pacific mid-latitude sources.

The COOL simulation produces a substantially different distribution of tra-

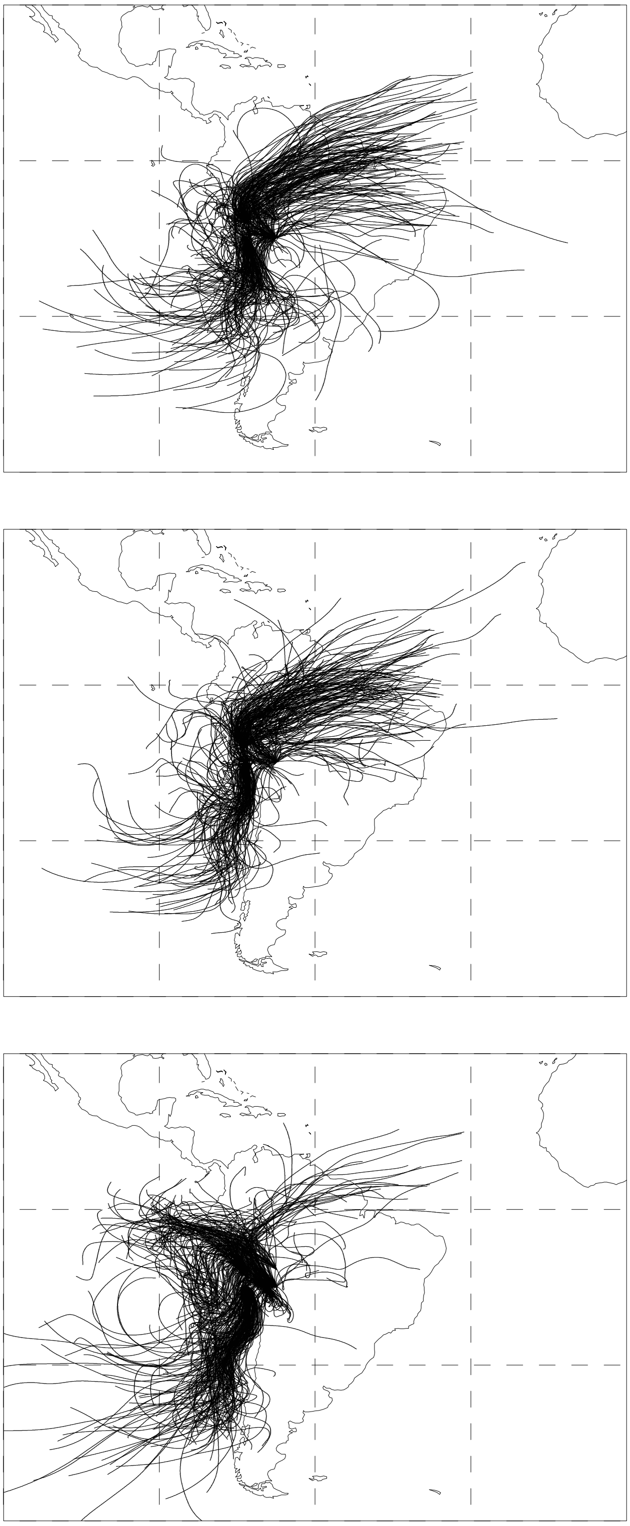

Figure 6.24: Moisture trajectories for the top quartile of precipitation days in DJF for PD (top), CLIMAP (middle) and COOL (bottom). Trajectories track moisture back to location four days prior to precipitation event.

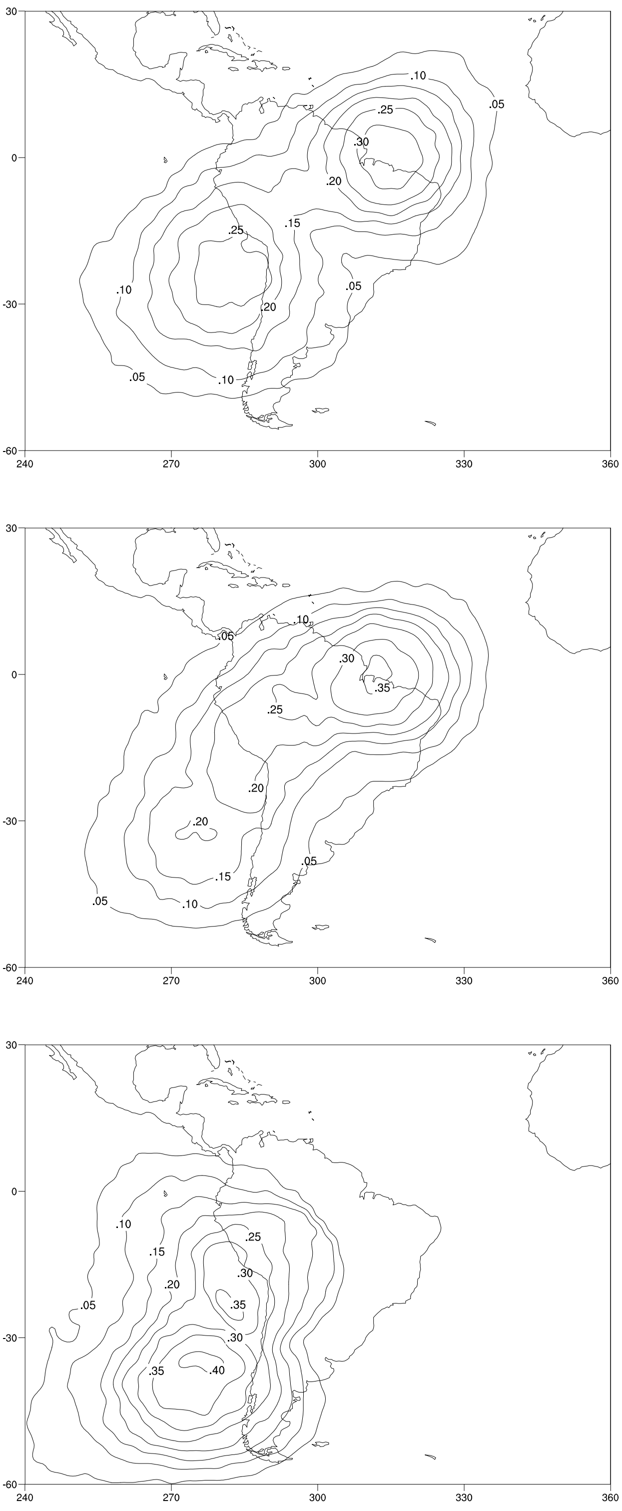

Figure 6.25: Moisture trajectory density four days prior to precipitation events for the upper quartile of precipitation days in DJF for PD (top), CLIMAP (middle) and COOL (bottom). Contour interval is 0.05 or 5% of total trajectories.

jectories. The contribution of Atlantic moisture to the upper quartile of precipitation is greatly reduced, with an increased contribution from Pacific mid-latitude sources. This change in moisture source regions is consistent with the greater weakening of the easterly Atlantic to Pacific tropical circulation in COOL and the increase in northward flow along the west coast of South America as seen in Figure 6.23. While the topographic forcing is the same in the CLIMAP and COOL simulations, the change in ocean and land surface temperatures induces substantially different lower atmospheric circulation regimes over the region.

The change in moisture source regions for the COOL simulation may contribute to the greater isotopic depletion over the Andes in this simulation, as seen in Figure 6.23. Moisture from the Pacific mid-latitudes may undergo greater rainout during orographic lifting over the Andes, as suggested by the large increase in precipitation in COOL over the west coast of South America between 20°S and 10°S. A more detailed investigation of the isotopic signatures of Pacific and Atlantic moisture is beyond the scope of this study. However the change in moisture source regions in the COOL simulation suggests that changes in atmospheric circulation at the LGM may influence isotopic ratios in precipitation in addition to the role of temperature and precipitation changes.

We conclude that the results of the CLIMAP and COOL simulations are not inconsistent with the interpretation of LGM Andean ice core depletion as a result of greater rainout of moisture over the Amazon basin at the LGM [*Pierrehumbert*, 1999], as well as increased precipitation amounts over both the Amazon and Andes at the LGM [*Ramirez et al.*, 2003]. However the reduced contribution of Atlantic moisture in the COOL simulation implies that changes in rainout over the Amazon may be less important than the changed transport and rainout of Pacific moisture in this simulation. This effect is likely to be partly a result of the low resolution of the Andean mountain range in the model, as discussed in Chapter 5.

The interpretation of *Thompson et al.* [2000a] that the isotopic records reflect regional cooling is not strongly supported by our results, as cooling in our simulations is associated with both positive and negative Andean δ^{18}O anomalies depending on changes in local precipitation amount, rainout over the Amazon basin and moisture source. Instead, cooling of LGM SSTs and land surfaces influences the isotopic record indirectly through the resulting changes in precipitation and atmospheric circulation.

Tibetan Plateau

Over India and West Asia, the LGM modelled climate (Figures 6.26 and 6.27) is dominated by the influence of the increased elevation of the Tibetan Plateau, with local surface cooling of up to −11°C in CLIMAP and −16°C in COOL. The weakened Asian and Indian summer monsoons are associated with the reversal in the mean 850 hPa circulation over the tropical Indian Ocean to a predominantly easterly flow, bringing moisture from the western Pacific inland via the Bay of Bengal. Precipitation is reduced in both simulations over East Asia and southern India, but increased inland over West Asia and the Tibetan Plateau, consistent with the observed lower soluble aerosol content of LGM ice core records [*Thompson*, 2000] and evidence of higher lake levels on the Tibetan Plateau at the LGM [*Yu et al.*, 2000].

Over the Tibetan Plateau, surface temperatures are substantially cooler than the present day for both CLIMAP and COOL simulations, while precipitation is increased at the Tibetan ice core sites, with a larger increase at the Dasuopu site and in the COOL simulation. Our simulations are in a agreement with the reconstruction of colder and wetter conditions on the Tibetan Plateau at the LGM of *Thompson* [2000]. The observed LGM isotopic depletion in the Guliya core is −4.1‰ and −2‰ in the Dunde core [*Thompson et al.*, 1989, 1997]. For the CLIMAP simulation the LGM anomaly at Guliya is −6.1‰, −1.7‰ at Dunde and +1.3‰at Dasuopu. For the COOL simulation, the anomaly at Guliya is −13.4‰, −2.9‰ at Dunde and −3.9‰at Dasuopu.

The modelled isotopic anomalies at Guliya and Dunde are a result of cooler local surface temperatures, greater local precipitation and increased rainout of moisture during transport to the northern Tibetan Plateau. While the MUGCM may overestimate the extent of the precipitation response to increased elevation and cooler land surface temperatures, our results suggest that the CLIMAP SST reconstruction produces isotopic depletion over the Tibetan Plateau which corresponds to that observed in LGM ice core records. The imposition of cooler SSTs in the COOL simulation leads to greater land surface cooling and increased precipitation which results in an overestimation of isotopic anomalies.

The modelled isotopic response to LGM climate at Dasuopu cannot be compared with observations as the ice core record at this site only extends to 1000 years BP. However the modelled response at this location illustrates the role of non-local climate factors in influencing isotopic ratios in precipitation over

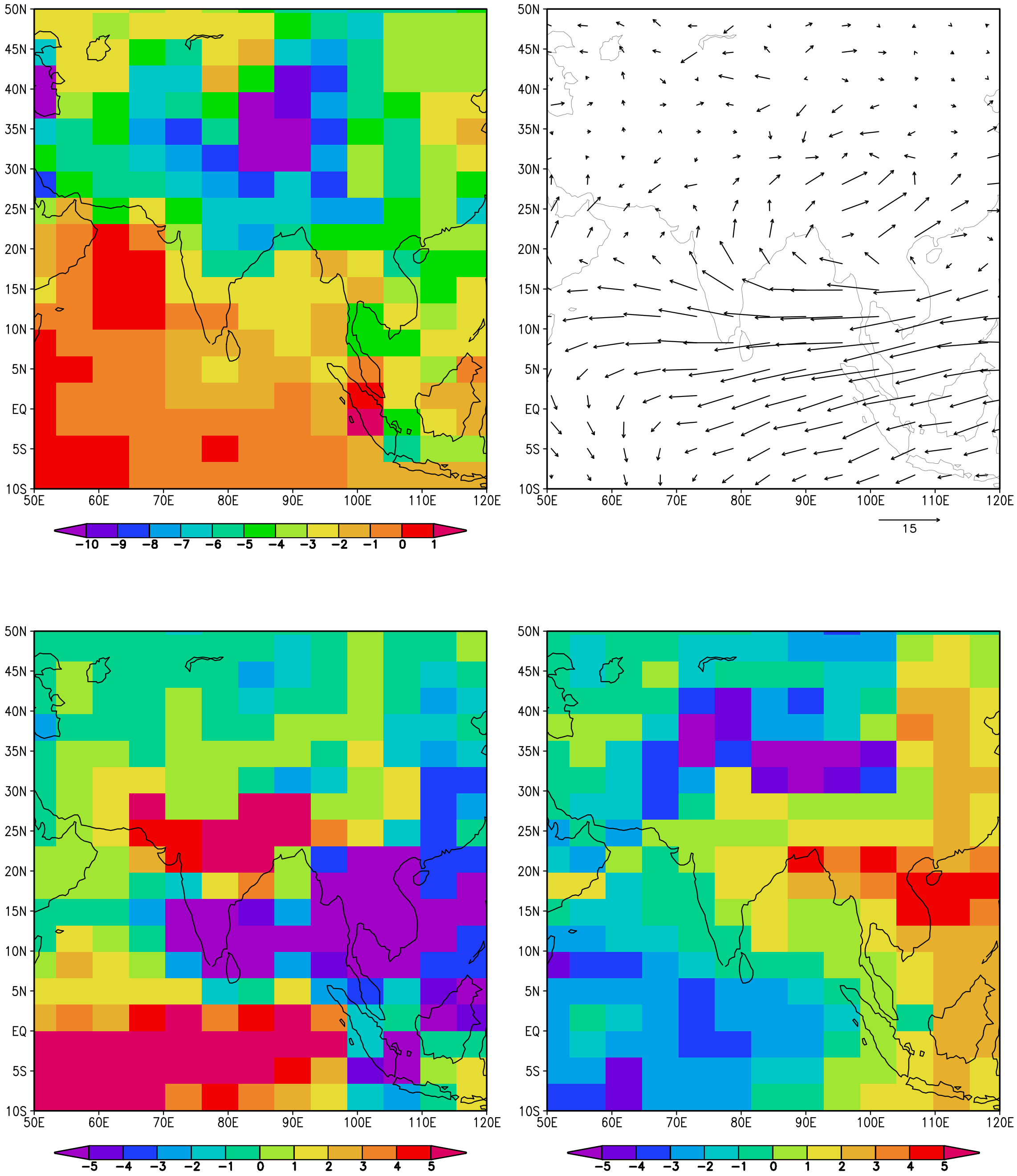

Figure 6.26: CLIMAP surface temperature (top left), 850 hPa wind (top right), precipitation (bottom left) and $\delta^{18}O$ (bottom right) anomalies over central Asia. Units are °C, m/s, mm/day and ‰ respectively.

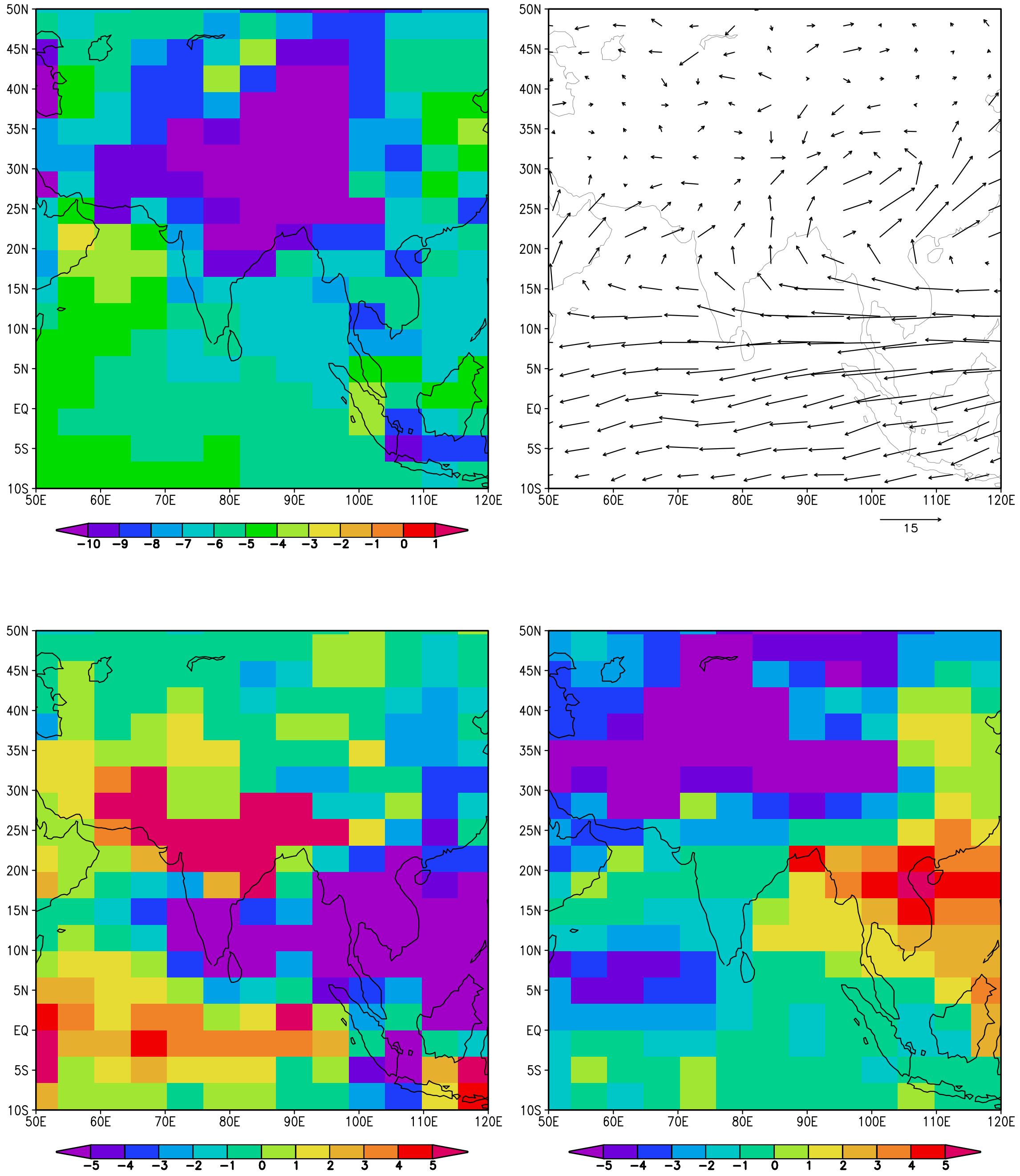

Figure 6.27: COOL surface temperature (top left), 850 hPa wind (top right), precipitation (bottom left) and δ^{18}O (bottom right) anomalies over central Asia. Units are °C, m/s, mm/day and ‰ respectively.

the Tibetan Plateau at the LGM. At Dasuopu, modelled local temperatures are cooler and precipitation increased in both simulations. However the isotopic anomaly is positive in CLIMAP due to the increased south-easterly flow of moisture from the nearby tropical oceans to the southern part of the Plateau, while in COOL the larger surface cooling dominates the isotopic signal.

6.5 Isotopes in the surface ocean and runoff

The responses of isotopic ratios in the surface ocean and river runoff to the modelled LGM climate are also examined. The large scale distribution of isotopes in the surface ocean is compared with the modelled present day distribution, and the modelled surface ocean isotopic ratios are compared with marine isotopic records from the tropical western and eastern Pacific. The modelled isotopic ratios in river runoff and coastal discharge are then described and compared with those simulated for the present day climate.

6.5.1 Surface ocean isotopic ratios

The modelled LGM surface ocean δ^{18}O is compared with the present day for DJF and JJA with the +1.2‰ enrichment due to global ice volume subtracted from the CLIMAP and COOL δ^{18}O values as shown in Figures 6.28 and 6.29. The surface isotopic anomalies therefore represent the component of the signal due to precipitation and evaporation changes at the LGM.

The main features of the CLIMAP surface ocean δ^{18}O distribution include an enrichment in the western Pacific due to reduced precipitation in both DJF and JJA. There is a relative depletion in the southern Pacific in the tropics and mid-latitudes due to an increase in precipitation in both seasons, and an enrichment in the equatorial Pacific where precipitation is reduced in the region of the ITCZ. A strong depletion is also observed in the tropical Indian Ocean associated with the large precipitation increase in this region.

The main differences with the COOL surface ocean δ^{18}O distribution include greater depletion in the eastern Pacific in COOL due to both increased precipitation and reduced evaporation in response to the cooler SSTs in this region. The western Pacific Warm Pool experience greater isotopic enrichment in COOL due to the larger reduction in precipitation simulated here. There is also a smaller depletion in the tropical Indian Ocean in COOL as the precipi-

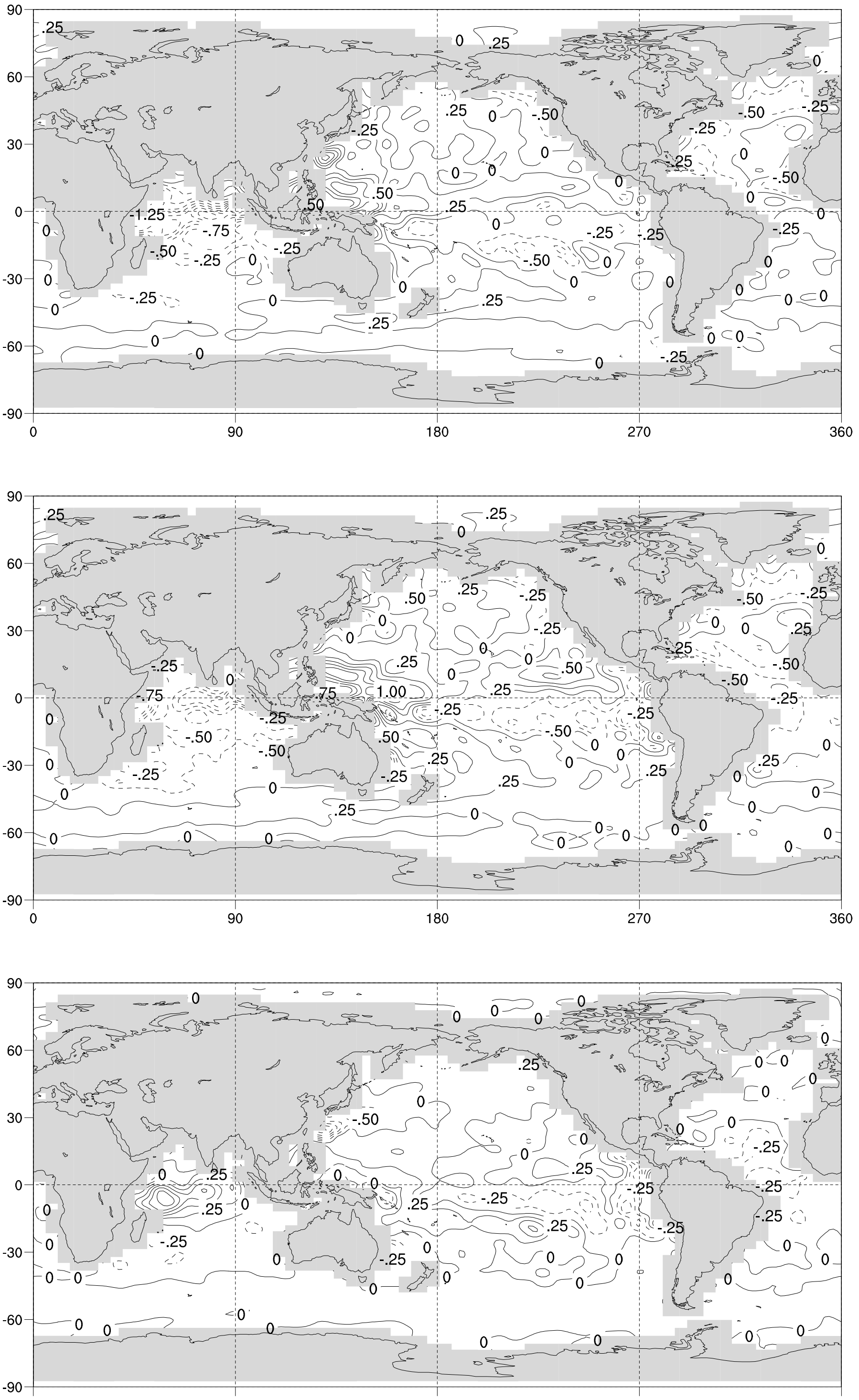

Figure 6.28: DJF surface ocean δ^{18}O anomalies (– 1.2‰): CLIMAP – PD (top), COOL – PD (middle) and COOL – CLIMAP (bottom). Contour interval is 0.25‰.

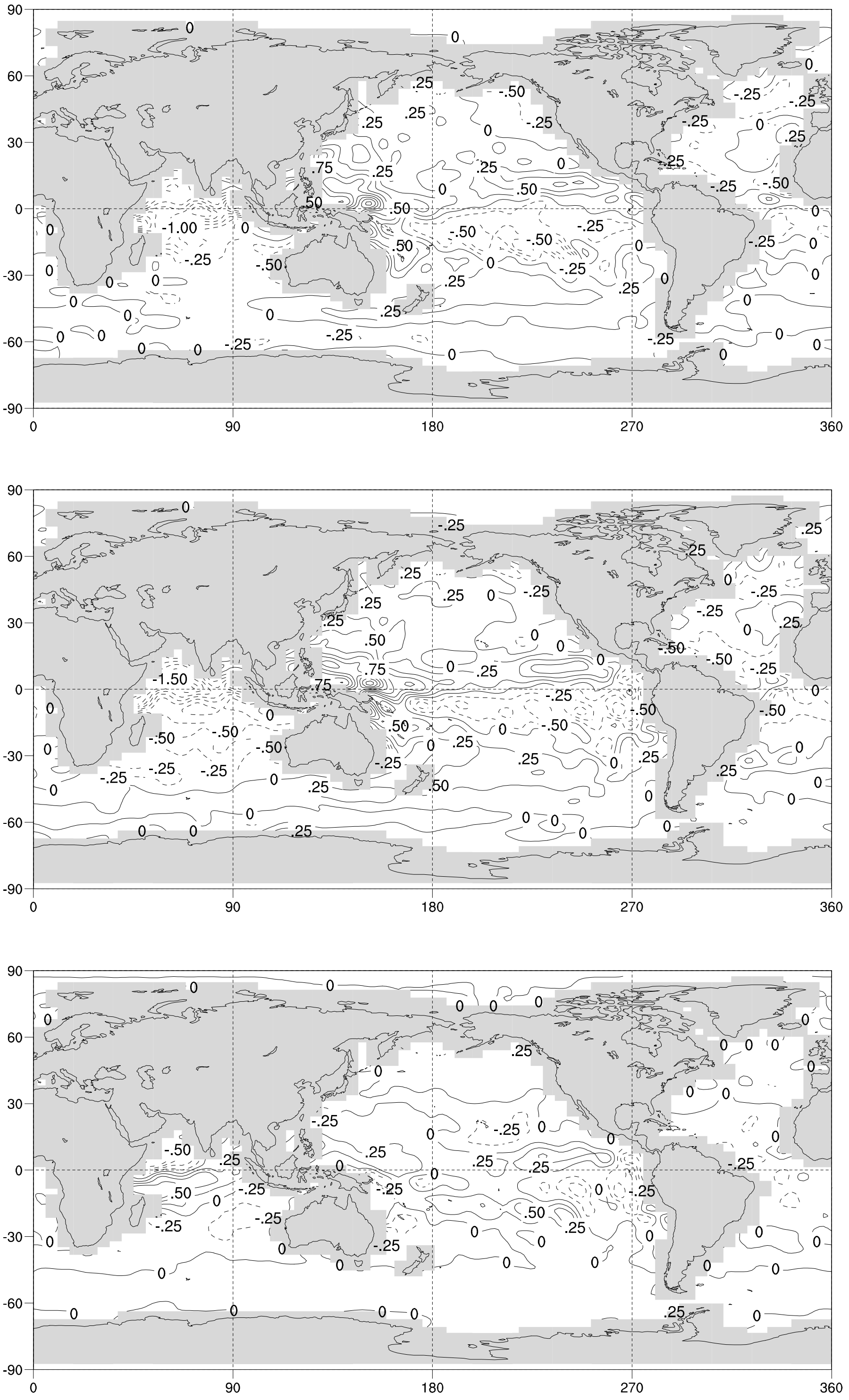

Figure 6.29: JJA surface ocean δ^{18}O (– 1.2‰) anomalies: CLIMAP – PD (top), COOL – PD (middle) and COOL – CLIMAP (bottom). Contour interval is 0.25‰.

tation increase in COOL is weaker than that in CLIMAP. The southward shift of the ITCZ in COOL produces increased isotopic depletion to the south of the equator and reduced depletion to the north in the tropical Pacific.

While the modelled surface ocean isotopic anomalies are clearly dominated by changes in precipitation, there is also a component of the signal associated with changes in evaporation. In particular, in the north-eastern Pacific where the Aleutian Low is strengthened, evaporation decreases and there are increases in the western Pacific Warm Pool and in the subtropical regions of increased SSTs. There is a strong isotopic response to the local increase in evaporation due to the SST "hotspot" off the east coast of Australia in the CLIMAP JJA SST reconstruction. The isotopic anomaly is positive here despite a local increase in precipitation.

6.5.2 Comparison with marine records

The modelled LGM surface ocean δ^{18}O anomalies are compared with measured LGM isotopic ratios from coral and foraminifera in the western and eastern tropical Pacific. The modelled surface ocean δ^{18}O anomalies are not converted into modelled coral δ^{18}O values as in Chapter 5, as this would combine uncertainty in the SST and local ocean δ^{18}O reconstructions. Instead, the modelled δ^{18}O and SST anomalies are compared with the local ocean δ^{18}O and SST components of the coral and foraminiferal record as measured using techniques such as Sr/Ca analysis in a range of studies.

Western Pacific

The observed LGM surface ocean δ^{18}O enrichment for the western equatorial Pacific is +0.2 to +0.5‰ [*Martinez et al.*, 1997] and 0‰ to +1.0‰ for the region directly to the north of Australia [*De Deckker et al.*, 2003], although *Visser et al.* [2003] and *Stott et al.* [2002] infer no change in western Pacific surface ocean δ^{18}O. Estimates of the SST change in the region vary from −2°C [*De Deckker et al.*, 2003] to −3.6°C [*Visser et al.*, 2003].

The simulated surface ocean δ^{18}O anomalies in the western Pacific largely respond to reductions in precipitation, as shown in Figures 6.30 and 6.31. A response to evaporation changes is seen to the north of Indonesia as well as east of Australia. The modelled CLIMAP surface ocean δ^{18}O anomaly in the tropical western Pacific has a mean value of +0.36‰. The largest positive anomalies

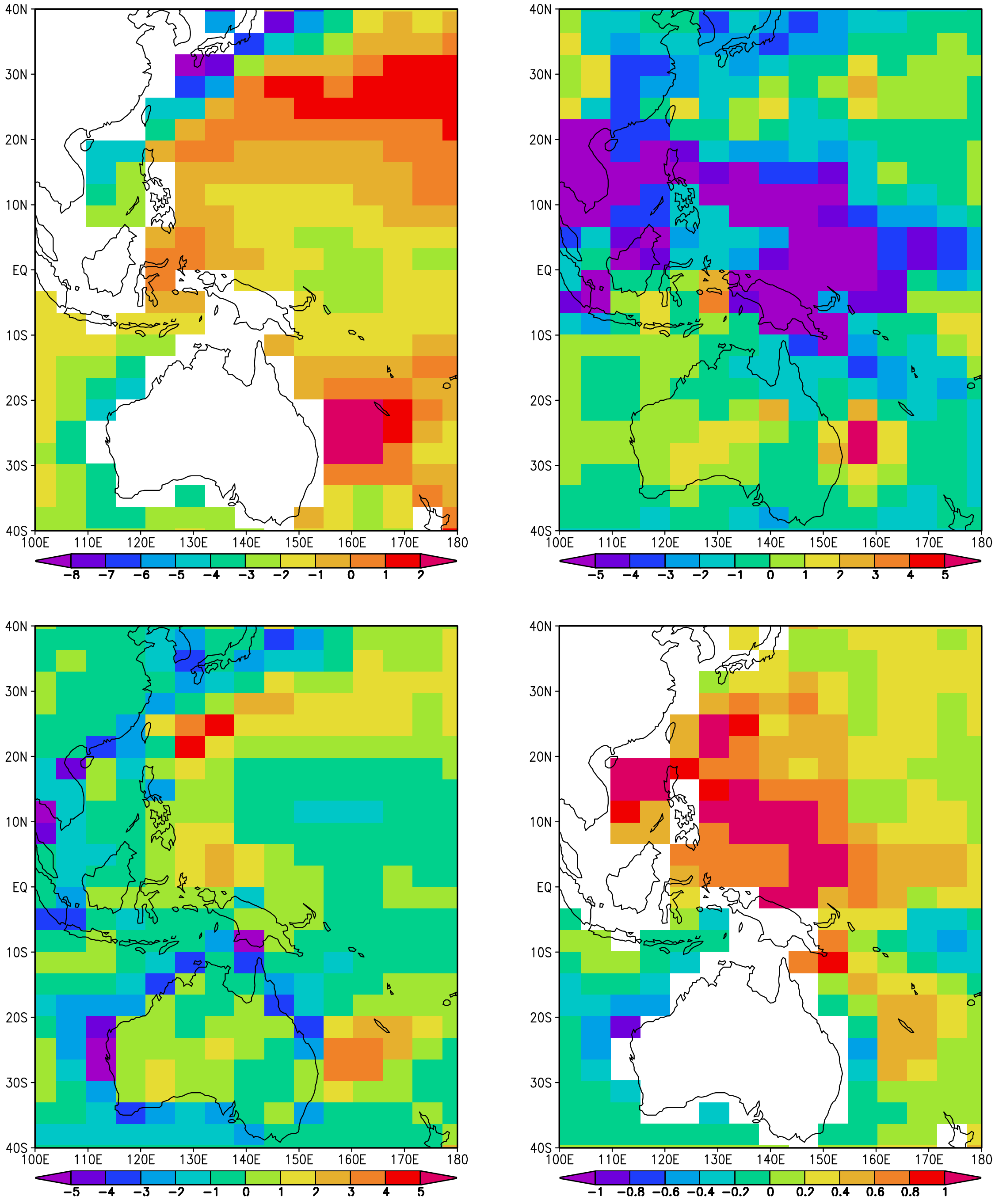

Figure 6.30: CLIMAP SST (top left), precipitation (top right) evaporation (bottom left) and surface ocean δ^{18}O (bottom right) anomalies in the tropical western Pacific. Units are °C, mm/day, mm/day and ‰ respectively.

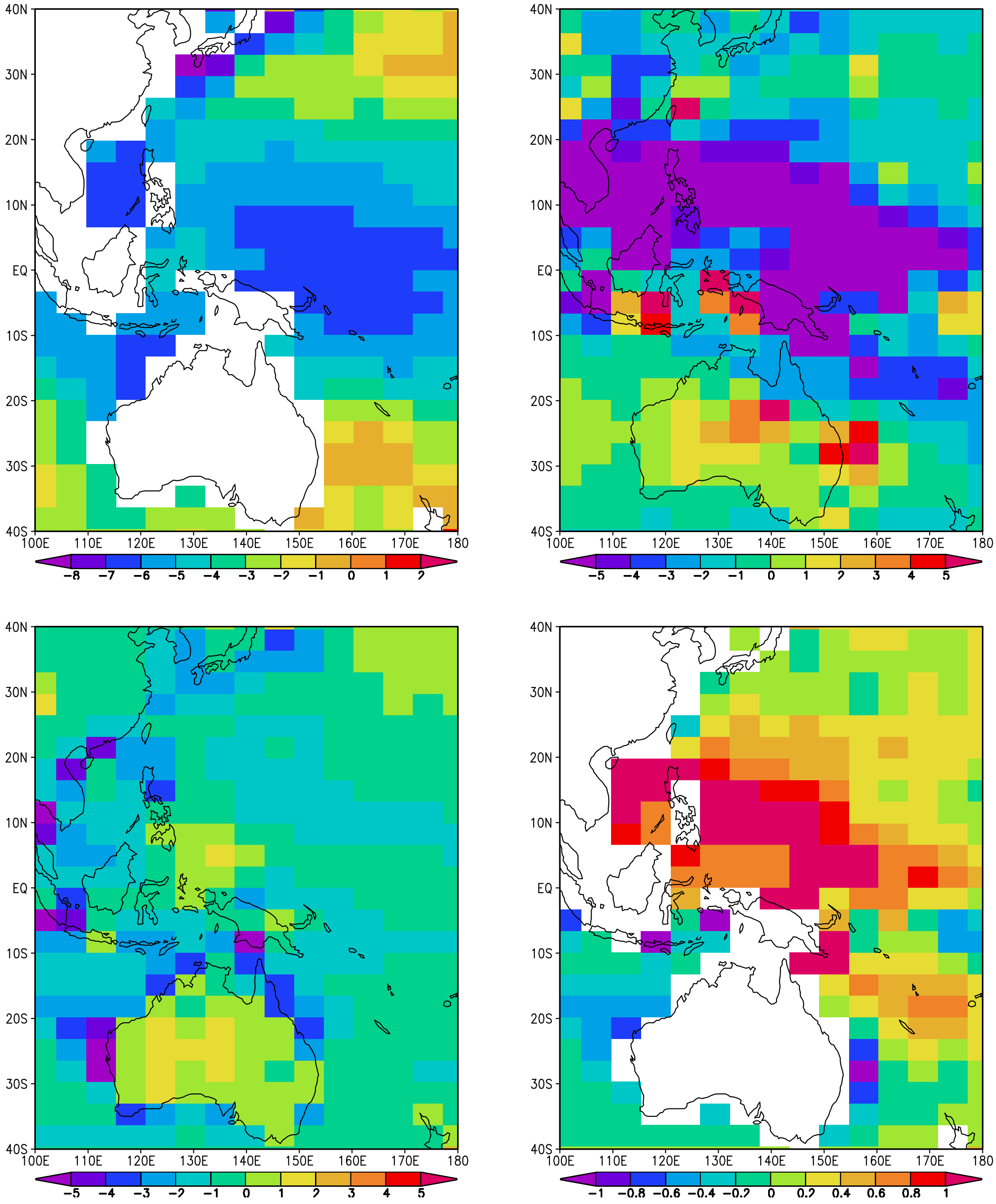

Figure 6.31: COOL SST (top left), precipitation (top right) evaporation (bottom left) and surface ocean δ^{18}O (bottom right) anomalies in the tropical western Pacific. Units are °C, mm/day, mm/day and ‰ respectively.

are above +1.5‰ in the region of reduced precipitation to the north of Papua New Guinea.

The COOL average surface ocean δ^{18}O anomaly over the tropical western Pacific is similar (+0.38‰), with regions of increased and reduced δ^{18}O relative to CLIMAP. As SSTs are cooler in the COOL simulation, evaporation and precipitation are reduced over ocean. The surface ocean δ^{18}O values are more enriched in the tropical western Pacific and more depleted in the tropical Indian ocean in the COOL simulation.

As the COOL western Pacific surface ocean δ^{18}O values are more enriched, and the local SSTs are cooler, the two signals would combine to produce more enriched coral and foraminiferal δ^{18}O values. This suggests that a possible explanation for the discrepancies between reconstructed Warm Pool LGM SSTs is the assumption of unchanged local surface ocean δ^{18}O, which would lead to the overestimation of SST cooling reconstructed from marine isotopic records. Our simulations imply that if Warm Pool SSTs were cooler at the LGM than the present day, a reduction in precipitation would lead to an enrichment of local surface ocean δ^{18}O.

Eastern Pacific

A similar comparison was carried out in the eastern equatorial Pacific. *Koutavas et al.* [2002] infer 1.2°C cooling from isotopic records at the Galapagos Island, with no change in local surface ocean δ^{18}O. Additional results from Mg/Ca and alkenone palaeothermometry studies at the same location also found cooling of 1.2°C, implying that the entire foraminiferal isotopic signal is due to the SST change.

As shown in Figures 6.32 and 6.33, the CLIMAP SSTs are slightly warmer at the Galapagos Islands than present day, while they are 3°C cooler in COOL. The cooling is approximately 1°C greater to the north of the equator in both simulations. As a result, both simulations produce decreased precipitation in the region centred on 10°N and increased precipitation to the south of the equator.

The modelled surface ocean δ^{18}O anomalies are close to zero at Galapagos for both simulations, with a slight evaporation increase leading to a local δ^{18}O enrichment of +0.2‰ in CLIMAP and an increase in both precipitation and evaporation leading to an unchanged δ^{18}O at Galapagos in COOL. While these results support the findings of *Koutavas et al.* [2002], the substantial (±0.8‰)

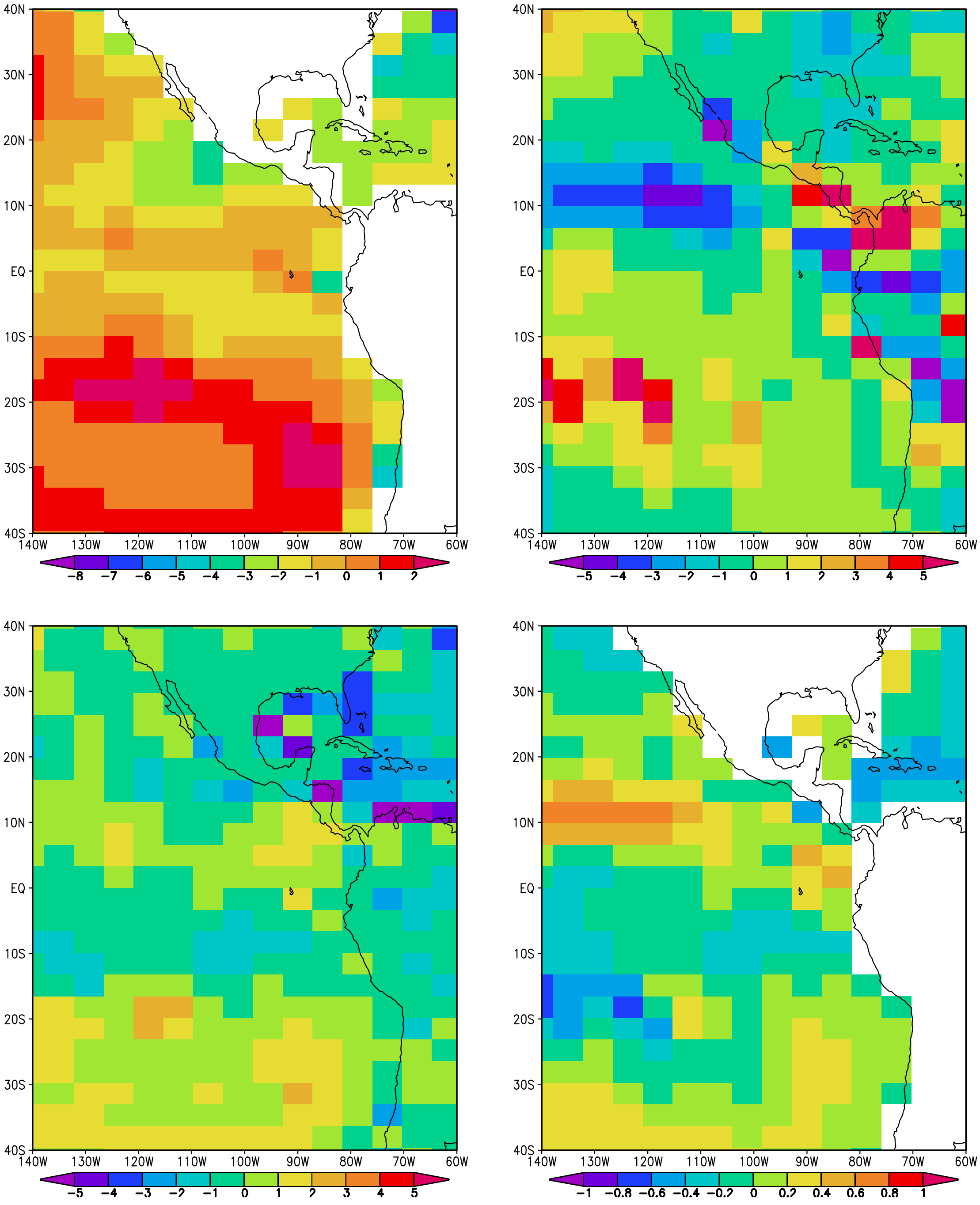

Figure 6.32: CLIMAP SST (top left), precipitation (top right) evaporation (bottom left) and surface ocean δ^{18}O (bottom right) anomalies in the tropical eastern Pacific. Units are °C, mm/day, mm/day and ‰ respectively.

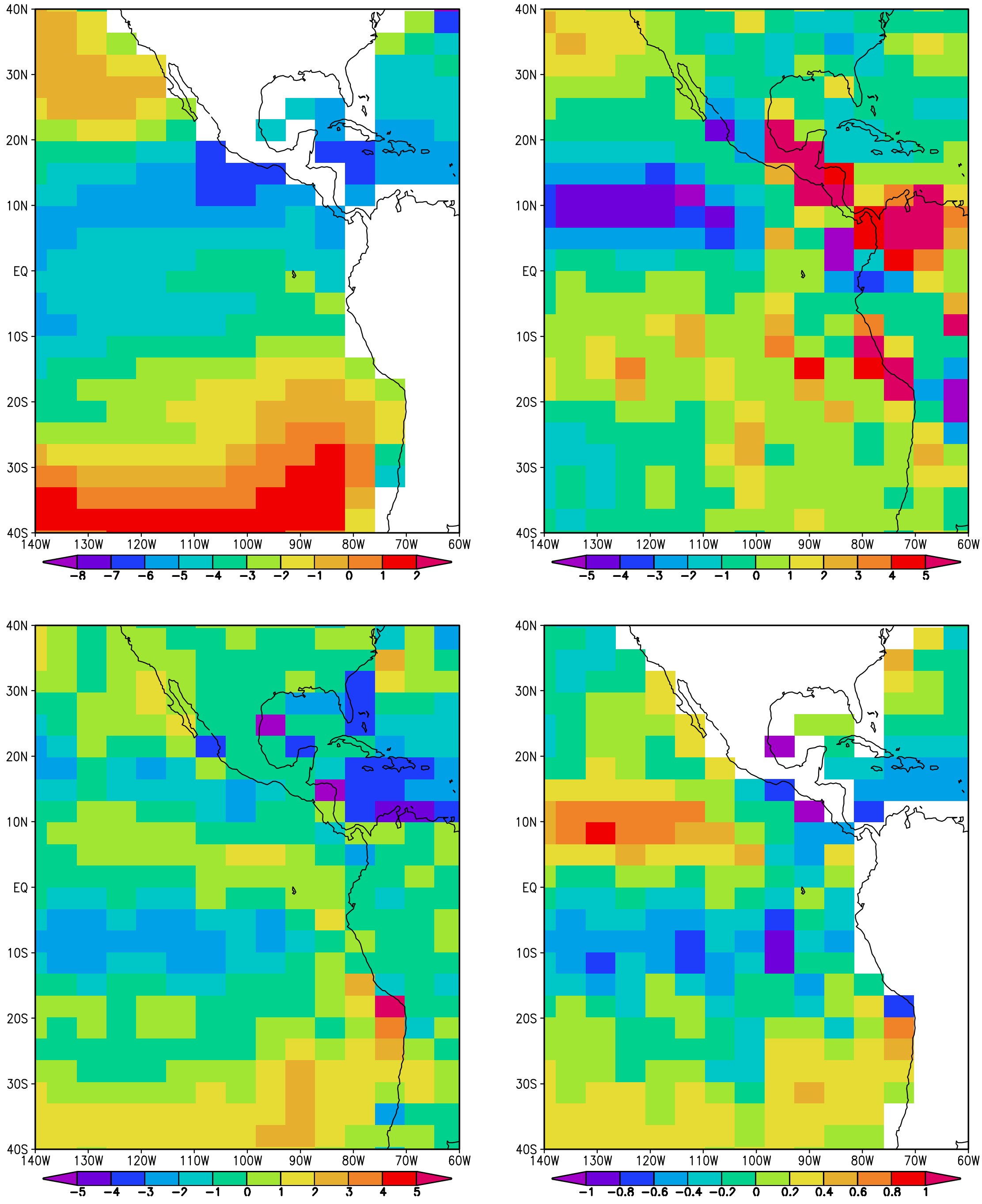

Figure 6.33: COOL SST (top left), precipitation (top right) evaporation (bottom left) and surface ocean δ^{18}O (bottom right) anomalies in the tropical eastern Pacific. Units are °C, mm/day, mm/day and ‰ respectively.

δ^{18}O anomalies to the north and south of Galapagos in COOL emphasise that the unchanged local δ^{18}O is a result of specific climate conditions simulated at this location rather than being generally applicable.

6.5.3 River runoff isotopic ratios

The isotopic contribution to the surface ocean due to river runoff was also compared for the present day, CLIMAP and COOL runs. The LGM model topography was used to calculate the runoff rates in the river runoff scheme for the CLIMAP and COOL runs, and the runoff added to the ocean at coastal grid points corresponding to the LGM land extent. As the LGM coastal grid points are generally not the same as those for the present day continents it is not possible to compare discharge or surface ocean δ^{18}O anomalies directly. Instead the annual average local runoff and surface ocean δ^{18}O values are compared for each simulation.

Western Pacific and Indian Ocean

As shown in Figure 6.34, local runoff decreases over East Asia, Indonesia and Papua New Guinea in both CLIMAP and COOL simulations compared with the present day due to the reduction in precipitation over these areas. The reduction in the COOL simulation is less than that for CLIMAP over elevated topography, reflecting the precipitation response to cooling over elevated topography in the model.

The reduced local runoff leads to a decrease in ocean discharge in the western Pacific Warm Pool and the South China and East China Seas, while the increased precipitation over West Asia produces greater runoff and discharge from the Himalayas into the Indian Ocean. The surface ocean isotopic ratios are enriched compared with the present day over the tropical western Pacific in both CLIMAP and COOL simulations due to the decrease in precipitation, as discussed in the previous Subsection. The influence of reduced river runoff on the surface ocean isotopic ratio is most evident around the coast of Papua New Guinea where the relative enrichment is greatest in both simulations.

The modelled runoff may be compared with the study of *De Deckker et al.* [2003] who found evidence for decreased runoff off the coast of Papua New Guinea at the LGM as recorded in the enrichment of foraminiferal isotopic ratios. While the model resolution is not sufficient to reproduce the local features

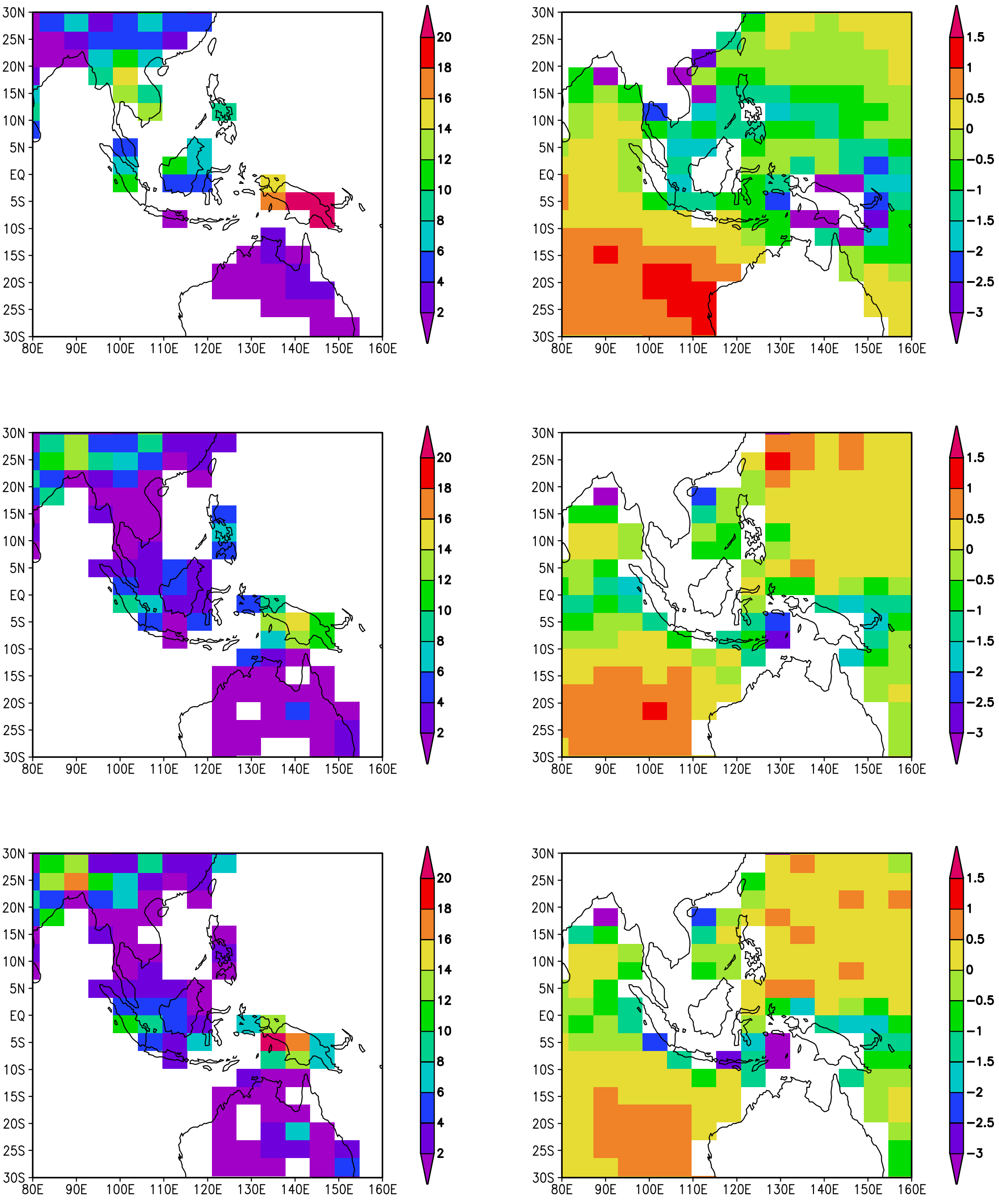

Figure 6.34: Western Pacific local runoff (top) and surface ocean δ^{18}O (bottom): PD (left), CLIMAP (middle) and COOL (right). Units are mm/day and ‰ respectively. Surface ocean δ^{18}O -1.2‰ for CLIMAP, COOL.

of the isotopic distribution in this region, the reduced runoff and discharge in both the CLIMAP and COOL simulations is in agreement with their results.

Tropical South America

As shown in Figure 6.35, the modelled runoff and discharge for the present day over tropical South America is lower than observed due to the underestimation of precipitation over the Amazon basin, as discussed in Chapter 4. The CLIMAP simulation produces more runoff and river discharge in Central America and in parts of Brazil and a decrease over the Andes. The runoff over the Amazon basin is still very small, with a slight decrease in discharge at the grid boxes corresponding to the mouth of the Amazon River.

The COOL simulation produces more runoff on average over tropical South America, with an increased discharge along the north-eastern coast of Brazil. The discharge at the mouth of the Amazon River is double that of the PD or CLIMAP simulations, although still substantially less than the observed present day discharge. The increase in runoff in the COOL simulation confirms the increase in precipitation minus evaporation over the Amazon basin identified in the discussion of LGM Andean ice core records above.

The contribution of river runoff to the difference in the surface ocean δ^{18}O between the COOL and CLIMAP runs is approximately $-1‰$ at the mouth of the Amazon, and greater to the north and off the west coast of Peru. *Guilderson et al.* [2001] estimate a maximum change in surface ocean δ^{18}O of $+0.2‰$ at Barbados due to a halving of Amazon runoff at the LGM. However this study is unable to validate this prediction due to the absence of horizontal transport in the version of the surface ocean isotopic scheme used to simulate LGM climate.

6.6 Discussion: isotope–climate relationships

6.6.1 Isotopes in precipitation

Having examined the change in isotopic ratios in precipitation for the LGM and present day, we can now consider the question of whether the glacial time scale (LGM to present day) isotopic response to climate forcing resembles the present day seasonal or interannual isotope–climate relationships. The implications for the reconstruction of past climate from continental isotopic records in Andean and Tibetan ice cores are also considered.

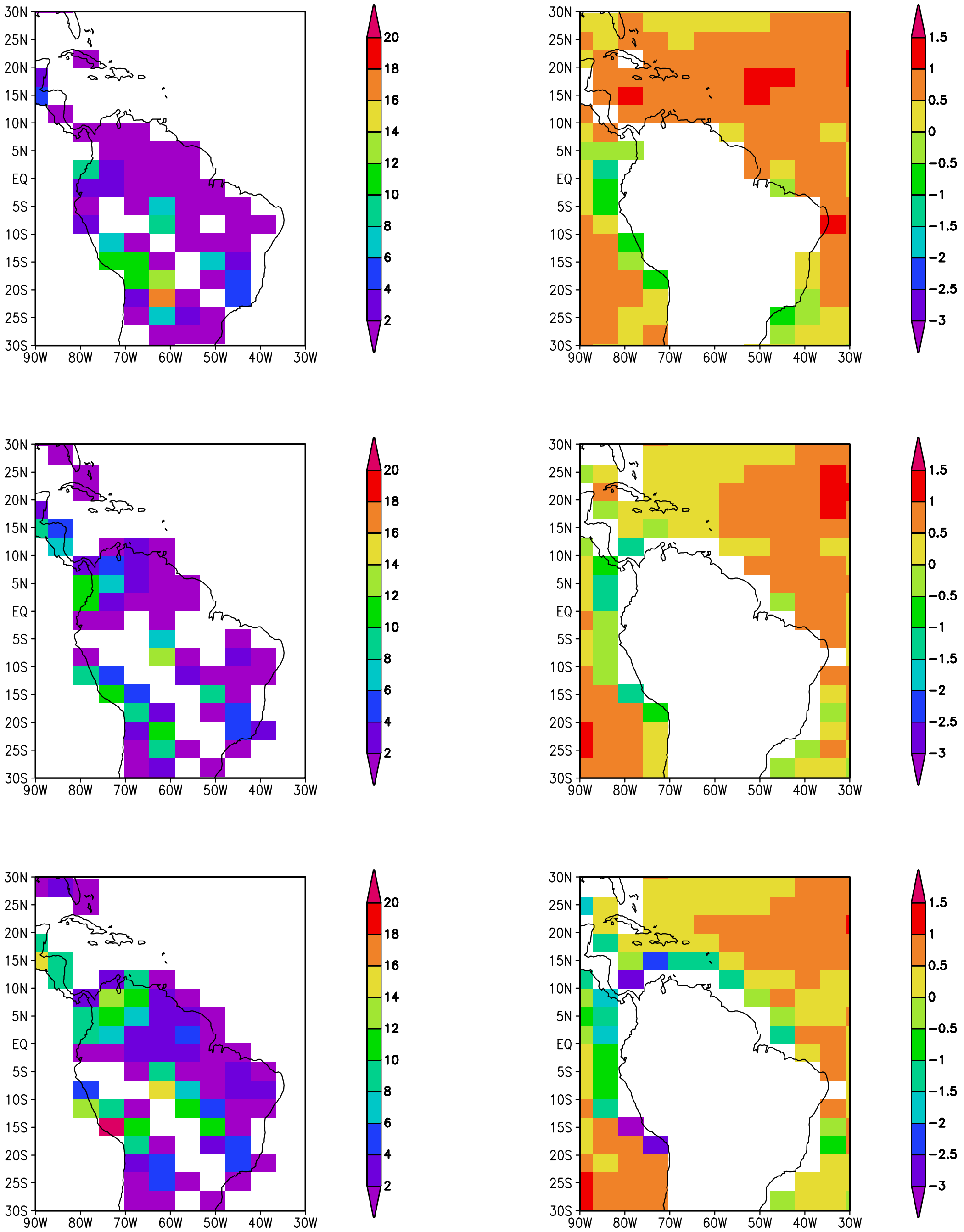

Figure 6.35: South American local runoff (left) and surface ocean δ^{18}O (right): PD (top), CLIMAP (middle) and COOL (bottom). Units are mm/day and ‰ respectively. Surface ocean δ^{18}O −1.2‰ for CLIMAP, COOL.

For the present day, the seasonal cycle of δ^{18}O in precipitation varies with temperature, precipitation amount and changes in moisture source and rainout during transport in the simulation presented in Chapter 5. In tropical areas with a small annual temperature range and large precipitation range the strongest correlation is between monthly precipitation amount (associated with rainout over the transport path) and δ^{18}O, resulting in a negative correlation between δ^{18}O and temperature.

On interannual time scales, tropical isotopic ratios in precipitation are also controlled by variations in precipitation amount both locally and over the transport path. As interannual precipitation variability is associated with temperature variation (cooler and wetter conditions occurring together) over tropical continents, the isotopic signal reflects increased rainout due to both temperature and precipitation amount effects. Regional variability of rainout associated with ENSO and the monsoon also influences tropical precipitation isotopic ratios.

Climate reconstructions from Andean ice core δ^{18}O records at the LGM have generally attempted to relate a single climate parameter with the isotopic record, such as temperature [*Thompson et al.*, 2000a], runoff over the Amazon basin [*Pierrehumbert*, 1999] or changes in precipitation over the Amazon and Andes [*Ramirez et al.*, 2003]. Tibetan Plateau ice core records of the LGM have most commonly been interpreted as records of local or regional cooling [eg. *Thompson et al.*, 1997; *Thompson*, 2000].

The results of the CLIMAP and COOL simulations of LGM climate provide a test of the sensitivity of isotopes in precipitation to changes in a range of climate parameters. Our simulations of LGM climate indicate that over tropical South America and the subtropical Tibetan Plateau, local changes in both precipitation and temperature at the LGM influence isotopic ratios in precipitation over ice core sites. The different signs of the isotopic anomalies over the Andes and southern Tibetan Plateau in the CLIMAP and COOL simulations suggests that precipitation may be more important than temperature as both simulations produce local cooling over the ice core sites.

In addition to local conditions, changes in rainout during transport at the LGM are a significant control on precipitation δ^{18}O at tropical ice core sites, as for the present day. Over the tropical Andes, the decrease in precipitation minus evaporation over the Amazon basin for CLIMAP and increase for COOL is consistent with the different isotopic anomalies simulated over the Andes. Changes in moisture source regions may also produce changes in the isotopic content of precipitation, as suggested by the shift to a mid-latitude Pacific moisture source for summer precipitation in the COOL simulation.

Over the Tibetan Plateau, the precipitation δ^{18}O anomalies at the LGM are associated with changes in rainout over coastal India and the southern Plateau. Changes in the mean atmospheric circulation related to the weakened southwesterly monsoon flow results in a greater contribution of local tropical oceanic moisture with a less isotopically depleted signature to precipitation over the southern Tibetan Plateau.

While we do not quantify the contribution to the tropical isotopic signal of each component of climate, it is clear that for both the Andes and Tibetan Plateau, changes in a single climate parameter locally or in source regions are not able to explain the changes in modelled precipitation δ^{18}O at the LGM. The modelled isotopic ratios respond in a complex manner to changes in local temperature and precipitation, rainout during transport, changes in continental moisture recycling and moisture source regions. While the precise changes simulated may differ from those in the real climate system, we suggest that a similar combination of factors produces the isotopic depletion at the LGM measured in tropical ice core records.

6.6.2 Isotopes in the surface ocean

Our simulations of LGM climate demonstrate that changes in tropical SSTs produce changes both in the local evaporation and precipitation regimes and in the large scale tropical circulation (Walker circulation, Hadley cell, Asian monsoon). It is therefore not appropriate to assume unchanged local ocean δ^{18}O values under conditions of altered SSTs unless additional proxy evidence supports this assumption. The comparison of multiple isotopic records in key regions such as the western and eastern equatorial Pacific allows a consistent picture of the tropical climate to be reconstructed, including shifts in the position of the ITCZ and the existence of a large scale El Niño-like condition which are not apparent from single locations.

The interpretation of modern marine isotopic records often assumes that the SST and precipitation–evaporation component of the isotopic signal will be of the same sign so that warmer SSTs and increased precipitation lead to more positive coral or foraminiferal δ^{18}O values at a given location. However in the case of large scale climate changes such as those on glacial time scales, the SST and precipitation components of the signal may vary inversely. For example, regions of decreased SSTs may also experience increases in precipitation due to the relatively greater cooling of adjacent areas or the displacement of major components of tropical atmospheric circulation. The resulting isotopic response in the marine record will therefore be a damped SST signal which may lead to an underestimation of cooling at a particular location.

The SST reconstruction error due to the assumption of unchanged precipitation and evaporation is estimated for the CLIMAP and COOL simulations by calculating the change in coral δ^{18}O from LGM to present day after subtraction of the ice volume component. This change in coral δ^{18}O is converted directly to a SST change assuming the relationship $\Delta\text{SST} = \Delta\delta^{18}\text{O}/(-0.2)$ from Equation 5.3. The resulting SST change is compared with the change in the prescribed annual average SSTs to give an SST reconstruction error:

$$\Delta SST\ error = \Delta SST_{reconstructed} - \Delta SST_{prescribed} \tag{6.1}$$

The SST reconstruction errors calculated for CLIMAP and COOL simulations are shown in Figure 6.36. The errors are largest where large precipitation anomalies exist, including the Indian Ocean and western Pacific, and in many cases exceed the magnitude of the inferred glacial SST anomalies.

Changes in evaporation may also influence the surface ocean isotopic records in some cases. For example, the cooling of tropical SSTs leads to a decrease in evaporation which acts to reduce the surface ocean δ^{18}O values. This will reduce the SST cooling signal in proxy records, as identified by *Gagan et al.* [1998] for glacial to mid-Holocene changes in the western Pacific. The simultaneous decrease (increase) of both precipitation and evaporation under conditions of cooled (warmed) SSTs will produce an isotopic response which will depend on the relative extent of isotopic fractionation undergone in the evaporation and condensation processes as well as the local surface ocean moisture flux balance.

6.7 Summary

Simulations of LGM climate were carried out using CLIMAP SST boundary conditions and modified boundary conditions with cooled tropical SSTs. Our model simulations show that changes to the tropical SST component of the LGM forcing have a substantial influence on precipitation, evaporation, land surface

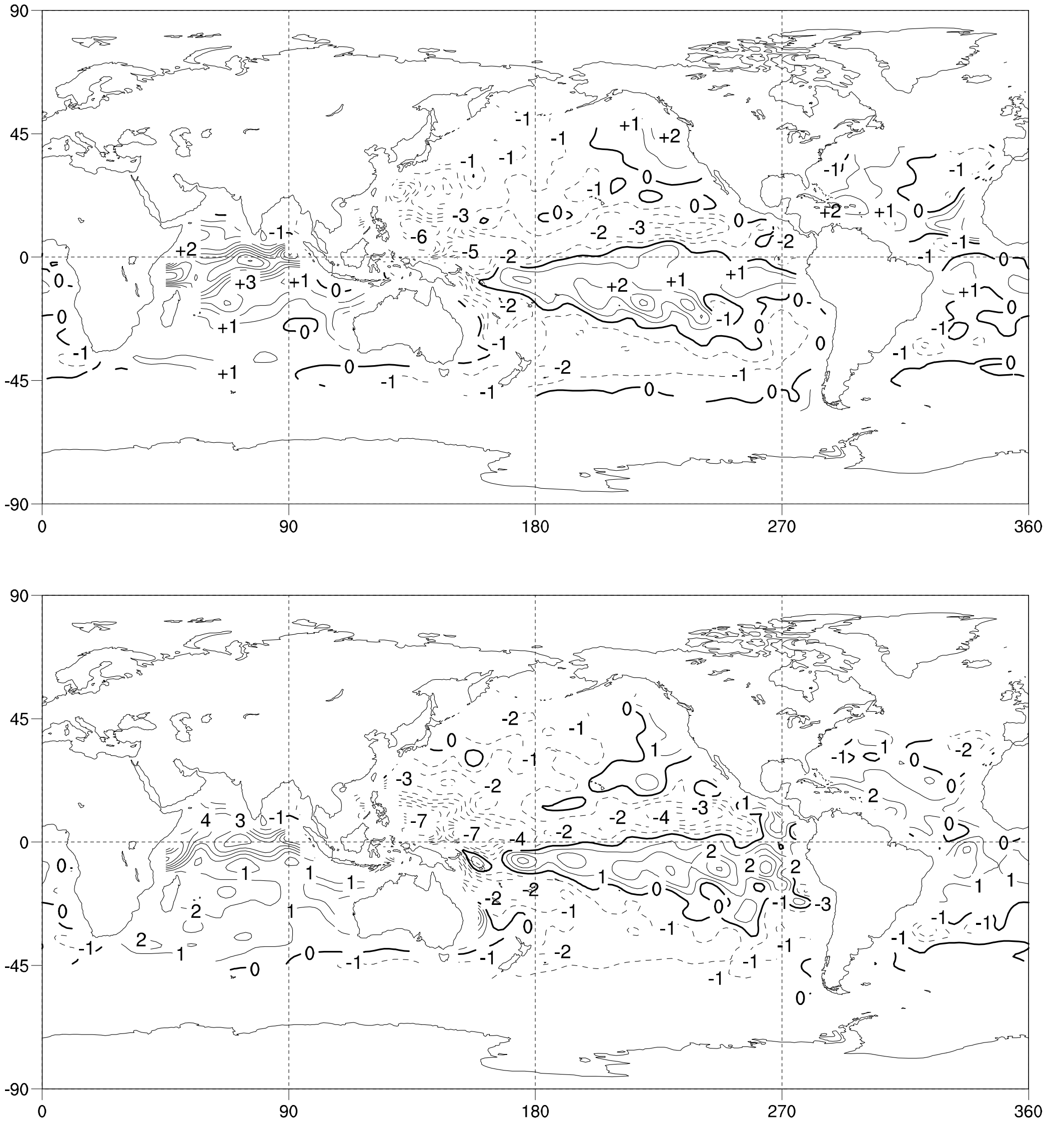

Figure 6.36: Error in LGM SSTs reconstructed from coral $\delta^{18}O$ if precipitation and evaporation are assumed to be unchanged from present day for CLIMAP (a) and COOL (b) simulations. Contour interval is 1°C.

temperatures and atmospheric circulation. The isotopic ratios in precipitation and the surface ocean respond to the changes in climate induced by the different SST conditions.

The simulated LGM climate with cooled tropical SSTs produces cooler continental surface temperatures at all latitudes. MSLP is increased and precipitation decreased over the tropical Pacific and Indian Oceans, with a decrease in pressure and increase in precipitation over the tropical Atlantic. Evaporation decreases over tropical oceans in COOL, while precipitation and evaporation generally increase over land, with an implied increase in the recycling of continental moisture.

The trade winds are weakened in the eastern Pacific in both simulations, but unchanged in the western Pacific in CLIMAP and increased in COOL. The Asian summer monsoon circulation is reduced in both simulations while the winter monsoon is strengthened in CLIMAP and weakened in COOL due to the different land–ocean surface temperature contrasts. The Hadley cell is slightly intensified in both simulations in DJF and weakened in JJA in response to changes in mean SSTs and SST gradients. The ITCZ is shifted south in the COOL simulation in response to the changed SST distribution.

Isotopic ratios in precipitation are generally enriched over the tropical oceans in both simulations due to ocean enrichment and reduced precipitation, with local depletion where precipitation increases over the Indian Ocean in CLIMAP and the equatorial Pacific in COOL. Over tropical continents, isotopic ratios in precipitation respond to a combination of changes in surface temperature, precipitation amount and transport.

Over the tropical Andes, contributions to the change in precipitation δ^{18}O include local changes in precipitation amount and temperature, as well as rainout and recycling over the Amazon. Andean moisture source regions are significantly different to the present day in the COOL simulation, with a shift in atmospheric circulation in response to the SST and land surface temperature changes. The COOL simulation produces isotopic depletion over the Andes ice core sites which is in better agreement with the observed LGM isotopic depletion at Huascaran and Sajama, although the relative importance of rainout of Pacific and Atlantic moisture may not be correctly simulated due to the low elevation of the Andes in the model.

Over the Tibetan Plateau, cooling and increased precipitation produces substantial depletion over the northern Plateau in both CLIMAP and COOL simulations. The depletion is greater in the COOL simulation than that observed in Guliya and Dunde ice core records due to the greater increase in precipitation in this simulation. At Dasuopu on the southern Plateau, changes in monsoon rainout and moisture sources lead to an isotopic enrichment in CLIMAP and a small depletion in COOL relative to the present day, indicating the importance of non-local controls on the isotopic signal on glacial time scales.

Over the tropical oceans, isotopic ratios in precipitation are generally enriched by 1-2‰, with stronger enrichment in the COOL simulation due to reduced tropical precipitation. There is a negative isotopic anomaly in the southern tropical Pacific due to increased precipitation with the southward shift of the ITCZ. Increased precipitation in the Indian Ocean in CLIMAP leads to isotopic depletion, although this effect is reduced in COOL. Increased precipitation in the eastern equatorial Pacific and decreased precipitation in the western equatorial Pacific produce isotopic anomalies in both simulations which are enhanced in the COOL simulation.

In the western Pacific Warm Pool, surface ocean δ^{18}O values are enriched on both simulations in agreement with the reconstructed LGM surface ocean values of *De Deckker et al.* [2003] and *Martinez et al.* [1997]. At Galapagos in the eastern equatorial Pacific, the assumption by *Koutavas et al.* [2002] of unchanged surface ocean δ^{18}O at the LGM is in agreement with both simulations, although this appears to be due to the location of the site at the boundary between regions of increased and decreased precipitation and ocean δ^{18}O.

The differences in continental runoff between the PD, CLIMAP and COOL simulations produce substantial isotopic anomalies at coastal grid boxes in modelled surface ocean δ^{18}O. Both CLIMAP and COOL simulations reproduce the decrease in runoff over Papua New Guinea and the resulting positive LGM surface ocean δ^{18}O anomalies inferred from palaeo-records. Over South America, the relatively greater continental precipitation in COOL leads to a strong increase in runoff and discharge, with a doubling of Amazon River discharge and resulting decrease in surface ocean δ^{18}O off the east coast of South America.

The simulated isotopic distribution at the LGM is not completely consistent with observed LGM isotopic records for either CLIMAP or cooled tropical SST reconstructions. Although unchanged tropical SSTs do not produce sufficient isotopic depletion in Andean precipitation, cooled tropical SSTs result in an overestimation of isotopic depletion in Tibetan Plateau precipitation. Both COOL and CLIMAP simulations produce surface ocean δ^{18}O which is broadly in agreement with marine isotopic records in the tropical western and eastern Pacific. We note that the tropical SST cooling imposed for the COOL simulation is larger than many observational records suggest, and that the imposition of smaller cooling of tropical SSTs such as that proposed by *Crowley* [2000] may produce an intermediate response which is more consistent with LGM isotopic records.

Chapter 7

Conclusions

The incorporation of stable water isotopic tracers in GCMs provides a powerful tool for the investigation of the sensitivity of these key palaeoclimate proxies to climate forcing on a range of time scales. This study has utilised an isotopic tracer scheme in an atmospheric GCM to investigate the variability of isotopic ratios in precipitation and the surface ocean in the tropical climate.

7.1 Modelling stable water isotopes

In order to facilitate the investigation of the temporal and spatial variability of surface ocean isotopic ratios, a surface ocean isotopic scheme was developed to calculate the isotopic ratios in the upper ocean from atmosphere–ocean fluxes. The modelled surface ocean isotopic distribution was found to be in agreement with observed tropical and mid-latitude surface ocean isotopic ratios, with enriched surface ocean δ^{18}O simulated in regions of high evaporation in the subtropics and depleted surface ocean δ^{18}O simulated in regions of high precipitation such as the tropical western Pacific.

In addition, a river runoff scheme was developed to calculate the normal water and isotopic runoff over land surfaces and to provide an estimate of the surface ocean isotopic signal associated with runoff. The surface ocean isotopic scheme was modified to incorporate horizontal transport using upper ocean currents from an ocean model simulation, producing a better match with the observed surface ocean isotopic distribution. A further modification to the runoff scheme consisted of the incorporation of isotopic tracers in a prognostic snow scheme, enabling the isotopic content of snow melt and the seasonal influence of snow melt on the surface ocean isotopic distribution to be simulated.

7.2 Present day isotope-climate relationships

This study has quantified the relationship between isotopic ratios in precipitation and the surface ocean for present day tropical climate in a simulation forced with GISST2.3b monthly SSTs and sea ice coverage for 1950–1999. Using the atmospheric GCM with the inclusion of the surface ocean isotopic tracer scheme and river runoff scheme, isotopic ratios in both precipitation and the surface ocean were simulated.

We find that the isotopic signal in tropical precipitation is dominated by the influence of local precipitation amount over ocean surfaces, and by precipitation amount during moisture transport over land surfaces on seasonal and interannual time scales. We have confirmed that the seasonal precipitation δ^{18}O is primarily controlled by precipitation amount in the tropics, leading to a negative correlation with temperature where greater isotopic depletion occurs during warmer summer months.

In regions which experience an annual monsoon, the summer wet season precipitation is the most isotopically depleted, and the total rainout of moisture during transport inland from ocean source regions is more important than local precipitation amount. In tropical South America, the greater rainout over the Amazon during summer leads to greater isotopic depletion of moisture transported from the Atlantic to the Andes. Over the southern Tibetan Plateau, seasonal isotopic depletion is associated with rainout of Asian summer monsoon moisture.

The interannual isotope–climate relationship in the tropics is also driven by precipitation amount. Over ocean, precipitation anomalies associated with ENSO produce the largest interannual isotopic anomalies. Over land, variability of local precipitation and rainout during transport both contribute to the interannual isotopic signal. Where precipitation and temperature are inversely correlated on interannual time scales, an indirect positive temperature–δ^{18}O correlation results.

Over the Asian and Indian monsoon regions, interannual variability of monsoon strength produces an isotopic signal in precipitation. On the southern Tibetan Plateau, greater monsoon precipitation is associated with more negative annual average δ^{18}O, while further north the isotopic signal is more closely associated with local precipitation variability than local temperature or monsoon strength. The influence of ENSO is also seen in the isotopic record over the southern Tibetan Plateau.

In our simulation of present day climate, the interannual isotopic signal in precipitation over the Andes varies with rainout over the Amazon basin more strongly than with local precipitation amount or temperature. While previous studies have identified an ENSO signal in Andean ice core δ^{18}O, the model is limited in its ability to simulate this relationship due to the low elevation of the Andes mountain range in the model topography.

Surface ocean isotopic ratios simulated by the model are controlled by the balance between local precipitation and evaporation. This representation is shown to be able to capture the main features of tropical seasonal and interannual surface ocean isotopic variability within the limitations of the modelled precipitation and evaporation distribution. The strong surface ocean δ^{18}O ENSO response is reproduced by the model, and it is observed that warmer and wetter conditions tend to occur together on interannual time scales in the tropics, facilitating the interpretation of isotopic records of ENSO-related SST and precipitation variability.

7.3 Glacial isotope-climate relationships

Simulations of the climate of the LGM have been carried out in order to identify the isotope-climate relationship on glacial time scales, and compare this with present day relationships. The simulation of LGM climate with CLIMAP and cooled tropical SST boundary conditions allowed a comparison of isotopic ratios in precipitation and the surface ocean with continental and marine isotopic records in order to determine which SST reconstruction was most consistent with LGM isotopic proxy records.

Isotopic ratios in precipitation respond to changes in local precipitation and temperature as well as rainout during transport and changes in moisture source regions in the simulated LGM climate. Over the Andes, local precipitation amount and rainout over the Amazon are the dominant controls on LGM isotopic ratios, while a change in the relative contribution of mid-latitude Pacific moisture is also observed in the simulation with cooled tropical SSTs. Over the Tibetan Plateau, cooling and increased precipitation in both simulations leads to more depleted precipitation δ^{18}O over the northern region of the Plateau, while changes in rainout and moisture source influences the isotopic response over the southern Tibetan Plateau.

We therefore conclude that no single climate parameter is responsible for increased isotopic depletion in tropical precipitation at the LGM in our simulations. Instead, a combination of climate controls operates on the glacial time scale, including local precipitation, rainout during transport and changes in moisture source regions. We also find that LGM isotopic depletion in tropical ice cores cannot be attributed primarily to local or regional cooling as suggested in previous studies [eg. *Thompson*, 2000]. Over the Andes and southern Tibetan Plateau, the CLIMAP simulation produces positive isotopic anomalies despite cooler surface temperatures due to reduced local precipitation and rainout during transport.

The CLIMAP simulation produces precipitation δ^{18}O anomalies over the Tibetan Plateau which are more consistent with ice core records from Guliya and Dunde, while the COOL simulation produces isotopic anomalies at the sites of the Huascaran and Sajama ice cores in the Andes which are in closer agreement with the observed depletion in these records. We therefore suggest that an intermediate cooling of tropical SSTs or the imposition of varied regional Pacific, Atlantic and Indian Ocean cooling may produce an isotopic response which is more consistent with LGM continental proxy records.

The surface ocean isotopic ratio is a function of local precipitation and evaporation on glacial time scales as for the present day, once the effect of the change in mean ocean δ^{18}O is excluded. The modelled surface ocean δ^{18}O at the LGM reflects the reduced precipitation over the majority of the tropical ocean in both simulations, with local increases in surface ocean isotopic depletion in regions of increased precipitation. Western Pacific Warm Pool surface ocean δ^{18}O is enriched and eastern equatorial Pacific surface ocean δ^{18}O unchanged relative to the present day in both simulations, in agreement with marine isotopic records.

As changes in surface ocean δ^{18}O are not uniformly associated with changes in local SST, the present day assumption of the coexistence of warmer and wetter conditions is not necessarily applicable. In addition, we find that the reconstruction of LGM SSTs from marine isotopic records will lead to substantial errors in regions where local precipitation and evaporation vary from the present day if unchanged surface ocean δ^{18}O is assumed. We therefore emphasise the importance of multi-proxy reconstructions of LGM SST and surface ocean δ^{18}O in order to separate these components of the isotopic record.

7.4 Concluding remarks

The isotopic ratio in precipitation is fundamentally determined by the extent of rainout of the heavy isotope between the moisture source region and precipitation site. For tropical precipitation, rainout may vary locally with precipitation amount and the extent of vertical cooling during deep convection. For continental sites, rainout may vary during transport inland, as well as during cooling due to orographic lifting of moisture. Secondary influences on the isotopic ratio in tropical precipitation include changes in the isotopic ratio of ocean source moisture or the proportion of evaporation from isotopically depleted continental moisture.

Our simulations of LGM climate suggest that the climate controls on isotopic ratios in precipitation on present day seasonal and interannual time scales are not necessarily the same as those on glacial time scales. While the physical fractionation process are unchanged, the thermodynamic history of moisture reaching ice core sites in the Andes and Tibetan Plateau may be substantially different. In particular, changes in the extent of rainout during transport and changes in moisture source regions will alter local isotope–climate relationships from those observed for the present day. It is therefore desirable to reconstruct the entire history of moisture archived in tropical ice cores in order to correctly interpret the climate records which they contain.

The use of numerical climate models incorporating isotopic tracers can contribute to the iterative process of comparison between modelled and observed isotopic signals in precipitation and surface ocean required to achieve an accurate reconstruction of past climate. The model can be used to simulate the climate including the various nonlinear feedbacks and complex interactions between isotopes and climate variability which are neglected in simple palaeoclimate reconstruction techniques. The simulated isotopic distribution can then be compared with observational records to constrain the range of climate conditions consistent with the palaeoclimate record.

While individual models are limited in their simulation of climate by factors such as topographic resolution and the representation of precipitation, the comparison of several models with different parameterisations offers the possibility of a more robust reconstruction of past climate. Comparison of simulations of present day and glacial climate from several models containing stable water isotope tracers is a logical extension of the present day and palaeoclimate modelling intercomparison projects. The use of atmospheric models with simple surface ocean isotopic schemes such as that presented in this study may provide a complementary approach to the development of full coupled atmosphere–ocean isotopic tracer models to investigate the interaction between isotopic variability in the atmosphere and ocean.

7.5 Future research

A number of avenues of future research are suggested by this study. These include the further development of GCMs with isotopic tracer schemes, and the utilisation of such models for the simulation of past climates. The importance of physical parameterisations of convection and land surface processes for the simulation of isotopic ratios could be investigated via an isotope model intercomparison project, as planned by the IAEA in the near future. Further observational time series of stable water isotope ratios in atmospheric vapour, precipitation and in the upper ocean would assist in verifying the modelled isotopic distributions.

Additional simulations of the LGM and other palaeo-epochs such as the mid-Holocene are required to further constrain the boundary conditions consistent with palaeo-records, as discussed above. Ensembles of model simulations as well as the use of a range of models could be used to improve the robustness of the results in a similar manner to the PMIP intercomparison study. The use of coupled atmosphere–ocean models or atmospheric GCMs coupled to slab ocean models would allow the investigation of changes in the isotopic signal associated with interannual variability such as ENSO under past climate conditions. In order to carry out more detailed comparisons with individual proxy records, parameterisations of the isotopic processes associated with coral growth or ice core deposition may also be incorporated into isotopic tracer schemes.

Appendix A

List of Common Abbreviations

AIR	All India Rainfall
AMIP	Atmospheric Model Intercomparison Project
BP	Before present
CLIMAP	Climate Long-range Investigation, Mapping and Prediction
DJF	December - January - February
ECHAM	European Centre Hamburg
ECMWF	European Centre for Medium-range Weather Forecasting
ENSO	El Niño - Southern Oscillation
EOF	Empirical Orthogonal Function
GCM	General Circulation Model
GISS	Goddard Institute for Space Studies
GNIP	Global Network of Isotopes in Precipitation
GSO	Global Sea-water Oxygen-18 (database)
IPCC	Intergovernmental Panel on Climate Change
ITZC	Inter-Tropical Convergence Zone
JJA	June - July - August
LGM	Last Glacial Maximum
LMD	Laboratoire de Météorologie Dynamique
MSLP	Mean sea level pressure
MUGCM	Melbourne University General Circulation Model
MWL	Meteoric Water Line
NCAR	National Center for Atmospheric Research
NCEP	National Centers for Environmental Prediction
NGDC	National Geophysical Data Center
PD	Present day

PDO	Pacific Decadal Oscillation
PMIP	Paleoclimate Modeling Intercomparison Project
SACZ	South Atlantic Convergence Zone
SMOW	Standard Mean Ocean Water
SOI	Southern Oscillation Index
SPCZ	South Pacific Convergence Zone
SST	Sea surface temperature
TRIP	Total Runoff Integrating Pathways

References

Anderson, D., W. Prell, and N. Barrat, Estimates of sea surface temperature in the coral sea at the last glacial maximum, *Paleoceanography*, *4*, 615–627, 1989.

Araguás-Araguás, L., and K. Froehlich, Stable isotope composition of precipitation over Southeast Asia, *Journal of Geophysical Research*, *103*, 28,721–28,721, 1998.

Araguás-Araguás, L., K. Froehlich, and K. Rozanski, Deuterium and oxygen-18 isotopic composition of precipitation and atmospheric moisture, *Hydrological Processes*, *14*, 1341–1355, 2000.

Argete, A., and I. Simmonds, Comparison of temporal cloud variability simulated by a GCM with observations from the Nimbus-7 Satellite, *Atmósphera*, *9*, 1–21, 1996.

Arora, V. K., and G. J. Boer, A variable velocity flow routing algorithm for GCMs, *Journal of Geophysical Research*, *104*, 30,965–30,979, 1999.

Arora, V. K., F. H. S. Chiew, and R. B. Grayson, A river flow routing scheme for general circulation models, *Journal of Geophysical Research*, *104*, 14,347–14,357, 1999.

Baertschi, P., Absolute ^{18}O content of Standard Mean Ocean Water, *Earth and Planetary Science Letters*, *31*, 341–344, 1976.

Barnes, D. J., and J. M. Lough, On the nature and causes of density banding in massive coral skeletons, *Journal of Experimental Marine Biology and Ecology*, *167*, 91–108, 1993.

Barnes, D. J., R. B. Taylor, and J. M. Lough, On the inclusion of trace materials into massive coral skeletons. Part II: Distortions in skeletal records of annual climate cycles due to growth processes, *Journal of Experimental Marine Biology and Ecology*, *194*, 251–275, 1995.

Beck, J. W., Sea-surface temperature from coral skeletal strontium/calcium ratios, *Science*, *257*, 644–647, 1992.

Beck, J. W., J. Recy, F. Taylor, R. L. Edwards, and G. Cabioch, Abrupt changes in early Holocene tropical sea surface temperature derived from coral records, *Nature*, *385*, 705–707, 1997.

Berger, A. L., Long-term variations of daily insolation and quaternary climatic change, *Journal of Atmospheric Science*, *35*, 2362–2367, 1978.

Bigg, G. R., and E. J. Rohling, An oxygen isotope data set for marine waters, *Journal of Geophysical Research*, *105*, 8527–8535, 2000.

Bourke, W., B. McAvaney, K. Puri, and R. Thurling, Global modelling of atmospheric flow by spectral methods, in *Methods in Computational Physics*, edited by J. Chang, pp. 267–324, Academic Press, New York, 1977.

Bradley, R. S., *Paleoclimatology: Second Edition*, Academic Press, San Diego, Ca., 1999.

Bradley, R. S., H. F. Diaz, G. N. Kiladis, and J. K. Eischeid, ENSO signals in continental temperature and precipitation records, *Nature*, *327*, 497–501, 1987.

Bradley, R. S., M. Vuille, D. Hardy, and L. G. Thompson, Low latitude ice cores record Pacific sea surface temperatures, *Journal of Geophysical Research*, *30*, doi:10.1029/2002GL016,546, 2003.

Broecker, W. S., Oxygen isotope constraints on surface ocean temperatures, *Quaternary Research*, *26*, 121–134, 1986.

Broecker, W. S., Mountain glaciers: Recorders of atmospheric water vapour content, *Global Biogeochemical Cycles*, *11*, 589–597, 1997.

Bromwich, D. H., A. N. Rogers, P. Kallberg, R. I. Cullather, J. W. C. White, and K. J. Kreutz, ECMWF analyses and reanalyses depiction of ENSO signal in Antarctic precipitation, *Journal of Climate*, *13*, 1406–1420, 2000.

Brutsaert, W. A., The roughness length for water vapour, sensible heat and other scalars, *Journal of Atmospheric Science*, *32*, 2028–2031, 1975.

Bush, A. B. G., and S. G. H. Philander, The role of ocean-atmosphere interactions in tropical cooling during the Last Glacial Maximum, *Science*, *279*, 1341–1344, 1998.

Chappell, J., A. Omura, T. Esat, M. McCulloch, J. Pandolfi, Y. Ota, and B. Pillans, Reconciliation of late Quaternary sea levels derived from coral terraces at Huon Peninsula with deep sea oxygen isotope records, *Earth and Planetary Science Letters*, *141*, 227–236, 1996.

Charles, C. D., D. E. Hunter, and R. G. Fairbanks, Interaction between the ENSO and the Asian monsoon in a coral record of tropical climate, *Science*, *277*, 925–928, 1997.

Charles, C. D., D. Rind, R. Healy, and R. Webb, Tropical cooling and the isotopic composition of precipitation in general circulation model simulations of ice age climate, *Climate Dynamics*, *17*, 489–502, 2001.

Ciais, P., and J. Jouzel, Deuterium and oxygen 18 in precipitation: Isotopic model, including mixed cloud processes, *Journal of Geophysical Research*, *99*, 16,793–16,803, 1994.

CLIMAP Project Members, The surface of ice age earth: Quantitative geologic evidence is used to reconstruct boundary conditions for the climate 18,000 years ago, *Science*, *191*, 1131–1138, 1976.

CLIMAP Project Members, Seasonal reconstruction of the Earth's surface at the last glacial maximum, *Tech. Rep. 36*, Geological Society of America Chart Series, 1981.

Cobb, K. M., C. D. Charles, and D. E. Hunter, A central tropical Pacific coral demonstrates Pacific, Indian and Atlantic decadal climate connections, *Geophysical Research Letters*, *28*, 2209–2212, 2001.

Cole, J. E., and R. G. Fairbanks, The Southern Oscillation recorded in the oxygen isotopes of corals from Tarawa Atoll, *Paleoceanography*, *5*, 669–683, 1990.

Cole, J. E., R. G. Fairbanks, and G. T. Shen, Recent variability in the Southern Oscillation: Isotopic results from a Tarawa Atoll coral, *Science*, *260*, 1790–1793, 1993a.

Cole, J. E., D. Rind, and R. G. Fairbanks, Isotopic responses to interannual climate variability simulated by an atmospheric general circulation model, *Quaternary Science Reviews*, *12*, 387–406, 1993b.

Cole, J. E., D. Rind, R. Webb, J. Jouzel, and R. Healy, Climatic controls on interannual variability of precipitation δ^{18}O: Simulated influence of temperature, precipitation amount and vapour source region, *Journal of Geophysical Research*, *104*, 14,223–14,235, 1999.

Cole, J. E., R. B. Dunbar, T. R. McClanahan, and N. A. Muthiga, Tropical Pacific forcing of decadal SST variability in the western Indian Ocean over the past two centuries, *Science*, *287*, 617–619, 2000.

Craig, H., Isotopic variations in meteoric waters, *Science*, *133*, 1702–1703, 1961.

Craig, H., and L. I. Gordon, Deuterium and oxygen-18 variations in the ocean and marine atmosphere, in *Stable Isotopes in Oceanic Studies and Paleotemperatures*, Laboratory of Geological and Nuclear Science, Pisa, Italy, 1965.

Craig, H., L. I. Gordon, and Y. Horibe, Isotopic exchange effects in the evaporation of water, *Journal of Geophysical Research*, *68*, 5079–5087, 1963.

Crowley, T. J., CLIMAP SSTs re-revisited, *Climate Dynamics*, *16*, 241–255, 2000.

Dai, A., and T. M. L. Wigley, Global patterns of ENSO-induced precipitation, *Geophysical Research Letters*, *27*, 1283–1286, 2000.

Dai, A., I. Y. Fung, and A. D. Del Genio, Surface observed global land precipitation variations during 1900–1988, *Journal of Climate*, *10*, 2943–2962, 1997.

Dansgaard, W., Stable isotopes in precipitation, *Tellus*, *16*, 436–468, 1964.

De Deckker, P., N. J. Tapper, and S. van der Kaars, The status of the Indo-Pacific Warm Pool and adjacent land at the Last Glacial Maximum, *Global and Planetary Change*, *35*, 25–35, 2003.

De Villiers, S., B. K. Nelson, and A. R. Chivas, Biological controls on coral Sr/Ca and δ^{18}O reconstructions of sea surface temperatures, *Science*, *269*, 1247–1249, 1995.

De Wit, J. C., C. M. V. der Straaten, and W. G. Mook, Determination of the absolute hydrogen isotope ratio of V-SMOW and SLAP, *Geostandards Newsletter*, *4*, 33–36, 1980.

Deardorff, J., A parameterization of ground-surface moisture content for use in atmospheric prediction models, *Journal of Applied Meteorology*, *16*, 1182–1185, 1977.

Delaygue, G., J. Jouzel, and J.-C. Dutay, Oxygen 18-salinity relationship simulated by an oceanic general circulation model, *Earth and Planetary Science Letters*, *178*, 113–123, 2000.

Delaygue, G., E. Bard, C. Rollion, J. Jouzel, M. Stievenard, J.-C. Duplessy, and G. Ganssen, Oxygen isotope/salinity relationship in the northern Indian Ocean, *Journal of Geophysical Research*, *106*, 4565–4574, 2001.

Dommenget, D., and M. Latif, A cautionary note on the interpretation of EOFs, *Journal of Climate*, *15*, 216–225, 2002.

Dong, B., and P. J. Valdes, Simulations of the Last Glacial Maximum climate using a general circulation model: Prescribed versus computed sea surface temperatures, *Climate Dynamics*, *14*, 571–591, 1998.

Druffel, E. R. M., and S. Griffen, Large variations of surface ocean radiocarbon: Evidence of circulation changes in the southwestern Pacific, *Journal of Geophysical Research*, *98*, 20,249–20,259, 1993.

Dunbar, R. B., B. K. Linsley, and G. M. Wellington, Eastern Pacific corals monitor El Niño/Southern Oscillation, precipitation and sea surface temperature variability over the past three centuries, in *Climate variations and Forcing Mechanisms over the Last 2000 Years*, edited by P. D. Jones, R. S. Bradley, and J. Jouzel, pp. 375–407, Springer, Berlin, 1996.

Duplessy, J. C., Oxygen isotope studies and Quaternary marine climates, in *Climate variations and variability: Facts and theories*, edited by A. Berger, pp. 181–192, D. Reidel, Norwell, Mass., 1981.

Duplessy, J. C., E. Bard, L. Labeyrie, J. Duprat, and J. Moyes, Oxygen isotope records and salinity changes in the Northeastern Atlantic Ocean during the last 18,000 years, *Paleoceanography*, *8*, 341–350, 1993.

Ehhalt, D. H., Vertical profiles of HTO, HDO and H_2O in the troposphere, *Tech. Rep. NCAR-TN/STR-100*, National Center for Atmospheric Research, Boulder, Co., 1974.

Evans, M. N., R. G. Fairbanks, and J. L. Rubenstone, A proxy index of ENSO teleconnections, *Nature*, *394*, 732–733, 1998.

Fairbanks, R. G., A 17,000-year glacio-eustatic sea level record: Influence of glacial melting rates on Younger Dryas event and deep-ocean circulation, *Nature*, *342*, 637–642, 1989.

Fairbanks, R. G., Evaluating climate indices and their geochemical proxies measured in corals, *Coral Reefs*, *16*, 93–100, 1997.

Farrera, I., et al., Tropical climates at the Last Glacial Maximum: A new synthesis of terrestrial palaeoclimate data. 1. Vegetation, lake-levels and geochemistry, *Climate Dynamics*, *15*, 823–856, 1999.

Fels, S. B., and M. D. Schwarzkopf, The simplified exchange approximation: A new method for radiative transfer calculations, *Journal of Atmospheric Science*, *32*, 1475–1488, 1975.

Fennessy, M. J., et al., The simulated Indian monsoon: A GCM sensitivity study, *Journal of Climate*, *7*, 33–43, 1994.

Gadgil, S., and S. Sajani, Monsoon precipitation in the AMIP runs, *Climate Dynamics*, *14*, 659–689, 1998.

Gagan, M. K., A. R. Chivas, and P. J. Isdale, High-resolution isotopic records from corals using ocean temperature and mass spawning chronometers, *Earth and Planetary Science Letters*, *121*, 549–558, 1994.

Gagan, M. K., L. K. Ayliffe, D. Hopley, J. A. Cali, G. E. Mortimer, J. Chappell, M. T. McCulloch, and M. J. Head, Temperature and surface-ocean water balance of the mid-Holocene tropical western Pacific, *Science*, *279*, 1014–1018, 1998.

Gagan, M. K., L. K. Ayliffe, J. W. Beck, J. E. Cole, E. R. M. Druffel, R. B. Dunbar, and D. P. Schrag, New views of tropical paleoclimates from corals, *Quaternary Science Reviews*, *19*, 45–64, 2000.

Gat, J. R., and E. Matsui, Atmospheric water balance in the Amazon basin: An isotopic evapotranspiration model, *Journal of Geophysical Research*, *96*, 13,179–13,188, 1991.

Gates, W. L., and A. B. Nelson, A new (revised) tabulation of the Scripps topography on a one-degree grid. Part 1: Terrain heights, *Tech. Rep. R-1276-1-ARPA*, The Rand Corporation, Santa Monica, Ca., 1975.

Gates, W. L., et al., An overview of the results of the Atmospheric Model Intercomparison Project (AMIP I), *Bulletin of the American Meteorological Society*, *80*, 29–55, 1999.

Gordon, H. B., and S. P. O'Farrell, Transient climate change in the CSIRO coupled model with dynamic sea ice, *Monthly Weather Review*, *125*, 875–907, 1997.

Grootes, P. M., M. Stuiver, L. G. Thompson, and E. Mosley-Thompson, Oxygen isotope changes in tropical ice, Quelccaya, Peru, *Journal of Geophysical Research*, *94*, 1187–1187, 1989.

Grootes, P. M., M. Stuiver, J. W. C. White, S. Johnsen, and J. Jouzel, Comparison of oxygen isotope records from the GISP2 and GRIP Greenland ice cores, *Nature*, *366*, 552–554, 1993.

Guilderson, T. P., R. G. Fairbanks, and J. L. Rubenstone, Tropical temperature variations since 20,000 years ago: Modulating interhemispheric climate change, *Science*, *263*, 663–665, 1994.

Guilderson, T. P., R. G. Fairbanks, and J. L. Rubenstone, Tropical Atlantic coral oxygen-isotopes: Glacial-interglacial sea surface temperatures and climate change, *Marine Geology*, *172*, 75–89, 2001.

Hahn, D. J., and J. Shukla, An apparent relationship between Eurasian snow cover and Indian monsoon rainfall, *Journal of Atmospheric Science*, *33*, 2461–2462, 1976.

Harangozo, S., A search for ENSO teleconnections in the west Antarctic Peninsula climate in Austral winter, *International Journal of Climatology*, *20*, 663–679, 2000.

Henderson, K. A., L. G. Thompson, and P. N. Lin, The recording of El Niño in the ice core δ^{18}O records from Nevado Huascaran, Peru, *Journal of Geophysical Research*, *104*, 31,053–31,065, 1999.

Hewitt, C. D., A. J. Broccoli, J. F. B. Mitchell, and R. J. Stouffer, A coupled model study of the last glacial maximum: Was part of the North Atlantic relatively warm?, *Geophysical Research Letters*, *28*, 1571–1574, 2001.

Hirst, A. C., S. P. O'Farrell, and H. B. Gordon, Comparison of a coupled ocean-atmosphere model with and without oceanic eddy-induced advection, *Journal of Climate*, *13*, 139–163, 2000.

Hoffmann, G., and M. Heimann, Water isotope modeling in the Asian monsoon region, *Quaternary International*, *37*, 115–128, 1997.

Hoffmann, G., and M. Heimann, Water isotope module of the ECHAM atmospheric general circulation model: A study on timescales from days to several years, *Journal of Geophysical Research*, *103*, 16,871–16,896, 1998.

Hoffmann, G., et al., Coherent isotope history of Andean ice cores over the last century, *Geophysical Research Letters*, *30*, doi:10.1029/2002GL014,870, 2003.

Hostetler, S. W., and A. C. Mix, Reassessment of ice-age cooling of the tropical ocean and atmosphere, *Nature*, *399*, 673–676, 1999.

Hunt, B. G., A model study of some aspects of soil hydrology relevant to climatic modelling, *Quarterly Journal of the Royal Meteorological Society*, *111*, 1071–1085, 1985.

Hurrell, J. W., and K. E. Trenberth, Global sea surface temperature analyses: Multiple problems and their implications for climate analysis, modeling and reanalysis, *Bulletin of the American Meteorological Society*, *80*, 2661–2678, 1999.

IAEA/WMO, Global Network of Isotopes in Precipitation. The GNIP Database, Accessible at: http://isohis.iaea.org, 2001.

Ichiyanagi, K., A. Numaguti, and K. Kato, Interannual variation of stable isotopes in Antarctic precipitation in response to El Niño-Southern Oscillation, *Geophysical Research Letters*, *29*, doi:10.1029/2000GL012,815, 2002.

Imbrie, J., and N. Kipp, A new micropaleontological method for quantitative paleoclimatology: Application to a late Pleistocene Caribbean core, in *The Late Cenezoic Glacial Ages*, edited by K. K. Turekian, pp. 71–179, Yale University Press, New Haven, 1971.

IPCC, *Climate Change 2001: The Scientific Basis*, Cambridge University Press, Cambridge, 2001.

Johnsen, S., W. Dansgaard, H. B. Clausen, and C. C. Langway, Oxygen isotope profiles through Antarctic and Greenland ice sheets, *Nature*, *235*, 429–434, 1972.

Johnsen, S., W. Dansgaard, and J. W. C. White, The origin of Arctic precipitation under present and glacial conditions, *Tellus*, *41*, 452–469, 1989.

Joussaume, S., and J. Jouzel, Paleoclimate tracers: An investigation using an atmospheric general circulation model under ice age conditions. 2. Water isotopes, *Journal of Geophysical Research*, *98*, 2807–2830, 1993.

Joussaume, S., and K. E. Taylor, Status of the Paleoclimate Modelling Intercomparison Project (PMIP), in *Proceedings of the First International AMIP Scientific Conference*, pp. 425–430, 1995.

Joussaume, S., R. Sadourny, and J. Jouzel, A general circulation model of water isotope cycles in the atmosphere, *Nature*, *311*, 24–29, 1984.

Jouzel, J., and L. Merlivat, Deuterium and oxygen 18 in precipitation: Modeling of the isotopic effects during snow formation, *Journal of Geophysical Research*, *89*, 11,749–11,757, 1984.

Jouzel, J., C. Lorius, J. R. Petit, C. Genthon, N. I. Barkov, V. M. Kotlyakov, and V. M. Petrov, Vostok ice core: A continuous isotope temperature record over the last climatic cycle (160,000 years), *Nature*, *329*, 403–408, 1987a.

Jouzel, J., G. L. Russell, R. J. Suozzo, R. D. Koster, W. C. White, and W. S. Broecker, Simulations of the HDO and $H_2^{18}O$ atmospheric cycles using the

NASA GISS general circulation model: The seasonal cycle for present-day conditions, *Journal of Geophysical Research*, *92*, 14,739–14,760, 1987b.

Jouzel, J., R. D. Koster, R. J. Suozzo, and G. L. Russell, Stable water isotope behaviour during the last glacial maximum: A general circulation model analysis, *Journal of Geophysical Research*, *99*, 25,791–25,801, 1994.

Jouzel, J., et al., Validity of temperature reconstruction from water isotopes in ice cores, *Journal of Geophysical Research*, *102*, 26,471–26,487, 1997.

Juillet-Leclerc, A., and G. A. Schmidt, A calibration of the oxygen isotope paleothermometer of coral aragonite from Porites, *Geophysical Research Letters*, *28*, 4135–4138, 2001.

Juillet-Leclerc, A., J. Jouzel, L. Labeyrie, and S. Joussaume, Modern and last glacial maximum sea surface δ^{18}O derived from an Atmospheric General Circulation Model, *Earth and Planetary Science Letters*, *146*, 591–605, 1997.

Kalnay, E., et al., The NCEP/NCAR 40-year reanalysis project, *Bulletin of the American Meteorological Society*, *77*, 437–471, 1996.

Kang, I. S., et al., Intercomparison of the climatological variations of Asian summer monsoon precipitation simulated by 10 GCMs, *Climate Dynamics*, *19*, 383–395, 2002a.

Kang, I. S., et al., Intercomparison of Atmospheric GCM simulated anomalies associated with the 1997/1998 El Niño, *Journal of Climate*, *15*, 2791–2805, 2002b.

Kendall, C., and J. J. McDonell, *Isotopic Tracers in Catchment Hydrology*, Elsevier Science, Berlin, 1998.

Kiladis, G. N., and H. Diaz, Global climatic anomalies associated with extremes in the Southern Oscillation, *Journal of Climate*, *2*, 437–471, 1989.

Knutson, D. W., R. W. Buddemeier, and S. V. Smith, Coral chronometers–seasonal growth bands in reef corals, *Science*, *177*, 270–272, 1972.

Koster, R. D., D. P. de Valpine, and J. Jouzel, Continental water recycling and $H_2^{16}O$ concentrations, *Geophysical Research Letters*, *20*, 2215–2218, 1993.

Koutavas, A., J. Lynch-Stieglitz, T. M. Marchitto, and J. P. Sachs, El-Niño-like pattern in ice age tropical Pacific sea surface temperature, *Science*, *297*, 226–230, 2002.

Laval, K., and L. Picon, Effect of a change of the surface albedo of the Sahel on climate, *Journal of Atmospheric Science*, *43*, 2418–2429, 1986.

Laval, K., R. Raghava, J. Polchev, R. Sadourney, and M. Forichon, Simulation of the 1987 and 1988 Indian monsoons using the LMD GCM, *Journal of Climate*, *9*, 3357–3371, 1996.

Lawrence, J., and S. Gedzelman, Low stable isotope ratios of tropical cyclone rains, *Geophysical Research Letters*, *23*, 527–530, 1996.

Lawrence, J., and S. Gedzelman, Stable isotope ratios of rain and vapour in 1995 hurricanes, *Journal of Geophysical Research*, *103*, 11,381–11,400, 1998.

Le Bec, N., A. Juillet-Leclerc, T. Corrège, D. Blamart, and T. Delcroix, A coral δ^{18}O record of ENSO driven sea surface salinity variability in Fiji (south-western tropical Pacific), *Geophysical Research Letters*, *27*, 3897–3900, 2000.

Levitus, S., Climatological Atlas of the World Ocean, *Tech. Rep. 13*, NOAA, Washington DC, 1982.

Linsley, B. K., R. B. Dunbar, G. M. Wellington, and D. A. Mucciarone, A coral-based reconstruction of Intertropical Convergence Zone variability over Central America since 1707, *Journal of Geophysical Research*, *99*, 9,977–9,994, 1994.

Lough, J. M., Rainfall variations in Queensland, Australia: 1891–1986, *International Journal of Climatology*, *11*, 745–768, 1991.

Louis, J., A parametric model of vertical eddy fluxes in the atmosphere, *Boundary Layer Meteorology*, *17*, 187–202, 1979.

Majoube, M., Fractionnement en oxygène 18 et en deuterium entre l'eau et sa vapeur, *Journal de Chimie Physique et de Physico-chimie Biologique*, *10*, 1423–1436, 1971a.

Majoube, M., Fractionnement en oxygène 18 entre la glace et la vapeur d'eau, *Journal de Chimie Physique*, *68*, 625–636, 1971b.

Manabe, S., J. Smagorinsky, and R. Strickler, Simulated climatology of a general circulation model with a hydrologic cycle, *Monthly Weather Review*, *93*, 769–798, 1965.

Mantua, N. J., S. R. Hare, Y. Zhang, J. M. Wallace, and R. C. Francis, A Pacific interdecadal climate oscillation with impacts on salmon production, *Bulletin of the American Meteorological Society*, *78*, 1069–1079, 1997.

Martinez, J. I., P. De Deckker, and A. R. Chivas, New estimates for salinity changes in the Western Pacific Warm Pool during the Last Glacial Maximum: Oxygen-isotope evidence, *Marine Micropaleontology*, *32*, 311–340, 1997.

Mathieu, R., D. Pollard, J. E. Cole, J. W. C. White, R. S. Webb, and S. L. Thompson, Simulation of stable water isotope variations by the GENESIS GCM for modern conditions, *Journal of Geophysical Research*, *107*, doi:10.1029/2001JD900,255, 2002.

McBride, J. L., and N. Nicholls, Seasonal relationships between Australian rainfall and the Southern Oscillation, *Monthly Weather Review*, *111*, 1998–2004, 1983.

McConnaughey, T. A., 13C and 18O isotopic disequilibrium in biological carbonates, *Geochimica et Cosmochimica Acta*, *53*, 151–162, 1989.

McCulloch, M. T., M. K. Gagan, G. E. Mortimer, A. R. Chivas, and P. J. Isdale, A high-resolution Sr/Ca and δ^{18}O coral record from the Great Barrier Reef, Australia, and the 1982-1983 El Niño, *Geochimica et Cosmochimica Acta*, *58*, 2747–2754, 1994.

McPeters, R. D., A. J. Krueger, P. K. Bhartia, and J. R. Herman, Nimbus-7 Total Ozone Mapping Spectrometer (TOMS) Data Products User's Guide, *Tech. Rep. 1384*, NASA Goddard Space Flight Center, 1996.

Meehl, G. A., A reexamination of the mechanisms of the semiannual oscillation in the Southern Hemisphere, *Journal of Climate*, *4*, 911–925, 1991.

Meehl, G. A., Influence of the land surface on the Asian summer monsoon: External conditions versus internal feedbacks, *Journal of Climate*, *7*, 1033–1049, 1994.

Merlivat, L., Molecular diffusivities of $H_2^{16}O$, $HD^{18}O$ and $H_2^{18}O$ in gases, *Journal of Chemical Physics*, *69*, 2864–2871, 1978.

Merlivat, L., and J. Jouzel, Global climatic interpretation of the deuterium-oxygen-18 relationship for precipitation, *Journal of Geophysical Research*, *80*, 5455–5467, 1979.

Merlivat, L., and G. Nief, Fractionnement isotopique lors des changements d'ètat solide-vapeur et liquide-vapeur de l'eau à des températures inférieures à 0°C, *Tellus*, *19*, 122–127, 1967.

Noone, D. C., A physical assessment of variability and climate signals in Antarctic precipitation and the stable water isotope record, Ph.D. thesis, University of Melbourne, Melbourne, Australia, 2001.

Noone, D. C., and I. Simmonds, GCM study of synoptic influences on the isotope record in Antarctic ice cores, *Pages News*, *9*, 8–9, 2001.

Noone, D. C., and I. Simmonds, Associations between $\delta^{18}O$ of water and climate parameters in a simulation of atmospheric circulation for 1979–1995, *Journal of Climate*, *15*, 3150–3169, 2002.

Noone, D. C., J. Turner, and R. Mulvaney, Atmospheric signals and characteristics of accumulation in Dronning Maud Land, Antarctica, *Journal of Geophysical Research*, *104*, 19,191–19,211, 1999.

Oki, T., and Y. C. Sud, Design of Total Runoff Integrating Pathways (TRIP): A global river channel network, *Earth Interactions*, *2*, E1013, 1998.

Parthasarathy, B., A. A. Munot, and D. R. Kothawale, All-India monthly and seasonal rainfall series: 1871-1993, *Theoretical and Applied Climatology*, *49*, 217–224, 1994.

Paul, A., S. Mulitza, J. Patzold, and T. Wolff, Simulation of oxygen isotopes in a global ocean model, in *Use of Proxies in Paleoceanography: Examples from the South Atlantic*, edited by G. Fischer and G. Wefer, pp. 655–686, Springer-Verlag, Berlin, 1999.

Peixoto, J. P., and A. H. Oort, *Physics of Climate*, American Institute of Physics, New York, 1992.

Peltier, W. R., Ice age paleotopography, *Science*, *265*, 195–201, 1994.

Philander, S. G., *El Niño, La Niña and the Southern Oscillation*, Academic Press, San Diego, 1990.

Pierrehumbert, R. T., Huascaran δ^{18}O as an indicator of tropical climate during the Last Glacial Maximum, *Geophysical Research Letters*, *26*, 1345–1348, 1999.

Pinot, S., G. Ramstein, S. P. Harrison, I. C. Prentice, J. Guiot, M. Stute, and S. Joussaume, Tropical paleoclimates of the Last Glacial Maximum: Comparison of the Paleoclimate Modeling Intercomparison Project (PMIP) simulations and paleodata, *Climate Dynamics*, *15*, 857–874, 1999.

Pitman, A. J., Z. L. Yang, J. G. Cogley, and A. Henderson-Sellers, Description of Bare Essentials of Surface Transfer for the Bureau of Meteorology Research Centre AGCM, *Tech. Rep. 32*, Bureau of Meteorology Research Centre, Melbourne, Australia, 1991.

Quinn, T. M., F. Taylor, and T. Crowley, A 173 year stable isotope record from tropical South Pacific coral, *Quaternary Science Reviews*, *12*, 407–418, 1993.

Ramirez, E., et al., A new Andean deep ice core from Nevado Illimani (6350m), Bolivia, *Earth and Planetary Science Letters*, *212*, 337–350, 2003.

Raynaud, D., J. Jouzel, J. M. Barnola, J. Chappellaz, R. J. Delmas, and C. Lorius, The ice core record of greenhouse gases, *Science*, *259*, 926–934, 1993.

Rayner, N. A., E. B. Horton, D. E. Parker, C. K. Folland, and R. B. Hackett, Version 2.2 of the Global sea-Ice and Sea Surface Temperature Data Set, 1903-1994, *Tech. Rep. 74*, Hadley Centre, United Kingdom, 1996.

Reynolds, R. W., A real-time global sea surface temperature analysis, *Journal of Climate*, *1*, 75–86, 1988.

Rind, D., Components of the ice age circulation, *Journal of Geophysical Research*, *92*, 4241–4281, 1987.

Rind, D., Relating paleoclimate data and past temperature gradients: Some suggestive rules, *Quaternary Science Reviews*, *19*, 381–390, 2000.

Rind, D., and D. Peteet, Terrestrial conditions at the last glacial maximum and CLIMAP sea-surface temperature estimates: Are they consistent?, *Quaternary Research*, *24*, 1–22, 1985.

Rohling, E. J., and G. R. Bigg, Paleosalinity and δ^{18}O: A critical assessment, *Journal of Geophysical Research*, *103*, 1307–1318, 1998.

Ropelewski, C. F., and M. S. Halpert, Quantifying Southern Oscillation – precipitation relationships, *Journal of Climate*, *9*, 1042–1059, 1996.

Rostek, F., G. Ruhland, F. C. Bassinot, P. J. Muller, L. D. Labeyrie, Y. Lancelot, and E. Bard, Reconstructing sea surface temperatures and salinity using δ^{18}O and alkenone records, *Nature*, *364*, 319–312, 1993.

Rozanski, K., C. Sonntag, and K. O. Munnich, Factors controlling the stable isotopic composition of European precipitation, *Tellus*, *34*, 142–150, 1982.

Rozanski, K., L. Araguás-Araguás, and R. Gonfiantini, Isotopic patterns in model global precipitation, in *Climate Change in Continental Isotopic Records*, edited by P. K. Swart, K. C. Lohman, J. McKenzie, and S. Savin, Geophysical Monograph No. 78, pp. 1–36, Washington, 1993.

Russell, G. L., and J. R. Miller, Global river runoff calculated from a global atmospheric general circulation model, *Journal of Hydrology*, *117*, 241–254, 1990.

Sausen, R., S. Schubert, and L. Dumenil, A model of river runoff for use in coupled atmosphere-ocean models, *Journal of Hydrology*, *155*, 337–352, 1994.

Schmidt, G. A., Oxygen-18 variation in a global ocean model, *Geophysical Research Letters*, *25*, 1201–1204, 1998.

Schmidt, G. A., Error analysis of paleosalinity calculations, *Paleoceanography*, *14*, 422–429, 1999a.

Schmidt, G. A., Forward modeling of carbonate proxy data from planktonic foraminifera using oxygen isotope tracers in a global ocean model, *Paleoceanography*, *14*, 482–497, 1999b.

Schmidt, G. A., G. Hoffmann, and D. Thresher, Isotopic tracers in coupled models — A new paleo-tool, *Pages News*, *9*, 10–11, 2001.

Schwarzkopf, M. D., and S. B. Fels, The simplified exchange method revised: An accurate, rapid method for computation of infrared cooling rates and fluxes, *Journal of Geophysical Research*, *96*, 9075–9096, 1991.

Siegenthaler, U., and H. Oeschger, Correlation of O-18 in precipitation with temperature and altitude, *Nature*, *285*, 314–317, 1980.

Simmonds, I., The analysis of the ‘spin-up’ of a general circulation model, *Journal of Geophysical Research*, *90*, 5637–5660, 1985.

Simmonds, I., and W. F. Budd, A simple parameterization of ice leads in a GCM and the sensitivity of climate to a change in Antarctic ice concentrations, *Annals of Glaciology*, *14*, 266–269, 1990.

Simmonds, I., and W. F. Budd, Sensitivity of the Southern Hemisphere circulation to leads in the Antarctic ice pack, *Quarterly Journal of the Royal Meteorological Society*, *117*, 1003–1024, 1991.

Simmonds, I., and P. Hope, Seasonal and regional responses to changes in Australian soil moisture conditions, *International Journal of Climatology*, *10*, 1105–1139, 1998.

Simmonds, I., and T. H. Jacka, Relationships between the interannual variability of Antarctic sea ice and the Southern Oscillation, *Journal of Climate*, *8*, 637–647, 1995.

Simmonds, I., and I. N. Smith, The effect of the prescription of zonally-uniform sea surface temperatures in a general circulation model, *Journal of Climatology*, *6*, 641–659, 1986.

Simmonds, I., M. Dix, P. Rayner, and G. Trigg, Local and remote response to zonally uniform sea-surface temperature in a July general circulation model, *International Journal of Climatology*, *9*, 111–131, 1989.

Simmonds, I., D. Bi, and P. Hope, Atmospheric water vapour flux and its association with rainfall over China in summer, *Journal of Climate*, *12*, 1353–1367, 1999.

Slingo, J. M., M. Blackburn, A. Betts, R. Brugge, B. Hoskins, M. Miller, and L. Clark-Steenman, Mean climate and transience in the tropics of the

UGAMP GCM: Sensitivity to convective parameterisation, *Quarterly Journal of the Royal Meterological Society*, *120*, 881–922, 1994.

Smith, I. N., A GCM simulation of global climate interannual variability: 1950-1988, *Journal of Climate*, *8*, 709–718, 1995.

Smith, S. R., and C. R. Stearns, Antarctic pressure and temperature anomalies surrounding the minimum in the Southern Oscillation Index, *Journal of Geophysical Research*, *98*, 13,071–13,083, 1993.

Sonzogni, C., E. Bard, and F. Rostek, Tropical sea surface temperature during the last glacial period: A view based on alkenones in Indian Ocean sediments, *Quaternary Science Reviews*, *17*, 1185–1201, 1998.

Sperber, K. R., and T. N. Palmer, Interannual tropical rainfall variability in general circulation model simulations associated with the Atmospheric Modelling Intercomparison Project, *Journal of Climate*, *9*, 2727–2750, 1996.

Sperber, K. R., S. Hameed, G. L. Potter, and J. S. Boyle, Simulation of the northern summer monsoon in the ECMWF model: Sensitivity to horizontal resolution, *Monthly Weather Review*, *122*, 2461–2481, 1994.

Stewart, M. K., Stable isotope fractionation due to evaporation and isotopic exchange of falling waterdrops: Applications to atmospheric processes and evaporation from lakes, *Journal of Geophysical Research*, *80*, 1133–1146, 1975.

Stott, L., C. Poulsen, S. Lund, and R. Thunell, Super ENSO and global climate oscillations at millenial time scales, *Science*, *297*, 222–226, 2002.

Strain, P. M., and F. C. Tan, Seasonal evolution of oxygen isotope-salinity relationships in high-latitude surface waters, *Journal of Geophysical Research*, *98*, 14,589–14,598, 1993.

Stute, M., M. Forster, H. Frischkom, A. Serejo, J. F. Clark, P. Schlosser, W. S. Broecker, and G. Bonani, Cooling of tropical Brazil (5°C) during the Last Glacial Maximum, *Science*, *256*, 379–383, 1995.

Taylor, C. B., The vertical variations of the isotopic concentrations of tropospheric water vapour over continental Europe and their relationship to tropospheric structure, *Tech. Rep. INS-R-107*, DSIR, Lower Hutt, New Zealand, 1972.

Taylor, R. B., D. J. Barnes, and J. M. Lough, On the inclusion of trace materials into massive coral skeletons: 1. Materials occurring in the environment in short pulses, *Journal of Experimental Marine Biology and Ecology*, *185*, 225–278, 1995.

Thompson, L. G., Ice core evidence from Peru and China, in *Climate Since A.D. 1500*, edited by R. S. Bradley and P. D. Jones, Rutledge, London, 1992.

Thompson, L. G., Ice core evidence for climate change in the Tropics: Implications for our future, *Quaternary Science Reviews*, *19*, 19–35, 2000.

Thompson, L. G., E. Mosley-Thompson, P. M. Grootes, M. Pourchet, and S. Hastenrath, Tropical glaciers: Potential for ice core paleoclimate reconstructions, *Journal of Geophysical Research*, *89*, 4638–4646, 1984.

Thompson, L. G., E. Mosley-Thompson, J. F. Bolzan, and B. R. Koci, A 1500-year record of tropical precipitation in ice cores from Quelccaya ice cap, Peru, *Science*, *229*, 971–973, 1985.

Thompson, L. G., E. M.-T. Dansgaard, and P. M. Grootes, The Little Ice Age as recorded in the stratigraphy of the tropical Quelccaya ice cap, *Science*, *234*, 361–364, 1986.

Thompson, L. G., E. Mosley-Thompson, M. E. Davis, J. F. Bolzan, J. Dai, T. Yao, N. G. X. Wu, L. Klein, and Z. Xie, Holocene-late Pleistocene climatic ice core records from Qinghai-Tibetan Plateau, *Science*, *246*, 474–477, 1989.

Thompson, L. G., E. Mosley-Thompson, M. E. Davis, P. N. Lin, K. A. Henderson, J. Cole-Dai, and J. F. Bolzan, Late glacial stage and Holocene tropical ice core records from Huascaran, Peru, *Science*, *269*, 46–50, 1995.

Thompson, L. G., E. Mosley-Thompson, and K. A. Henderson, Ice-core palaeoclimate records in tropical South America since the Last Glacial Maximum, *Journal of Quaternary Science*, *15*, 377–394, 2000a.

Thompson, L. G., T. Yao, E. Mosley-Thompson, M. E. Davis, K. A. Henderson, and P. N. Lin, A high resolution millenial record of the South Asian monsoon from Himalayan ice cores, *Science*, *289*, 1916–1919, 2000b.

Thompson, L. G., et al., Tropical climate instability: The last glacial cycle from a Qinghai-Tibetan ice core, *Science*, *276*, 18211,825, 1997.

Thompson, L. G., et al., A 25,000-year tropical climate history from Bolivian ice cores, *Science*, *282*, 1858–1864, 1998.

Tiedtke, M., J. F. Geleyn, A. Hollingsworth, and J. F. Louis, ECMWF model-parameterization of sub-grid scale processes, *Tech. Rep. 10*, European Centre for Medium Range Weather Forecasts, Reading, England, 1979.

Treble, P., W. F. Budd, and P. Hope, Identification of synoptic-scale climatic patterns associated with rainfall δ^{18}O in southern Australian rainfall, *Journal of Hydrology*, submitted.

Trenberth, K. E., The definition of El Niño, *Bulletin of the American Meteorological Society*, *78*, 2771–2777, 1997.

Troup, A. J., The southern oscillation, *Quartely Journal of the Royal Meteorological Society*, *91*, 490–506, 1965.

Tudhope, A. W., Recent changes in climate in the far western equatorial Pacific and their relationship to the Southern Oscillation: Oxygen isotope records from massive corals, Papua New Guinea, *Earth and Planetary Science Letters*, *136*, 575–590, 1995.

Tudhope, A. W., C. P. Chilcott, M. T. McCulloch, E. R. Cook, J. Chappell, R. M. Ellam, D. W. Lea, J. M. Lough, and G. B. Shimmield, Variability in the El Niño-Southern Oscillation through a glacial-interglacial cycle, *Science*, *291*, 1511–1517, 2001.

Urban, F. E., J. E. Cole, and J. T. Overpeck, Influence of mean climate change on climate variability from a 155-year tropical Pacific coral record, *Nature*, *407*, 989–993, 2000.

Valdes, P. J., South American palaeoclimate model simulations: How reliable are the models?, *Journal of Quaternary Science*, *15*, 357–368, 2000.

Visser, K., R. Thunnel, and L. Stott, Magnitude and timing of temperature change in the Indo-Pacific warm pool during deglaciation, *Nature*, *421*, 152–155, 2003.

Vuille, M., R. S. Bradley, R. Healy, M. Werner, D. R. Hardy, L. G. Thompson, and F. Keimig, Modeling δ^{18}O in precipitation over the tropical Americas, Part II: Simulation of stable isotope signals in Andean ice cores, *Journal of Geophysical Research*, *108*, doi:10.1029/2001JD002,039, 2003a.

Vuille, M., R. S. Bradley, M. Werner, R. Healy, and F. Keimig, Modeling δ^{18}O in precipitation over the tropical Americas, Part I: Interannual variability and climatic controls, *Journal of Geophysical Research*, *108*, doi:10.1029/2001JD002,038, 2003b.

Wadley, M. R., G. R. Bigg, E. J. Rohling, and A. J. Payne, On modelling present-day and last glacial maximum oceanic δ^{18}O distributions, *Global and Planetary Change*, *32*, 89–109, 2002.

Walland, D. J., and I. Simmonds, Sub-grid-scale topography and the simulation of Northern Hemisphere snow cover, *International Journal of Climatology*, *16*, 961–982, 1996.

Walsh, K. J. E., I. Simmonds, and M. Collier, Sigma-coordinate calculation of topographically-forced baroclinicity around Antarctica, *Dynamics of Atmospheres and Oceans*, *33*, 1–29, 2000.

Wang, B., and Z. Fan, Choice of South Asian summer monsoon indices, *Bulletin of the American Meteorological Society*, *80*, 629–638, 1999.

Watkins, A. B., and I. Simmonds, Sensitivity of numerical prognoses to Antarctic sea ice distribution, *Journal of Geophysical Research*, *100*, 22,681–22,696, 1995.

Weaver, R. L., and V. Iroisi, Passive microwave data for snow and ice research: Planned products from the DMSP SMM/I system, *Tech. Rep. WCRP-18, WMO ID-No. 272*, World Meteorological Organisation, Geneva, 1988.

Webster, P. J., and N. Streten, Late Quaternary ice age climates of tropical Australasia: Intepretations and reconstructions, *Quaternary Research*, *10*, 279–309, 1978.

Webster, P. J., and S. Yang, Monsoon and ENSO: Selectively interacting systems, *Quarterly Journal of the Royal Meteorological Society*, *118*, 877–926, 1992.

Wellington, G. M., R. B. Dunbar, and G. Merlen, Calibration of stable oxygen isotope signatures in Galapagos corals, *Paleoceanography*, *11*, 467–480, 1996.

Werner, M., and M. Heimann, Modelling interannual variability of water isotopes in Greenland and Antarctica, *Journal of Geophysical Research*, *107*, doi:10.1029/2001JD900,253, 2002.

White, J. W. C., and S. D. Gedzelman, The isotopic composition of atmospheric water vapour and the concurrent meteorological conditions, *Journal of Geophysical Research*, *89*, 4937–4939, 1984.

Williamson, D. L., and P. J. Rasch, Two-dimensional semi-Lagrangian transport with shape-preserving interpolation, *Monthly Weather Review*, *117*, 102–129, 1989.

Williamson, D. L., and P. J. Rasch, Water vapour transport in the NCAR CCM2, *Tellus*, *46A*, 34–51, 1994.

Wilson, M. F., and A. Henderson-Sellers, A global archive of land cover and soils data for use in general circulation climate models, *Journal of Climatology*, *5*, 119–143, 1985.

Wu, X., I. Simmonds, and W. Budd, Modeling of Antarctic sea ice in a general circulation model, *Journal of Climate*, *10*, 593–609, 1997.

Xie, P., and P. A. Arkin, Global precipitation: A 17-year monthly analysis based on gauge observations, satellite estimates and numerical model outputs, *Bulletin of the American Meteorological Society*, *78*, 2539–2558, 1996.

Yang, Z. L., The sensitivity of a general circulation model to soil hydrology parameterization, Master's thesis, University of Melbourne, Melbourne, Australia, 1989.

Yao, T., Y. Shi, and L. G. Thompson, High resolution record of paleoclimate since the Little Ice Age from Tibetan ice cores, *Quaternary International*, *37*, 19–23, 1997.

Yao, T., V. Masson, and J. Jouzel, Relationship between δ^{18}O in precipitation and surface air temperatures in the Urumqi River Basin, east Tianshan Mountains, China, *Geophysical Research Letters*, *26*, 3473–3476, 1999.

Yapp, C. J., A model for the relationships between precipitation D/H ratios and precipitation intensity, *Journal of Geophysical Research*, *87*, 9614–9620, 1982.

Yu, G., B. Xue, S. Wang, and J. Liu, Lake records and LGM climate in China, *Chinese Science Bulletin*, *45*, 1158–1164, 2000.

Zhang, Y., J. M. Wallace, and D. S. Battisti, ENSO-like interdecadal variability: 1900–93, *Journal of Climate*, *10*, 1004–1020, 1997.

Zimmerman, U., D. H. Ehhalt, and K. O. Munnich, Soil-water movement and evapotranspiration: Changes in isotopic composition of the water, in *Proceedings of the IAEA Symposium on Isotope Hydrology*, pp. 567–584, Vienna, Austria, 1967.